NTNU – Trondheim
Norwegian University of
Science and Technology

Fault-tolerant Sensor Fusion Based on Inertial Measurements and GNSS

Torleiv Håland Bryne

Master of Science in Engineering Cybernetics
Submission date: June 2013
Supervisor: Thor Inge Fossen, ITK

Norwegian University of Science and Technology
Department of Engineering Cybernetics

NTNU
Norwegian University of
Science and Technology

Faculty of Information Technology,
Mathematics and Electrical Engineering
Department of Engineering Cybernetics

MSC THESIS DESCRIPTION SHEET

Name:	Torleiv Håland Bryne
Department:	Engineering Cybernetics
Thesis title (Norwegian):	Feiltolerant sensorintegrasjon basert på treghetssensorer og GNSS
Thesis title (English):	Fault-tolerant sensor fusion based on inertial measurements and GNSS

Thesis Description: The purpose of the thesis is to develop and simulate a fault-tolerant nonlinear observer for INS and GNSS sensor fusion to be utilized onboard a marine craft.

The following items should be considered:

1. Literature study on previous work should included Kalman filter methods and nonlinear observer theory for strapdown inertial navigation systems (INS).
2. Construct a vessel simulator in MATLAB for generation of INS and GNSS measurements. Include physical noise models for sensors and biases (drift).
3. Choose methods for signal quality check, voting and averaging. Test the methods using the simulator. Classify the different signal modes (freeze, normal, drift, etc.) and specify these as status variables, which can be used by the observer/sensor fusion system. Implement this in the simulator for testing of failure modes.
4. Design a fault-tolerant nonlinear observer for position, velocity and attitude (PVA) based on Mahony, Grip and co-authors and test single-point failures and other realistic failure situations.
5. Extend the nonlinear observer to include a vessel model and show how the vessel model can be used in a fault-tolerant observer design. The vessel model should be treated as additional measurement and combined with the sensors in the filter. Assume that the control inputs are measured and that the model parameters are known.
6. Conclude your results.

Start date:	2013-01-14
Due date:	2013-06-17

Thesis performed at:	Department of Engineering Cybernetics, NTNU
Supervisor:	Professor Thor I. Fossen, Dept. of Eng. Cybernetics, NTNU

This document was typeset in LaTeX.

Abstract

The standard observer for inertial navigation system (INS) have for many years been the extended Kalman filter. Due to extensive research, in recent years, on nonlinear observer applied with low-cost inertial sensors can this possible change.

Fault-tolerance are in many applications necessary. In dynamic positioning operations are fault-tolerance required. This thesis dealt with development of a fault-tolerant nonlinear observer for integration of INS and Global Navigation Satellite Systems (GNSS). Furthermore, the observer was applied for dynamic positioning, by developing a simulator to obtain vessel motion and sensor readings. The main focus were on GNSS errors and faults. Based on this were methods used to detect and handle outlier detection, sensor freeze, high variance of GNSS sensors and GNSS bias. Furthermore, a novel GNSS drift detection algorithm, applicable for marine vessel, was developed. Moreover, senor voting and sensor weighting was carried out by developing a voting algorithm. Also a model-based observer was utilized to provide redundant acceleration information to the INS.

The chosen INS/GNSS observer proved to be a good basis for the fault-tolerant additions. Outliers, sensor freeze, high variance and bias of the GNSS sensors were detected and handled accordingly. GNSS drift was detected and a possible drive-off situation was prevented. Furthermore, utilizing a model-based observer to obtain redundant acceleration information was shown to be successful.

Sammendrag

Standard estimatoren for treghetsnavigasjonssystem (TNS) har i mange år vært det utvidede Kalman filteret. På grunn av omfattende forskning på ulineære estimatorer, benyttet med lavkost treghetshetssensorer, kan dette være i endring.

Feiltoleranse er i mange applikasjoner nødvendig. I operasjoner med bruk av dynamiske posisjoneringssystemer er feiltoleranse en nødvendighet. Denne avhandlingen omhandler utviklingen av en feiltolerant unlinærestimator for integrering av TNS og et globalt satellittnavigasjonssystem. Videre ble estimatoren benyttet i dynamisk posisjonering ved å utvikle en simulator for å simulere et fartøys bevegelser samt sensormålinger. Hovedfokueset lå på feilhåndtering av målingene fra det globalt satellittnavigasjonssystemet. Basert på dette, ble metoder brukt å oppdage og håndtere avvikende målinger, sensor frys, høy sensorer varians og sensor bias. Videre ble en ny metode for å oppdage drift på målingene fra satellittnavigasjonssystemet, som kan brukes på marine farkoster, utviklet. Videre ble senor-voting og sensorvekting utført ved å utvikle en sensor-voting algoritme. Det ble også benytte en modellbasert estimator for å oppnå ekstra informasjon om fartøyets akselerasjon som kunne være til bruk for TNS.

Den valgte estimatoren, basert på TNS og et global satellittnavigasjonssystem viste seg å være et godt grunnlag for de feiltolerante utvidelsene. Avvikende målinger, sensor frys, satellittmålinger med høy varians samt målinger med bias ble oppdaget og håndtert deretter. Driftende målinger, fra satellittnavigasjonssystemet, ble detektert og en mulig drive-off situasjon ble forebygget. Bruken av en modellbasert estimator for å oppnå ekstra informasjon om fartøyets akselerasjon viste seg å være vellykket.

Preface

This master concludes the work done in TTK4900, the mandatory final evaluation of the Masters program given by the Department of Engineering Cybernetics, Norwegian University of Science and Technology.

Knowledge of ordinary differential equations and classical physics such as kinematics and kinetics will be useful to understand this text. Also, knowledge of SNAME notation and terminology of to describe motion of a marine vessel will be useful.

I would like to thank my supervisor, professor Thor Inge Fossen, for his guidance and enthusiasm during the course of work with this thesis. I am deeply appreciative.

A big thanks also goes to my colleagues, at the department's master office D134, for providing a good working environment during the course of this work. Of these people, a special thanks goes to Fredrik Alvenes and Andreas R. Dahl for valuable discussions and input. Also, a thanks goes out to Torstein Thode Kristoffersen for his feedback on this thesis.

Last, but not least. I would like to thank those three closest to me, for their enthusiasm, encouragement and for putting everything into perspective.

Torleiv Håland Bryne
Trondheim, Norway
June 17, 2013

Contents

List of Figures

List of Tables

List of Abbreviations

CPM	Control plant model
DA	Dead-Reckoning
dGNSS	Differential Global Navigation Satellite System
dGPS	Differential GPS
DNV	Det Norske Veritas
DOF	Degree of Freedom
DOF	Degrees of Freedom
DP	Dynamic Positioning
ECEF	Earth Centered Earth Fixed
EKF	Extended Kalman Filter
FTC	Fault-Tolerant Control
GC	Center of Gravity
GDOP	Geometric Dilution of Precision
GES	Globally Exponentially Stability
GNSS	Global Navigation Satellite Systems
HDOP	Horizontal Dilution of Precision
HPR	Hydroacoustic Positioning Reference
IMO	International Maritime Organization
IMU	Inertial Measurement Unit
INS	Inertial Navigation System
KF	Kalman Filter

ODE	Ordinary Differential Equation
PDOP	Position Dilution of Precision
PE	Persistent Excitation
PF	Particle Filter
PVA	Position, Velocity and Attitude
RK4	The Explicit Runge Kutta numerical Integration Method of Order Four
RLS	Recursive Least Squares
TDOP	Time Dilution of Precision
UAV	Unmanned Aerial Vehicle
UKF	Unscented Kalman Filter
VDOP	Vertical Dilution of Precision

Chapter 1

Introduction

1.1 Background

Part of the foundation for a successful, efficient and safe marine operation is to have access to a high quality and reliable position, velocity and attitude (PVA) estimates. Dynamic Positioning (DP) is an example of such an operation. The PVA estimates, together with the signal processing, are provided by the navigation system, as presented in Fossen (2011). In general such systems consists of one or more motion sensors in combination with filtering and observer software as, seen in Figure 1.1.

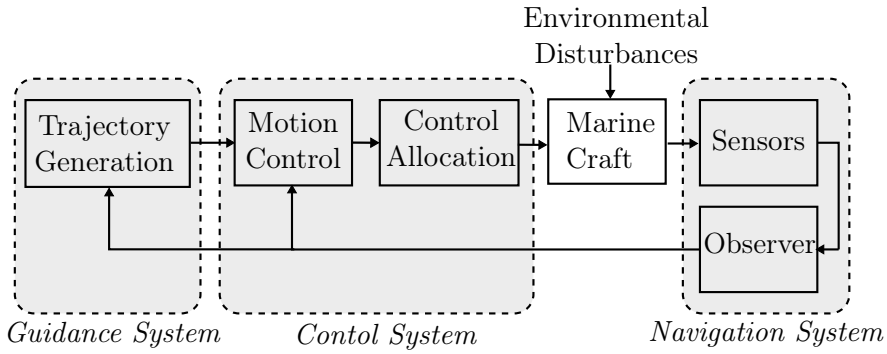

Figure 1.1: A simplified overview of the Guidance, Navigation and Control (GNC) signal flow. See Fossen (2011) for details.

Utilization of Global Navigation Satellite Systems (GNSS), such as the Global Positioning System (GPS), has become the industry standard for position reference during terrestrial navigation. The success of the GPS Navs-

tar system is part of the reason for the development of alternative satellite navigation systems, like Glonass and Gallileo.

More complex navigation systems for obtaining PVA estimates are Inertial Navigation Systems (INS). Such systems can be utilized to obtain PVA estimates without external measurements or if these measurements are not available for a certain period of time. This is called dead-reckoning (DA) and is performed by using inertial measurements in conjunction with a predictor or estimator. When the external measurements are lost a dynamic navigation model, like (2.19) - (2.22), is utilized to predict the movements of the vehicle [1]. However, as mentioned by Maybeck (1979, Ch.6), the INS position estimate will drift over time caused by integration of biased inertial measurements. This drift is unbounded if not compensated for. To compensate for such drift are external measurements, with no or low long term error used. Hence, the need for accurate PVA estimates during DA have resulted in INS to become high cost technology because of the quality demand regarding the sensors. However, this is now changing because of advances in low-cost MEMS based inertial sensors. An example of this is Iozan et al. (2012), where the Earth's rotation was measured with an MEMS gyroscope. Details regarding INS can be found in Section 2.2.

Fault-tolerance is vital in control applications. Equipment such as sensors can fail during operation. Hence, the control system must be able to handle such events. This also includes other sensor changes and dropouts. The International Maritime Organization (IMO) has proposed a number of safety regulations and recommendations to increase safety during marine operations. Guidelines regarding vessels equipped with a DP system can be found in e.g. Maritime Safety Commitee (MSC) Circular 645 (1994). One of these are the redundancy requirements. According to Sørensen (2012) the following redundancy definition can be made

[1] The dynamic navigation model of (2.19) - (2.22) is used for so called "flat Earth" navigation which is useful for stationkeeping operations like Dynamics Positioning

Definition 1.1. ***Redundancy*** *means the ability of a component or system to maintain or restore its function when a single fault has occurred. This property can be obtained by installation of multiple components, systems, or alternative means of performing a function.*

More information regarding DP requirements can be found in Det Norske Veritas (2011).

1.2 Previous Work

Inertial navigation for marine application is far from novel. From Fossen (2011) one can read that the first north seeking gyrocompass was patented as far back as 1908 by Anschutz. Whereas the Elmer Speery compass was patented and adopted by the US Navy in 1911. INS have evolved much since then. Nowadays, the state of the art gyroscopes are based on fiber optics and laser. However, as mentioned in the previous Section, new low-cost MEMS based units change the rules of the game because of the quality enhancement of low-cost units. Nowadays INS technology is adopted in e.g. cell phones, gaming controllers as well as in road and unmanned vehicles.

There are two types on inertial navigation systems. Gimbal systems and strapdown systems. The former mechanical aligns the gimbal platform to a fixed orientation in space when the body, which the Gimal platform is a attached to, moves. Inertial measurements are obtained by readout of the Gimbal platform's motion. Strapdown systems on the other hand is fixed to the body and moves with the body it is attached to. A short introduction to inertial navigation is given by Vik (2012). A rigorous study can by found in Britting (2010).

Kalman Filter Based Navigation

Kalman (1960) introduced the widely known linear stochastic estimator known as the *Kalman filter* (KF). The nonlinear extension, the *Extended Kalman filter* (EKF) was developed by Smith et al. (1962) and Schmidt (1966).

Maybeck (1979, Ch.6) illustrated how the extended Kalman filter can be utilized for inertial navigation purposes. For this application, the EKF is utilized to statistically minimize the error estimates of the parameters related to the navigation system. This is done by making use of the statistical characteristics of the errors, of both the inertial and aiding measurement components, to combine the information into one set of estimates. The aiding component can be measurements from e.g. GNSS, hydroacoustic positioning, Doppler radar, altimeter and many others senors depending on the given application. Maybeck (1979) presents both a direct and indirect[2] navigation filter strategy for incorporating the aiding reference measurements. For indirect strategies, may error models on the form

$$\begin{aligned} \delta\dot{\boldsymbol{p}}^n &= \delta\boldsymbol{v}^n \\ \delta\dot{\boldsymbol{v}}^n &= -\boldsymbol{S}(\delta\boldsymbol{\Theta})\boldsymbol{f}_{\text{IMU}} + \delta\boldsymbol{g}^n + \boldsymbol{R}_b^n(\boldsymbol{\Theta})\boldsymbol{e}_a^b \\ \delta\dot{\boldsymbol{\Theta}} &= \boldsymbol{R}_b^n(\boldsymbol{\Theta})\boldsymbol{g}_g^b \end{aligned} \tag{1.1}$$

be utilized. System (1.1)[3] is based upon the *psi-angle error model* of Leondes (1963). $\boldsymbol{\Theta}$ is the attitude, hence $\delta\boldsymbol{\Theta}$ is the attitude error. Furthermore, $\boldsymbol{e}_a^b$ and $\boldsymbol{e}_g^b$ are the accelerometer and gyro errors respectively. Update the actual PVA estimates are done indirectly based upon models such as (1.1).

One drawback of navigation based on EKF is that the GNSS solution can be obtained with another Kalman filter. This introduces colored noise and

[2]Called *error state space Kalman filter* in Maybeck (1979).

[3]This error model assumes that the NED frame is inertial. For more general error models can e.g. Britting (2010) by advised.

hence violates the assumption that both process and measurement noise have to be Gaussian white noise for the second filter. See Kalman (1960) for details. One combats this problem by choosing the indirect approach since the error dynamics of (1.1) is quite slow. Then, the navigation filter will run at lower frequency than the GNSS filter. The chosen frequency is typically between $1 - 10$ Hz according to Vik (2012). Then, the input noise of the navigation filter can be approximated to band limited white noise.

There exist other nonlinear extensions of the Kalman filter in addition to EKF. Namely the *Unscented Kalman filter* (UKF) and the *Particle filter* (PF). Theory and practical applications of both methods, utilized for navigation purposes, are present by Gustafsson (2012). For further information on stochastic systems and Kalman filter theory in general can Brown and Hwang (2011) can be studied.

Nonlinear Observers and Attitude Resolving

The extended Kalman filter has been the standard observer for navigation purposes however, during the last 15 years have extensive research on nonlinear observers for strapdown INS systems been carried out. The first nonlinear observer for attitude estimation was introduced as early as 1991. Salcudean (1991) introduced the nonlinear attitude observer by utilizing a unit quaternion to represent the attitude together with a Lyapunov approach to prove exponential convergence. However, this observer is based on a direct quaternion measurement and zero bias of the angular velocity measurements. In real-life, the former assumption usually requires a static inertial measurement to attitude mapping. From Fossen (2011) can this mapping can e.g. be obtained as in (1.2) from the IMU measurements.

$$\begin{aligned}\phi &= \arctan\left(\frac{f_{\text{IMU,y}}}{f_{\text{IMU,z}}}\right)\\ \theta &= \arctan\left(\frac{f_{\text{IMU,x}}}{\sqrt{f_{\text{IMU,y}}^2 + f_{\text{IMU,z}}^2}}\right)\\ \psi_m &= \arctan\left(\frac{m_{\text{IMU,y}}}{m_{\text{IMU,x}}}\right)\end{aligned} \tag{1.2}$$

The two former angles in (1.2) are calculated from the accelerometer, whereas the latter is solved from the magnetometer. The latter mapping requires that the roll and pitch angles are zero. From Vik (2012) may the heading also be resolved from the gyroscope according to

$$\psi = \arctan\left(\frac{-w^*_{\text{IMU,y}}}{-\omega^*_{\text{IMU,x}}}\right) \tag{1.3}$$

where are w^* is solved form the mappings of ϕ and θ. A detailed presentation of direct heading mapping using the magnetometer and non-zero roll and pitch angles can be found in Fossen (2011). Furthermore, after the Euler angle mapping is obtained, may the quaterion representation be calculated. The algorithm, calculating the quaterion from the Euler angles, can be found in e.g Fossen (2011).

Such attitude mapping as described above can, according to Grip et al. (2012a), result is a different noise characteristics than the original noise characteristics of the measurements used to produce it. For instance, the noise characteristics are depending on how well conditioned the attitude resolution is a given time. However, the attitude by can be calculated using other methods. **Wahba's problem** is posed as

$$\sum_{j=1}^{n} \|\boldsymbol{v}_j^* - \boldsymbol{M}\boldsymbol{v}_j\|, \quad n \geq 2 \tag{1.4}$$

where the attitude is calculated by minimizing the object function of (1.4). The attitude is given by the rotation matrix $\boldsymbol{M}$, see Wahba (1966) for details. The same principle is utilized by the QUEST algorithm, where a minimum of two non parallel reference vectors are needed to compute the quaternion estimate. See Shuster and Oh (1981) for more information. It should be mentioned that such methods in their pure form have no filtering properties. Hence, noisy measurements will yield a noisy attitude estimate. Crassidis et al. (2007) presents a survey of attitude estimation techniques based on QUEST, EKF, Multiplicative EKF, UKF and PF. The authors recommend especially Multiplicative EKF approaches over e.g. QUEST to obtain the attitude estimate because of better filtering properties.

A nonlinear observer for integration of Differential GPS (dGPS) was presented by Vik et al. (1999). As with the Salcudean observer, the attitude observer was proven exponentially stable. In addition accelerometer and gyro bias estimates were included in the observer. The position and velocity estimates where proven to be quasi equilibrium asymptotically stable. Furthermore, Vik and Fossen (2001) continued the work of Vik et al. (1999) by proving the origin of the GNSS and INS integration observer to be globally exponentially stable (GES) by exploiting the constraint of the quaternion, i.e. $\|\boldsymbol{q}\| = 1$ and applying Barbalat's lemma. For more on quaternions, see Appendix B.1. Thienel and Sanner (2003) also proved exponential stability of the gyro bias estimates however, this required persistency of excitation (PE).

Hamel and Mahony (2006) introduced a nonlinear attitude observer based on passivity and inertial vector measurements to obtain attitude and gyro bias estimates. No mapping from inertial measurements to the corresponding attitude measurement was needed. Mahony et al. (2008) expanded the results of Hamel and Mahony (2006), by developing a almost GES observer utilizing quotations. Stationary reference vectors or unbiased gyro rate measurements where assumed. Later on Hua (2010) developed an integration observer of

INS and GNSS velocity measurements with non-stationary reference vectors to obtained the result of semi-global exponential stability. However, gyro bias estimation was not considered. Batista et al. (2012) presents a GES attitude observer with a single time varying reference vector where a rotation matrix experiential converges to $SO(3)$. The assumptions of Mahony et al. (2008) was relaxed by Grip et al. (2012a), by utilizing a parameter projection algorithm to prove semi-global convergence of the attitude estimate for time varying non-stationary reference vectors and biased inertial measurements. Here, the rotation matrix was utilized to represent the attitude information. Furthermore, Grip et al. (2012b) proposed a nonlinear observer for integration of GNSS and IMU measurements with gyro bias estimation. Here was the theory of observers for interconnected nonlinear and linear systems, purposed in Grip et al. (2012c), utilized. The position and velocity estimator was interconnected with the attitude observer developed in Grip et al. (2012a). Grip et al. (2013, Submitted) takes on the attitude estimation problem by utilizing quaternions. In addition to the previous results of Grip et al. (2012b), also acceleromter bias estimation was included. These however, requires PE in order to converge to the actual biases. Grip et al. (2013, Submitted) also poses the navigation problem in the ECEF frame, see Appendix B.1, making the observer useful for applications where the navigating vehicle is not constrained to a smaller geographical area.

Vessel Model Based Navigation

Vessel model based navigation utilized for DP is far from novel. A Kalman filter approach was presented e.g by Sælid et al. (1983). A overview of Kalman filter applied for dynamic positioning and autopilot design was given by Fossen and Perez (2009). An other nonlinear observer, exploiting passivity and the vessel model applied for dynamic positioning, was developed by Fossen and Strand (1999), which guaranteed global exponential stability (GES).

The vessel modeled has also during recent years been utilized as aiding measurement for inertial navigation systems. In Hegrenæs et al. (2008) and Hegrenæs and Hallingstad (2011) were the velocity from the vessel model, together with sea current estimates, utilized as a velocity aiding measurements for INS. The methodology was applied on underwater vehicles. Bryson and Sukkarieh (2004) utilized a vehicle model as aiding for INS applied on an unmanned aerial vehicle (UAV).

1.3 Motivation for Nonlinear Theory and Fault-Tolerant Methods

Utilizing nonlinear theory instead of e.g. the EKF can yield several advantages. First the computational load can be reduced since Riccati equations are avoided. According to Fossen (2011) will a discrete-time Kalman filter results in $n(n+1)/2$ difference equations, where n is the number of states. For PVA estimation, may the choice of Kalman, as navigation filter, result in hundreds of ordinary difference equations (ODE) to be solved on-line[4]. By avoiding those, online computational cost can be reduced significantly. Furthermore, a nonlinear observer may be ran faster because the cascade of two Kalman filters is avoided. Direct nonlinear observers can, according to Fossen (2012b), run at $50-1000$ Hz. However, this is not the biggest advantages regarding a maritime application. By reducing the number of ODEs to solve, the size of code can be reduced. Again, this could lead to more maintainable software. This is highly desirable in an industrial perspective since increased maintainability can reduce the number of software induced faults in the navigation and control system, presented in Figure 1.1. Furthermore, by utilizing nonlinear control techniques can global stability be proven and

[4]At least 136 difference equation are needed if three positions, three velocities, four attitude parameters (quaternions used for attitude representation), three gyro biases and three accelerometer biases should be estimated.

thus, robustness can be proven. If exponential stability is proven, a given convergence rate is also given. Advise Khalil (2002) for more information on asymptotic and exponential stability of nonlinear systems.

Regarding attitude representation, the unit quaternion was chosen. The quaternion approach is singular free and only four parameters are needed to represent a given rotation. In opposite, a rotation matrix representation can result in nine parameters to determine online. Furthermore, trigonometric functions are avoided. This is highly useful for integrity reasons in real-time operations due to such functions are represented with a limited accuracy in a computer. Furthermore, the need of a normalized quaternion can easily be enforced in a computer control system, see (2.57) and Section 2.7 for more.

By utilizing the results from Grip et al. (2013, Submitted) is the attitude estimation combined with position and velocity estimates. Stability, of the connected observers, has been proven by utilizing nonlinear feedback theory as shown in Grip et al. (2012c).

As stated by Blanke (2001), is it not just desirable to detect faults and issue an alarm to the operator, but also handle simple faults automatically. In a sensor context, such faults can be indicated by sensor freeze, wild point, increased variance. A more complicated scenario is to detect slowly varying drift of measurements from a given sensor.

Definition 1.1 implies the need for a fault-tolerant system. One can debate the redundancy obtained by three installed GNSS antennas on a offshore vessel. The following cases illustrate why such a configuration is not truly redundant.

- Ionospheric disturbances such as scintillations can kill all GNSS signals for shorter or longer periods of time. See Section 2.3 for details,
- Faulty dGNSS links such that the differential link will bias the position

measurements. Such incidents have resulted in drive-offs. See Section 2.3.2 for details.

- Multipath affecting all GNSS receivers. This is a possibility when a smaller ship is in the vicinity of a e.g larger offshore installation.

Such events are highly avoidable during for instance during drilling operations. One can debate that other measurements principles such as hydroacoustic positioning reference (HPR) systems, can be utilized if GNSS is not available. However, the same problems are also present with HPR systems. The sound profile might change and effect all HPR systems. HPR signal to noise ratio can also become worsened by e.g thruster noise.

Faults and fault-tolerance regarding dGNSS are studied and discussed in Chen and Verhoeven (2005), Chen et al. (2008) and Chen et al. (2009). Cases of drive-offs where investigated and concluded on. The barrier methodology was also introduced. However, regarding the last barrier, "Barrier element 3 - dGPS quality control function", yields complicated dGPS selves checks. Also simpler and possibly more robust methodology should be investigated in order to detect abnormalities that can cause drive-offs which the dGPS selves check did not detect.

1.4 Contribution and Focus of Thesis

This thesis takes on a study of combining INS and GNSS into a fault-tolerant system by utilizing the nonlinear observer developed by Grip et al. (2013, Submitted) as basis. The observer was utilized for on DP scenario. A simulator was also developed for measurement generation.

The focus of fault-tolerance was primarily on detection and handling of GNSS sensor faults to prevent e.g undesirable sensor data to propagate in the control system. This is motivated by "*Experience from industrial applications has shown that the most frequent control system failure are caused by*

sensor failures", Sørensen (2012) and the summary of the incidents at the Norwegian Continental Shelf presented in Chen and Verhoeven (2005). "*All drive-offs were DP control system related. Notably, five of these six drive-offs were initiated due to wrong position data associated with dGPS*". Also fault-tolerance regarding the acceleromter was studied. The contributions related to GNSS and accelerometer fault-tolerant techniques were:

- Signal processing and senor checks for detecting outliers, freeze and high variance.

- Development of a voting algorithm together with performing measurement weighting.

- Development of a novel GNSS drift detection scheme. To the author's knowledge have such methods not yet been published. However, one cannot exclude that inhouse development, at DP vendors, have tried to battle this problem.

- Providing redundant acceleration information, in the event of accelerometer failure, by exploiting an additional model based observer.

See Section 4.5 and Section 4.6 for details.

The observer of Grip et al. (2013, Submitted) is fixed gained. This was modified by:

- Online tuning of the gain related to the position estimate. This was done by utilizing the calculated variance of the position measurements together with the exponential function.

See Chapter 4, Section 4.5.

1.5 Organization of Thesis

The organization of this thesis follows as, where the respective chapters contains:

2: The Preliminaries chapter contains background information regarding marine craft dynamics and notation. The strapdown navigation equations are addressed. Furthermore, information on GNSS, fault-tolerances and DP systems are also presented.

3: The Vessel Simulator chapter addresses the vessel modeling including environmental forces and moments needed to construct a basic vessel simulator. Furthermore, GNSS and IMU measurements was also modeled. These were utilized by the observer presented in Chapter 4.

4: The Observer Design chapter takes on a observer for INS and GNSS integration developed by Grip et al. (2013, Submitted). Furthermore, fault-tolerant methods was included to detect GNSS faults. An additional model based observer was also utilized to provide redundant acceleration information in the event of accelerometer failure.

5: The Results and Discussion section illustrates the findings and the effect of the fault-tolerant framework added to the Grip et al. (2013, Submitted) observer. Related discussions are preformed.

6: The last chapter of this thesis, Conclusion and Further Work, contains the concluding remarks and recommendations for further studies.

Additional information, background material and results are found in Appendix A - F.

Chapter 2

Preliminaries

This section constitute the theoretical base of this thesis. This base consist of vessel kinematics and kinetics together with navigation, senor and filtering relevant theory.

2.1 Marine Craft Dynamics and Notation

From Fossen (2011) the field of dynamics are divided into two parts, Kinematics are Kinetics. The former takes on the geometrical aspects motion, while the latter focuses on the forces and moments causing motion. Furthermore, Fossen (2011) states the kinematics and kinetics of a marine craft can be stated on vectorial form as

$$\dot{\boldsymbol{\eta}} = \boldsymbol{J}_{\boldsymbol{\Theta}}(\boldsymbol{\eta})\boldsymbol{\nu} \tag{2.1}$$

$$\boldsymbol{M}\dot{\boldsymbol{\nu}} + \boldsymbol{C}(\boldsymbol{\nu})\boldsymbol{\nu} + \boldsymbol{D}(\boldsymbol{\nu})\boldsymbol{\nu} + \boldsymbol{g}(\boldsymbol{\eta}) = \boldsymbol{\tau} + \boldsymbol{\tau}_{\text{wind}} + \boldsymbol{\tau}_{\text{wave}} \tag{2.2}$$

where $\boldsymbol{\eta}$, $\boldsymbol{\nu}$ and $\boldsymbol{\tau}$ are the generalized position, velocity and force vectors respectively given in (2.3)

$$\boldsymbol{\eta} = \begin{bmatrix} \boldsymbol{p}^n_{b/n} \\ \boldsymbol{\Theta}_{nb} \end{bmatrix}, \quad \boldsymbol{\nu} = \begin{bmatrix} \boldsymbol{v}^b_{b/n} \\ \boldsymbol{\omega}^b_{b/n} \end{bmatrix}, \quad \boldsymbol{\tau} = \begin{bmatrix} \boldsymbol{f}^b_b \\ \boldsymbol{m}^b_b \end{bmatrix} \tag{2.3}$$

From Fossen (2011) is $\boldsymbol{p}^n_{b/n} \in \mathbb{R}^3$ given as the position in the NED frame, $\{\text{n}\}$. Furthermore, $\boldsymbol{\Theta}_{nb} \in \mathcal{S}^3$ represents the Euler angles, i.e the attitude of the vessel. $\boldsymbol{v}^b_{b/n} \in \mathbb{R}^3$ and $\boldsymbol{\omega}^b_{b/n} \in \mathbb{R}^3$ represents the linear and angular

velocity of the BODY frame, {b} with respect to NED frame, {n}. Both decomposed in {b}. The forces and moments acting on the vessel is denoted $\boldsymbol{f}_b^b \in \mathbb{R}^3$ and $\boldsymbol{m}_b^b \in \mathbb{R}^3$ respectively. $\mathbb{R}^3$ denotes the *Euclidean space* of dimension three. The set, $\mathcal{S}^3$ is sphere. $\boldsymbol{J}_{\boldsymbol{\Theta}}(\boldsymbol{\eta})\boldsymbol{\nu}$ is the six degree of freedom attitude transformation matrix. $\boldsymbol{M}$, $\boldsymbol{C}(\boldsymbol{\nu})$ and $\boldsymbol{D}(\boldsymbol{\nu})$ represent the inertia, Coriolis-Centripetal and damping matrices respectively. $\boldsymbol{g}(\boldsymbol{\eta})$ represents the restoring forces and moments. Details regarding the vessel kinematics and kinetics together and the different reference frames can be found in Appendix B.

2.2 Strapdown Inertial Navigation Fundamental

2.2.1 Inertial Navigation

Inertial navigation utilizes fundamental principles of inertia. Mainly two types of sensors are used in inertial navigation, accelerometers and gyroscopes. In conduction with electronics and software these sensor constitute a inertial navigation system (INS). The accelerometer measures the acceleration of a moving object, while the gyroscope measures the angular velocity. A summary of the basics principles and different types of accelerometers and gyroscopes can be found in Vik (2012). A more complete introduction to inertial navigation can be found in Britting (2010) and Savage (1981).

Typically three accelerometers and three gyroscopes are combined to one unit. This is called an inertial measurement unit (IMU) and measures 6 degree of freedom, see Fossen (2011) for more. The IMU measures three orthogonal accelerations and three orthogonal angular velocities. Furthermore, acceleration measurements[1] are integrated twice while the angular velocities are integrated once respectively by the INS to obtain the posi-

[1] Acceleration measurements are sometimes called specific forces measurements

tion and attitude. Some IMUs also include magnetometers and are often incorrectly referred to as "9-DOF inertial measurement units".

2.2.2 The Strapdown Equations

Throughout the navigation process are the strapdown equations soled by the INS in order to compute the PVA estimates.

Be defining $\boldsymbol{p}^n := \boldsymbol{p}^n_{b/n}$ and $\boldsymbol{p}^i := \boldsymbol{p}^i_{b/i}$ can (2.4) relate the position in the {n} and {i} frame according to

$$\boldsymbol{p}^i = \boldsymbol{R}^i_n \boldsymbol{p}^n \tag{2.4}$$

as given in Britting (2010). Furthermore, $\boldsymbol{R}^i_n \in SO(3)$ is the rotation matrix between the NED frame and the inertial frame. By applying the $SO(3)$ property, see (B.1) in Appendix B.1, can the position in the {n} frame be written as

$$\boldsymbol{p}^n = (\boldsymbol{R}^i_n)^\intercal \boldsymbol{p}^i = \boldsymbol{R}^n_i \boldsymbol{p}^i. \tag{2.5}$$

To obtain the differential equation for $\boldsymbol{p}^n$ one performs time derivation on (2.5). By utilizing the chain rule the following emerges

$$\dot{\boldsymbol{p}}^n = \boldsymbol{R}^n_i \dot{\boldsymbol{p}}^i + \dot{\boldsymbol{R}}^n_i \boldsymbol{p}^i \tag{2.6}$$

Moreover, by exploiting the relationship

$$\dot{\boldsymbol{R}}^a_b = \boldsymbol{R}^a_b \boldsymbol{S}(\boldsymbol{\omega}^b_{ab}) \tag{2.7}$$

from (B.6), can (2.6) as

$$\begin{aligned}\dot{\boldsymbol{p}}^n &= \boldsymbol{R}_i^n \dot{\boldsymbol{p}}^i + \boldsymbol{R}_i^n \boldsymbol{S}(\boldsymbol{\omega}_{i/n}^i)\boldsymbol{p}^i \\ &= \dot{\boldsymbol{p}}^n - \boldsymbol{R}_i^n \boldsymbol{S}(\boldsymbol{\omega}_{n/i}^i)\boldsymbol{p}^i \\ &= \boldsymbol{v}^n - \boldsymbol{R}_i^n \boldsymbol{S}(\boldsymbol{\omega}_{n/i}^i)\boldsymbol{p}^i. \end{aligned} \tag{2.8}$$

Furthermore, can (2.8) by written as

$$\dot{\boldsymbol{p}}^n = \boldsymbol{v}^n - \boldsymbol{R}_i^n \boldsymbol{S}(\boldsymbol{\omega}_{n/i}^i)\boldsymbol{R}_n^i \boldsymbol{p}^n. \tag{2.9}$$

By utilizing the similarity transform, see (B.7) will (2.8) take the following form

$$\dot{\boldsymbol{p}}^n = \boldsymbol{v}^n - \boldsymbol{S}(\boldsymbol{\omega}_{n/i}^n)\boldsymbol{p}^n. \tag{2.10}$$

Regarding the velocity differential equation, can $\dot{\boldsymbol{v}}^n$ be stated from Britting (2010) in the {n} frame as

$$\dot{\boldsymbol{v}}^n = \boldsymbol{R}_i^n \big(\ddot{\boldsymbol{p}}^i - \boldsymbol{S}(\boldsymbol{\omega}_{n/e}^i + 2\boldsymbol{\omega}_{e/i}^i)\boldsymbol{R}_n^i \boldsymbol{v}^n - \boldsymbol{S}(\boldsymbol{\omega}_{e/i}^i)^2 \boldsymbol{p}^i\big) \tag{2.11}$$

Furthermore, Britting (2010) defines the gravity vector in the {n} frames as

$$\boldsymbol{g}^n := \boldsymbol{G}^n - \boldsymbol{R}_i^n \boldsymbol{S}(\boldsymbol{\omega}_{e/i}^i)^2 \boldsymbol{p}^{\boldsymbol{i}} \tag{2.12}$$

and state that

$$\boldsymbol{f}^n = \boldsymbol{R}_e^n \ddot{\boldsymbol{p}}^i - \boldsymbol{G}^n \tag{2.13}$$

where $\boldsymbol{G}^n$ is the gravity acceleration due to the Earth. By rearranging (2.12) with respect to $\boldsymbol{G}^n$ and inserting $\boldsymbol{G}^n$ into (2.13) results in

$$\boldsymbol{f}^n = \boldsymbol{R}_e^n \ddot{\boldsymbol{p}}^i - \big(\boldsymbol{g}^n + \boldsymbol{R}_i^n \boldsymbol{S}(\boldsymbol{\omega}_{e/i}^i)^2\big). \tag{2.14}$$

Moreover, by rearranging (2.14) with respect to e.g $\boldsymbol{R}_e^n \ddot{\boldsymbol{p}}^i$ and substitute this

into (2.11) yields

$$\begin{aligned}\dot{\boldsymbol{v}}^n &= \boldsymbol{R}_i^n \ddot{\boldsymbol{p}}^i - \boldsymbol{R}_i^n \boldsymbol{S}(\boldsymbol{\omega}_{n/e}^i + 2\boldsymbol{\omega}_{e/i}^i)\boldsymbol{R}_n^i \boldsymbol{v}^n - \boldsymbol{R}_i^n \boldsymbol{S}(\boldsymbol{\omega}_{e/i}^i)^2 \\ &= \boldsymbol{f}^n + \boldsymbol{g}^n + \boldsymbol{R}_i^n \boldsymbol{S}(\boldsymbol{\omega}_{e/i}^i)^2 - \boldsymbol{R}_i^n \boldsymbol{S}(\boldsymbol{\omega}_{n/e}^i + 2\boldsymbol{\omega}_{e/i}^i)\boldsymbol{R}_n^i \boldsymbol{v}^n - \boldsymbol{R}_i^n \boldsymbol{S}(\boldsymbol{\omega}_{e/i}^i)^2 \\ &= \boldsymbol{f}^n + \boldsymbol{g}^n - \boldsymbol{R}_i^n \boldsymbol{S}(\boldsymbol{\omega}_{n/e}^i + 2\boldsymbol{\omega}_{e/i}^i)\boldsymbol{R}_n^i \boldsymbol{v}^n. \end{aligned} \tag{2.15}$$

By applying the similarity transform again from (B.7), can (2.15) be written as

$$\dot{\boldsymbol{v}}^n = \boldsymbol{f}^n + \boldsymbol{g}^n - \boldsymbol{S}(\boldsymbol{\omega}_{n/e}^n + 2\boldsymbol{\omega}_{e/i}^n)\boldsymbol{v}^n. \tag{2.16}$$

As given in Section 1.4 this thesis will perform a case study with a vessel operating in a confined geographical area. Thus, performing flat Earth navigation. In this case the {n} frame is assumed to be inertial as given in Table B.1. Hence, the $\boldsymbol{S}(\boldsymbol{\omega}_{i/n}^i)$ and $\boldsymbol{S}(\boldsymbol{\omega}_{n/e}^n + 2\boldsymbol{\omega}_{e/i}^n)$ terms will be zero. Furthermore, by defining

$$\bar{\boldsymbol{\omega}}_{b/n}^b =: \begin{bmatrix} 0 \\ \boldsymbol{\omega}_{b/n}^b \end{bmatrix} \tag{2.17}$$

can the attitude differential equation (B.26), utilizing quaternions as attitude representation, be written as

$$\dot{\boldsymbol{q}}_b^n = \frac{1}{2}\boldsymbol{q}_b^n \otimes \bar{\boldsymbol{\omega}}_{b/n}^b \tag{2.18}$$

From (2.10), (2.16) and (2.18) together with fact that the all the skew-symmetric is zero results in the following dynamic equations given in the {n} frame

$$\dot{\boldsymbol{p}}^n = \boldsymbol{v}^n \tag{2.19}$$

$$\dot{\boldsymbol{v}}^n = \boldsymbol{f}^n + \boldsymbol{g}^n \tag{2.20}$$

$$\dot{\boldsymbol{q}}_b^n = \frac{1}{2}\boldsymbol{q}_b^n \otimes \bar{\boldsymbol{\omega}}_{b/n}^b \tag{2.21}$$

Equations (2.19) - (2.21) coincides with the problem formulation presented

in Grip et al. (2013, Submitted) by assuming that the {n} frame is inertial. For the definition of flat Earth navigation, see Appendix B.5. However, in this thesis will

$$\dot{\boldsymbol{q}}_b^n = \boldsymbol{T}_q(\boldsymbol{q})\boldsymbol{\omega}_{b/n}^b \tag{2.22}$$

from (B.24) be used to describe the attitude differential equation of (2.21).

2.2.3 INS Errors and Error Sources

According to Fossen (2011) will the PVA estimates from the INS drift due to sensor biases when the one looses aiding sensors measurements such as GNSS. Vik and Fossen (2001) states that the most dominating error sources in an INS system are biases, scale factors, misalignment and temperature variations. As mentioned above, the accelerometers and gyroscope measurements are integrated twice and once respectively. Because of this, the senors biases will propagate throughout the INS. Hence, the INS estimates will drift caused by integration of errors over time. To prevent this aiding measurements are needed. Maybeck (1979) give a summery of possible reference sensors. The aiding sensor utilized in this work will be position measurements from GNSS. For more information on GNSS can be found the following Section.

2.3 Global Navigation Satellite Systems

Global Navigation Satellite Systems (GNSS), such as GPS, GLONASS, Beidou and Galileo, calculate three-dimensional position of the GNSS receiver. For details on the GPS systems can Parkinson and Spilker (1996a,b) be advised.

2.3.1 GNSS Position Measurements

The three-dimensional position measurement of the GNSS receiver is based upon raw *pseudorange* measurements. This is the perceived distance from the satellite to the GNSS receiver. The pseudorange measurement for n satellites are given, from Vik et al. (1999), as

$$\rho^i = \sqrt{(\boldsymbol{x}_s^i - \boldsymbol{x})^\intercal (\boldsymbol{x}_s^i - \boldsymbol{x})} + c\tau^* + \epsilon_\rho^i, \qquad i \in [1, \dots n] \tag{2.23}$$

where $\boldsymbol{x}_s^i \in \mathbb{R}^3$ is the position of satellite i and $\boldsymbol{x}^i \in \mathbb{R}^3$ is the position of the i^{th} GNSS receiver. Furthermore, c is the speed of light whereas τ^* is the receiver clock error. ϵ_ρ^i represents other smaller pseudorange errors and noise. The position measurement is usually obtained by linearizing (2.23) and then applying a recursive least squares (RLS) algorithm or an extended Kalman filter.

The receiver position, $\boldsymbol{x}$ is calculated in the {e} frame. From Fossen (2011) can the position $\boldsymbol{x}^e$ this be be transformed to the {n} frame by applying

$$\boldsymbol{x}^n = \boldsymbol{R}_e^n \boldsymbol{x}^e \tag{2.24}$$

where $\boldsymbol{R}_e^n$ is the rotation matrix between the ECEF and the NED frame.

Parkinson and Spilker (1996a) states that GPS accuracy is manly affected by two factors. The ranging accuracy and the geometric constellation of the satellites. Where the latter results in geometric dilution of precision (GDOP). Furthermore, Parkinson and Spilker (1996a, Ch. 1) writes the position root mean square error as

$$\text{Position Error RMS} = \text{GDOP} \cdot \text{RMS}_{\text{UERE}}. \tag{2.25}$$

where UERE means *user equivalent range error*. Furthermore, (2.25) can be

written as

$$\sqrt{\sigma_x^2 + \sigma_y^2 + \sigma_z^2 + \sigma_\tau^2} = \text{GDOP} \cdot \sigma_{\text{UERE}}. \tag{2.26}$$

Other Dilution of Precision parameters are Position Dilution of Precision (PDOP), Horizontal Dilution of Precision (HDOP), Vertical Dilution of Precision (VDOP) and Time Dilution of Precision (TDOP). From the standard one-sigma error model in Parkinson and Spilker (1996a, Ch. 11) is the HDOP smaller than the VDOP. This indicates that the horizontal components of the GSP measurements are more precise that then vertical components. In Section 3.2.2 will this fact be used regarding the choice of GNSS standard deviation. For more on Dilution of Precision can Parkinson and Spilker (1996a, Ch. 5) be advised.

2.3.2 GNSS Ranging Erros and Faults

Parkinson and Spilker (1996a, Ch. 11) describe that GNSS systems are affected by six classes of errors. There are:

- Ephemeris Errors
- Satellite Clock errors
- Ionosphere errors
- Troposphere errors
- Multipath errors
- Receiver errors

According to Parkinson and Spilker (1996a) can dual-frequency GPS receivers compensate for the ionospheric refraction which delays the pseudorange measurement. Furthermore, Parkinson and Spilker (1996a) also states that this approach is significantly better than using a model of the delay, of the raw pseudorange measurements, introduced by the ionosphere.

Parkinson and Spilker (1996a) stats that troposphere errors are introduced by variations in temperature, pressure and humidity in the lower part of the atmosphere. A model can be used to reduce these effects.

Multipath errors are introduced be GNSS signals that are reflected of ob-

jects. To reduce this problem from a vessel, one could locate the receiver as high as possible so reflections will be minimized. For dGNSS is multipath the main error sources.

Reciver errors will in general introduce measurement noise and bias caused by the electronics and algorithms used to calculated the position measurements.

Differential GNSS (dGNSS) can be utilized in the attempt to compensate for the errors mentioned above. The concept is as follows; The user receives differential corrections from fixed ground stations in order to compensate from errors introduced in the position measurement calculation. The location of the ground stations are known. According to Parkinson and Spilker (1996b) the most common method to perform these differential corrections for dGPS is that the reference station estimates the error in the pseudorange measurement for each satellite in view. These estimates are based on a.i. the station's known location. Then the estimates or corrections are broadcasted to the users in range. However, dGNSS not will be able remove multipath and receiver noise errors.

In additions to errors can faults, like satellite clock failure, receiver failure or differential link failure, introduce errors in the GNSS solution which can result in dramatic consequences. Such consequences for a mobile offshore drilling unit are described in Chen et al. (2009). Furthermore, Chen et al. presents four failure cases for dGNSS as presented in Table 2.1. Moreover,

Table 2.1: dGNSS Failure Modes

	Loss of Position Data	Erroneous Position Data
Failure of individual dGNSS	A	C
Simultaneous failure multiple dGNSS	B	D

Chen et al. (2009) presents that dGNSS failure mode C and D could lead to more significant loss of position if the erroneous position data is provided to the DP control system. The reason for this is the case A and B will issue and alarm to the DPO. C and D may not. Hence, situation C and D may result in critical situations such as drive-off. The failure modes presented in Table 2.1, according to Chen et al. (2009), be caused by both external or internal errors and faults. The external causes are associated with the state of the GNSS satellites, signal medium or the differential link. Regarding the internal causes, are these introduced by GNSS equipment, differential link equipment and the dGNSS unit. These causes are presented in Appendix B.6. Details can be found in Chen et al. (2009).

As presented above can faulty dGNSS measurement can result in drifting dGNSS position measurements. Jumps may also occur as shown presented in Chen et al. (2009). Chen et al. (2009) states that erroneous position data may result in

- Position jump
- Slow position drift
- Fast position drift

There is reported incidents with position jump of 65 meters. Regarding the slow drift of measurements reported in Chen et al. (2009) was a result of the position measurements indicated a fixed position, however the vessel was actually moving. Chen et al. (2009) also mentions two cases where the position measurement drifted 10 to 20 meters in a few sampling intervals.

The purpose of this thesis is develop a fault-tolerant observer and not to develop a satellite simulator. Therefore are just some of the errors above and in Appendix B.6 tried to be replicated in Chapter 3 and not simulated. This is further motivated by the fact that the observer should handle faults and failure regardless of cause. Therefor was a a full GNSS simulator not

developed. For details of the simulated GNSS measurements, faults and failures can Section 3.2.2 be advised.

2.4 Fault-Tolerant Control

According to Blanke (2001), does fault-tolerant control (FTC) employs software to monitor behavior of redundant components within the system. If a fault has occurred, appropriate actions are taken to prevent critical damage or failure. The overall goal, in contrast to fail-safe systems, is to keep the system operational, preferable a normal performance. The main goal of fail-safe systems are to perform a safe performance reduction to a fail-safe state or shutdown when a critical fault is detected.

Regarding the FTC can, according to Isermann (2006) the following definitions be stated:

Definition 2.1. ***Fault Detection:*** *Determination of faults present in a system and time of detection;*

Definition 2.2. ***Fault Isolation:*** *Determination of kind, location and time of detection of a fault by evaluating symptoms. Follows fault detection;*

Definition 2.3. ***Fault Identification:*** *Determination of the size and time-variant behavior of a fault. Follows fault isolation;*

Definition 2.4. ***Fault Diagnosis:*** *Determination of kind, size, location and time of detection of a fault by evaluating symptoms. Follows fault detection. Includes fault detection, isolation and identification;*

Frank et al. (1999) presents can a nonlinear system can be written as

$$\dot{\boldsymbol{x}} = \boldsymbol{f}(\boldsymbol{x}, \boldsymbol{u}, \boldsymbol{\theta}_f, \boldsymbol{\theta}_d) \tag{2.27}$$

$$\boldsymbol{y} = \boldsymbol{h}(\boldsymbol{x}, \boldsymbol{u}, \boldsymbol{\theta}_{fs}) \tag{2.28}$$

where $\boldsymbol{x} \in \mathbb{R}^n$, $\boldsymbol{u} \in \mathbb{R}^m$ is the state vector and input vector respectively. Further, the $\boldsymbol{y} \in \mathbb{R}^p$ is the output vector. The system parameters is described by $\boldsymbol{\theta}_f \in \mathbb{R}^l$ when no faults are present. $\boldsymbol{\theta}_d$ represents the model mismatch, i.e $\boldsymbol{\theta}_d = \mathbf{0}$ if the model is an exact representation of the real-life system. $\boldsymbol{\theta}_{fs} \in \mathbb{R}^{l_s}$ represented the output parameters. If $\boldsymbol{\theta}_{fs}$ deviates from the nominal values, a sensor fault has occurred. Moreover, from Frank et al. (1999) can the two following definitions be stated

Definition 2.5. ***Residual Generation*** *is the construction of signals that are accentuated by the changes is the parameter vector (faults).*

Definition 2.6. ***Residual Evaluation*** *is the decision and isolation of the occurrence of changes in the parameter vector.*

Previous results regarding fault-tolerant control applications be found in Frank (1990).

The fault-tolerance methodology applied in this thesis will primarily focus of fault detection regarding GNSS. From Frank (1990) can the measurement part of such a model be written in continuous time as

$$\boldsymbol{y}(t) = \boldsymbol{C}\boldsymbol{x}(t) + \boldsymbol{F}\boldsymbol{d}(t) + \boldsymbol{G}\boldsymbol{f}(t) \tag{2.29}$$

where $\boldsymbol{x}(t)$ is the state vector. In this case, $\boldsymbol{x}$ is given as

$$\boldsymbol{x} = \begin{bmatrix} \boldsymbol{p}_{b/n}^n \\ \boldsymbol{v}_{b/n}^n \end{bmatrix}, \qquad \boldsymbol{x} \in \mathbb{R}^6. \tag{2.30}$$

$\boldsymbol{d}(t)$ is unknown inputs vector, e.g measurements noise. $\boldsymbol{f}(t)$ are the respective sensor faults. The $\boldsymbol{C}$, $\boldsymbol{F}$ and $\boldsymbol{G}$ matrices are in this case the same, given as

$$\boldsymbol{C} = \boldsymbol{F} = \boldsymbol{G} = \begin{bmatrix} \boldsymbol{I}_{3\times3} & \mathbf{0}_{3\times3} \end{bmatrix} \tag{2.31}$$

and describe how the actual position, measurement noise and sensor faults

effects the measurement, $\boldsymbol{y}$.

The linear observer dynamics can be written as

$$\dot{\hat{\boldsymbol{x}}} = (\boldsymbol{A} - \boldsymbol{KC})\hat{\boldsymbol{x}} + \boldsymbol{Bu} + \boldsymbol{Ky} \tag{2.32}$$

$$\hat{\boldsymbol{y}} = \boldsymbol{C}\hat{\boldsymbol{x}}. \tag{2.33}$$

where $\boldsymbol{K}$ is given in (4.19). Since GNSS faults are to be studied in this thesis, the linear part of the dynamical model of (2.19) - (2.21) can be utilized in a fault-tolerant design. Then the input $\boldsymbol{u}$ can be stated as

$$\boldsymbol{u} = \hat{\boldsymbol{f}}^n + \boldsymbol{g}^n \tag{2.34}$$

where $\hat{\boldsymbol{f}}^n$ nonlinear acceleration estimate in the {n} frame and $\boldsymbol{g}^n$ is gravity given in {n}. Furthermore, from Chapter 4 $\hat{\boldsymbol{f}}^n$ is given as

$$\hat{\boldsymbol{f}}^n = \hat{\boldsymbol{R}}_b^n(\boldsymbol{f}_{\text{IMU}} - \boldsymbol{b}_a + \hat{\boldsymbol{\sigma}}) \tag{2.35}$$

which result $\boldsymbol{u}$ to be nonlinear. Hence, the system matrix $\boldsymbol{A}$ and the input allocation matrix, $\boldsymbol{B}$ is given as

$$\boldsymbol{A} = \begin{bmatrix} \boldsymbol{0}_{3\times3} & \boldsymbol{I}_{3\times3} \\ \boldsymbol{0}_{3\times3} & \boldsymbol{0}_{3\times3} \end{bmatrix}, \qquad \boldsymbol{B} = \begin{bmatrix} \boldsymbol{0}_{3\times3} \\ \boldsymbol{I}_{3\times3} \end{bmatrix}. \tag{2.36}$$

This however requires that the neither the IMU measurements $\boldsymbol{f}_{\text{IMU}}^b$ and $\boldsymbol{\omega}_{\text{IMU}}^b$ or the gyro and acceleration bias estimates, $\boldsymbol{b}_g^b$ and $\boldsymbol{b}_a^b$, fail or provide erroneous bias estimates.

Furthermore, the estimation error can be defined as

$$\boldsymbol{e} := \boldsymbol{y} - \hat{\boldsymbol{y}} = \boldsymbol{C}(\boldsymbol{x} - \hat{\boldsymbol{x}}) + \boldsymbol{Fd} + \boldsymbol{Gf} \tag{2.37}$$

and can according to Frank (1990) be used as the residual presented above in Definition 2.5. Moreover, Blanke (2001) proposes that the residual could

be obtained by filtering the estimation error with a filter, $\boldsymbol{W}(s)$. Then, the residual, $\boldsymbol{r}$, can be written as

$$\boldsymbol{r} = \boldsymbol{W}(s)\boldsymbol{e}. \tag{2.38}$$

This can be useful since the estimation error, $\boldsymbol{e}$, also is sensitive to other disturbances and noise which is not necessarily fault induced. Furthermore, Blanke (2001) states that $\boldsymbol{W}$ should be designed such that the residual, $\boldsymbol{r}$, is sensitive to faults and minimizing the sensitivity to noise effects. In a maritime application such errors and disturbance can be sensor measurement noise and wave-induced motion.

2.5 Dynamic Positioning and System Requirements

This section will present the DP model together with the DP controller and DP requirements.

2.5.1 The 3 DOF DP Model

Fossen (2011) states that ships and semi-submersibles are controlled in 3 DOF of motion. The controllable degrees of freedom is described by motion in surge, sway and yaw and is deemed sufficient for control purposes since the roll and pitch angles usually are small and heave is generally uncontrollable for floating vessels. The state vectors of the reduced model then take the form of

$$\boldsymbol{\eta} = \begin{bmatrix} x^n & y^n & \psi^n \end{bmatrix}^\mathsf{T}, \quad \boldsymbol{\nu} = \begin{bmatrix} u^b & v^b & r^b \end{bmatrix}^\mathsf{T} \tag{2.39}$$

whereas the control inputs are given as

$$\boldsymbol{\tau}_{\text{control}} = \begin{bmatrix} \tau_x^b & \tau_y^b & \tau_\psi^b \end{bmatrix}^\mathsf{T} \tag{2.40}$$

and decomposed in the {b} frame. Furthermore, as presented in Appendix B.1, is the full rotation matrix (B.9) reduced to one principal rotation around the z-axis. Hence, rotation matrix $\boldsymbol{R}_b^n(\boldsymbol{\Theta}_{nb})$ reduces to

$$\boldsymbol{R}_b^n(\psi) = \begin{bmatrix} \cos(\psi) & -\sin(\psi) & 0 \\ \sin(\psi) & \cos(\psi) & 0 \\ 0 & 0 & 1 \end{bmatrix}. \tag{2.41}$$

From Sørensen (2012) is the 3 DOF DP control plant model (CPM) for non-anchored vessels given as

$$\dot{\boldsymbol{\eta}}^n = \boldsymbol{R}(\psi)\boldsymbol{\nu}^b \tag{2.42}$$

$$\boldsymbol{M}\dot{\boldsymbol{\nu}}^b + \boldsymbol{D}\boldsymbol{\nu}^b = \boldsymbol{\tau} + \boldsymbol{R}^\intercal(\psi)\boldsymbol{b}^b \tag{2.43}$$

where $\boldsymbol{M}$ is the inertial matrix, $\boldsymbol{D}$ is the linear damping matrix, $\boldsymbol{b} \in \mathbb{R}^3$ is the bias vector and $\boldsymbol{R}(\psi)$ is the rotation matrix in yaw. This model is valid for $w = p = q = 0$, which implies that the dynamics in heave, roll and pitch are negligible. The bias consist of non-modeled dynamics such as e.g. current, wind and Coriolis forces and moments. Also coupled effects from the neglected roll and pitch dynamics might are also included here. Furthermore, the bias is usually estimated with a first-order model as described in Fossen (2011)

$$\dot{\hat{\boldsymbol{b}}} = -\boldsymbol{T}^{-1}\hat{\boldsymbol{b}} + \boldsymbol{K}\tilde{\boldsymbol{y}} \tag{2.44}$$

or just with integration of the injection term given as

$$\dot{\hat{\boldsymbol{b}}} = \boldsymbol{K}\tilde{\boldsymbol{y}} \tag{2.45}$$

where $\boldsymbol{T}$ is the time constant matrix, $\boldsymbol{K}$ is some positive gain, and $\tilde{\boldsymbol{y}} = \boldsymbol{y} - \hat{\boldsymbol{y}}$ is the discrepancies between the measured position of the vessel and the position estimate. For information regard position measurements and

estimates, see Section 2.3 and Chapter 4.

2.5.2 DP Controller and the Reference Model

From Fossen (2011) can the DP controller be stated in the following manner

$$\boldsymbol{\tau}_{\text{controller}} = -\boldsymbol{R}_b^n(\psi)^\intercal \big(\boldsymbol{K}_p \tilde{\boldsymbol{\eta}}^n + \boldsymbol{K}_d \tilde{\boldsymbol{\nu}}^n + \boldsymbol{K}_i \int_0^t \tilde{\boldsymbol{\eta}}^n(\tau)\, \mathrm{d}\tau \big) \tag{2.46}$$

where $\tilde{\boldsymbol{\eta}} = \hat{\boldsymbol{\eta}} - \boldsymbol{\eta}_d$ and $\tilde{\boldsymbol{\nu}} = \hat{\boldsymbol{\nu}} - \boldsymbol{\nu}_d$. Usually is $\boldsymbol{\nu}_d = \boldsymbol{0}$ because of the controller, (2.46), is mostly used for stationkeeping.

$\boldsymbol{\eta}_d$ and $\boldsymbol{\nu}_d$ can also be obtained from a reference model, such as (2.47)

$$\boldsymbol{\eta}_d^{(3)} + (2\boldsymbol{\Lambda} + \boldsymbol{I})\boldsymbol{\Omega}\ddot{\boldsymbol{\eta}}_d + (2\boldsymbol{\Lambda} + \boldsymbol{I})\boldsymbol{\Omega}^2\dot{\boldsymbol{\eta}}_d + \boldsymbol{\Omega}^3\boldsymbol{\eta}_d = \boldsymbol{\Omega}^3\boldsymbol{r}^n \tag{2.47}$$

where $\boldsymbol{r}^n$ is the desired position reference, to avoid abrupt changes in $\tilde{\boldsymbol{\eta}}$ and $\tilde{\boldsymbol{\nu}}$. Such abrupt changes in the position and velocity error can result in unnecessary use of thrust. Saturating, effects of the desired velocity is also recommended by Fossen (2011). This is so to prevent the desired velocity, $\dot{\boldsymbol{\eta}}_d = \boldsymbol{\nu}_d$, to exceed the physical limitation of the craft. For details regarding reference models can Fossen (2011) be advised.

2.5.3 DP System Recommadations and Requirements

The classification society Det Norske Veritas (2011) states a general commendation that the accuracy of the position reference data is generally to be within:

- A radius of 2% of water depth for bottom-based systems
- Within a radius of 3 m for surface-based systems.

In moderate weather Det Norske Veritas (2011) gives the following recommendation which also incorporates heading: *"(...) in moderate weather conditions and with a fully operational DP system the vessel should generally be able to demonstrate position keeping accuracy typically within a* 3 *meter radius and* $\pm 1^\circ$ *of heading, given sufficient accurate position and heading reference input."*

Regarding fault-tolerance, Det Norske Veritas (2011) states several requirements as follows:

107 *When several systems are combined to provide a mean reference, the mean value used shall not change abruptly by one system being selected or deselected.*

108 *Failures in a positioning reference system that might give degraded quality, loss of position signal or loss of redundancy shall initiate an alarm.*

110 *If a positioning reference system can freeze or otherwise produce corrupt data output, a method shall be provided to enable rejection of the data.*

111 *When more than one positioning reference system is required, then each shall be independent with respect to signal transmission and interfaces.*

- *Guidance note 1: In order for two satellite based systems to be considered as independent it must be possible to set them up with different differential correction signals.*

2.6 Signal Processing Methods

In order increase the fault-tolerance of the Grip et al. (2013, Submitted) observer are the signals from the respective measurements needed to be monitored and processed. This Section will presents methods utilized such

that the observer will be in compliance with the DNV requirements stated above.

2.6.1 Signal Quality Check

The variance of a sensor measurements can indicate the quality of the measurements. Sørensen (2012) states that er very low or vary high variance of a sensor might indicate a faults or failure. A very low variance might indicate freeze, whereas high variance might be a symptom of a sensor failure or an inaccurate measurement. Hence variance testing must be applied to check if the respective measurements should be trusted. Other signal processing methods can be utilized to detect errors like measurement jumps and wild-points. See Section 2.3.2 for details on GNSS error and fault.

Wild-Point Testing

According to Sørensen (2012) can measurement outliers such as spikes and wild-points be excluded by the state estimator by assuming that the sampled measurement measurement, $\boldsymbol{y}[k]$, should lie within an upper and lower limit. The reasonable check can be implemented such that only measurements fulfilling

$$\boldsymbol{y}[k] \in [\bar{\boldsymbol{y}}_k - a\,\boldsymbol{\sigma},\, \bar{\boldsymbol{y}}_k + a\,\boldsymbol{\sigma}] \tag{2.48}$$

are made available to the state estimator in the control system. $\bar{\boldsymbol{y}}_k$ and $\boldsymbol{\sigma}$ are the average and standard deviation of the previous measurements respectively. Furthermore $\pm a\boldsymbol{\sigma}$ is the outlier threshold. Sørensen (2012) states that a should be in the interval between 3 and 9.

Signal Variance and Freeze testing

Sørensen (2012) states that the variance of a given signal, $\boldsymbol{y}[k]$, can be calculated from historic data like

$$\boldsymbol{\sigma}^2[k] = \frac{1}{n-1}\left(\sum_{i=k-(n-1)}^{k} \boldsymbol{y}[i]-, \bar{\boldsymbol{y}}_k^2\right) \tag{2.49}$$

where n is the size of the moving window or buffer containing the data history and $\bar{\boldsymbol{y}}$ is the mean of the moving window at a given time, k.

2.6.2 Signal Voting, Averaging and Weighting

If multiple sensors are used to obtain redundancy, see Section 2.4 from more on redundancy, should voting and weighting be performed to produce the best possible measurement to the user.

Voting can be performed to detect discrepancies between the individual sensors or detect that one sensor is bias by comparing it to the others. The first situation is possible with two sensors. The latter case is only possible with three or more sensor available. If so, can a given sensor can be rejected if the sensor deviates from the others by more than a predefined threshold.

Weighting of redundant sensor measurements can be done according to Gustafsson (2012) where fusion of independent measurements e.g are performed by utilizing a special case of weighted least-squares. Gustafsson present the following loss function

$$V^{\mathrm{WLS}}(\boldsymbol{x}) = \sum_{k=1}^{N}(\boldsymbol{y}_k - \boldsymbol{H}_k\boldsymbol{x}_k)^\intercal \boldsymbol{R}_k^{-1}(\boldsymbol{y}_k - \boldsymbol{H}_k\boldsymbol{x}_k). \tag{2.50}$$

By choosing, $N = 3$ and $\boldsymbol{H} = \boldsymbol{I}_{3\times 3}$, can $\hat{\boldsymbol{y}}^{WLS}$ be written as

$$\hat{\boldsymbol{y}}^{WLS} = \boldsymbol{P}\big(\boldsymbol{R}_1^{-1}\boldsymbol{y}_1 + \boldsymbol{R}_2^{-1}\boldsymbol{y}_2 + \boldsymbol{R}_3^{-1}\boldsymbol{y}_3\big) \tag{2.51}$$

where, $\boldsymbol{P}$, is the covariance matrix given as

$$\boldsymbol{P} = \big(\boldsymbol{R}_1^{-1} + \boldsymbol{R}_2^{-1} + \boldsymbol{R}_3^{-1}\big)^{-1} \tag{2.52}$$

and $\boldsymbol{R}_i$ are the covariance of the individual sensors. Regarding the sensor, the following are assumed sensor model are assumed from position measurements

$$\begin{aligned} \boldsymbol{y}_1 &= \boldsymbol{x} + \boldsymbol{e}_1, \quad \boldsymbol{e}_1 \sim \mathbf{N}(0, \boldsymbol{R}_1) \\ \boldsymbol{y}_2 &= \boldsymbol{x} + \boldsymbol{e}_2, \quad \boldsymbol{e}_2 \sim \mathbf{N}(0, \boldsymbol{R}_2) \\ \boldsymbol{y}_3 &= \boldsymbol{x} + \boldsymbol{e}_3, \quad \boldsymbol{e}_3 \sim \mathbf{N}(0, \boldsymbol{R}_3). \end{aligned} \tag{2.53}$$

Then $\boldsymbol{R}_i$ is given as

$$\boldsymbol{R}_i = \begin{bmatrix} \sigma^2_{\mathrm{GNSS,x_i}} & 0 & 0 \\ 0 & \sigma^2_{\mathrm{GNSS,y_i}} & 0 \\ 0 & 0 & \sigma^2_{\mathrm{GNSS,z_i}} \end{bmatrix}. \tag{2.54}$$

2.7 Simulation Theory

In the implementation of the nonlinear observer the corrector and predictor paradigm of the discrete Kalman filter is exploited. From Fossen (2011) the corrector and predictor equations can be written as

$$\begin{aligned} &\text{Corrector} \quad && \hat{\boldsymbol{x}}(k) = \bar{\boldsymbol{x}} + \boldsymbol{K}_d[\boldsymbol{y}(k) - \bar{\boldsymbol{y}}(k)] \\ &\text{Predictor} \quad && \bar{\boldsymbol{x}}(k+1) = \hat{\boldsymbol{x}}(k) + h\boldsymbol{f}(\hat{\boldsymbol{x}}(k), \boldsymbol{u}(k)) \end{aligned} \tag{2.55}$$

where the injection term is given as $\boldsymbol{K}_d(\boldsymbol{y} - \hat{\boldsymbol{y}})$. Furthermore, $\boldsymbol{K}_d = h\boldsymbol{K}$, where h is the sampling time. If no measurements are available, the predictor takes the form of

$$\bar{\boldsymbol{x}}(k+1) = \bar{\boldsymbol{x}}(k) + h\boldsymbol{f}(\hat{\boldsymbol{x}}(k), \boldsymbol{u}(k)) \tag{2.56}$$

This is dead-reckoning. A general corrector-predictor algorithm for observers is presented in Fossen (2011).

According to Section B.1 may the quaternion no longer be unity caused by numerical integration, in a computer, of the quaterion differential equation, (B.24). This problem can be compensated be renormalizing the quaternion according to

$$\boldsymbol{q}_b^n(k+1) = \frac{\boldsymbol{q}_b^n(k+1)}{\|\boldsymbol{q}_b^n(k+1)\|} \tag{2.57}$$

for each time step as given in (B.27).

Chapter 3

Vessel Simulator

The purpose of the simulator was to generate a complete 6 DOF motion of a vessel exposed to environmental forces. Using the vessel model as a basis, a so called 9 DOF, IMU and GNSS measurements where obtained from the simulated kinetics and kinematics such that the respective inertial and position measurements can be provided to the user and the observer.

Regarding the vessel type a semi-submersible was chosen. Such a vessel is illustrated in Figure 3.1. The vessel parameters where obtained from `rig.m` provided by the MSS Toolbox, see MSS. Marine Systems Simulator (2010).

Figure 3.1: Illustration of a semi-submersible. Vessel name: West Venture. Photo: Seadrill.

A fault injection method was also constructed in order to simulate sensor faults.

3.1 Simulator Model of Vessel with Environmental Forces and Moments

In order to obtained some degree of real-life motion of the vessel due to weather condition, wave and current forces and moments was taken in account when designing the simulator. Hence, both oscillatory and drifting motion of the simulated vessel were obtained. From this, the total simulation modeled of the vessel with environmental forces can be written as

$$\dot{\boldsymbol{\eta}} = \boldsymbol{J}_{\boldsymbol{\Theta}}(\boldsymbol{\eta})\boldsymbol{\nu}_r + \begin{bmatrix} \boldsymbol{v}_c^n \\ \mathbf{0} \end{bmatrix} \tag{3.1}$$

$$\boldsymbol{M}\dot{\boldsymbol{\nu}}_r + \boldsymbol{C}(\boldsymbol{\nu}_r)\boldsymbol{\nu}_r + \boldsymbol{D}(\boldsymbol{\nu}_r)\boldsymbol{\nu}_r + \boldsymbol{g}(\boldsymbol{\eta}) = \boldsymbol{\tau}_{\text{control}} + \boldsymbol{\tau}_{\text{wave}} \tag{3.2}$$

according to (B.55) - (B.56) as stated in Appendix B.3.2. $\boldsymbol{\eta} \in \mathbb{R}^6$ is the generalized position of the vessel whereas $\boldsymbol{\nu}_r \in \mathbb{R}^6$ is the relative velocity

$$\boldsymbol{\nu}_r = \boldsymbol{\nu} - \boldsymbol{\nu}_c. \tag{3.3}$$

Moreover, ν_c is the current velocity. Since relative velocity was utilized in the vessel simulator was the Coriolis matrix, $\boldsymbol{C}(\boldsymbol{\nu}_r)$, parameterized independent of linear velocity. See Appendix B.3.2 for details.

Wind forces and moments was discarded in construction of the simulator. Both oscillatory and drifting environmental forces and moments was obtained from the inclusion of first-order wave and forces and moments together with the respective current. Because of this was wind forces and moments not included in the simulator mode,l of 3.1 - (3.2), since the second-order environmental forces was obtained be the inclusion of current. Figure 3.2 illustrates of the environmental disturbances are introduced in the simulator.

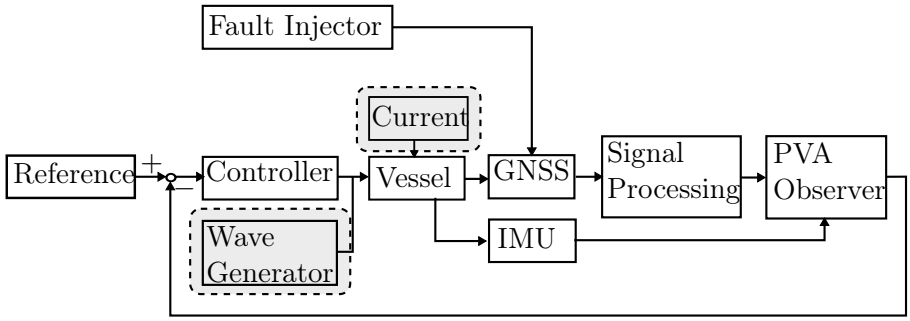

Figure 3.2: Simulator. Overview of how the environmental forces and moments acts on the vessel.

Current

As seen above and in Appendix B.3.2 can the current be added in the kinetics be exploiting that the kinetics can be simulated with relative generalized velocity, $\boldsymbol{\nu}_r$. The current, $\boldsymbol{v}_c^n$, in the simulator model of (3.1) is given as

$$\boldsymbol{v}_c^n = \begin{bmatrix} V_c \cos(\alpha_c) \cos(\beta_c) \\ V_c \sin(\beta_c) \\ V_c \sin(\alpha_c) \cos(\beta_c) \end{bmatrix} \tag{3.4}$$

from (B.59). Furthermore, the angle of attack, α_c was chosen to zero. Hence, the current only has horizontal components. The speed current speed, V_c was chosen to 1 [m/s] and the side slip angle, β_c was chosen to $\beta_c = -30°$. Hence, the current was given as

$$\boldsymbol{v}_c^n = \begin{bmatrix} 0.5 \cdot \cos(-30°) \\ 0.5 \cdot \sin(-30°) \\ 0 \end{bmatrix}. \tag{3.5}$$

The simulation of the current (3.5) is shown in Figure 3.3.

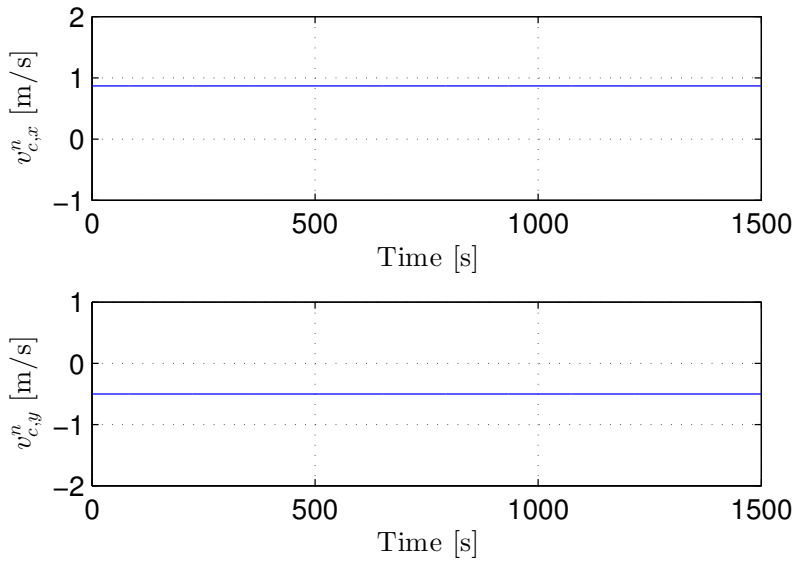

Figure 3.3: Vessel Simulator. Two dimensional, constant irrational current.

Wave-Induced Forces and Moments

The wave-induced forces and moments where calculated by utilizing linear wave theory as presented in Appendix B.3.1.

The *JONSWAP* spectra was chosen to obtain a wave spectra values for the North Sea was chosen as presented in Section B.3.1. According to Sørensen (2012) are wave periods in the range of 5 to 20 seconds quite common. Hassani et al. (2012) and reference therein presents that a high sea state usually lies within $\boldsymbol{\omega}_0 \in [0.45\frac{\text{rad}}{\text{s}} - 0.67\frac{\text{rad}}{\text{s}}]$ and $H_s \in [2.69\text{m} - 9.71\text{m}]$. Based on this the chosen wave frequency was $w_0 = 0.5$. This result in a wave period of

$$T_0 = \frac{2\pi}{w_0} = 12.5664 \tag{3.6}$$

Furthermore, significant wave height was chosen to be $H_s = 7$. By utilizing the `wavespec.m` the in the MSS Toolbox, was the JONSWAP spectra was

calculated as following

```
S = wavespec(7,[H_s, w_0, gamma], w, 1);
```

For more on MSS Toolbox, see MSS. Marine Systems Simulator (2010).

From Fossen (2011) can the first-order wave frequency induced forces and moments, $\boldsymbol{\tau}_{\text{wave 1st}}$, be approximated as second-order transfer function driven by a Gaussian, zero mean process. For each degree of freedom can the following transfer function

$$h(s)_{\text{wave},i}(s) = \frac{K_w^{\{i\}} s}{s^2 + 2\lambda^{\{i\}}\omega_0^{\{i\}}\sigma + \left(\omega_0^{\{i\}}\right)^2} \tag{3.7}$$

model the wave frequency motion according to Fossen (2011). Furthermore, the parameters of (3.7) was found. σ was calculated according to (B.44) as

$$\left(\sigma^{\{i\}}\right)^2 = \max_{o<\omega<\infty} S(\omega). \tag{3.8}$$

Whereas, λ was found by was calculated by curve fitting the spectra, $P_{\xi\xi}(\omega)$, of the linear transfer function, $h(s)$, to the JONSWAP spectra, $S(\omega)$. The resulting wave spectra together with the linear approximation can be seen in Figure 3.4. This resulted in $\sigma = 2.7592$ and $\lambda = 0.107$. However, $\lambda = 0.10$ was chosen since this is recommended by Fossen (2011).

Moreover, can (3.7) can be written in state-space form(B.45) - (B.46) such as

$$\dot{\boldsymbol{\xi}}_w = \boldsymbol{A}_w\boldsymbol{\xi}_w + \boldsymbol{E}_w\boldsymbol{w} \tag{3.9}$$

$$\boldsymbol{y}_{\text{wave}} = \boldsymbol{C}_w\boldsymbol{\xi}_w. \tag{3.10}$$

which again can be utilized in a computer simulation. Furthermore, as given in Appendix B.3.1, can the total wave forces and moments can be

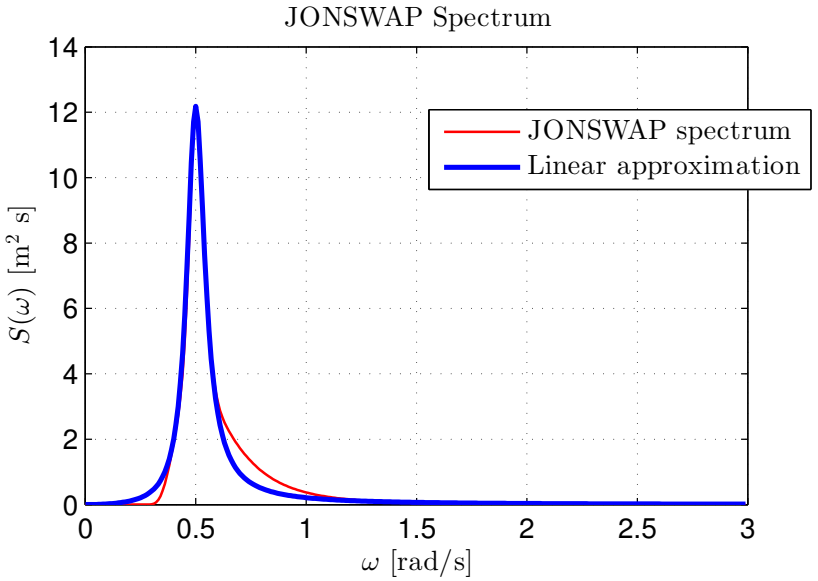

Figure 3.4: Simulator: JONSWAP spectrum wave spectra together with the curve fitted linear transfer function approximation of the wave spectra

approximated by

$$\boldsymbol{\tau}_{\text{wave}} \approx \boldsymbol{K}\boldsymbol{H}_s(s)\boldsymbol{w}(s). \tag{3.11}$$

In the simulator, the scaling matrix, $\boldsymbol{K}$, was chosen equal to inertia matrix, $\boldsymbol{M}$, to obtain a realistic wave-induced motion of the simulated vessel.

In order to simulate (3.9) - (3.10) in MATLAB® a numerical integration method had to be chosen. First, the eigenvalues of $\boldsymbol{A}_w$ was calculated. This resulted in complex conjugated eigenvalues of

$$-0.2245 \pm 0.4468i \tag{3.12}$$

in each degree of freedom. Because of the complex eigenvalues with small real part, Euler integration was deemed to not be the best choice because of the lack of stability for under-damped systems, see Egeland and Gravdahl (2002) for details. Instead, The Explicit Runge Kutta numerical integration

method of order four (RK4) was used. For more on RK4, see Appendix C. The eigenvaules of the 6 DOF wave model is given in Appendix A. Chosen step time, h, was chosen to be 0.01. $\boldsymbol{w}$ is a Gaussian, zero mean, processes. The standard deviation of $\boldsymbol{w}$ was chosen as

$$\boldsymbol{\sigma}_w = [1,\ 1,\ 1,\ 1,\ 1,\ 1]^\intercal. \tag{3.13}$$

Simulation result of the wave-induced forces and moments can be found in Appendix D.

Model Parameters and State-Space Model

The $\boldsymbol{M}$, $\boldsymbol{D}$ and $\boldsymbol{G}$ are provided from `rig.m` provided by the MSS Toolbox, see MSS. Marine Systems Simulator (2010). Hence, $\boldsymbol{g}(\boldsymbol{\eta})$ have to be calculated from the $\boldsymbol{G}$ matrix. From (B.37) is $\boldsymbol{g}(\eta)$ given a

$$\boldsymbol{g}(\boldsymbol{\eta}) = \boldsymbol{G}\boldsymbol{\eta}^n \tag{3.14}$$

since $\boldsymbol{G}$ is linearized around $\phi = \theta = 0$. Then, $\boldsymbol{g}(\boldsymbol{\eta})$ is independent of the heading angle, ψ.

The Coriolis matrix, $\boldsymbol{C}(\boldsymbol{\nu}_r)$, calculated by the function `MRB_and_Omega_b2Coriolis.m` as

```
C_r = M_RB_and_Omega_b2Coriolis(M_RB, omega_b_bn, r_g_2_b);
```

in MATLAB® at every iteration of the simulator. Then, $\boldsymbol{C}_r$ is obtained independently of a the linear velocity. See Appendix B.3.2 for details. As presented in the beginning of Section 3.1 were wind forces and moments not considered in the simulator. The same goes for 2nd-order wave forces and moments. Hence, for simulation purposes (3.1)-(3.2) can be written in

state-space form as

$$\begin{bmatrix} \dot{\boldsymbol{\eta}}^n \\ \dot{\boldsymbol{\nu}}_r^b \end{bmatrix} = \begin{bmatrix} \mathbf{0}_{6x6} & \boldsymbol{J}_{\boldsymbol{\Theta}}(\boldsymbol{\eta}) \\ -\boldsymbol{M}^{-1}\boldsymbol{G} & -\boldsymbol{M}^{-1}(\boldsymbol{C}+\boldsymbol{D}) \end{bmatrix} \begin{bmatrix} \boldsymbol{\eta}^n \\ \boldsymbol{\nu}_r^b \end{bmatrix} + \begin{bmatrix} \mathbf{0}_{6x6} \\ -\boldsymbol{M}^{-1} \end{bmatrix} \boldsymbol{\tau}_{\text{control}} + \begin{bmatrix} \mathbf{0}_{6x6} \\ -\boldsymbol{M}^{-1} \end{bmatrix} \boldsymbol{\tau}_{\text{wave 1st. order}} \tag{3.15}$$

where

$$\boldsymbol{\eta}^n = [x^n, y^n, z^n, \phi, \theta, \psi]^\intercal, \quad \boldsymbol{\nu}_r^b = [u_r^b, v_r^b, w_r^b, p^b, q^b, r^b]^\intercal \tag{3.16}$$

and $\boldsymbol{J}_{\boldsymbol{\Theta}}(\boldsymbol{\eta})$ is given by (B.28) as

$$\boldsymbol{J}_{\boldsymbol{\Theta}}(\boldsymbol{\eta}) = \begin{bmatrix} \boldsymbol{R}_b^n(\boldsymbol{\Theta}_{nb}) & \mathbf{0}_{3x3} \\ \mathbf{0}_{3x3} & \boldsymbol{T}_\Theta(\boldsymbol{\Theta}_{nb}) \end{bmatrix}. \tag{3.17}$$

The vessel was simulated in MATLAB® with step length, $h = 0.01$ with combined forward and backwards Euler. Regarding the step length, $h = 0.01$ was chosen in order to obtain 100 Hz IMU measurements. Combined forward and backwards Euler was chosen to ensure a stable integration in a event of oscillatory wave input because of the highly underdamped eigenvalues of the second-order system (3.15). An example with zero generalized position

and velocity angular velocity gives in the following eigenvaules

$$\mathbf{\Lambda} = \begin{bmatrix} 0 \\ 0 \\ 0 \\ -0.0651 \pm 0.6214i \\ 0 \\ 0 \\ -0.0651 \pm 0.6214i \\ -0.0050 \\ -0.0125 \\ -0.0752 \pm 0.7482i \\ -0.0358 \pm 0.3566i \\ -0.0100 \end{bmatrix}. \tag{3.18}$$

In order to show the wave-induced motion of the vessel, (3.15) was simulation without control input. The results can be found in Appendix D, Figure D.4.

3.2 Simulating GNSS and IMU Measurements

Four different measurements was proved by the simulator. The position measurements were obtained from the simulated GNSS, while the latter three measurement were provided by an IMU. I.e acceleration, angular rate and magnetic field measurements from an accelerometer, a gyroscope and a magnetometer respectively. How the measurements where obtained from the simulator can be seen in Figure 3.5.

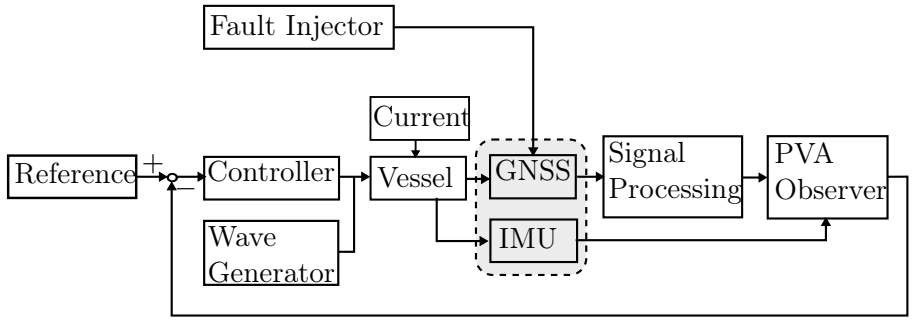

Figure 3.5: Simulator. Overview of how the sensor measurements where obtained in the simulator.

3.2.1 Measurement Models

GNSS Measurements

The GNSS measurements was obtained from NED the position of the vessel by utelizing the simulator model as basis. Then, measurement noise and possibly bias or drifting terms was added before provided to the user. Hence, the simulated GNSS measurements are model as

$$\boldsymbol{p}^n_{\text{GNSS}} = \boldsymbol{p}^n_{b/n} + \boldsymbol{w}^n + \boldsymbol{b}^n_{\text{GNSS}} \tag{3.19}$$

where $\boldsymbol{p}^n_{b/n} = [x^n, y^n, z^n]$, $\boldsymbol{w}^n$ is zero mean, Gaussian measurement noise and $\boldsymbol{b}^n_{\text{GNSS}}$ is an given bias or drifting term. $\boldsymbol{p}^n_{b/n}$ is provided directly from the simulated vessel instead of simulating a total satellite range space solution based upon (2.23), from Section 2.3.

IMU Measurements

The IMU measurements was, provided by extracting the acceleration, angular velocity from the simulator model. The magnetometer measurement, on the other hand, was obtained by finding the magnetic field at a given loca-

tion before transforming it to the {b} and adding noise and bias terms. From Mahony et al. (2008) the following measurements model are utilized

$$\boldsymbol{f}^b_{\text{IMU}} = \boldsymbol{R}^b_n(\boldsymbol{\Theta})(\dot{\boldsymbol{v}}^n_{b/n} - \boldsymbol{g^n}) + \boldsymbol{b}^b_{\text{acc}} + \boldsymbol{w}^b_{\text{acc}} \tag{3.20}$$

$$\boldsymbol{\omega}^b_{\text{IMU}} = \boldsymbol{\omega}^b_{b/n} + \boldsymbol{b}^b_{\text{gyro}} + \boldsymbol{w}^b_{\text{gyro}} \tag{3.21}$$

$$\boldsymbol{m}^b_{\text{IMU}} = \boldsymbol{R}^n_b(\boldsymbol{\Theta})\boldsymbol{m}^n + \boldsymbol{b}^b_{\text{mag}} + \boldsymbol{w}^b_{\text{mag}}. \tag{3.22}$$

$\boldsymbol{\omega}^b_{b/n}$ and $\boldsymbol{m}^n$ together with the Euler angles, $\boldsymbol{\Theta}$, was extracted directly from the simulator. Values of $\boldsymbol{m}^n$ need to be predefined in advance of any simulation. Furthermore, $\boldsymbol{m}^n$ was assumed constant since all simulation was carried with vessel motion constrained to a smaller geographical area. However,the term $\boldsymbol{R}^b_n\dot{\boldsymbol{v}}^n_{b/n}$ has to be calculated in order to obtain the accelerometer measurements since only $\dot{\boldsymbol{v}}^b_r$ and $\boldsymbol{R}^b_n$ are provided directly from the simulator.

From (B.60) is the irrational current defined as

$$\dot{\boldsymbol{v}}^n_c := \boldsymbol{0} \tag{3.23}$$

Furthermore, the velocity of the irrational current, $\boldsymbol{v}^b_c$, in the {b} frame is then given as

$$\boldsymbol{v}^b_c = \boldsymbol{R}^b_n(\boldsymbol{\Theta}_{nb})\boldsymbol{v}^n_c \tag{3.24}$$

Moreover, $\dot{\boldsymbol{v}}^b_c$ is given as

$$\dot{\boldsymbol{v}}^b_c = \dot{\boldsymbol{R}}^b_n(\boldsymbol{\Theta}_{nb})\boldsymbol{v}^n_c + \boldsymbol{R}^b_n(\boldsymbol{\Theta}_{nb})\dot{\boldsymbol{v}}^n_c \tag{3.25}$$

by applying the chain rule. Then, because of (3.23), $\dot{\boldsymbol{v}}^b_c$ will be given as

$$\dot{\boldsymbol{v}}^b_c = \dot{\boldsymbol{R}}^b_n(\boldsymbol{\Theta}_{nb})\boldsymbol{v}^n_c = -\boldsymbol{S}(\boldsymbol{\omega}^b_{b/n})\boldsymbol{v}^b_c \tag{3.26}$$

from the Definition B.1 of irrational currents. Furthermore, since the current

is given in the {n} frame, must the former results be calculated from

$$\dot{\boldsymbol{v}}_c^b = -\boldsymbol{S}(\boldsymbol{\omega}_{b/n}^b)\boldsymbol{R}_n^b\boldsymbol{v}_c^n \tag{3.27}$$

Finally, $\dot{\boldsymbol{v}}^b$ is given as

$$\dot{\boldsymbol{v}}^b = \dot{\boldsymbol{v}}_r^b + \dot{\boldsymbol{v}}_c^b \tag{3.28}$$

by rearranging the definition of relative velocity from (B.36), i.e

$$\boldsymbol{\nu_r} := \boldsymbol{\nu} - \boldsymbol{\nu_c} \Rightarrow \boldsymbol{\nu}^b = \boldsymbol{\nu}_r^b + \boldsymbol{\nu}_c^b. \tag{3.29}$$

Hence, the acceleration measurement of (3.20) was then implemented as

$$\begin{aligned}\boldsymbol{f}_{\text{IMU}}^b &= \dot{\boldsymbol{v}}_r^b - \boldsymbol{S}(\boldsymbol{\omega}_{b/n}^b)\boldsymbol{R}_n^b\boldsymbol{v}_c^n - \boldsymbol{R}_n^b(\boldsymbol{\Theta})\boldsymbol{g^n} + \boldsymbol{b}_{\text{acc}}^b + \boldsymbol{w}_{\text{acc}}^b \\ &= \dot{\boldsymbol{v}}_r^b + \dot{\boldsymbol{v}}_c^b - \boldsymbol{R}_n^b(\boldsymbol{\Theta})\boldsymbol{g^n} + \boldsymbol{b}_{\text{acc}}^b + \boldsymbol{w}_{\text{acc}}^b \\ &= \dot{\boldsymbol{v}}_{b/n}^b - \boldsymbol{R}_n^b(\boldsymbol{\Theta})\boldsymbol{g^n} + \boldsymbol{b}_{\text{acc}}^b + \boldsymbol{w}_{\text{acc}}^b.\end{aligned} \tag{3.30}$$

The rotation matrix, $\boldsymbol{R}_n^b$, and the skew-symertic matrix, $\boldsymbol{S}(\boldsymbol{\omega}_{b/n}^b)$, were calculated with the `Rzyx.m` and `Smtrx.m` functions respectively. Both provided by the MSS Toolbox.

3.2.2 Choice of Sensor Parameters, Errors and Faults

Sampling Time

Three 5 Hz GNSS units together with one 100 Hz IMU was simulated. This resulting a the sampling a sampling time of

$$\begin{aligned}f_{\text{GNSS}} = 5 \text{ Hz} &\Rightarrow T_{\text{GNSS}} = 0.2 \text{ s} \\ f_{\text{IMU}} = 100 \text{ Hz} &\Rightarrow T_{\text{IMU}} = 0.01 \text{ s}\end{aligned} \tag{3.31}$$

for both type of sensors.

In order simulate realistic sensor measurements both white noise and sensor biases was included. White noise for both sensor was added by using the `normrnd.m` function in the Statistics Toolbox in MATLAB® .

The magnetic field was chosen to

$$\boldsymbol{m}^n = \begin{bmatrix} 16836.0 \text{ nT} & -176.3 \text{ nT} & 47137.8 \text{ nT} \end{bmatrix}^\intercal \tag{3.32}$$

which is the magnetic field from the offshore installation Ekofisk on the Norwegian continental shelf in the North Sea. The magnetic field of (3.32) was calculated by utilizing the service of National Geophysical Data Center (2013). Data from 1^{th} of January 2013 was utilized.

IMU Errors

The standard deviation of white noise accelerometer, gyroscope and magnetometer can be found in Table 3.1 whereas the biases of the IMU measurments in found Table 3.2. The gyro biases was chosen different from the gyro bias presented in Grip et al. (2013, Submitted), however they were chosen in the same order of magnitude.

Table 3.1: IMU Noise

	Std. Accelerometer	Std. Gyro	Std. Magnetometer
x	0.2 m/s^2	0.1 deg/s	$1.25 \cdot 10^{-3}$ nT
y	0.2 m/s^2	0.1 deg/s	$1.25 \cdot 10^{-3}$ nT
z	0.2 m/s^2	0.1 deg/s	$1.25 \cdot 10^{-3}$ nT

The reason for the choice of zero accelerometer bias and magnetometer bias is shown and discussed in Chapter 5, Section 5.1. The accelerometer and magnetometer was assumed to be pre-calibrated. The validity of this assumption is discussed in 5.8.

Table 3.2: IMU Bias

	Accelerometer	Gyro	Magnetometer
x	0 m/s^2	0.17 deg/s	0 nT
y	0 m/s^2	−0.18 deg/s	0 nT
z	0 m/s^2	0.14 deg/s	0 nT

GNSS Errors and Faults

The chosen standard deviation of the GNSS white measurement noise can be found in Table 3.3. Both normal operation and fault induced noise is presented. The normal operation column is, in Table 3.3, is based upon to assumptions

- Use of dual frequency receiver to cancel ionospheric disturbances, see Section 2.3.
- dGNSS is utilized.

From Parkinson and Spilker (1996a,b) can such assumptions yield a position measurement with better accuracy than 1 meter standard deviation (1σ). Moreover, Section 2.3.2 presents i.a. that VDOP is larger than HDOP. This is why the chosen white noise standard deviations of the vertical measurement components are set higher. The latter type is activated in the simulator by the fault injection method illustrated in Figure 3.6.

In Table 3.4 can one find the GNSS bias types and magnitude. Table 3.5 shows the chosen wild-points utilized in the simulator. 12 different wild-points were chosen such that each of the wild-point could be replicated for each simulation and still yield different values throughout each simulation. The motivation for this is that robustness of the fault-tolerant methods utilized in this thesis could be tested since the wild-point for each sensor would not be same for each wild-point occurrence.

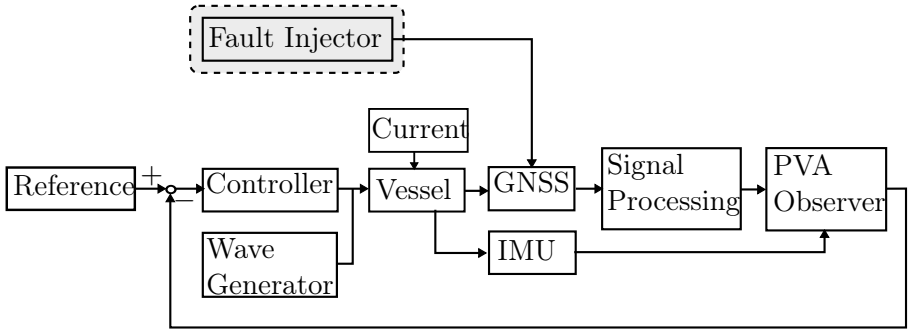

Figure 3.6: Simulator. Overview of how the GNSS sensor faults are injected in the simulator.

Table 3.3: GNSS Measurement Noise

	Std. White Noise Normal Operation	Std. White Noise Fault Induced
p_x^n	1 m	10 m
p_y^n	1 m	10 m
p_z^n	1.2 m	12 m

From the statements above can these faults can present them selves as

- Single antenna bias. Cause might be multipath and a receiver error.
- All antennas will be biased from e.g. multipath, bad GDOP or Differential link error.
- Abrupt changes in the measurement such as wild-points or jumps.
- Loss of position reference from e.g. atmospheric scintillation.
- Freeze from e.g. a fault in software or electronics failure.
- Drift from e.g. differential link error or satellite clock failure.

Table 3.4: GNSS Measurement Biases

	GNSS Bias Jump	GNSS Bias Fast Drift
p_x^n	5 m	0.1 m/s
p_y^n	−5 m	0.15 m/s
p_z^n	0 m	0.25 m/s

Table 3.5: GNSS Measurement Wild-points

	Number 1	Number 2	Number 3	Number 4
p_x^n	21.0078 m	16.6023 m	−23.9294 m	15.5738 m
p_y^n	−19.0980 m	15.0930 m	−21.7540 m	14.1580 m
p_z^n	−23.8725 m	−18.8663 m	−27.1925 m	17.6975 m

	Number 5	Number 6	Number 7	Number 8
p_x^n	−13.3694 m	−16.3493 m	19.4711 m	13.4695
p_x^n	12.1540 m	−14.8630 m	−17.7010 m	12.2450 m
p_z^n	−15.1925 m	18.5787 m	−22.1262 m	−15.3062 m

	Number 9	Number 10	Number 11	Number 12
p_x^n	−14.3440 m	−19.8792 m	−31.0398 m	29.0444 m
p_y^n	−13.0400 m	18.0720 m	28.2180 m	26.4040 m
p_z^n	16.3000 m	−22.5900 m	35.2725 m	−33.0050 m

Regardless of the underlying causes should the fault-tolerant methods handle errors or faults. Because of this, the fault-tolerant observer was subjected to multiple error and fault scenarios, related to the use of GNSS as position reference. These were

- Wild-point of multiple GNSS measurements.
- Freeze of single GNSS antenna measurements.
- Increased variance of a single GNSS antenna measurements.
- Jump in measurement (constant bias).
- Drift of all GNSS antenna measurements.

The corresponding results can be found in Chapter 5.

3.3 DP Controller

The DP controller was chosen as

$$\boldsymbol{\tau}_{\text{controller}} = \boldsymbol{R}_b^n(\psi)^\intercal \boldsymbol{K}_p \tilde{\boldsymbol{\eta}}^n - \boldsymbol{R}_b^n(\psi)^\intercal \boldsymbol{K}_d \tilde{\boldsymbol{\nu}}^n - \boldsymbol{R}_b^n(\psi)^\intercal \boldsymbol{K}_i \int_0^t \tilde{\boldsymbol{\eta}}^n(\tau)\, \mathrm{d}\tau \quad (3.33)$$

and sampled at 10 Hz. The integral $\int_0^t \tilde{\boldsymbol{\eta}}^n(\tau)\, \mathrm{d}\tau$ was calculated by utilizing Forward Euler with step length $h_{\text{control}} = 0.1$ according to

$$\boldsymbol{\eta}_{\text{int}}(k+1) = \boldsymbol{\eta}_{\text{int}}(k) + h_{\text{control}} \cdot \tilde{\boldsymbol{\eta}}. \quad (3.34)$$

Moreover, this resulted in the following controller at time step, k

$$\boldsymbol{\tau}_{\text{controller}}(k) = -\boldsymbol{R}_b^n(\psi)^\intercal(k) \Big[\boldsymbol{K}_p \tilde{\boldsymbol{\eta}}^n(k) + \boldsymbol{K}_d \tilde{\boldsymbol{\nu}}^n(k) + \boldsymbol{K}_i \boldsymbol{\eta}_{\text{int}}(k) \Big]. \quad (3.35)$$

Any given change in control set-point was filter through a third-order reference model, as presented in Section 2.5.2. How the controller and reference model was implemented in the simulator is illustrated in Figure 3.7

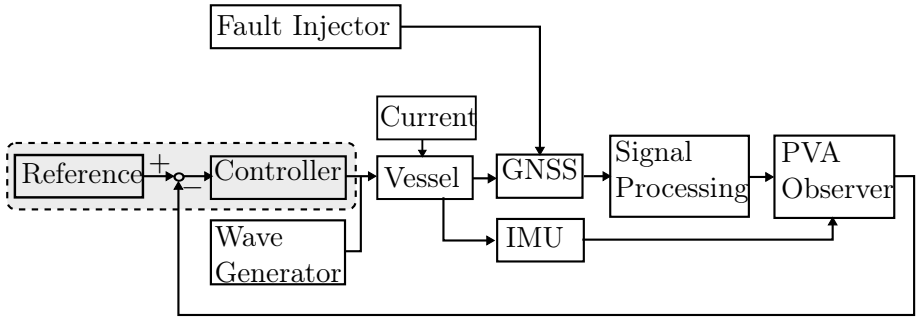

Figure 3.7: Simulator. Overview of how the controller and reference model where implemented in the simulator.

Chapter 4

Observer Design

The chosen observer for this thesis is the INS/GNSS integration observer proposed by Grip et al. (2013, Submitted). Section 4.1 and 4.2 present the basis for the observer together with the observer equation. Furthermore, Section 4.3 takes on the aspects regarding the implementation of the observer in discrete time. Section 4.4 follows with the observer tuning, whereas Section 4.5 and Section 4.6 takes on the fault-tolerance additions to the observer developed by Grip et al. (2013, Submitted).

4.1 Dynamical Formulation

A special condition of the problem formulation in Grip et al. (2013, Submitted) follows from Section 2.2.2 as

$$\dot{\boldsymbol{p}}^n = \boldsymbol{v}^n \tag{4.1}$$

$$\dot{\boldsymbol{v}}^n = \boldsymbol{f}^n + \boldsymbol{g}^n(\boldsymbol{p}^n) \tag{4.2}$$

$$\dot{\boldsymbol{q}}_b^n = \boldsymbol{T}_q(\boldsymbol{q})\boldsymbol{\omega}_{b/n}^b \tag{4.3}$$

$$\dot{\boldsymbol{b}}_g^b = \boldsymbol{0} \tag{4.4}$$

where the NED frame is assumed inertial. Hence, flat earth navigation is assumed. The definition of Flat Earth navigation is found in Appendix B.5, Definition B.2. This is a safe assumption of for a stationkeeping applications utilized by marine vessels. Hence, the rotation of the earth is neglected in opposite of Grip et al. (2013, Submitted). By knowledge of the longitude and

latitude can the gravity vector, $\boldsymbol{g}^n(\boldsymbol{p}^n)$, can be calculated according to Hsu (1996). However, here a constant gravity vector, $\boldsymbol{g}^n(\boldsymbol{p}^n) = [0,\ 0,\ 9.81]^\intercal$, is assumed because the observer will be applied in a stationkeeping operation. Hence, the vessel is contained to a small geographical area and thus the gravity can be assumed constant during the operation.

Sensor Configuration

The nonlinear PVA observer to be presented in this chapter is based upon the following sensor configuration based on IMU and GNSS measurements:

1. Position measurement: $\boldsymbol{p}^n_{\text{GNSS}} = \boldsymbol{p}^n$
2. Velocity measurement(full or partial): $\boldsymbol{v}^n_{\text{GNSS}} = \boldsymbol{C}_{\boldsymbol{v}}\boldsymbol{v}^n$, where $\boldsymbol{C}_{\boldsymbol{v}}$ may be a zero matrix, identify matrix or some other constellation. In this thesis will not GNSS velocity be utilized.
3. Angular Velocity measurement: $\boldsymbol{\omega}^b_{nb,\text{IMU}} = \boldsymbol{\omega}^b_{nb} + \boldsymbol{b}^b_g$
4. Acceleration measurement: $\boldsymbol{f}^b_{\text{IMU}} = \boldsymbol{f}^b + \boldsymbol{b}^b_a$.
5. Magnetic field measurement: $\boldsymbol{m}^b_{\text{IMU}} = \boldsymbol{m}^b$

Furthermore, the magnetic field, $\boldsymbol{m}^n$ is assumed to be known.

4.2 Nonlinear Observer for Position, Velocity and Attitude

As presented in Chapter 1 was the observer proposed in Grip et al. (2013, Submitted) was chosen. The observer with the corresponding sensor is illustrated in Figure 4.1. The assumptions posted by Grip et al. (2013, Submitted) regarding the basis the observer can be found in Appendix B.4.

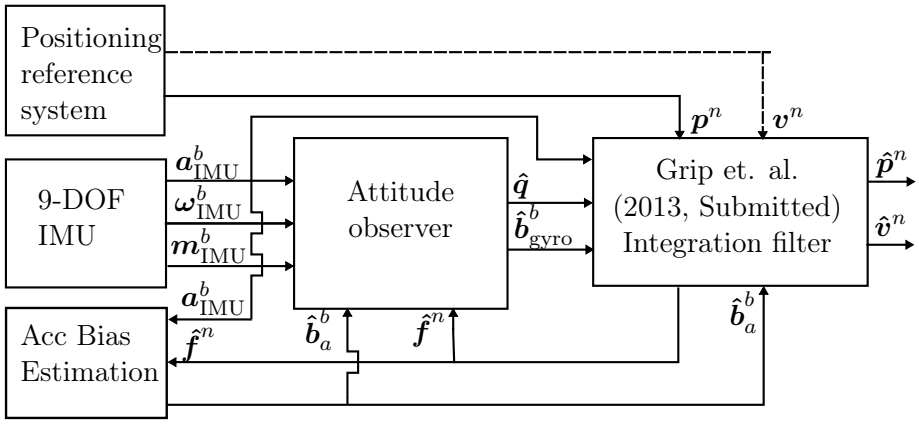

Figure 4.1: The observer of Grip et al. (2013, Submitted). In this case the position reference system is GNSS. Furthermore, the velocity measurement is optionally. The attitude observer estimates a quaterion, $\hat{\boldsymbol{q}}$, and the gyro bias, $\hat{\boldsymbol{b}}^b_{\text{gyro}}$. From the acceleration measurement together with attitude and accelerometer bias estimates, $\hat{\boldsymbol{b}}^b_{\text{acc}}$, is an acceleration estimate in the {n} frame calculated. Furthermore, $\hat{\boldsymbol{f}}^n$ is feed back to the attitude observer where it is utilized in the attitude and gyro bias estimation. The integration filter estimates position and velocity in the {n} frame.

4.2.1 Attitude and Gyro Bias Estimation

By applying the attitude differential equation from Section 4.1 can the attitude observer from Figure 4.1 be written as

$$\dot{\hat{\boldsymbol{q}}}^n_b = \boldsymbol{T}(\hat{\boldsymbol{q}}^{\boldsymbol{n}}_{\boldsymbol{b}})(\boldsymbol{\omega}^b_{b/n,\text{IMU}} - \hat{\boldsymbol{b}}^b_g + \hat{\boldsymbol{\sigma}}) \tag{4.5}$$

Moreover, the gyro bias estimate is written as

$$\dot{\hat{\boldsymbol{b}}}^b_g = \text{Proj}(\hat{\boldsymbol{b}}^b_g, -k_I\hat{\boldsymbol{\sigma}}) \tag{4.6}$$

Furthermore, in this case is the nonlinear injection term, $\hat{\boldsymbol{\sigma}}$, provided by Grip et al. (2013, Submitted), is defined as

$$\hat{\boldsymbol{\sigma}} := k_1 \underline{\boldsymbol{m}}^b \times \boldsymbol{R}(\boldsymbol{q}_b^n)^\intercal \underline{\boldsymbol{m}}^n + k_2 \underline{\boldsymbol{f}}^b \times \boldsymbol{R}(\boldsymbol{q}_b^n)^\intercal \underline{\hat{\boldsymbol{f}}}^n \tag{4.7}$$

where, k_I, k_1 and k_2 are scalar constants larger than zeros. The injection term is given as in Mahony et al. (2008), where the normalized magnetometer and accelerometer output, $\underline{\boldsymbol{m}}^b$ and $\underline{\boldsymbol{f}}^b$, respectively are used as reference vectors. Furthermore, the reference vectors are constructed as

$$\underline{\boldsymbol{f}}^b := \frac{\boldsymbol{f}_{\text{IMU}}^b - \hat{\boldsymbol{b}}_a^b}{\max\{\|\boldsymbol{f}_{\text{IMU}}^b - \hat{\boldsymbol{b}}_a^b\|, \delta\}} \quad \underline{\boldsymbol{m}}^b := \frac{\boldsymbol{m}_{\text{IMU}}^b}{\|\boldsymbol{f}_{\text{IMU}}^b\|} \tag{4.8}$$

with the corresponding magnetic field in the {n} frame, $\underline{\boldsymbol{m}}^n$, given as

$$\underline{\boldsymbol{m}}^n := \frac{\boldsymbol{m}^n}{\|\boldsymbol{m}^n\|}. \tag{4.9}$$

The latter is assumed to be known as stated in Section 4.1. Moreover, $\hat{\boldsymbol{b}}_a^b$ and $\hat{\boldsymbol{f}}^n$ are provided by the acceleration bias estimator and integration filter blocks from Figure 4.1, respectively. $\hat{\boldsymbol{f}}^n$ and $\underline{\hat{\boldsymbol{f}}}^n$ are addressed in Section 4.2.2, whereas $\hat{\boldsymbol{b}}_a^b$ is addressed Section 4.2.3.

Grip et al. (2012a) continued the work Mahony et al. (2008) by including a gyroscope bias estimate projection algorithm. By doing so almost global stability was obtained for the case of non-stationary reference vectors. The gyro bias estimate update law can be given as

$$\dot{\hat{\boldsymbol{b}}}_g = \text{Proj}(\hat{\boldsymbol{b}}_g, -k_I \boldsymbol{\sigma}) \tag{4.10}$$

where

$$\text{Proj}(\hat{\boldsymbol{b}}_g, -k_I\boldsymbol{\sigma}) = \begin{cases} \left(\boldsymbol{I} - c(\hat{\boldsymbol{b}}_g)\dfrac{\hat{\boldsymbol{b}}_g\hat{\boldsymbol{b}}_g^\intercal}{\hat{\boldsymbol{b}}_g^\intercal\hat{\boldsymbol{b}}_g}\right)(-k_I\boldsymbol{\sigma}) & \hat{\boldsymbol{b}}_g^\intercal\hat{\boldsymbol{b}}_g > 0 \text{ and} \\ & \hat{\boldsymbol{b}}_g^\intercal(-k_I\boldsymbol{\sigma}) > 0 \\ -k_I\boldsymbol{\sigma} & \text{otherwise} \end{cases} \tag{4.11}$$

and

$$c(\hat{\boldsymbol{b}}_g) = \min\left(1, \frac{\hat{\boldsymbol{b}}_g^\intercal\hat{\boldsymbol{b}}_g - M_b^2}{\hat{M}_b^2 - M_b^2}\right). \tag{4.12}$$

The projection algorithm (4.11) will coincide with the second projection algorithm in Krstic et al. (1995, App. E) by choosing the adaptation gain, $\boldsymbol{\Gamma} = k_I$, where k_I is scalar.

4.2.2 Position and Velocity Integration Observer

From Grip et al. (2013, Submitted) and the flat Earth navigation assumption can the position and velocity estimate equations be written as

$$\dot{\hat{\boldsymbol{p}}}^n = \hat{\boldsymbol{v}}^n + \theta\boldsymbol{K}_{pp}(\boldsymbol{p}^n_{\text{GNSS}} - \hat{\boldsymbol{p}}^n) + \boldsymbol{K}_{pv}(\boldsymbol{v}^n_{\text{GNSS}} - \boldsymbol{C}_{\boldsymbol{v}}\hat{\boldsymbol{v}}^n) \tag{4.13}$$

$$\begin{aligned}\dot{\hat{\boldsymbol{v}}}^n = {} & \hat{\boldsymbol{f}}^n + \boldsymbol{g}^n(\hat{\boldsymbol{p}}^n) + \theta^2\boldsymbol{K}_{vp}(\boldsymbol{p}^n_{\text{GNSS}} - \hat{\boldsymbol{p}}^n) \\ & + \theta\boldsymbol{K}_{vv}(\boldsymbol{v}^n_{\text{GNSS}} - \boldsymbol{C}_{\boldsymbol{v}}\hat{\boldsymbol{v}}^n)\end{aligned} \tag{4.14}$$

$$\begin{aligned}\dot{\hat{\boldsymbol{\xi}}} = {} & -\boldsymbol{R}(\hat{\boldsymbol{q}}^n_b)\boldsymbol{S}(\hat{\boldsymbol{\sigma}})\boldsymbol{f}^b_{\text{IMU}} \\ & + \theta^3\boldsymbol{K}_{\xi_p}(\boldsymbol{p}^n_{\text{GNSS}} - \hat{\boldsymbol{p}}^n) + \theta^2\boldsymbol{K}_{\xi_v}(\boldsymbol{v}^n_{\text{GNSS}} - \boldsymbol{C}_{\boldsymbol{v}}\hat{\boldsymbol{v}}^n)\end{aligned} \tag{4.15}$$

$$\hat{\boldsymbol{f}}^n = \boldsymbol{R}(\hat{\boldsymbol{q}}^n_b)(\boldsymbol{f}^b_{\text{IMU}} - \hat{\boldsymbol{b}}^b_a) + \boldsymbol{\xi} \tag{4.16}$$

According to Grip et al. (2013, Submitted) describes $\boldsymbol{\xi}$ the discrepancy between the attitude estimate and position measurement. $\boldsymbol{\xi}$ should theroticaly zero mean when the estimates have converged. Moreover, regarding the

reference vectors in the Section 4.2.1, it follows that

$$\underline{\hat{\boldsymbol{f}}}^n := \frac{\hat{\boldsymbol{f}}^n}{\max\{\|\hat{\boldsymbol{f}}^n\|, \delta\}} \tag{4.17}$$

where δ where added in the case where $\hat{\boldsymbol{f}}^n$ is small. Furthermore, δ is given as

$$0 < \delta < m_{\boldsymbol{f}}. \tag{4.18}$$

The choice of $m_{\boldsymbol{f}}$ is explained in Assumption B.2. Moreover, Grip et al. (2013, Submitted) states that the gain matrices of (4.19) should be chosen such that $\boldsymbol{A} - \boldsymbol{K}\boldsymbol{C}$ is Hurwitz.

$$\begin{aligned} \boldsymbol{A} &= \begin{bmatrix} \boldsymbol{0}_{3\times3} & \boldsymbol{I}_{3\times3} & \boldsymbol{0}_{3\times3} \\ \boldsymbol{0}_{3\times3} & \boldsymbol{0}_{3\times3} & \boldsymbol{I}_{3\times3} \\ \boldsymbol{0}_{3\times3} & \boldsymbol{0}_{3\times3} & \boldsymbol{0}_{3\times3} \end{bmatrix} \quad \boldsymbol{C} = \begin{bmatrix} \boldsymbol{I}_{3\times3} & \boldsymbol{0}_{3\times3} & \boldsymbol{0}_{3\times3} \\ \boldsymbol{0}_{3\times3} & \boldsymbol{C_v} & \boldsymbol{0}_{3\times3} \end{bmatrix} \\ \boldsymbol{K} &= \begin{bmatrix} \boldsymbol{K_{pp}} & \boldsymbol{K_{pv}} \\ \boldsymbol{K_{vp}} & \boldsymbol{K_{vv}} \\ \boldsymbol{K_{\xi p}} & \boldsymbol{K_{\xi v}} \end{bmatrix} \end{aligned} \tag{4.19}$$

$\theta \geq 1$ is a tuning parameter chosen to ensure stability.

4.2.3 Accelerometer Bias Estimation

This section will address the bias estimation of the accelerometer. The goal is to obtain

$$\hat{\boldsymbol{b}}_a^b \to \boldsymbol{b}_a^b. \tag{4.20}$$

According to Mahony et al. (2008) the specific force measured by the accelerometer can be modeled according to

$$\boldsymbol{a}_{\text{imu}}^b = \boldsymbol{R}_n^b(\boldsymbol{\Theta})(\dot{\boldsymbol{v}}_{m/b}^n - \boldsymbol{g}^n) + \boldsymbol{b}_a^b + \boldsymbol{w}_a^b \tag{4.21}$$

In order to obtain the estimate of the bias, $\boldsymbol{b}_a^b$ the following acclerometer reading is defined

$$\boldsymbol{f}_{\text{IMU}}^b := \boldsymbol{f}^b + \boldsymbol{b}_a^b \tag{4.22}$$

Hence, the specific force is given as

$$\boldsymbol{f}^b = \boldsymbol{f}_{\text{IMU}}^b - \boldsymbol{b}_a^b. \tag{4.23}$$

As with the gyro bias estimates is a parameter projection utilized. This is based on the algorithm developed in Grip et al. (2012a). A over-parenthesized vector $\boldsymbol{w}$ is defined according to

$$\boldsymbol{w} := \begin{bmatrix} \|\boldsymbol{b}_a^b\| \\ \boldsymbol{b}_a^b \end{bmatrix} \tag{4.24}$$

as in Grip et al. (2013, Submitted). The regressor $\boldsymbol{\phi}$[1] is defined as

$$\boldsymbol{\phi} := \begin{bmatrix} \mathbf{1} \\ -2\boldsymbol{f}_{\text{IMU}}^b \end{bmatrix}. \tag{4.25}$$

It follows that the adaptive projection algorithm is stated as

$$\dot{\hat{\boldsymbol{w}}} = \text{Proj}(\hat{\boldsymbol{w}}, \boldsymbol{\Gamma}\boldsymbol{\phi}(\hat{\boldsymbol{y}} - \boldsymbol{\phi}^\intercal)\hat{\boldsymbol{w}}) \tag{4.26}$$

where

$$\hat{\boldsymbol{y}} = \min\{\|\hat{\boldsymbol{f}}^n\|^2, M_{\boldsymbol{f}}^2\} - \|\boldsymbol{f}_{\text{IMU}}^b\|^2 \tag{4.27}$$

The projection is determined be first following definition of a compact set of the estimates of $\hat{\boldsymbol{p}}^n$ and $\boldsymbol{p}$ is made

$$\hat{\boldsymbol{w}} := \begin{bmatrix} \hat{\boldsymbol{p}}^n \\ \hat{\boldsymbol{b}}_{\boldsymbol{a}}^{\boldsymbol{b}} \end{bmatrix} \tag{4.28}$$

[1]Should not be mistaken for the roll angle, ϕ

According to Grip et al. (2013, Submitted) it is assumed that the knowledge of $M_{\boldsymbol{w}}$ is known which bound the magnitude of $\boldsymbol{w}$ where $\hat{\boldsymbol{w}}$ is bonded by $M_{\hat{\boldsymbol{w}}}$ as

$$\|\hat{\boldsymbol{w}}\| \leq M_{\hat{\boldsymbol{w}}} \tag{4.29}$$

The assumptions regarding $M_{\hat{\boldsymbol{w}}}$ can be found in Appendix B.4.

4.2.4 Observer with Accelerometer Bias Estimation

Based on the inclusion of accelerometer bias estimation in the previous Section, is the dynamics of $\boldsymbol{\xi}$ modified by adding $\boldsymbol{R}(\hat{\boldsymbol{q}}_b^n)\dot{\hat{\boldsymbol{b}}}_a^b$ on the right-hand side of (4.15). Then, the total observer take the form of

$$\dot{\hat{\boldsymbol{p}}}^n = \hat{\boldsymbol{v}}^n + \theta \boldsymbol{K}_{pp}(\boldsymbol{p}_{\text{GNSS}}^n - \hat{\boldsymbol{p}}^n) \tag{4.30}$$

$$\dot{\hat{\boldsymbol{v}}}^n = \hat{\boldsymbol{f}}^n + \boldsymbol{g}^n(\hat{\boldsymbol{p}}^n) + \theta^2 \boldsymbol{K}_{vp}(\boldsymbol{p}_{\text{GNSS}}^n - \hat{\boldsymbol{p}}^n) \tag{4.31}$$

$$\begin{aligned}\dot{\hat{\boldsymbol{\xi}}} = &-\boldsymbol{R}(\hat{\boldsymbol{q}}_b^n)\boldsymbol{S}(\hat{\boldsymbol{\sigma}})(\boldsymbol{f}_{\text{IMU}}^b - \hat{\boldsymbol{b}}_a^b) \\ &+ \boldsymbol{R}(\hat{\boldsymbol{q}}_b^n)\begin{bmatrix}\boldsymbol{0}_{3\times 1} & \boldsymbol{I}_{3\times 3}\end{bmatrix}\text{Proj}(\hat{\boldsymbol{w}}, \boldsymbol{\Gamma}(\hat{\boldsymbol{y}} - \boldsymbol{\phi}^\intercal \hat{\boldsymbol{w}})) \\ &+ \theta^3 \boldsymbol{K}_{\xi_p}(\boldsymbol{p}_{\text{GNSS}}^n - \hat{\boldsymbol{p}}^n) + \theta^2 \boldsymbol{K}_{pv}(\boldsymbol{v}_{\text{GNSS}}^n - \boldsymbol{C}_{\boldsymbol{v}}\hat{\boldsymbol{v}}^n)\end{aligned} \tag{4.32}$$

$$\dot{\hat{\boldsymbol{q}}}_b^n = \boldsymbol{T}(\hat{\boldsymbol{q}}_{\boldsymbol{b}}^{\boldsymbol{n}})(\boldsymbol{\omega}_{b/n,\text{IMU}}^b - \hat{\boldsymbol{b}}_g^b + \hat{\boldsymbol{\sigma}}) \tag{4.33}$$

$$\dot{\hat{\boldsymbol{b}}}_g^b = \text{Proj}(\hat{\boldsymbol{b}}_g^b, -k_I \hat{\boldsymbol{\sigma}}) \tag{4.34}$$

$$\dot{\hat{\boldsymbol{w}}} = \text{Proj}(\hat{\boldsymbol{w}}, \boldsymbol{\Gamma}(\hat{\boldsymbol{y}} - \boldsymbol{\phi}^\intercal \hat{\boldsymbol{w}})) \tag{4.35}$$

4.3 Implementation Aspects

The observer is implemented with combined Forward Euler and Backwards Euler for the position and velocity estimates of (4.30) - (4.31). Whereas for the attitude update is Euler integration utilized. The reason for the former choice is that Forward Euler and Backwards Euler are also stable for

underdamped second-order systems as stated in Fossen (2011). For more on Euler integration and numerical integration methods, see Appendix C.

From Section 2.7 it follows that utilizing corrector-predictor is useful when implementing continuous observers in discrete time. The is especially so for a given sensor with relatively slow sampling time like GNSS. Hence, the observer of (4.30)-(4.35) is implemented as follows, with the positions estimates are updated according to

$$\hat{\boldsymbol{p}}^n(k) = \bar{\boldsymbol{p}}^n(k) + h\, k_{\text{GNSS}}\, \theta \boldsymbol{K}_{pp}(\boldsymbol{p}^n_{\text{GNSS}}(k) - \bar{\boldsymbol{p}}^n(k)) \tag{4.36a}$$

$$\bar{\boldsymbol{p}}^n(k+1) = \hat{\boldsymbol{p}}^n(k) + h\, \hat{\boldsymbol{v}}(k). \tag{4.36b}$$

The update of the velocity estimate takes the following form

$$\hat{\boldsymbol{v}}^n(k) = \bar{\boldsymbol{v}}^n(k) + h\, k_{\text{GNSS}}\, \theta \boldsymbol{K}_{vp}(\boldsymbol{p}^n_{\text{GNSS}}(k) - \bar{\boldsymbol{p}}^n(k)) \tag{4.37a}$$

$$\bar{\boldsymbol{v}}^n(k+1) = \hat{\boldsymbol{v}}^n(k) + h(\hat{\boldsymbol{f}}^n(k) + \boldsymbol{g}^n(k)). \tag{4.37b}$$

The update of $\hat{\boldsymbol{\xi}}$ is given as

$$\hat{\boldsymbol{\xi}}(k) = \bar{\boldsymbol{\xi}}(k) + h\, k_{\text{GNSS}}\, \theta^3\, \boldsymbol{K}_{\xi_p}(\boldsymbol{p}^n_{\text{GNSS}} - \hat{\boldsymbol{p}}^n) \tag{4.38a}$$

$$\begin{aligned} \bar{\boldsymbol{\xi}}(k+1) = \hat{\boldsymbol{\xi}}(k) &- h\, \boldsymbol{R}(\hat{\boldsymbol{q}}^n_b)\boldsymbol{S}(\hat{\boldsymbol{\sigma}})(\boldsymbol{f}^b_{\text{IMU}} - \boldsymbol{b}^b_a) \\ &+ h\, \boldsymbol{R}(\hat{\boldsymbol{q}}^n_b) \begin{bmatrix} \boldsymbol{0}_{3\times 1} & \boldsymbol{I}_{3\times 3} \end{bmatrix} \dot{\hat{\boldsymbol{w}}} \end{aligned} \tag{4.38b}$$

where k_{GNSS} is given as

$$k_{\text{GNSS}} = \frac{f_{\text{IMU}}}{f_{\text{GNSS}}} = \frac{100 \text{ Hz}}{5 \text{ Hz}} = 20 \tag{4.39}$$

Furthermore the corrector-predictor attitude update is given as

$$\hat{\boldsymbol{q}}^n_b(k) = \bar{\boldsymbol{q}}^n_b(k) + h\, \frac{1}{2} \hat{\boldsymbol{q}}^{\boldsymbol{n}}_{\boldsymbol{b}} \otimes (\bar{\boldsymbol{\omega}}^b_{nb,\text{IMU}} - \bar{\hat{\boldsymbol{b}}}^b_g + \bar{\hat{\boldsymbol{\sigma}}}) \tag{4.40a}$$

$$\bar{\boldsymbol{q}}^n_b(k+1) = \hat{\boldsymbol{q}}^n_b(k) \tag{4.40b}$$

since the attitude observer run at the same frequency as the IMU providing the measurements. Still, the methodology is also quite useful if some of the IMU measurements are discarded by my signal processing methods. Then, the attitude estimate $k+1$ will be equal to the k^{th} estimate. After the predictor estimate is obtained, the quaternion, $\bar{\boldsymbol{q}}_b^n(k+1)$, has to be normalized to ensure it has the unity length ($\|\bar{\boldsymbol{q}}\| = 1$). This can be done according to

$$\bar{\boldsymbol{q}}_b^n(k+1) = \frac{\bar{\boldsymbol{q}}_b^n(k+1)}{\|\bar{\boldsymbol{q}}_b^n(k+1)\|}. \tag{4.41}$$

as given in (2.57). Furthermore, the the bias estimates are updated in the same manner as the attitude estimate. The gyro bias adaptation are given as

$$\hat{\boldsymbol{b}}_g^b(k) = \bar{\boldsymbol{b}}_g^b(k) \tag{4.42a}$$

$$\bar{\boldsymbol{b}}_g^b(k+1) = \hat{\boldsymbol{b}}_g^b(k) + h\,\dot{\hat{\boldsymbol{b}}}_g^b \tag{4.42b}$$

as described in Section 4.2.1, whereas the accelerometer bias estimate according to

$$\hat{\boldsymbol{w}}(k) = \bar{\boldsymbol{w}}(k) \tag{4.43a}$$

$$\bar{\boldsymbol{w}}(k+1) = \hat{\boldsymbol{w}}(k) + h\,\dot{\hat{\boldsymbol{w}}}. \tag{4.43b}$$

4.4 Observer Tuning

This Section will address the different tuning aspects of the Grip et al. (2013, Submitted) observer and presents the chosen tuning parameters.

From Grip et al. (2013, Submitted) is the projection tuned in the following manner

$$\|\hat{\boldsymbol{b}}_g^b\| \leq M_{\hat{\boldsymbol{b}}} = 0.51\,\frac{\text{rad}}{\text{s}}, \quad \|\hat{\boldsymbol{b}}_a^b\| \leq M_{\hat{\boldsymbol{w}}} = 1.1\,\frac{\text{m}}{\text{s}^2} \tag{4.44}$$

Regarding the accelerometer bias projection algorithm was the following

parameters chosen

$$M_{\boldsymbol{f}} = 1.1\|\boldsymbol{g}_n\| \frac{\mathrm{m}}{\mathrm{s}^2}, \quad m_{\boldsymbol{f}} = 0.9\|\boldsymbol{g}_n\| \frac{\mathrm{m}}{\mathrm{s}^2}, \quad \delta = 0.9 \cdot m_{\boldsymbol{f}} \frac{\mathrm{m}}{\mathrm{s}^2} \tag{4.45}$$

The adaptation gain of the acceleromter bias estimate, $\boldsymbol{\Gamma}$, was chosen to

$$\boldsymbol{\Gamma} = 10^{-4} \cdot \mathrm{diag}\big([1,\, 56,\, 56,\, 0.25]\big) \tag{4.46}$$

and

$$\boldsymbol{\Gamma} = 10^{-4} \cdot \mathrm{diag}\big([1,\, 12.5,\, 12.5,\, 0.25]\big) \tag{4.47}$$

for two separate cases studies. The results regarding these are found in Section 5.1.

Since the observer is implemented in discrete time the condition of $\boldsymbol{A} - \boldsymbol{KC}$ to be Hurwitz then means that eigenvaules of $\boldsymbol{A} - \boldsymbol{K_dC}$ lies within the unit circle, where $\boldsymbol{K}_d = h\, k_{\mathrm{GNSS}}\, \boldsymbol{K}$. $\boldsymbol{K}_d$ is the discrete time gain from Section 2.7. The observer sampling time, $h = 0.01$ which is the same frequency as the IMU provides measurements. k_{GNSS} is given as

$$k_{\mathrm{GNSS}} = \frac{f_{\mathrm{obsv}}}{f_{\mathrm{GNSS}}} = \frac{100\mathrm{Hz}}{5\mathrm{Hz}} = 20 \tag{4.48}$$

With the following gains and their respective values

$$\begin{aligned} \boldsymbol{K}_{pp} &= 0.6\boldsymbol{I}_{3\times3}, \quad \boldsymbol{K}_{pv} = 0.11\boldsymbol{I}_{3\times3} \\ \boldsymbol{K}_{vp} &= 2.737\boldsymbol{I}_{3\times3}, \quad \boldsymbol{K}_{vv} = 2.363\boldsymbol{I}_{3\times3} \\ \boldsymbol{K}_{\xi_p} &= 0.006\boldsymbol{I}_{3\times3}, \quad \boldsymbol{K}_{\xi_v} = 1.068\boldsymbol{I}_{3\times3} \end{aligned} \tag{4.49}$$

as stated in Grip et al. (2013, Submitted). This resulted in

the eigenvalues given as

$$\boldsymbol{\lambda} = \mathrm{eig}\Big(\boldsymbol{A} - \boldsymbol{K}_d\boldsymbol{C}\Big) = \begin{bmatrix} -0.0274 + 0.1329i \\ -0.0274 - 0.1329i \\ -0.0274 + 0.1329i \\ -0.0274 - 0.1329i \\ -0.0274 + 0.1329i \\ -0.0274 - 0.1329i \\ -0.0651 \\ -0.0651 \\ -0.0651 \end{bmatrix} \tag{4.50}$$

when $\boldsymbol{C}_v = \boldsymbol{0}_{3\times 3}$, implying no velocity measurements are used. Hence, meeting the Hurwitz requirement.

4.5 Fault-Tolerant Nonlinear Observer

This thesis proposes additions to the observer presented by Grip et al. (2013, Submitted). The purpose is to increase fault-tolerance and exploit possible performance improvements if multiple sensors are utilized. These additions are illustrated in the grayed area of Figure 4.2 and in Figure 4.3.

Figure 4.2 shows the total system where the fault-tolerant observer is a combination of signal processing and the observer of Grip et al. (2013, Submitted). Moreover, Figure 4.3 shows the signal processing block with three position reference sensors. These modifications were introduced since the Grip et al. (2013, Submitted) observer does not perform online quality check of the sensors system. Furthermore, the Grip et al. (2013, Submitted) observer have no embedded functionality to weight multiple sensor measurements directly such as the discrete Kalman filter, see Kalman (1960). The Kalman filter also weight new measurements based on the quality of the

measurements, the process noise and the covariance of the estimates. Such functionality should be integrated in observer of Grip Grip et al. (2013, Submitted) for performance issues, but also for industrial reasons. Redundancy is in many cases required. In DP operations are sensor redundancy one of many requirements. For a semi-submersibles, as simulated in this thesis, are tipple redundancy regarding the position reference required. See Appendix B.7 and Det Norske Veritas (2011) for details. To benefit from the redundancy provided by three position sensors must each sensor be monitored for error and faults. Otherwise may such neglect result in degraded performance, damages or even critical situations. Drive-off is an example of such incidents.

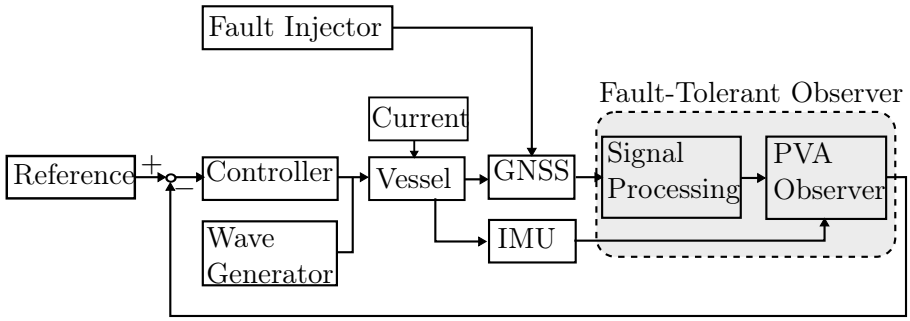

Figure 4.2: Observer. Overview of on how the Signal Processing and the PVA Observer of Grip et al. (2013, Submitted) constitute the Fault-tolerant observer in the simulator.

The addition and modification made to observer of Grip et al. (2013, Submitted) consist manly of three parts. These are given as

- Individual signal check of each sensor.
- A total signal check with voting and weighting of the available sensors.
- Time-varying gain, $\boldsymbol{K}_{pp}$, to atone for the changes in the reported quality of the available measurements.

Details are regarding these methods are presented in Section 4.5.1 - 4.5.3.

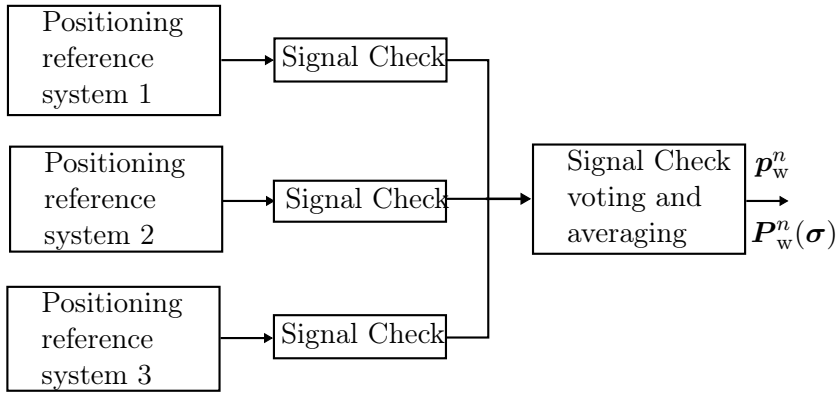

Figure 4.3: Observer. Overview of the Signal Processing with three position reference systems. The signal for each sensor is monitored by a signal checking procedure. Afterwards the sensors that is reported healthy are compared to each other by utilizing a voting mechanism. Finally, the procedure weights the measurements and provides a weighted position measurement together with calculated covariance to the PVA observer.

4.5.1 Signal Check of Individual Sensor Measurement

The signal checking procedure monitors the measured provided by each GNSS receiver. The monitoring consist of outlier detection, freeze and high variance monitoring. A high variance may be a result of a failure or might mask other underlying errors such as bias measurements. To detect drifting GNSS measurements are also monitoring of the vertical GNSS measurements performed.

From Section 2.6 can the outlier detection be obtained from (2.48) as

$$\boldsymbol{y}[k] \in [\bar{\boldsymbol{y}}_k - a\,\boldsymbol{\sigma},\, \bar{\boldsymbol{y}}_k + a\,\boldsymbol{\sigma}] \tag{4.51}$$

$\bar{\boldsymbol{y}}_k$ is the average of the previous measurements whereas $\pm a\boldsymbol{\sigma}$ are the wild point thresholds. Sørensen (2012) states that a should be in the interval

between 3 and 9. To reduce the amount of false alarms was a chosen to

$$a = 7.$$

Sørensen (2012) states that the variance of a given signal, $\boldsymbol{y}[k]$, can be calculated from historic data according to

$$\boldsymbol{\sigma}^2[k] = \frac{1}{n-1}\left(\sum_{i=k-(n-1)}^{k} \boldsymbol{y}[i] - \bar{\boldsymbol{y}}_k^2\right) \tag{4.52}$$

as given in (2.49), where n is the size of the window containing the historic data. Since the weighting formula from (2.51)

$$\hat{\boldsymbol{y}}^{WLS} = \boldsymbol{P}\big(\boldsymbol{R}_1^{-1}\boldsymbol{y}_1 + \boldsymbol{R}_2^{-1}\boldsymbol{y}_2 + \boldsymbol{R}_3^{-1}\boldsymbol{y}_3\big) \tag{4.53}$$

requires non biases measurements with Gaussian, zero mean measurement noise such as

$$\boldsymbol{y}_i = \boldsymbol{x} + \boldsymbol{e}_i, \quad \boldsymbol{e}_i \sim \mathbf{N}(0, \boldsymbol{R}_i), \quad i \in \{1, 2, 3\}. \tag{4.54}$$

This implies that all noise, $\boldsymbol{e}_i$, not satisfying $\boldsymbol{e}_i \sim \mathbf{N}(0, \boldsymbol{R}_i)$ must be detected, and the corresponding measurement excluded, in order for (4.53) to be valid.

Since this master thesis only utilizes one type of position sensor will such bias in the horizontal components be impossible to estimate correctly. This is due to the fact that no other direct information regarding the position exist. However, the vertical position can be assumed known since the mean height of a floating vessel over time is zero or any other constant value provided from the WGS-84 reference ellipsoid National Imagery and Mapping Agency (2000). Utilizing this as basis, was the a concept of detecting slowly varying changes in the vertical component of the GNSS measurements outlined.

Outline of GNSS Bias and Drift Detection

Since the height of the marine vessel is close to constant over time the is the vertical position defined as

$$p_z := 0. \tag{4.55}$$

This, however neglects the heave motion of the vessel. Even thought (4.55) is not absolutely valid, especially in rough weather conditions, is the mean of the vessel's height expected to be zero over time. Furthermore, a bias estimation is purposed as

$$b_{\text{GNSS,z}} = \int_{t_0}^{T} -\frac{1}{T_b} b_{\text{GNSS,z}} + k(\hat{p}_z - p_z)\ \mathrm{d}t \tag{4.56}$$

resulting the following bias estimation update

$$\begin{aligned} \dot{b}_{\text{GNSS,z}} &= -\frac{1}{T_b} b_{\text{GNSS, z}} + k_b \left(p_{\text{GNSS, z}} - p_{\text{vessel, z}}\right) \\ &= -\frac{1}{T_b} b_{\text{GNSS,z}} + k_b\, p_{\text{GNSS,z}} \end{aligned} \tag{4.57}$$

where T_b is a time constant and k_b is a positive gain larger than zero. A large k_b reduces detection time, whereas a small gain suppresses noise from the GNSS measurements. Since the algorithm is supposed to detect drift the time constant, T_b should not be chosen to large since any bias b_{GNSS} could vary significantly over time. A large T_b will introduce a significant phase lag. Regarding the magnitude of k_b will a very large value amplify the heave motion. This again can yield a false alarm if the corresponding GNSS bias alarm threshold is chosen to low.

What also should be mention is that the $\boldsymbol{\xi}$ state in the Grip et al. (2013, Submitted), see Section 4.2.2 can pick up deviations in the GNSS measurements. However, it can be observed in Section 5.6 that a slowly drifting GNSS will not be picked up by the $\boldsymbol{\xi}$ estimate.

Choosing $k_b = T_b^{-1}$ results in (4.57) to coincide with a first-order Butterworth filter. T_b and k_b was chosen to

$$T_b = 4, \quad k_b = \frac{1}{4}.$$

This yield a Butterworth filter with cutoff frequency

$$\begin{aligned} \omega_c &= 2\pi/T_b \\ &= \frac{1}{2}\pi \text{ [rad/s]} \end{aligned} \tag{4.58}$$

Status Provided by The Signal Check Procedure

The signal check procedure provides a status variable to the voting and weighting procedure to report the health of each GNSS sensor. The status variable can take six different values. The possible status is presented in Table 4.1.

Table 4.1: Status provided by the individual signal check procedure.

Status	Description
1	Normal. No errors detected.
2	Indication of wild point detected. Sensor reported erroneous.
3	Indication of sensor freeze detected. Sensor reported erroneous.
4	Indication of high variance detected. Sensor reported erroneous.
5	Indication of drift in vertical axis detected. Sensor reported erroneous.
-1	No measurement available for the use. Environmental disturbances or failure of electronics might be cases.

4.5.2 Signal Check, Voting and Averaging

The need of signal monitoring, voting and averaging is motivated by the DNV requirements, presented in Section 2.5.3, related to the utilization of multiple position reference sensors.

To detect if a sensor is deviating from the other GNSS measurements can voting be applied. The voting algorithm, developed in this thesis, is listed in pseudocode and presented in Algorithm 4.1. It was developed by utilizing three GNSS sensor measurements together with a threshold describing how much a sensor can deviate from an other sensor. The nominal threshold was set to 2.5. The basic concept of Algorithm 4.1 is to utilize the threshold as a radius in circles where the horizontal measurement components from each GNSS is the receptive origins. A deviation is detected if the circles do not intersect. If the circle based upon one sensor's measurements do not intersect with the two other circles will the sensor be disabled. After

Algorithm 4.1 Voting Procedure with three GNSS measurements

```
1 procedure VOTING(GNSS_1, GNSS_2, GNSS_3, threshold)
2     sensorcircles = create circles for each sensor with horizontal components as the center and the threshold as radius ( GNSS_i, threshold )
3     if the i^th sensor circle intersects with the other circle then
4         voting status ← appropriate status
5     else
6         voting status ← appropriate status
7     return voting status
```

the voting, mentioned in Algorithm 4.1, follows the weighing procedure. The weighting procedure is based the upon (2.51) where each sensor and covariance is multiplied with a variable taking two values. 1 if the sensor

is reported and verified by the voting produce to be healthy. 0 if not. The total voting and weighting Algorithm is presented in Algorithm 4.2.

Algorithm 4.2 GNSS Voting and Weighting Algorithm with three GNSS measurements.

```
1 procedure VOTING AND WEIGHTING(GNSS_1, GNSS_2, GNSS_3, threshold, time since GNSS was available)
2     status sensors = obtaining individual sensor state( )
3     [status vote, new sensor status] = preform vote( GNSS_i, sensor status, threshold)
4     Weighted GNSS meas, covariance] = perform weighting ( GNSS_i, status vote )
5     if sensor have been disabled then
6         smooth/fuse previous weighted position measurement with the new weighted position
7     return Weighted GNSS meas, GNSS status, covariance
```

According to Sørensen (2012) is it necessary to lowpass filter the voted signal if a sensor has been disabled. This should be done to prevent step in the position data provided to the state estimator. However, the filtering should be performed with care in order to prevented significant lag of filter's output. When a sensor is enabled or if no sensor reconfiguration has occurred states Sørensen (2012) that such filtering is not necessary. The same filter-like smoothing effect can also be obtained by utilizing the exponentiation function such as

$$\boldsymbol{y}_w(t) = (1 - e^{-\alpha t}) \cdot \boldsymbol{y}_{w_{\text{new}}}(t) + e^{-\alpha t} \cdot \boldsymbol{y}_{w_{\text{old}}}(t_0), \quad t \in [t_0, \infty] \tag{4.59}$$

where $\alpha > 0$ is a tuning parameter to decide how long the specific weighting should occur. t_0 is the time when a sensor was disabled. When a sensor is

not disabled will t be zero and (4.59) can be modified to

$$\boldsymbol{y}_w(t) = (1 - e^{-\alpha t}) \cdot \boldsymbol{y}_{w_{\text{new}}}(t) + k \cdot e^{-\alpha t} \cdot \boldsymbol{y}_{w_{\text{old}}}(t_0), \quad t \in [t_0, \infty] \tag{4.60}$$

where $k = 1$ if a sensor is disabled and, $k = 0$ if a sensor is not disabled. After some appropriate time or if the sensor is re-enabled should be k and t be set to $k = 0$ and $t = 0$. By choosing $\alpha = 1.2$ will a change in one meter from the new weighted signal be carried out 99.95% smoothly in 5 seconds. An illustration of this is shown in Figure 4.4.

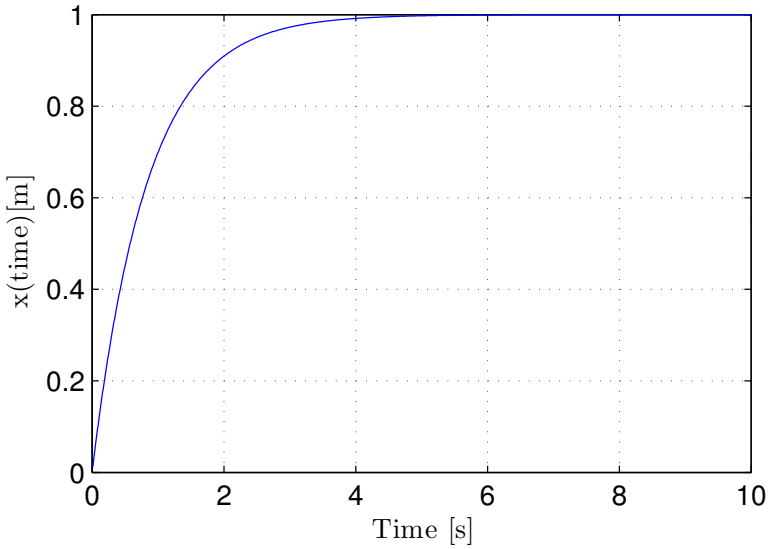

Figure 4.4: Observer. Illustration of smoothing, done by the weighing, when of a step in the measurements occurs. The exponential function is utilized

The status provided by Algorithm 4.2 to the observer is presented in Table 4.2.

Table 4.2: Status provided by the voting, weighing and signal check procedure

Status	Description
1	Normal. Three sensors enabled.
2	Reduced redundancy. Two sensor operational. One sensor reported erroneous.
3	Reduced redundancy. One sensor operational. Two sensor reported erroneous.
4	Reduced redundancy. Two sensor operational. One sensor discarded in voting.
5	Reduced redundancy. Two sensor operational. Discrepancy between sensors detected.
-1	No position reference available.

4.5.3 Introduction of Time-varying Gains

The observer presented by Grip et al. (2013, Submitted) are tuning with fixed gains. Thus, the initial tuning is not changed online if not gain scheduling is applied. This however requires that the gains are pre-calculated. Another strategy would be to determine gains online based on the current knowledge of the measurement noise and the estimate accuracy. Utilizing this a motivation, this thesis proposes that the gain tuning, described in Section 4.4, is extended to include a time-varying component.

In this work only a time-varying gain based in the calculated sensor variance is pursued. And since the thesis focus on a semi-submersible applying DP for station-keeping purposes is only the gain, $\boldsymbol{K}_{pp}$, correcting the position estimate made time-varying nominally. However, most of the gains were made time-varying during the initialization phase of the observer.

The magnitude of the time-varying gain, $\boldsymbol{K}_{pp}$, was chosen to be relatively large when the variance of the GNSS measurements were low and correspondingly low when the variance was reported to be high. The varying

structure of the gain was chosen similar to

$$K = \beta e^{-\alpha\sigma^2}, \quad \alpha > 0,\, \beta > 0, \tag{4.61}$$

resulting

$$0 \leq K \leq \beta. \tag{4.62}$$

Since the observer should correct the position estimate even when relative high sensor variance is reported was the structure of $\boldsymbol{K}_{pp}$ chosen to have two components as, one fixed and one time-varying yielding

$$\boldsymbol{K}_{pp_0} = \boldsymbol{K}_{pp,\text{fixed}} + \boldsymbol{K}_{pp,\text{varying}}. \tag{4.63}$$

where, $\boldsymbol{K}_{pp_0}$, is the nominal gain after the initialization phase. By utilizing a time-varying gain component with same properties as (4.61) resulted in the time-varying component of $\boldsymbol{K}_{pp}$ to become

$$\boldsymbol{K}_{pp,\text{varying}} = \text{diag}\Big(\beta\big[\exp(-\alpha\sigma_x^2),\, \exp(-\alpha,\, \exp(-\alpha\sigma_z^2)\big]\Big) \tag{4.64}$$

where $\boldsymbol{\sigma}^2 = \text{diag}([\sigma_x^2,\, \sigma_y^2,\, \sigma_z^2])$ is the reported covariance. From the relations stated above will $\boldsymbol{K}_{pp}$ be bounded above and below as given by

$$\boldsymbol{0}_{3\times 3} < \boldsymbol{K}_{pp_0,\text{fixed}} \leq \boldsymbol{K}_{pp_0} \leq \boldsymbol{K}_{pp_0,\text{fixed}} + \beta \cdot \boldsymbol{I}_{3\times 3}. \tag{4.65}$$

By choosing $\boldsymbol{K}_{pp,\text{varying}}$ in such a manner will result in the varying component of $\boldsymbol{K}_{pp}$ that decreases exponentially with increasing variance of the position measurement. Hence, the observer will correct the position estimate more when the senor measurements contains low amount of noise. In the opposite case will the observer correct less if the measurements are noisy. Furthermore, by keeping parts of $\boldsymbol{K}_{pp}$ fixed, will the Hurwitz requirement of $\boldsymbol{A} - \boldsymbol{K}\boldsymbol{C}$ posed by Grip et al. (2013, Submitted) will always be fulfilled since $\boldsymbol{K}_{pp}$ is always positive and bounded below and above. The gain related to the correction of the velocity and the $\boldsymbol{\xi}$ estimates are not changed in this

thesis.

Initial Observer Gains

In the initialization are the gains related to the attitude estimates also made time-varying. Grip et al. (2013, Submitted) stated that the initial gains of k_1 and k_2 should be set higher in the start up phase of the observer to speed up the converges of the attitude and the gyro bias estimates. Grip et al. (2013, Submitted) performed a gain scheduling strategy where the gains, k_1, k_2 and k_I, where reduced after 60 seconds. This thesis utilizes the exponential function instead. Instead of using the measurement variance as the decaying term, the time was utilized instead. This to increase observer speedup to ensure fast convergence without rapid changes of the gains, such a gain scheduling would imply. k_1, k_2 will then take the following form

$$k_1 = k_{1_0}(1 + \beta_{ref} e^{-\alpha_{ref} t}) \tag{4.66}$$

$$k_2 = k_{2_0}(1 + \beta_{ref} e^{-\alpha_{ref} t}) \tag{4.67}$$

where $\alpha_{ref} = 0.2$ and $\beta_{ref} = 3$ were chosen. Regarding the nominal gains were k_{1_0} and k_{2_0} chosen to

$$k_{1_0} = 1, \quad k_{2_0} = 0.55 \tag{4.68}$$

as in Grip et al. (2013, Submitted). The gain, k_I was fixed all this during this work and chosen to $k_I = 0.008$ as stated in Section 4.4.

The same strategy was chosen to increase the converges time for the position and velocity estimates as well. Accordingly, the following initial tuning strategy was chosen

$$\boldsymbol{K}_{pp} = \boldsymbol{K}_{pp_0}(1 + \beta_{pv} e^{-\alpha_{pv} t}) \tag{4.69}$$

$$\boldsymbol{K}_{vp} = \boldsymbol{K}_{vp_0}(1 + \beta_{pv} e^{-\alpha_{pv} t}). \tag{4.70}$$

The corresponding tuning parameters where chosen as $\alpha_{pv} = 0.1$ and $\beta_{pv} = 2$. The nominal gains were chosen to as $\boldsymbol{K}_{pp} = \boldsymbol{K}_{pp_0}$ where $\boldsymbol{K}_{pp_0}$ is time-varying gain presented in (4.63) above. $\boldsymbol{K}_{vp_0}$ where chosen to $\boldsymbol{K}_{vp_0} = 0.11 \cdot I_3$ as originally purposed by Grip et al. (2013, Submitted). From this is k_1, k_2, $\boldsymbol{K}_{pp}$ and $\boldsymbol{K}_{vp}$ is bounded below as seen in

$$0 < k_{1_0} \leq k_1 \leq k_{1_0}(1 + \beta_{ref}) \tag{4.71}$$

$$0 < k_{2_0} \leq k_2 \leq k_{2_0}(1 + \beta_{ref}) \tag{4.72}$$

$$\boldsymbol{0}_{3\times3} < \boldsymbol{K}_{pp_0} \leq \boldsymbol{K}_{pp} \leq \boldsymbol{K}_{pp_0}(1 + \beta_{pv}) \tag{4.73}$$

$$\boldsymbol{0}_{3\times3} < \boldsymbol{K}_{vp_0} \leq \boldsymbol{K}_{vp} \leq \boldsymbol{K}_{vp_0}(1 + \beta_{pv}) \tag{4.74}$$

4.6 Model-Based Fault-Tolerant Nonlinear Observer

The previous section dealt with fault-tolerance regarding managing position reference errors, faults and failures. This section will deal the event of acceleromter failure. Redundant acceleration information was obtained through a model based approach.

The redundant acceleration information was based on a observer applying a 3 DOF DP model from Section 2.5.1

$$\dot{\boldsymbol{\eta}}^n = \boldsymbol{R}(\psi)\boldsymbol{\nu}^b \tag{4.75}$$

$$\boldsymbol{M}\dot{\boldsymbol{\nu}}^b + \boldsymbol{D}\boldsymbol{\nu}^b = \boldsymbol{\tau} + \boldsymbol{R}^\intercal(\psi)\boldsymbol{b}^b \tag{4.76}$$

However changes were made. In previous work, utilizing model based approaches, such as Fossen and Strand (1999), is the current modeled as bias in kinetics. In this thesis is the current moved to the kinematics, as shown in Appendix B.3.2 and expressed as a velocity. Thus, the model with linear damping $\boldsymbol{D}$, wave-induced motion $\boldsymbol{\xi}$, relative velocity and constant irrational

current is given in (4.77) - (4.81). The model follows as

$$\dot{\boldsymbol{\xi}}^n = \boldsymbol{A}_w \boldsymbol{\xi}^n \tag{4.77}$$

$$\dot{\boldsymbol{\eta}}^n = \boldsymbol{R}(\psi)\boldsymbol{\nu}_r^b + \boldsymbol{v}_c^n \tag{4.78}$$

$$\dot{\boldsymbol{v}}_c^n = \boldsymbol{0} \tag{4.79}$$

$$\boldsymbol{M}\dot{\boldsymbol{\nu}}_r^b = -\boldsymbol{D}\boldsymbol{\nu}_r^b + \boldsymbol{\tau}^b \tag{4.80}$$

$$\boldsymbol{y} = \boldsymbol{\eta} + \boldsymbol{C}_w \boldsymbol{\xi}^n \tag{4.81}$$

During operation is the current in (4.79) in general not known, as presented by Fossen (2011). Thus, is have to be estimated based on the model, sensor measurements and the control inputs. The chosen strategy was to utilize the a nonlinear observer based upon Fossen and Strand (1999) where the bias estimation was performed in the kinematics. The reason for this choice is motivated by the fact that the current velocity can be extracted from the simulator and compared with the estimate afterwards in order to determine the estimation quality. In this respect was the additional observer, utilizing the vessel model, given as

$$\dot{\hat{\boldsymbol{\xi}}}^n = \boldsymbol{A}_w \hat{\boldsymbol{\xi}}^n + \boldsymbol{K}_1 \tilde{\boldsymbol{y}} \tag{4.82}$$

$$\dot{\hat{\boldsymbol{\eta}}} = \boldsymbol{R}(\hat{\psi})\hat{\boldsymbol{\nu}}_r^b + \hat{\boldsymbol{b}}^n + \boldsymbol{K}_2 \tilde{\boldsymbol{y}} \tag{4.83}$$

$$\dot{\hat{\boldsymbol{b}}}^n = -\boldsymbol{T}_b^{-1}\hat{\boldsymbol{b}}^n + \boldsymbol{K}_3 \tilde{\boldsymbol{y}} \quad \left(\text{alt. } \dot{\hat{\boldsymbol{b}}}^n = \boldsymbol{K}_3 \tilde{\boldsymbol{y}}\right) \tag{4.84}$$

$$\boldsymbol{M}\dot{\hat{\boldsymbol{\nu}}}_r^b = -\boldsymbol{D}\hat{\boldsymbol{\nu}}_r^b + \boldsymbol{\tau} + \boldsymbol{R}^T(\hat{\psi})\boldsymbol{K}_4 \tilde{\boldsymbol{y}} \tag{4.85}$$

$$\hat{\boldsymbol{y}} = \hat{\boldsymbol{\eta}}^n + \boldsymbol{C}_w \hat{\boldsymbol{\xi}}^n \tag{4.86}$$

where, $\hat{\boldsymbol{b}}$ represents the current estimate together with any unmodeled dynamics. In this context the unknown current. Here, as in the Fossen and Strand (1999) observer is $\boldsymbol{T}$ the time constant matrix, whereas $\tilde{\boldsymbol{y}} = \boldsymbol{y}^n - \hat{\boldsymbol{\eta}}^n$ are the discrepancies between the measured position and heading related to the model based nonlinear passive observer's estimates for surge, sway and yaw. $\boldsymbol{K}_i$ are some positive gains designed to fulfill the passivity require-

ments of the observer and inherently guaranteeing GES or GAS stability depending of the choice of bias estimation in (4.84). See Fossen and Strand (1999) for details.

The chosen update for the bias estimate, estimating the current velocity was chosen as

$$\dot{\hat{\boldsymbol{b}}}^n = \boldsymbol{K}_3 \tilde{\boldsymbol{y}} \tag{4.87}$$

since the current was modeled irrational and constant in the simulator.

Since no direct heading measurement, e.g. a compass, was available in this thesis, was the heading from the attitude observer, given by (4.33) and (4.34), utilized as heading reference for the 3 DOF model based observer presented above in (4.82)-(4.86). Moreover, just as for the observer presented in Section 4.2 is GNSS utilized as position reference. Together with the heading estimate and GNSS measurements are the control inputs are assumed to be known through measurements. Together will this constitute the information to obtain an estimate of the acceleration. The model based approach will provide redundant acceleration information as illustrated in Figure 4.5

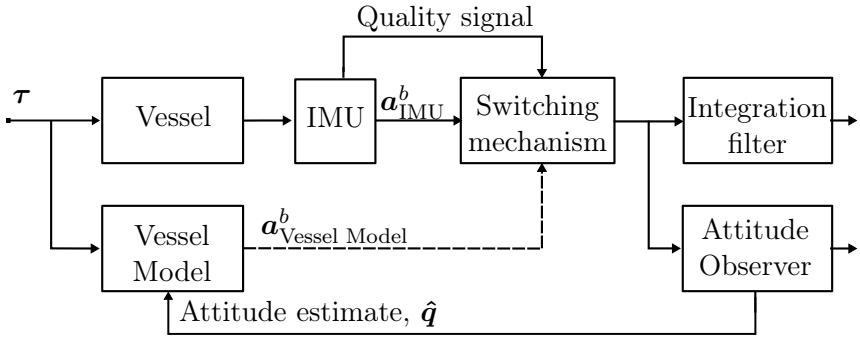

Figure 4.5: Observer. Overview of the strategy to exploit the vessel model in a fault-tolerant observer design. If quality of the IMU is reported to be incorrect or if the IMU measurements are reported to be of reduced quality a switching from the accelelerometer to the acceleration from ths vessel model is performed.

The equation for the accelerometer measurements are given in 3.30 as follow

$$\boldsymbol{f}^b_{\text{IMU}} = \boldsymbol{R}^b_n(\boldsymbol{\Theta})(\dot{\boldsymbol{v}}^n_{b/n} - \boldsymbol{g}^{\boldsymbol{n}}) + \boldsymbol{b}^b_{\text{acc}} + \boldsymbol{w}^b_{\text{acc}}. \tag{4.88}$$

Hence, the acceleration estimate, provided by the vessel model observer, should yield the same. However, one simplification have to be made for a 3 DOF model approach. The 3 DOF model have no information regarding the height of the vessel since this is assumed to be zero over time. Hence, is the estimate of $\dot{\boldsymbol{v}}^n_{b/n}$ assumed to have the following structure

$$\dot{\hat{\boldsymbol{v}}}^n_{b/n} = \begin{bmatrix} \dot{\hat{v}}^n_{b/n,x} & \dot{\hat{v}}^n_{b/n,y} & 0 \end{bmatrix}^{\mathsf{T}}. \tag{4.89}$$

Since the acceleromter does not provide relative acceleration measurements implies that (4.91) does not provide a sufficient acceleration information. This is due to the constant, irrational current is not taken in account when the vessel rotates, as can be seen in (4.91). $\dot{\hat{\boldsymbol{v}}}^b_r$ is extracted accordingly

$$\boldsymbol{M}\dot{\hat{\boldsymbol{\nu}}}^b_r = -\boldsymbol{D}\hat{\boldsymbol{\nu}}^b_r + \boldsymbol{\tau} + \boldsymbol{R}^T(\hat{\psi})\boldsymbol{K}_4\tilde{\boldsymbol{y}} \tag{4.90}$$

$$\Rightarrow \dot{\hat{\boldsymbol{\nu}}}^b_r = \boldsymbol{M}^{-1}\big(- \boldsymbol{D}\hat{\boldsymbol{\nu}}^b_r + \boldsymbol{\tau} + \boldsymbol{R}^T(\hat{\psi})\boldsymbol{K}_4\tilde{\boldsymbol{y}}\big). \tag{4.91}$$

In the simulator the acceleration component from the current was added by (3.27) given as

$$\dot{\boldsymbol{v}}^b_c = -\boldsymbol{S}(\boldsymbol{\omega}^b_{b/n})\boldsymbol{R}^b_n\boldsymbol{v}^n_c \tag{4.92}$$

The current is estimated in the {n} frame as $\hat{\boldsymbol{b}}^n$. By utilizing the same relations as in the simulator can the horizontal acceleration provided by the current estimate, based on the vessel model, be written as

$$\dot{\hat{\boldsymbol{b}}}^b = -\boldsymbol{S}(\boldsymbol{\omega}^b_{\text{IMU}} - \hat{\boldsymbol{b}}^b_g)\boldsymbol{R}^b_n(\hat{\psi})\hat{\boldsymbol{b}}^n. \tag{4.93}$$

where $\boldsymbol{\omega}^b_{\text{IMU}}$ is provided by gyroscope. $\hat{\boldsymbol{b}}^b_g$ and $\hat{\psi}$ are, on the other hand, provided by the attitude observer block seen in Figure 4.1. Thus, the to-

tal horizontal acceleration provided by the model based observer is given as

$$\dot{\boldsymbol{\nu}}^b = \dot{\boldsymbol{\nu}}_r^b + \dot{\hat{\boldsymbol{b}}}^b. \tag{4.94}$$

Then, gravity component must be atoned for. The known gravity vector, $\boldsymbol{g}^n$, from Section 4.1 have to be given in the {b} and added to horizontal acceleration as

$$\boldsymbol{f}^b_{\text{vessel model}} = \begin{bmatrix} \dot{\hat{\nu}}_x^b \\ \dot{\hat{\nu}}_y^b \\ 0 \end{bmatrix} - \boldsymbol{R}_b^n(\hat{\boldsymbol{\Theta}})^\intercal \boldsymbol{g}^n \tag{4.95}$$

where $\hat{\boldsymbol{\Theta}}$ is the attitude estimate. However, since the roll and pitch angles are assumed to be zero for the 3 DOF model. Because of this is the following assumed

$$\boldsymbol{R}_b^n(\hat{\boldsymbol{\Theta}}) \approx \boldsymbol{R}_b^n(\hat{\psi}). \tag{4.96}$$

Thus, can (4.95) to be simplified to

$$\boldsymbol{f}^b_{\text{vessel model}} \overset{\phi=\theta=0}{=} \begin{bmatrix} \dot{\hat{\nu}}_x \\ \dot{\hat{\nu}}_y \\ -g \end{bmatrix} = \begin{bmatrix} \dot{\hat{\nu}}_x \\ \dot{\hat{\nu}}_y \\ -9.81 \end{bmatrix} \tag{4.97}$$

since

$$\boldsymbol{R}_b^n(\hat{\psi})^\intercal \boldsymbol{g}^n = \begin{bmatrix} \cos(\hat{\psi}) & \sin(\hat{\psi}) & 0 \\ -\sin(\hat{\psi}) & \cos(\hat{\psi}) & 0 \\ 0 & 0 & 1 \end{bmatrix} \begin{bmatrix} 0 \\ 0 \\ g \end{bmatrix} = \begin{bmatrix} 0 \\ 0 \\ g \end{bmatrix} \tag{4.98}$$

where $g = 9.81$ as assumed in Section 4.1.

Chapter 5
Results and Discussion

This chapter will present the result related to the fault-tolerant observer described in the former chapter and how the observer coped with the sensor errors, fault and failur, stated in the Section 3.2.2. The observer was subjected the following scenarios regarding sensor error, faults and single point failures:

- Outlier detection of GNSS measurements.
- Freeze of GNSS measurements.
- Increased variance of on a GNSS measurements.
- Jump in measurement (constant bias).
- Slow drift of all GNSS antenna measurements.
- Loss of acceleration measurements.

Results will be shown and discussed. Both the magnetometer and acceleromter are assumed pre-calibrated for biases. The reasons for the latter are presented and discussed in Section 5.1. The first-order wave forces and moments were pre-calculated and reused for every simulation. This chapter is organized as follows

- Section 5.1: Case 1, Effect of acceleromter bias estimates.
- Section 5.2: Case 2, Outlier detection.
- Section 5.3: Case 3, GNSS sensor freeze.
- Section 5.4: Case 4, Increased noise of one sensor.

- Section 5.5: Case 5, Constant Biased GNSS measurements.
- Section 5.6: Case 6, Drift of all GNSS sensors.
- Section 5.7: Case 6, Utilizing vessel model as additional acceleration information.
- Section 5.8: Overall Discussion. Summarizing the discussions for each of the case studies.

5.1 Case 1: Accelerometer Bias Estimation and the Resulting Effect on the Attitude Estimate

The following Section will present results related to the accelerometer bias estimates and how these will effect the attitude estimate. This case in presented first due the effect choices and tuning regarding the accelerometer bias estimates effects have on the attitude estimate. To illustrate these effects was two simulation ran with different accelerometer bias estimation gain, $\mathbf{\Gamma}$. Both of gyro bias and attitude estimates where obtained by the nominal gains of

$$k_1 = 1, \mathrm{k}_2 = 0.55, \mathrm{k}_I = 0.008 \tag{5.1}$$

after the initialization phase when the exponential terms have become zero. See Section 4.4 and Section 4.5 for details. The control objective, in both simulations, was set to $\psi_d = 0$.

The bias estimation was started after 100 seconds. This was due to Grip et al. (2013, Submitted) recommends that the attitude estimates should have converged some such that the estimated acceleration in {n} frame

$$\hat{\boldsymbol{f}}^n = \boldsymbol{R}_b^n(\hat{\boldsymbol{q}})(\boldsymbol{f}_{\mathrm{IMU}}^b - \boldsymbol{b}_a^b) \tag{5.2}$$

would have had the time to settle before the accleleromter bias should be

started.

The first simulation was ran with accelerometer bias gain as

$$\boldsymbol{\Gamma} = 10^{-4} \cdot \operatorname{diag}\big([1,\, 56,\, 56,\, 0.25]\big). \tag{5.3}$$

Figure 5.1 presents gyroscope and accelerometer bias estimates. One can observe that the gyro biases estimates converge nicely to their true values. The accelerometer bias estimates converges at a slower rate, than the gyro bias. Furthermore, the accelerometer bias estimates are more rugged than the former estimates and converges with less accuracy. This might be expected since the acceleration bias estimates require PE, as stated in Section 4.2.3. In Figure 5.2 on can see the resulting attitude estimates when $\boldsymbol{\Gamma}$ was chosen according to (5.3).

The gyro and accelerometer bias estimate obtained by choosing $\boldsymbol{\Gamma}$ according to

$$\boldsymbol{\Gamma} = 10^{-4} \cdot \operatorname{diag}\big([1,\, 12.5,\, 12.5,\, 0.25]\big)$$

is shown in Figure 5.3. From Figure 5.3b one can clearly observe that the accelerometer biases did not not converge to the correct values. The consequence of this can be seen in Figure 5.4 where the attitude and especially the yaw estimate are estimated incorrectly. This is due to the acceleromter bias effects on the innovation, $\hat{\boldsymbol{\sigma}}$ of the attitude estimate seen in

$$\dot{\hat{\boldsymbol{q}}}_b^n = \boldsymbol{T}(\hat{\boldsymbol{q}}_{\boldsymbol{b}}^{\boldsymbol{n}})(\boldsymbol{\omega}_{b/n,\mathrm{IMU}}^b - \hat{\boldsymbol{b}}_g^b + \hat{\boldsymbol{\sigma}}) \tag{5.4}$$

where $\hat{\boldsymbol{\sigma}}$ is given as

$$\hat{\boldsymbol{\sigma}} = k_1 \underline{\boldsymbol{m}}^b \times \boldsymbol{R}(\boldsymbol{q}_b^n)^\intercal \underline{\boldsymbol{m}}^n + k_2 \underline{\boldsymbol{f}}^b \times \boldsymbol{R}(\boldsymbol{q}_b^n)^\intercal \underline{\hat{\boldsymbol{f}}}^n \tag{5.5}$$

from (4.7). Since the attitude estimate in Figure 5.2.

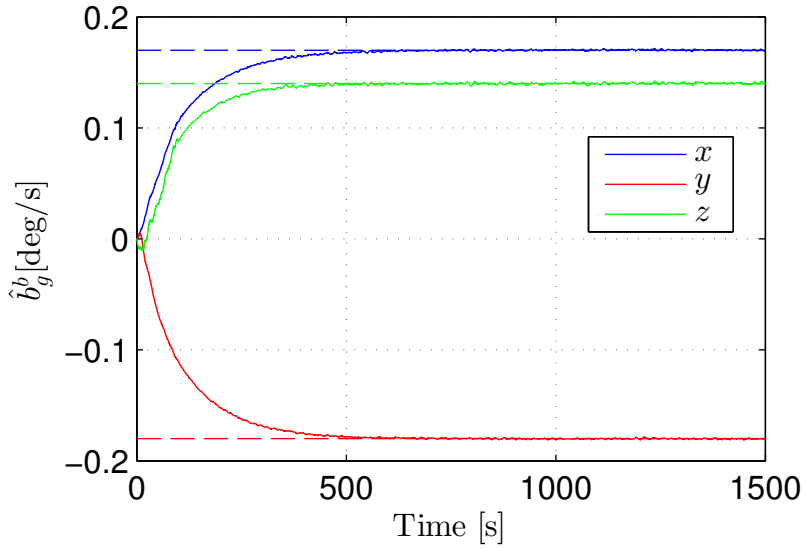

(a) Gyroscope Bias Estimates. Dotted lines are the fixed biases. Fixed lines are the online estimates.

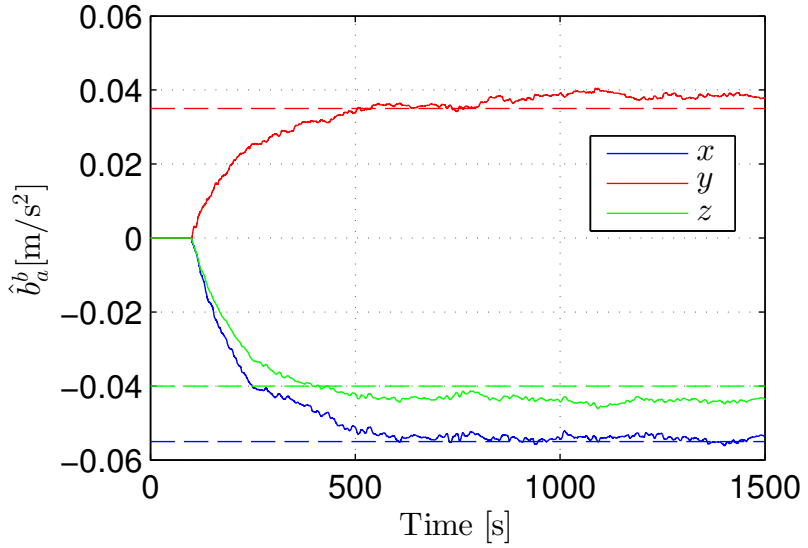

(b) Acceleromter Bias Estimates. Dotted lines are the fixed biases. Fixed lines are the online estimates.

Figure 5.1: Case 1, Accelerometer bias estimation. Estimates of gyroscope and acceleromter biases when accelerometer bias was estimated correctly.

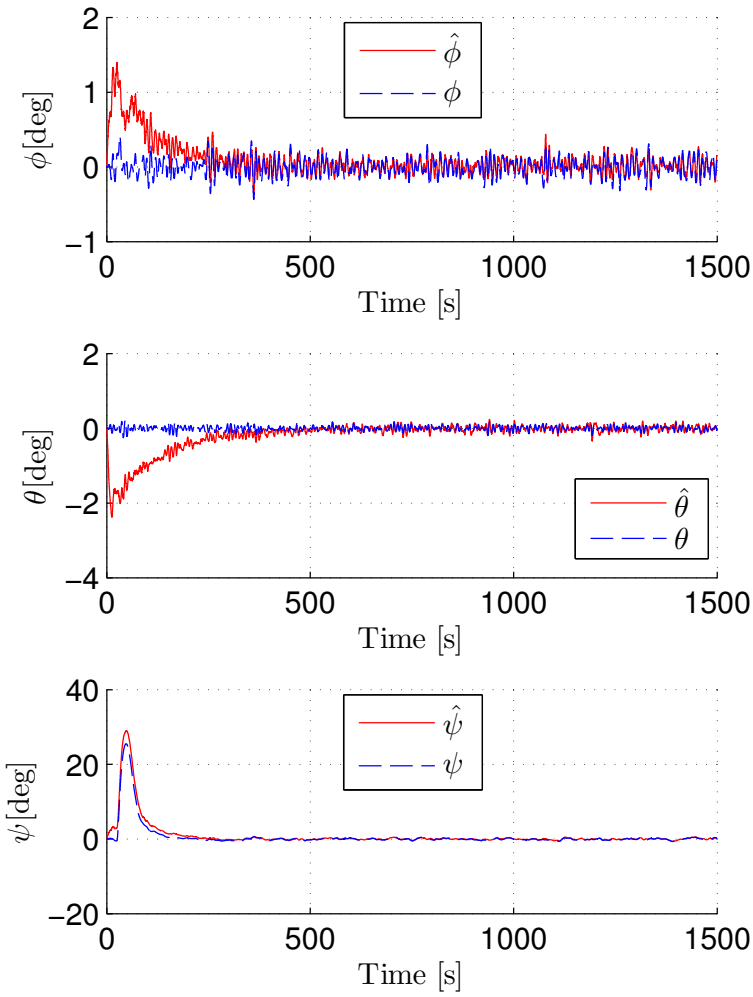

Figure 5.2: Case 1, Accelerometer bias estimation. Attitude estimate converted from quaterions to Euler angles when accelerometer bias was estimated correctly.

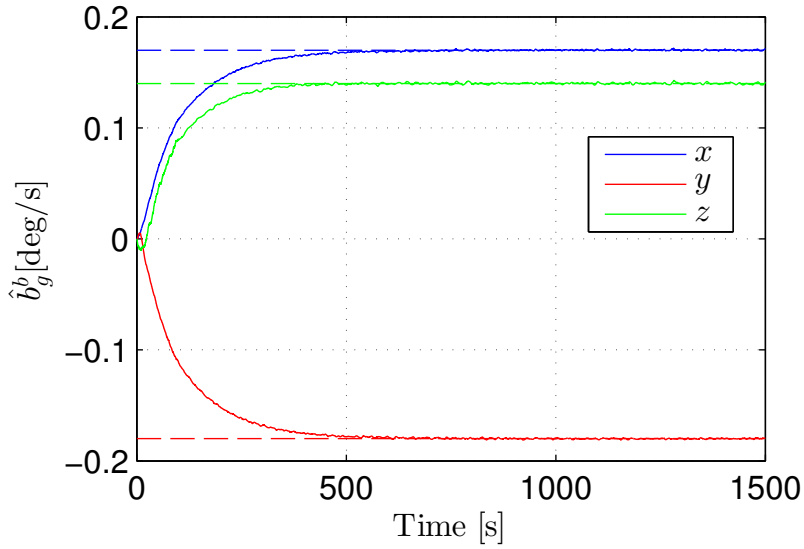

(a) Gyroscope Bias Estimates. Dotted lines are the fixed biases. Fixed lines are the online estimates.

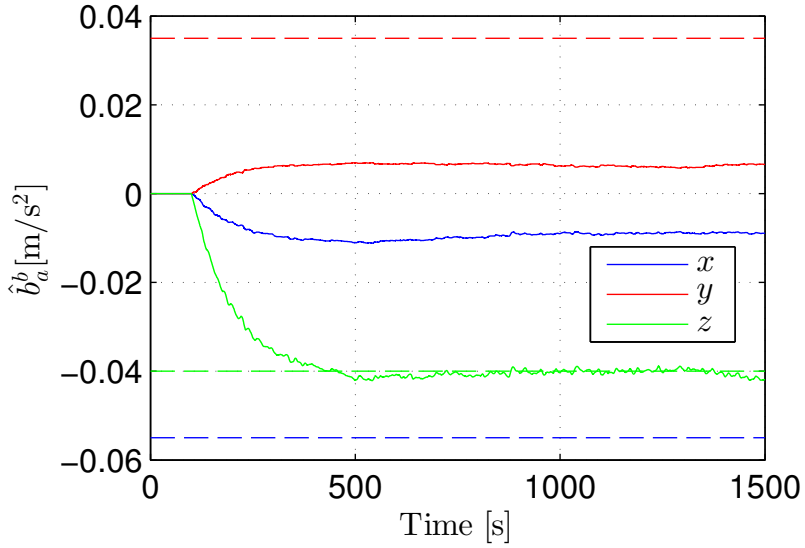

(b) Acceleromter Bias Estimates. Dotted lines are the fixed biases. Fixed lines are the online estimates.

Figure 5.3: Case 1, Accelerometer bias estimation. Estimates of gyroscope and acceleromter biases when accelerometer bias was estimated incorrectly.

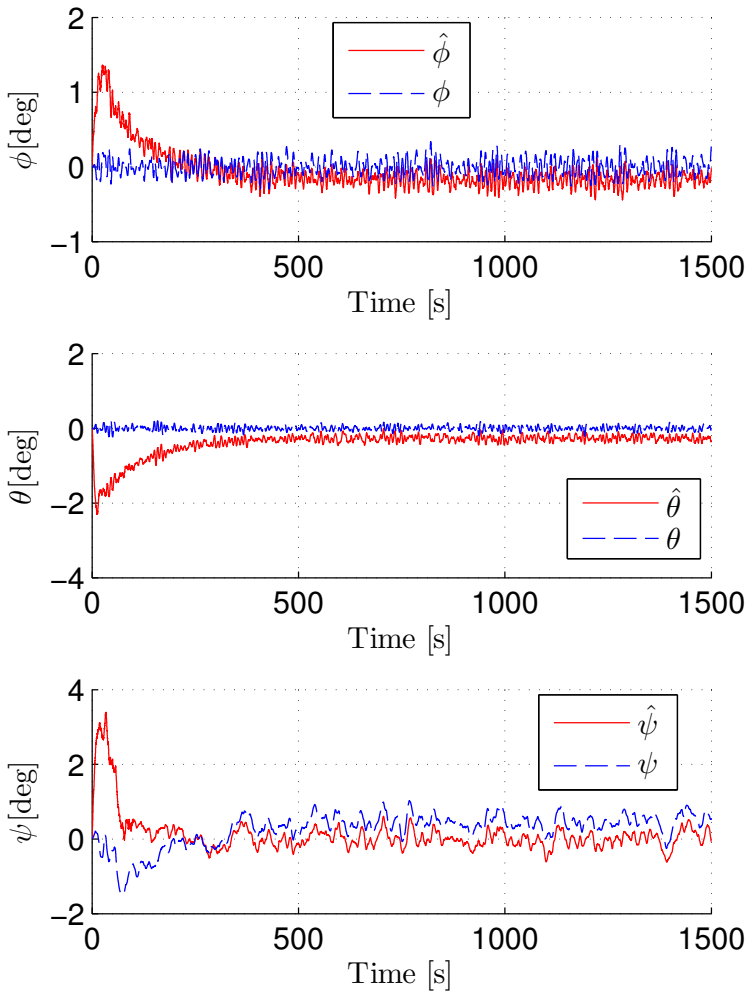

Figure 5.4: Case 1, Accelerometer bias estimation. Attitude estimate converted from quaterions to Euler angles when accelerometer bias was estimated incorrectly.

Discussion and Preliminary Conclusion

The attitude is estimated correctly with correct acceleromter bias estimation as stated above. From these simulation can it be observed that the attitude estimate are quite sensitive for accelerometer bias. Furthermore, the quality of the accelerometer bias estimates are also quite sensitive to adaptation gain, $\mathbf{\Gamma}$. This is due to the adaptation gain also effects the asymptotic values of the estimate, not just the transient behavior. Because of this, the rest of the case studies in this thesis are not acceleration bias compensated for online. Hence, the accelerometer is assumed pre-calibrated to atone for sensor bias.

The obtained result indicate that further investigation in acceleration bias estimates should be performed to yield a better performance of the acceleration bias estimates. For instance could the observer be ran on a smaller vessel with faster dynamics to see if this will yield changes regarding the quality of the acceleration bias estimates. The same goes for changes in the sea state. This will yield a different wave-induces vessel motion and hence could effect the excitation. This again can change the quality of the bias estimates.

What also should mentioned is that the gyro bias estimates are robust related to erroneous reference vector measurements. Even in the event of erroneous acceleration bias estimates does the gyro bias converge to the correct biases. This is seen from Figure 5.1a and Figure 5.3a. This can be due to the fact that the acceleromter bias estimate is a common denominator in both $\boldsymbol{f}^b$ and $\hat{\boldsymbol{f}}^n$. This will however not necessarily be so for a given magnetometer bias since the sensor bias will not effect actual magnetic field $\boldsymbol{m}^n$.

5.2 Case 2: GNSS Outlier Detection

The following case study will present the results regarding the outlier detection and how this will effect the position estimates. First will the effects without outlier detecting in the event of the outlier no outleir detection is enabled. Afterwards will the outlier detection be enabled and the corresponding results will be presented.

Both cases studies was simulated with three outliers per GNSS. Furthermore, both cases was simulated with the same outliers so comparison of performance will be based on the same outliers. Gaussian, zero mean noise will however change, but not change magnitude. Outlier were enabled for the respective sensors as described in Table 5.1

Table 5.1: Overview of GNSS outliers

GNSS Number	Time of outlier [s]
GNSS 1	400, 700 and 1000
GNSS 2	500, 800 and 1100
GNSS 3	600, 900 and 1200

The magnitude of the wild-points is presented in Table 3.5 in Section 3.2.2. The desired generalized position was set to

$$\boldsymbol{\eta}_d = \begin{bmatrix} 0 & 0 & 0 \end{bmatrix}^\intercal. \tag{5.6}$$

The controller was enabled after 25 seconds.

Outlier Detection Disabled

In this illustration of how outliers effect the system only GNSS 1 is used as position reference. Figure 5.5 show the measurements provided by GNSS 1. Figure 5.6 show the reported variance which is utilized in to calculated the

time varying gain $\boldsymbol{K}_{pp}$, see Section 4.5 for details regarding the time varying gain $\boldsymbol{K}_{pp}$.

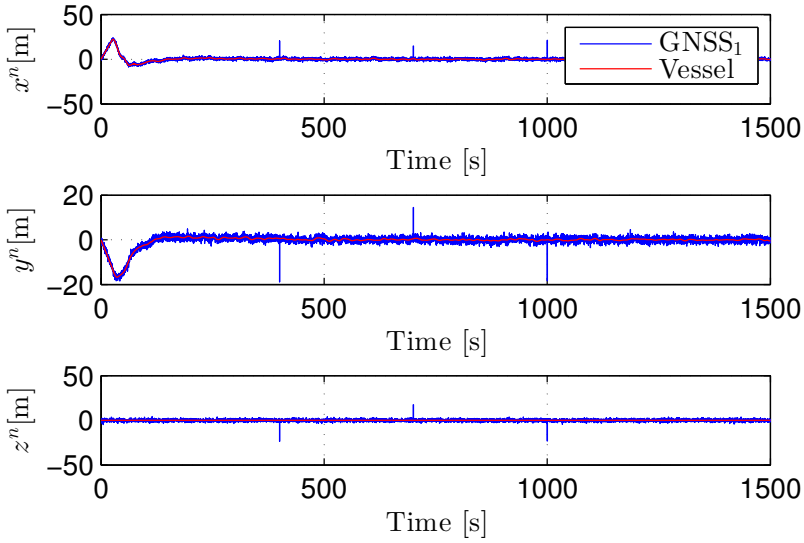

Figure 5.5: Case 3, Outlier detection. Measurements from GNSS 1 together with vessel position in the event of outlier detection is disabled.

Figure 5.7 show the North-East position of the vessel together with the measurements from GNSS 1 and the postion estimates. One can see that the vessel first drifts before the controller is enabled. Then, the vessel returns to the desired position. Moreover, one can also seen the position estimates need some time to converge to the correct state even when utilizing higher exponetial decaying gains in the initial phase. Furthermore, 5.7 shows that the position estimate are drawn slightly towards the spikes of the measurements. However, the magnitude of the change in the estimate is Even tough the position estimates are not significantly affected by the spikes in position measurements, can increased ripples can be observed at time 400, 700 and 1000. The lack of large changes in the position estimate can partly be explained by this thesis change of $\boldsymbol{K}_{pp}$ from fixed to time-varying based on

variance. Figure 5.6 clearly shows that the calculated variance is increasing. Hence, resulting a smaller $\boldsymbol{K}_{pp}$.

Regarding the velocity estimate a larger fluctuation is observed as seen in Figure 5.9. The can be explained by the fact that $\boldsymbol{K}_{vp}$ is still fixed hence measurements with large variance will not be attenuated as much compared to the position estimate.

The attitude estimates shown in Figure 5.10 display little impact by outliers even though the injection term, $\hat{\boldsymbol{\sigma}}$ shows spikes at the time of the GNSS outliers. This is shown in Figure 5.11. The reason for these spikes are introduced by $\hat{\boldsymbol{f}}^{\boldsymbol{n}}$ which is utilized in the calculation of the injection term $\hat{\boldsymbol{\sigma}}$ as stated in Section 4.2.2. These spikes are again introduced by $\boldsymbol{\xi}$ bacause of $\hat{\boldsymbol{f}}^n = \boldsymbol{R}(\hat{\boldsymbol{q}}_b^n)(\boldsymbol{f}_{\text{IMU}}^b - \hat{\boldsymbol{b}}_a^b) + \boldsymbol{\xi}$ and since $\boldsymbol{\xi}$ additional fluctuates in the event of outliers in the GNSS measurements as seen in Figure 5.12. The latter is cased by the injection term $\boldsymbol{K}_{\xi_p}(\boldsymbol{p}_{\text{GNSS}} - \boldsymbol{p_h at})$. As in the correction of the velocity estimates is $\boldsymbol{K}_{\xi_p}$ fixed. The additional fluctions seen in Figure 5.12 might have been smaller if also $\boldsymbol{K}_{\xi_p}$ had been time varying.

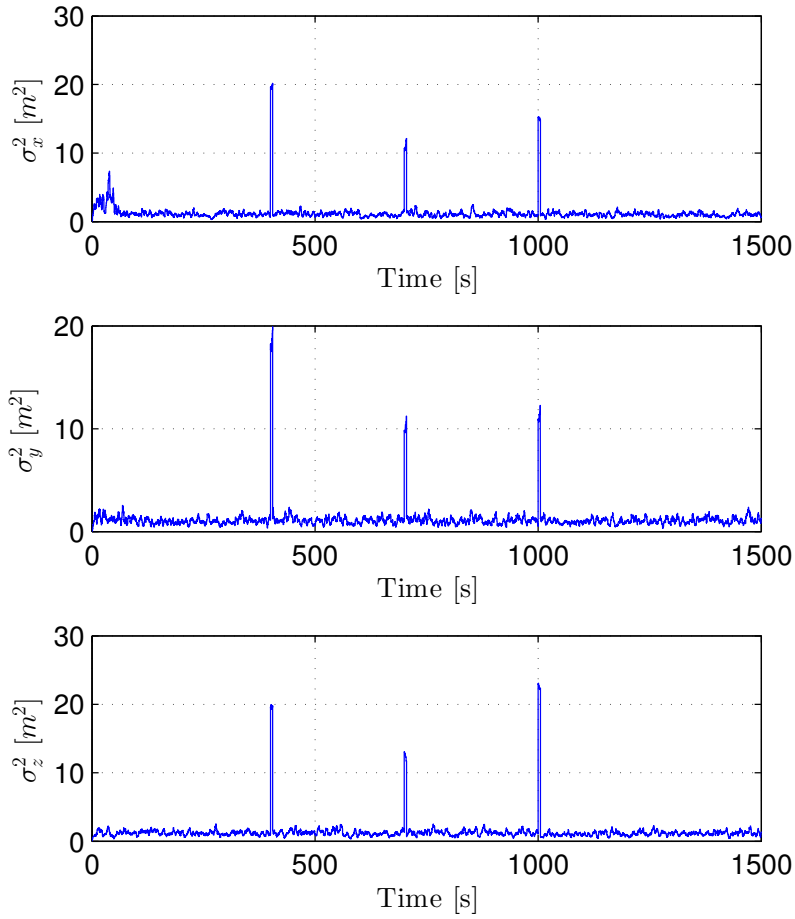

Figure 5.6: Case 3, Outlier detection. Weighted variance when only one GNSS 1 is provideing measurement Reported variance for each GNSS when the outlier detection is ignored

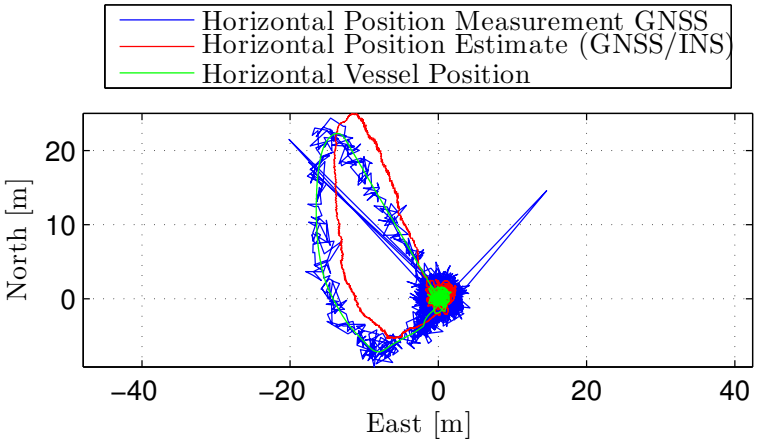

Figure 5.7: Case 2, Outlier detection. North-East position of the vessel together with position estimates and position measurements from GNSS 1 when outlier detection is disabled.

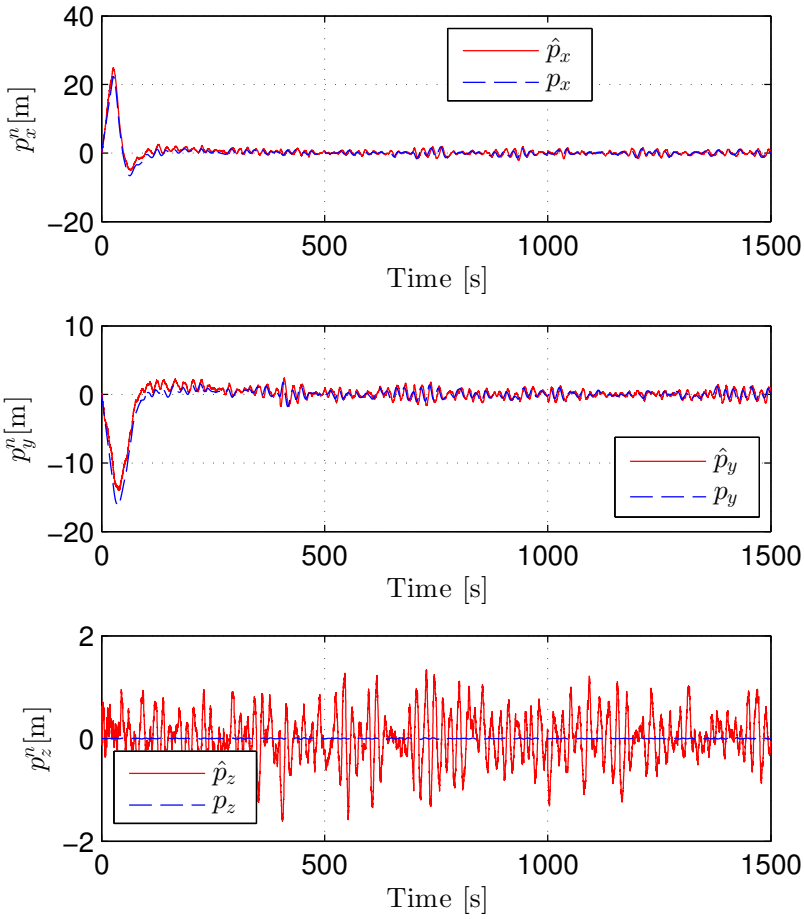

Figure 5.8: Case 2, Outlier detection. Position estimates together with vessel position when outlier detection is disabled

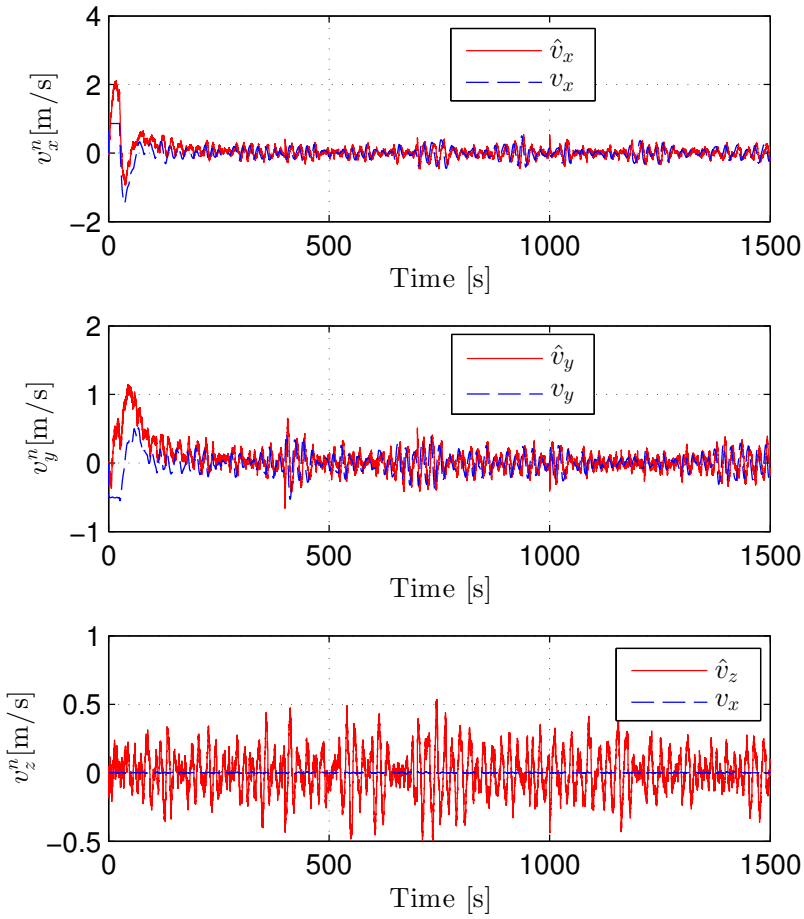

Figure 5.9: Case 2, Outlier detection. Velocity estimates together with vessel position when outlier detection is disabled

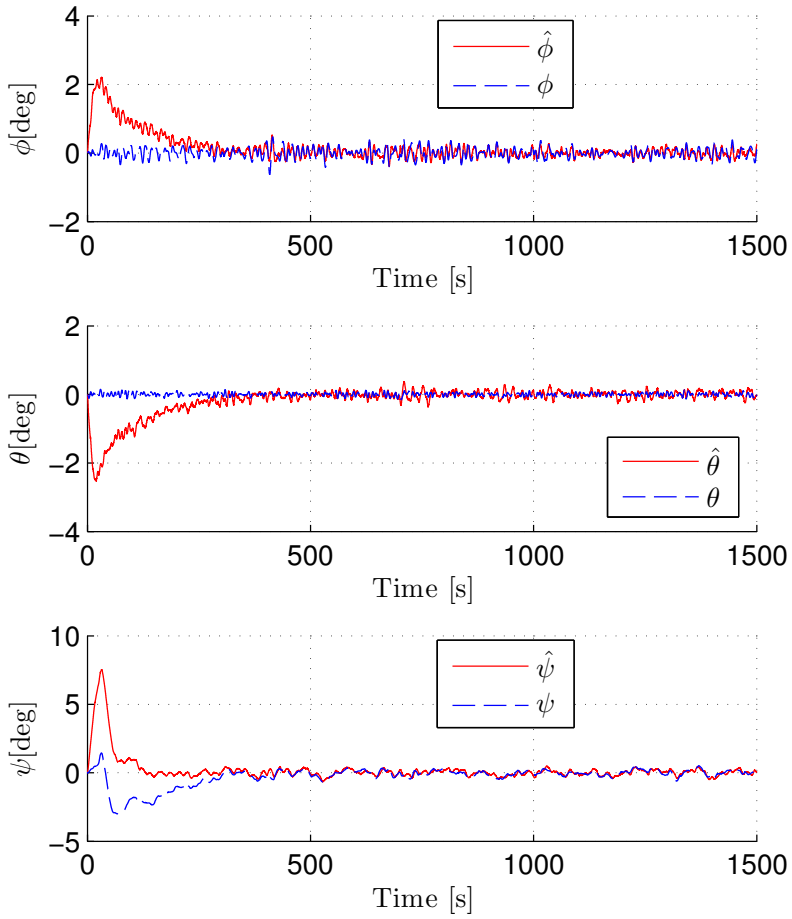

Figure 5.10: Case 2, Outlier detection. Attitude estimates represented in Euler angles together with vessel attitude when outlier detection is disabled

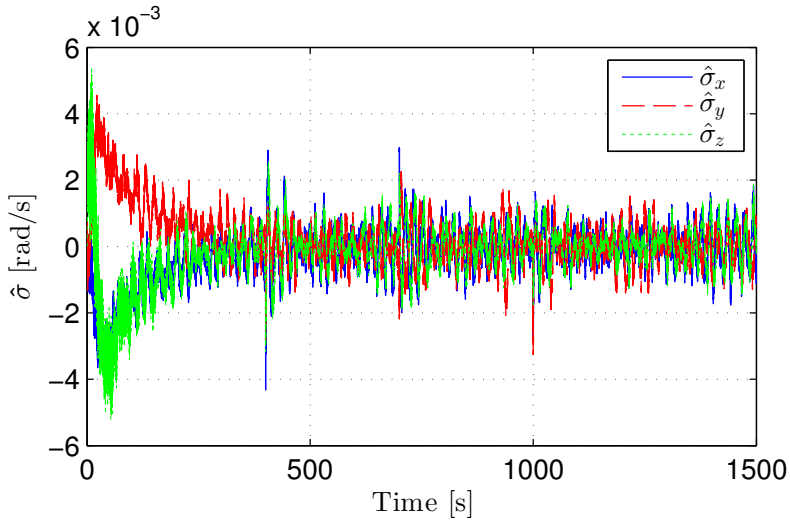

Figure 5.11: Case 2, Outlier detection. The injection term $\hat{\boldsymbol{\sigma}}$ when outlier detection is disabled

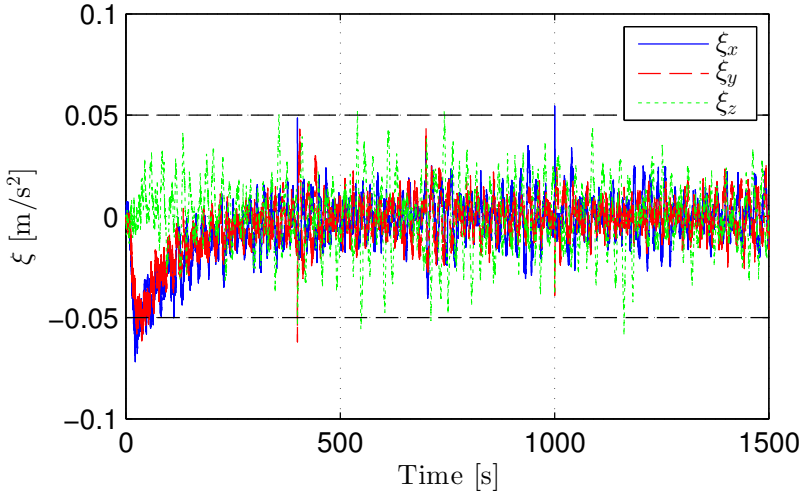

Figure 5.12: Case 2, Outlier detection. $\boldsymbol{\xi}$ when outlier detection is disabled

Outlier Detection Enabled

Now will the results of the outlier detection be shown. Furthermore, three GNSS sensors will be utilized to show the advantages of multiple sensors. In Figure 5.13 - 5.15 are the GNSS the measurements shown.

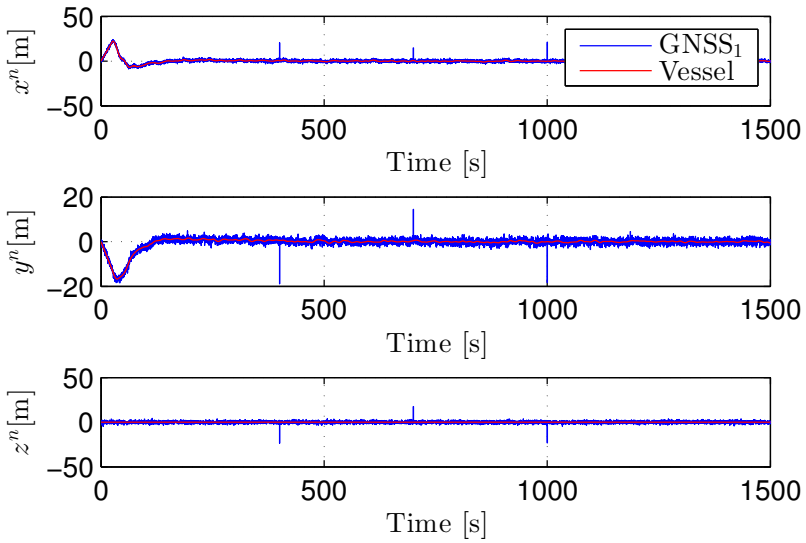

Figure 5.13: Case 2, Outlier detection. Measurements provided by GNSS$_1$. Outliers present at time 400, 700 and 1000 seconds

These measurements resulted in the GNSS status seen in Figure 5.17. Three outliers can be observed for each sensor. Moreover, Figure 5.18 presents the resulting weighted GNSS measurements. One can see that the outliers are detected and prevented from propagating to the weighted GNSS measurements. The weighted GNSS measurements are furthermore utilized in be the observer. Hence, the outliers are prevented from propagating to the estimator and inherently to the control system. This connection was shown in Figure 1.1 on page 1.

From Figure 5.17 one can observe that the outlier detection algorithm pre-

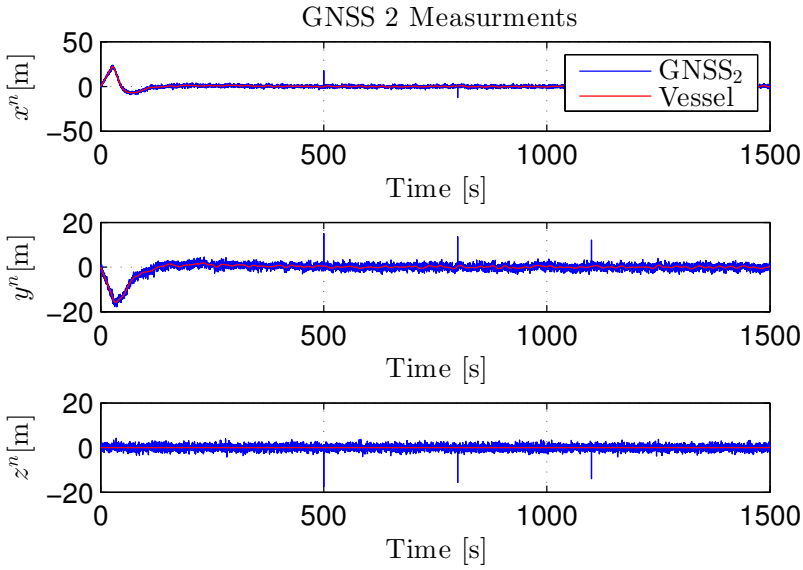

Figure 5.14: Case 2, Outlier detection. Measurements provided by GNSS$_2$. Outliers present at time 500, 800 and 1100 seconds

sented in Section 4.5 detecting the wild points when they occur. This is also indicated in Figure 5.16 where variance of minus one is reported when an outlier is detected. As stated in Section 4.5, is status 2 provided by the individual GNSS signal checking procedures in the event of an outlier. What can also be seen from Figure 5.17 is at 1089 seconds the voting and weighting procedure yielded status 4. Table 4.2 states that status 4 means that one sensor has been discarded because it was deemed to deviate from the two others. In this case was GNSS 2 excluded. Since no outlier nor bias or other drifting terms were injected by the fault generator at this time in the simulator, is the cause of this removal due to Gaussian measurement noise of GNSS 2. More precisely a Gaussian noise component in the outer regions of the noise distribution shown in Appendix B.8, Figure B.1. Moreover, in Figure 5.21 and Figure 5.22 are the respective position and velocity estimates shown when the outlier detection is enabled. The position estimate error,

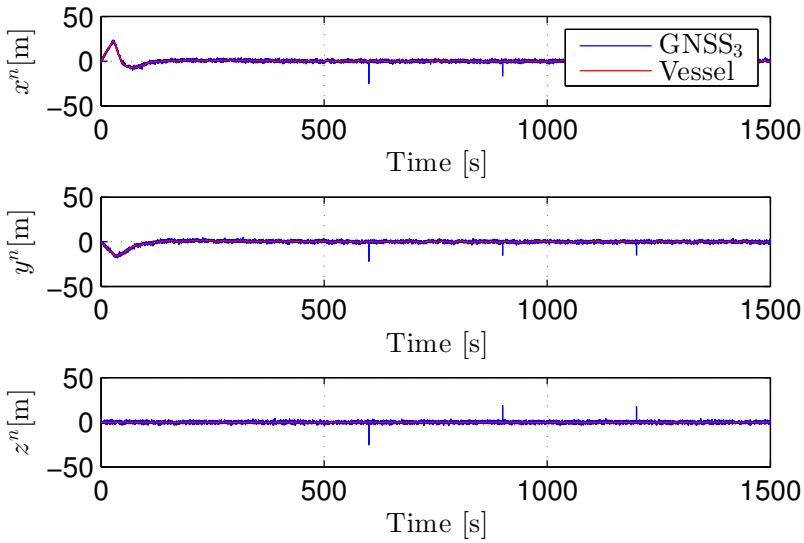

Figure 5.15: Case 2, Outlier detection. Measurements provided by GNSS$_3$. Outliers present at time 600, 900 and 1200 seconds

$\tilde{\boldsymbol{p}} = \boldsymbol{p}_{\text{GNSS}} - \hat{\boldsymbol{p}}$ is shown in Figure 5.23. In neither of the estimates are large rapid changes or spikes present. One can see after the initial converges that the position estimates error fluctuates around zero. Furthermore, it can be seen in Figure 5.20 that the observer, also for this simulation, need some time to obtain the correct position estimate.

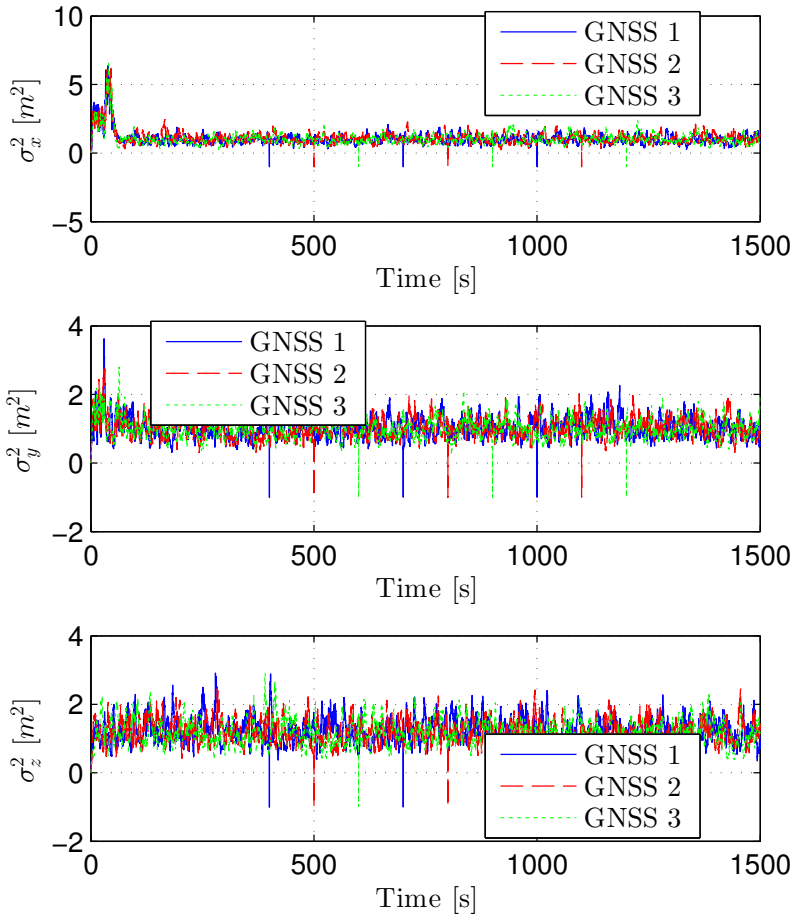

Figure 5.16: Case 2, Outlier detection. Reported variance from each sensor. Variance for outliers are reported to be -1 for illustrative purposes.

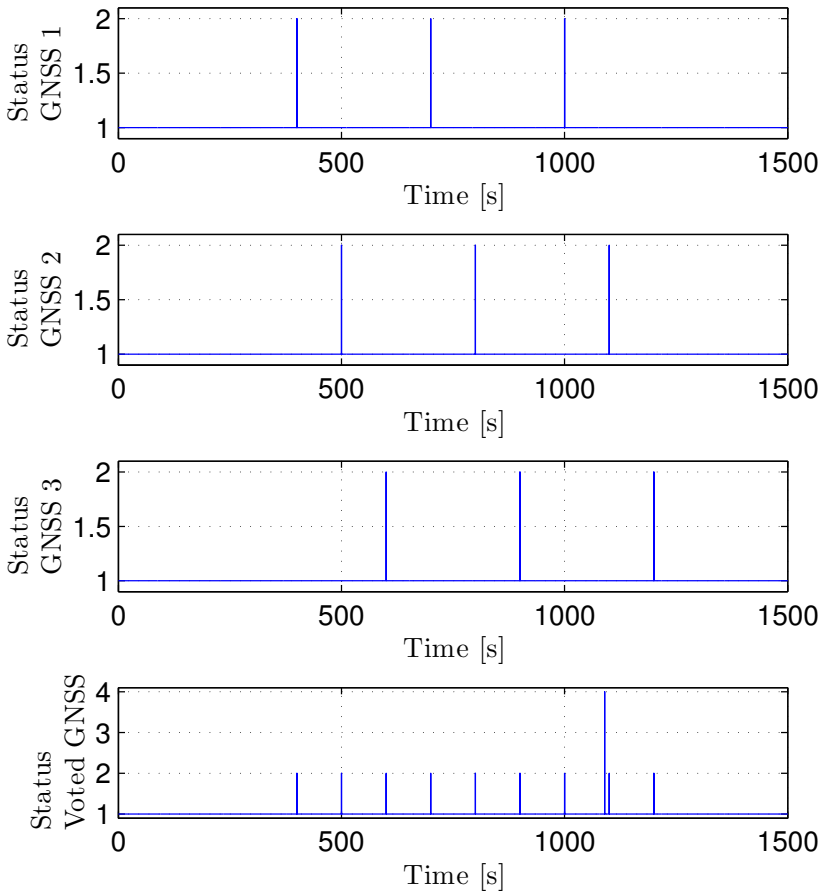

Figure 5.17: Case 2, Outlier detection. GNSS status

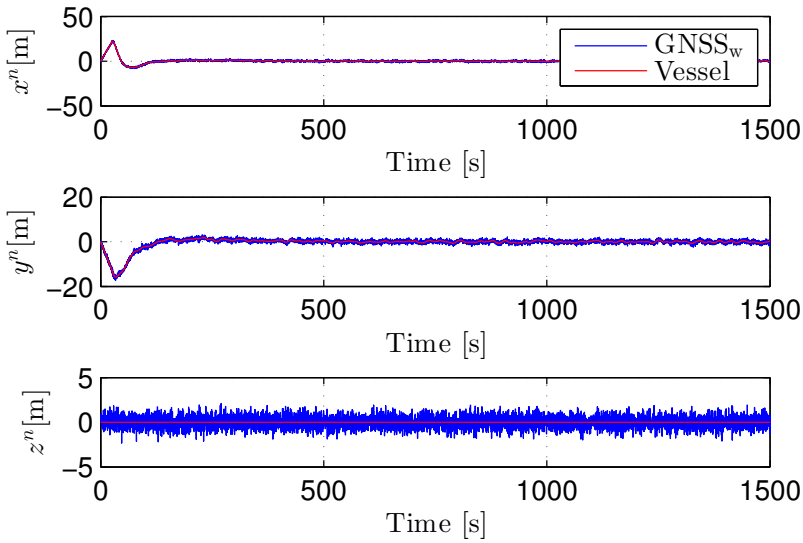

Figure 5.18: Case 2, Outlier detection. Weighted GNSS measurement used by the observer for position and velocity estimates

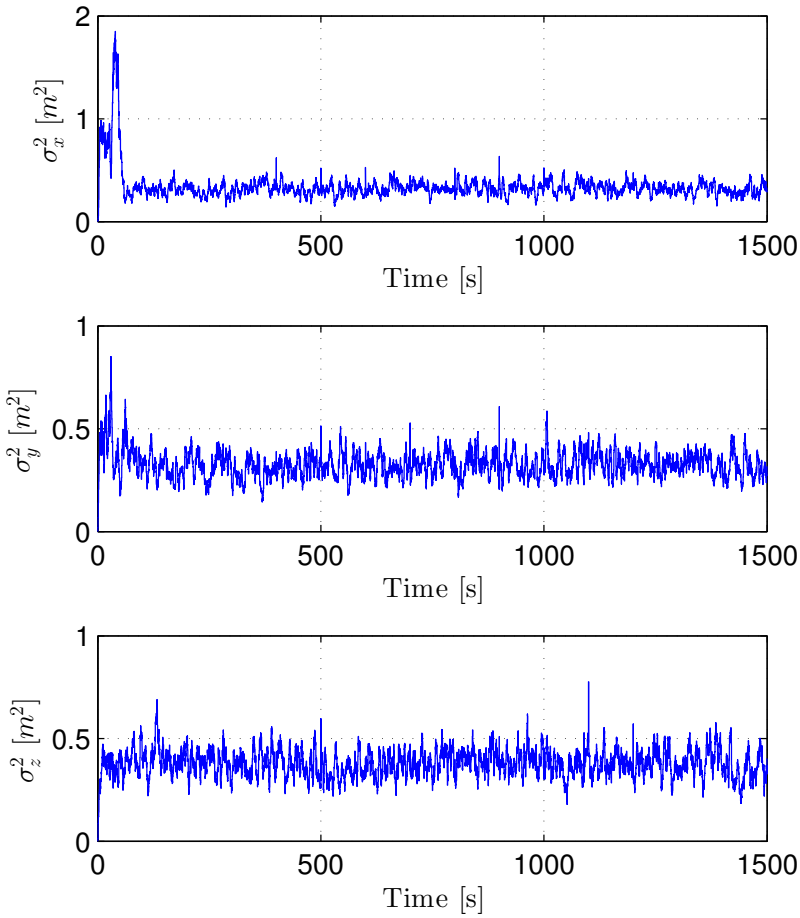

Figure 5.19: Case 2, Outlier detection. Covariance of three reported GNSS measurement when outliers are removed

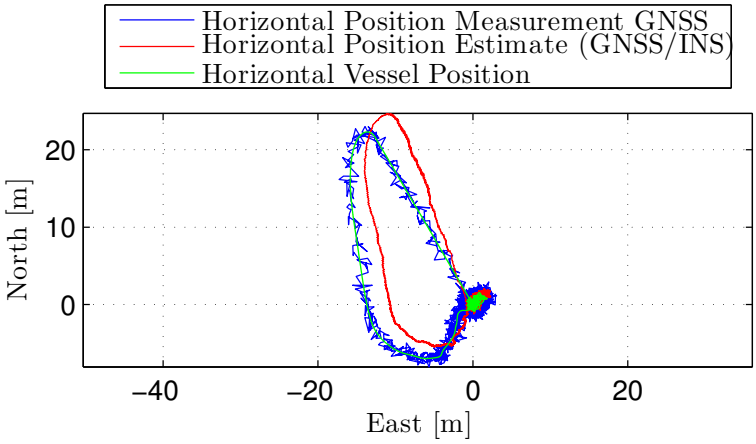

Figure 5.20: Case 2, Outlier detection. North-East position of the vessel together with weighted GNSS measurements and position estimates

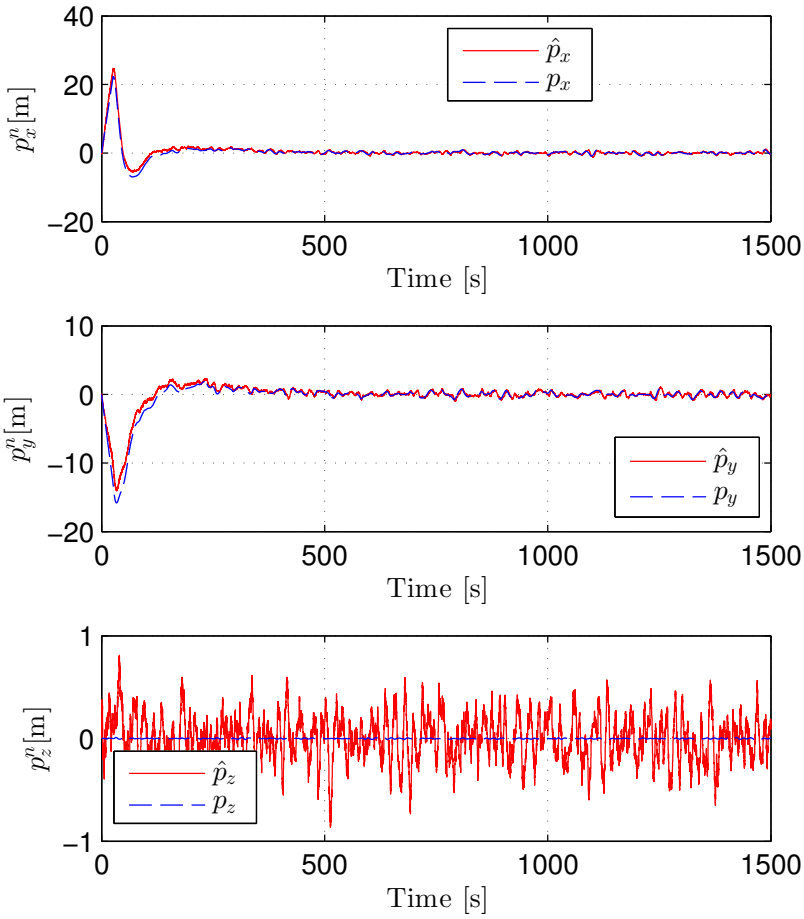

Figure 5.21: Case 2, Outlier detection. Position estimate when outliers in the GNSS measurements are present and outlier detection is applied. The estimates are shown together the actual vessel position

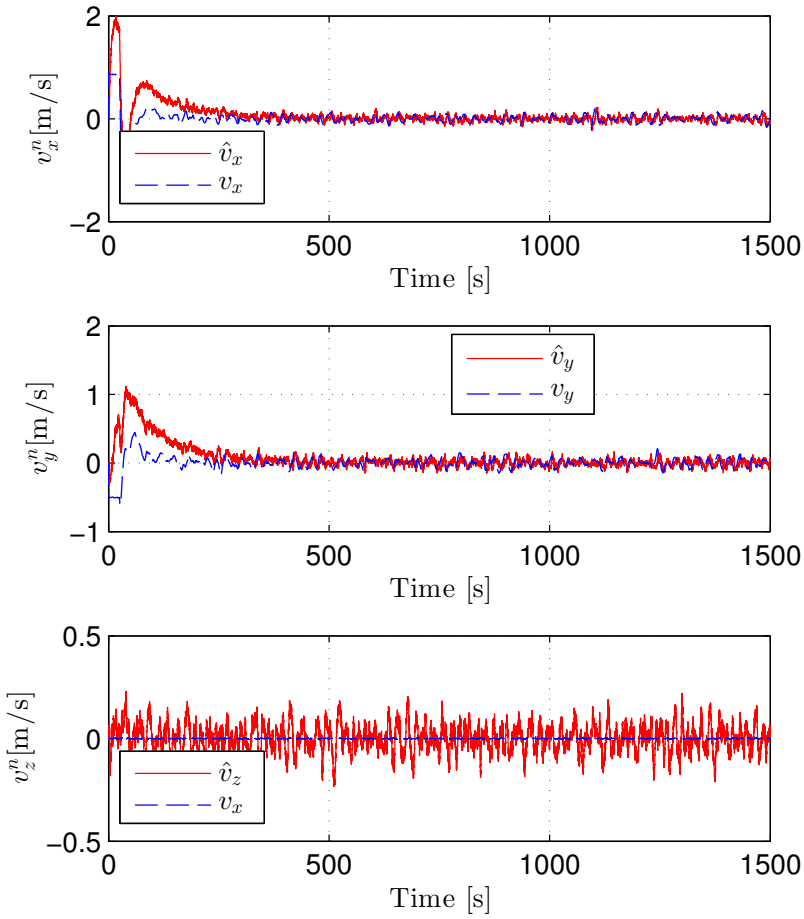

Figure 5.22: Case 2, Outlier detection. Velocity estimate when outliers in the GNSS measurements are present and outlier detection is applied. The estimates are shown together the actual vessel velocity

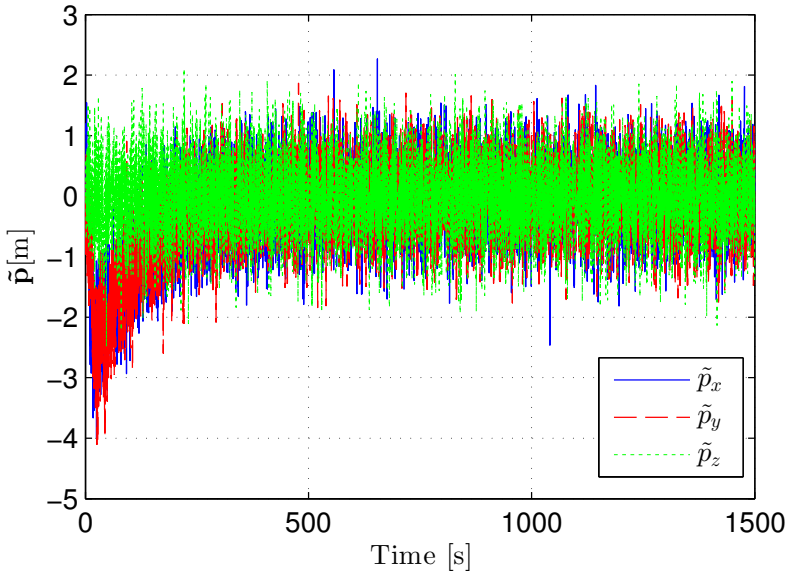

Figure 5.23: Case 2, Outlier detection. Estimation error, $\tilde{\boldsymbol{p}} = \boldsymbol{p}_{\text{GNSS}} - \hat{\boldsymbol{p}}$.

Discussion

From results above, one can argue that applying both outlier detection from each sensor together with voting can increase the total signal processing system ability to handle outlier detection. Even if the outlier detection mechanism where set with a high threshold to avoid false alarms are outliers excluded because of the voting, given that not all GNSS are exposed to the same interference yielding wild points for all sensor simultaneously.

By studying Figure 5.21 and Figure 5.22 can one observe that the respective estimates are fluctuating less that without outlier detection enabled. The velocity estimates are clearly better than in the event of wild point measurements are utilized by the observer. Furthermore, because of the time-varying gains and weighting of multiple measurements utilized for correction yields this less fluctuation of the estimates compared with the fault-free benchmark with fixed gains and only one GNSS sensor as seen in Appendix E.

What can be observed from the North-East position, shown in Figure 5.20, where the outlier detection is enabled are the position estimates closer to the vessel's actual position of the vessel when the control objection of horizontal position at $(0, 0)$ is met. The reason for this is that the outliers are totally removed. Thus, yield a less abrupt in the position estimate. In this thesis was a outlier detected if the measurement exceeded $\pm a\boldsymbol{\sigma}$, where $a = 7$. Since the chosen wild-points in this thesis had a large amplitude might a lower value be more appropriate in in order to detect smaller outliers.

Even though the position estimate error seen in Figure 5.23 seems quite large can one observer that the GNSS zero mean Guassian noise from the GNSS is attenuation significantly as seen in Figure 5.20. If a smaller amplitude of the position estimate is needed one should explore how wave filtering could be embedded in the Grip et al. (2013) observer. The amplitude of $\tilde{\boldsymbol{p}}$ will probably also be affected by the sea state since the also the GNSS sensor is affected by. The GNSS should also be roll and pitch compensated in a

real-life operation where the sensors are not directly given in the CG as in this thesis.

From Figure 5.7 and Figure 5.20, presenting the horizontal position estimates can it be seen that estimates in general need some time to converge to the correct state. This could have been combated by increasing the gain, $\boldsymbol{K}_{pp}$, associated with the position estimate. However, at the price of more wave-induced motion and measurement noise propagating to the position estimates. More aggressive tuning could be more feasible if wave filter was added to the observer of Grip et al. (2013, Sumbitted).

5.3 Case 3: Freeze of One GNSS Sensor

This section with take on the event of a GNSS sensor freeze and detecting it. Thus, avoiding faulty sensor outputs to propagate to the observer and control system. Two types of sensor freezes was tested. One where the freeze was short and present for 10 second. The other freeze was inserted to last for the remainder of the simulation. For both cases where the desired generalized position was set to

$$\boldsymbol{\eta}_d = \begin{bmatrix} 0 & 0 & 0 \end{bmatrix}^\intercal. \tag{5.7}$$

The controller was enabled after 25 seconds.

Short Freeze of GNSS 1 at 1000 Seconds

Figure 5.24 illustrates a 10 second freeze of GNSS 1 at time equals 1000 seconds. In Figure 5.25 can see the signal checking of GNSS 1 detects the freeze by reporting sensor freeze indicated by status 3. Furthermore, as seen in Figure 5.26 this is reported to the GNSS voting since the resulting voting status was 2 at the given time. Table 4.2, states the possible status

from the voting. Furthermore, is status 2 means that as two sensors are in operation and one is reported erroneous from the senors's signal checking procedure. Moreover, one can also see from Figure 5.26 that the voting procedure also ruled out one GNSS at four other occasion. This is indicated by status 4 were reported from the GNSS voting at four occasion. Moreover, the resulting covariance can be seen in Figure 5.27. One can observe the resulting covariance is not significantly affected the shorter outtakes of one of the three GNSS sensors during the simulation.

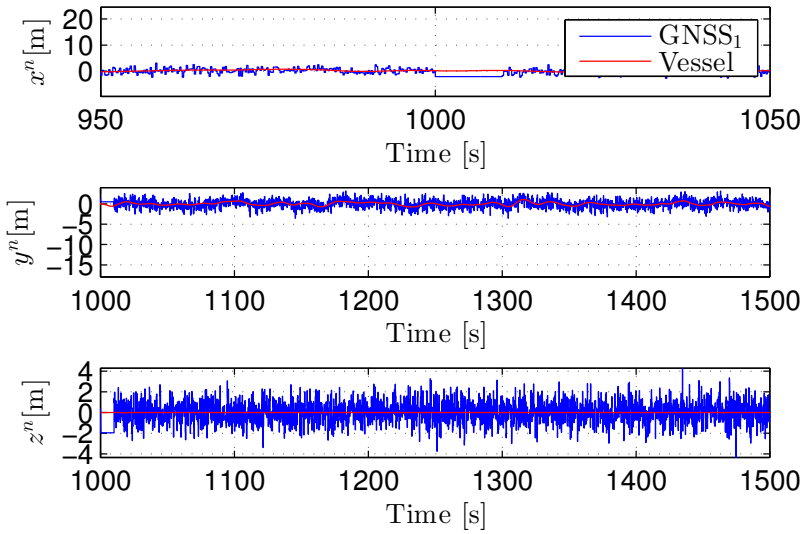

Figure 5.24: Case 3, GNSS freeze. Zoomed section of GNSS 1. Sensor freeze present at 1000 second and present for 10 seconds.

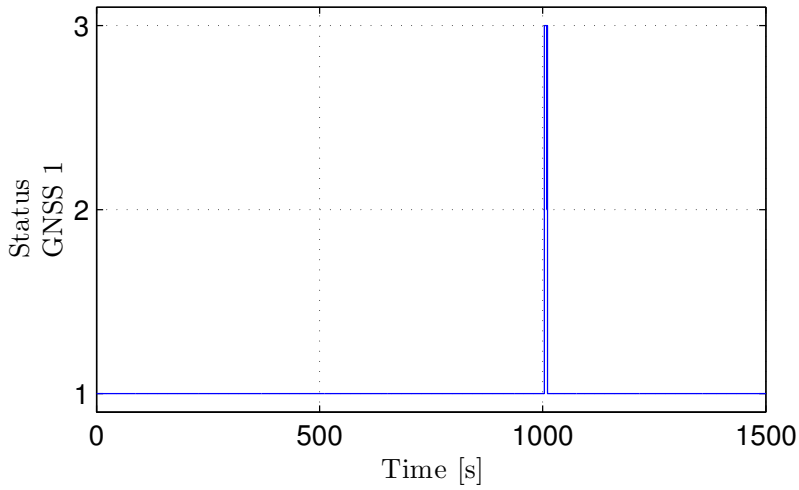

Figure 5.25: Case 3, GNSS freeze. Reported status of GNSS 1. Sensor freeze present at 1000 second and present for 10 seconds.

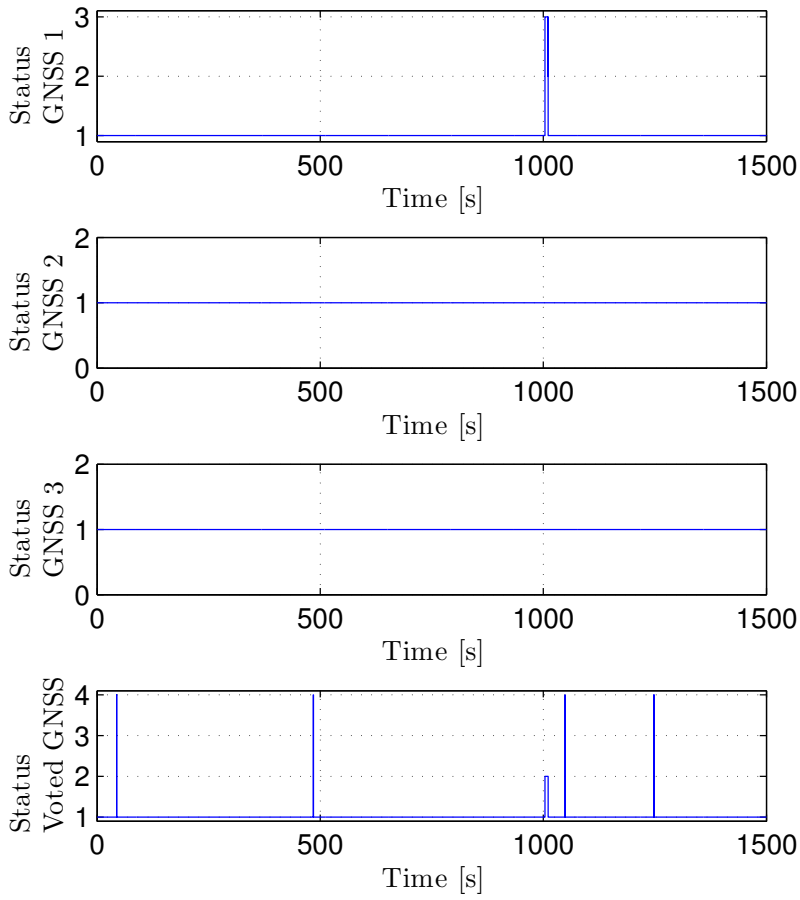

Figure 5.26: Case 3, GNSS freeze. Reported status of GNSS. Sensor freeze present at 1000 second and present for 10 seconds.

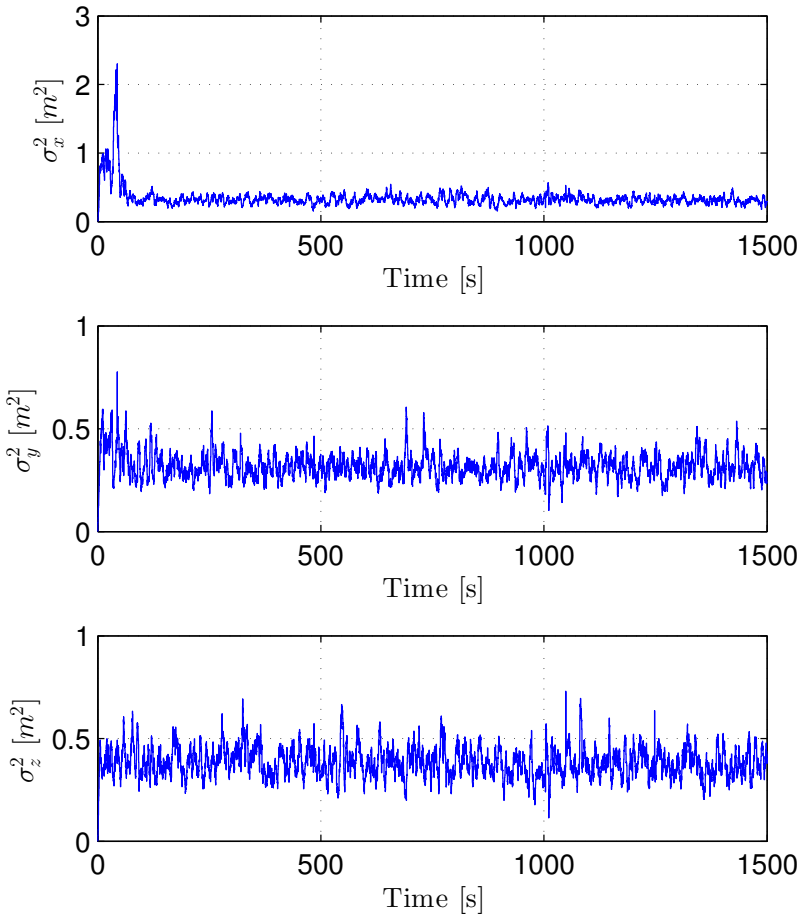

Figure 5.27: Case 3, GNSS freeze. Sensor freeze present at 1000 second and present for 10 seconds.

Permanent Freeze of GNSS 1 at 1000 Seconds

A larger sensor failure where one GNSS freezes at a longer of period of time is shown in Figure 5.28 - Figure 5.31. Figure 5.28 show the measurements provided by GNSS 1. In can be seen that sensor freeze occurred at time equals 1000 seconds. Furthermore, the status provided by GNSS 1 is presented in Figure 5.29. It can be seen that the sensor status was reported to be 3 after 1000 seconds of simulation. This indicated that a sensor freeze was detected.

Moreover, the combined status of all three GNSS sensor is given in Figure 5.30. Before time equals 1000 seconds was status 1 reported from the voting algorithm expect from one occurrence of status 4. The former indicates that all sensors are healthy and available. The latter indicated that one senor was deviating from the two others. Thus, the deviating GNSS was discarded from the voting before re-enabled shortly afterwards. After the sensor freeze was reported by the signal processing, associated with GNSS 1, was status 2 mostly reported by the voting algorithm. This indicated that two sensors were available and one sensors was reported erroneous and hence not included in sensor voting and weighting. At four occasions however, was status 5 reported. This was a result of the two available sensors reported that they were deviating from each other.

The covariance of the combined weighted GNSS measurements is given in 5.31. One can see that the covariance increased after 1000 seconds of simulation.

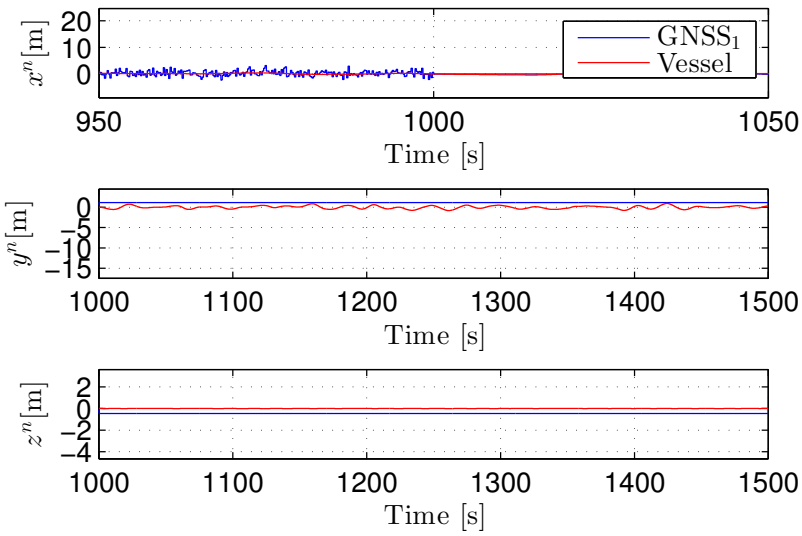

Figure 5.28: Case 3, GNSS freeze. Zoomed section of GNSS 1. Sensor freeze present at 1000 second and throughout the simulation.

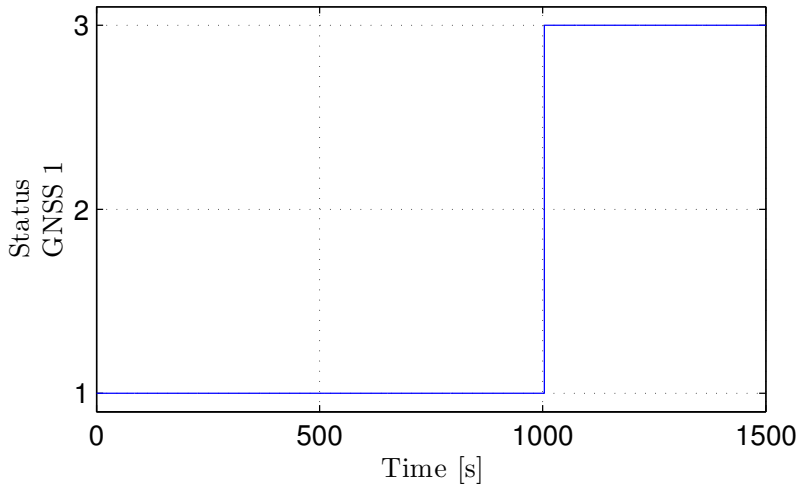

Figure 5.29: Case 3, GNSS freeze. Reported status of GNSS 1. Sensor freeze present at 0 second and through out the simulation

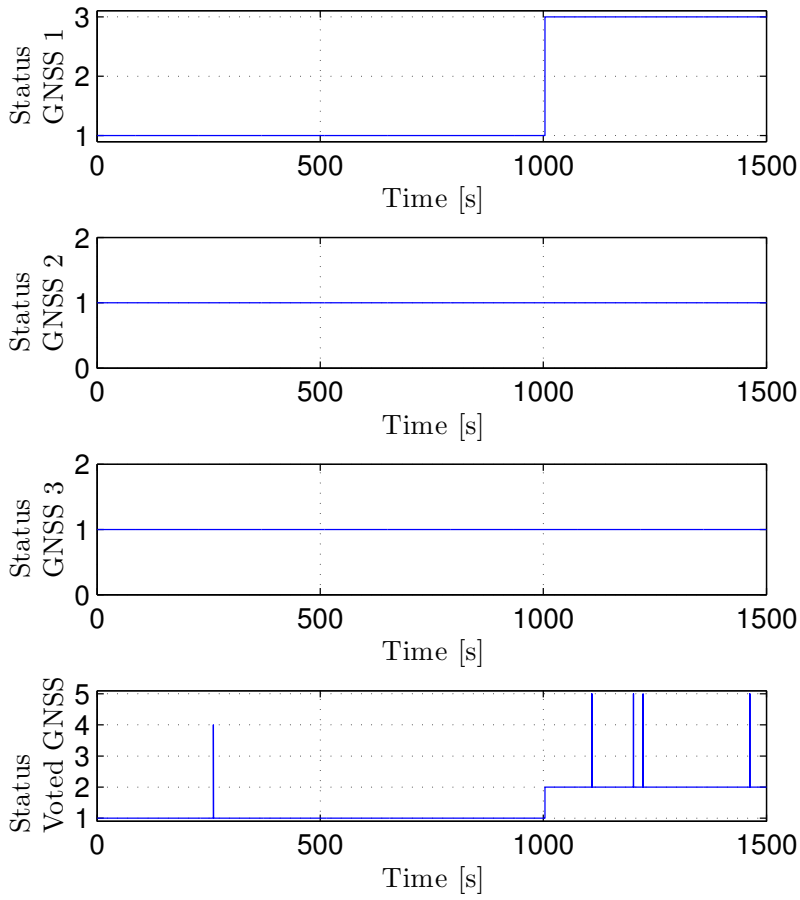

Figure 5.30: Case 3, GNSS freeze. Reported status from the GNSS voting and weighting. Sensor freeze present at 1000 second and throughout the simulation.

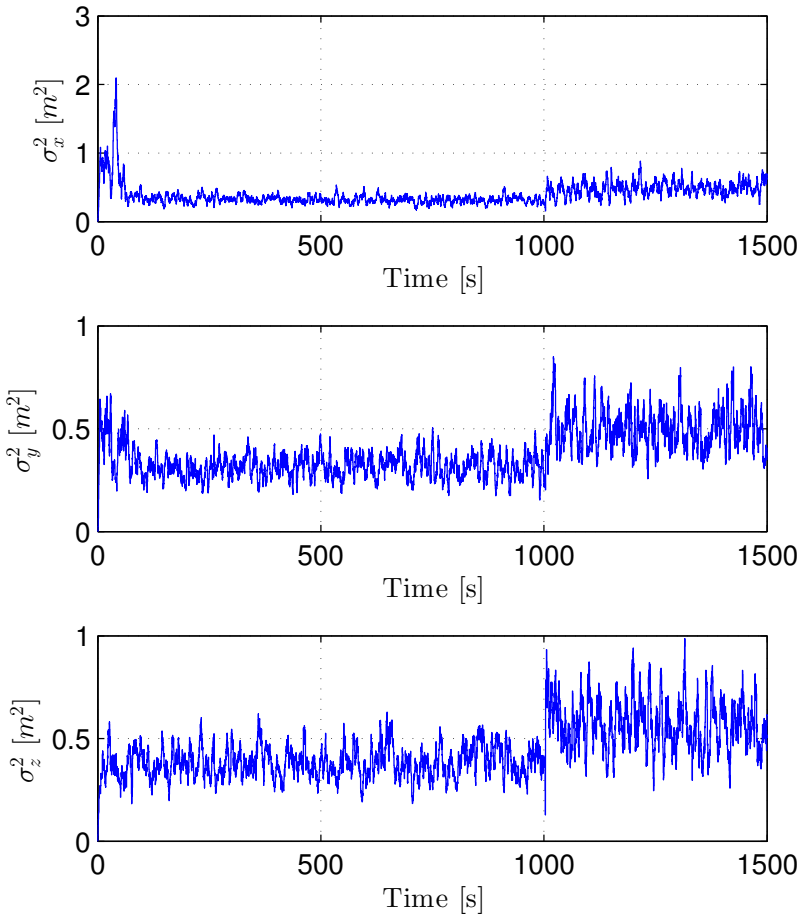

Figure 5.31: Case 3, GNSS freeze. Calculated covariance of the weighted GNSS. Sensor freeze present at 1000 second and throughout the simulation.

Discussion

As can be seen from both simulation that both shorter and longer sensor freeze is detected by the freeze detection algorithm. The algorithm is also able to enable a sensor when deemed healthy, however if the freeze detection threshold is set to low can this yield unwanted side effects. This is so because then the diversity in the moving window of historic data can get a variance close close to zero. This can again lead to problems when the sensor is deemed healthy and hence re-enabled . When the healthy measurements again are provided will all of these be deemed as wild points since these lies outside of the range of $\pm a\boldsymbol{\sigma}$. This is so because 1-sigma of the previous frozen measurements have become close or equal to zero. Setting the freeze detection threshold higher will possibly result in a false alarms. This be combated by disabling the wild point detection for five measurements to increase the standard deviation in the moving average.

GNSS 1 is permanently discarded by the fault detection in the latter simulation. How this affects the calculated covarience can be seen in Figure 5.31 from 1000 seconds where the covarience is seen to increase significantly. This is not unexpected since covariance grows larger with fewer measurements available and visa versa. Furthermore, this covariance will affect the tuning of the observer's position estimate because of the addition of the time-varying, $\boldsymbol{K}_{pp}$, gain. When the covariance increases, the gain will be reduced quite significantly because of the exponential decay form the fact that the varying part of the gain is given as

$$\boldsymbol{K}_{pp,varying} = \beta e^{-\alpha\sigma^2} \cdot \boldsymbol{I}_{3\times 3} \tag{5.8}$$

This strategy might be efficient for very accurate measurements with corresponding low convenience, but can reduce the gain to much if the measurements are still accurate when the covarience have increased due to the loss of one measurement. This is so even though the quality of the remaining

sensors have not changed. An other tuning strategy might have been to utilize a gain like

$$\boldsymbol{K}_{pp,varying} = \frac{\sigma}{\sigma^2 + \epsilon} \cdot \boldsymbol{I}_{3\times 3} \tag{5.9}$$

where ϵ is small number to avoid the gain $\boldsymbol{K}_{pp,varying}$ to grow towards infinity when reported variance is very quite small. Adaptive gains utilizing a update law is also another possible a strategy to investigate. The time-varying tuning in this thesis do not incorporated the quality of the respective estimates as the Kalman filter does by utilizing the variance estimate $\boldsymbol{P}(k)$ in the gain calculation. Similar tuning schemes could also be introduced in a time-varying tuning strategy.

Since this thesis also employs a GNSS bias detection by filtering, the vertical component of the, GNSS measurement can also a sensor freeze be picked up by the GNSS bias estimation. This will happen when the GNSS freezes outside of the GNSS bias threshold. When the filter has the same output as the fixed measurement, provides to the filter, will an alarm be raised. This will provide addition capability in detecting sensor freeze. However, this can also increase the difficulty of differentiating the respective sources of the fault.

5.4 Case 4: Increased Variance of One GNSS Sensor

This section will address the case where a GNSS sensor changes noise characteristics significant by a increase in the variance. From 2.6 can this be an indication of senor failure or an inaccurate measurement. Neither the fault or the inaccurate sensor data should propagate to the observer.

At time equals 1000 seconds is the standard deviation of the zero mean, Gaussian noise of GNSS 1 multiplied with 10. Also for the case is the

desired generalized position was set to

$$\boldsymbol{\eta}_d = \begin{bmatrix} 0 & 0 & 0 \end{bmatrix}^\intercal. \tag{5.10}$$

The controller was enabled after 25 seconds.

The corresponding measurement together with the vessel position is shown in Figure 5.32. Figure 5.33 show the zoomed version of the measurements around the time of significant increase in noise. The reported variance of each GNSS is shown in Figure 5.34 while the weighted covariance is shown in Figure 5.36. Furtermore, the weighted position measurement is shown in Figure 5.37. The resulting position estimates are shown in Figure 5.38 and Figure 5.39 where Figure 5.38 show the horizontal position estimates with the corresponding weighted position measurements and the horizontal vessel position. Figure 5.39 show the position estimates together with vessel position.

Form Figure 5.32 and Figure 5.33 can one clearly see the increased variance at time equals 1000 seconds. This is picked up by the variance calculation seen in Figure 5.34 where the variance for GNSS 1 is dramatically higher than the previous calculated variance and the calculated variance of GNSS 2 and GNSS 2 shortly after the possible failure event at time 100 seconds. Because of this is deemed as high variance since status 4 is reported by the signal checking procedure associated with GNSS 1. This is seen in Figure 5.35. What also can be seen from the reported status of GNSS 1 is that it changes between status 4 and 5 continuously in the remaining time of the simulation. This is due to fact that the vertical GNSS measurements are fluctuating with such large amplitude that the increased variance is picked up as vertical GNSS bias. This can be seen from Figure 5.40 where the bias of GNSS 1 exceeds the preset threshold related to the vertical GNSS bias estimate. Because GNSS 1 shortly after time equals 1000 seconds is reported to be erroneous result in only GNSS 2 and 3 is utilized measurements.

Regarding the quality of the position estimate it can be seen from Figure 5.38 that the horizontal position estimate in a large extent coincide with Figure E.2 in Appendix E where the fault free scenario with only one GNSS is shown. However, by comparing the horizontal estimates to north-east estimates Figure 5.20, where outliers where detected, can it be seen that the estimates are deviating some in northeastern direction from the weighted position measurements.

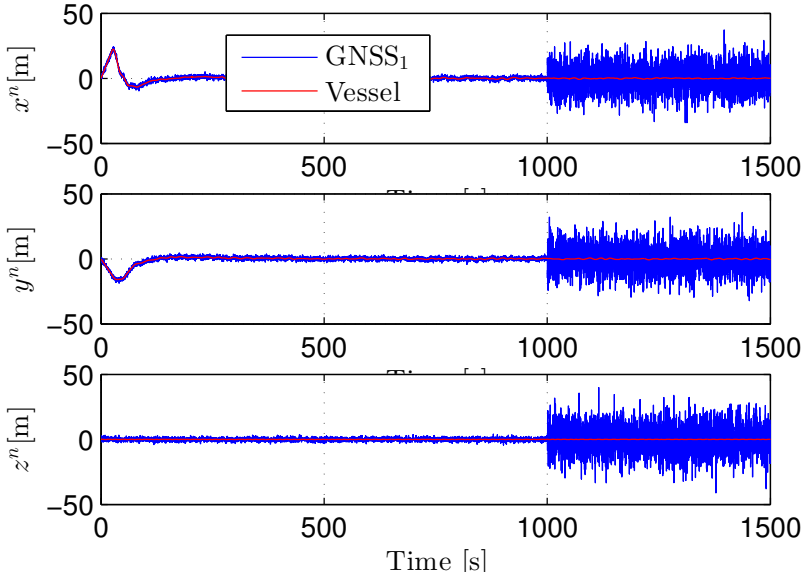

Figure 5.32: Case 4, Increased variance on GNSS 1

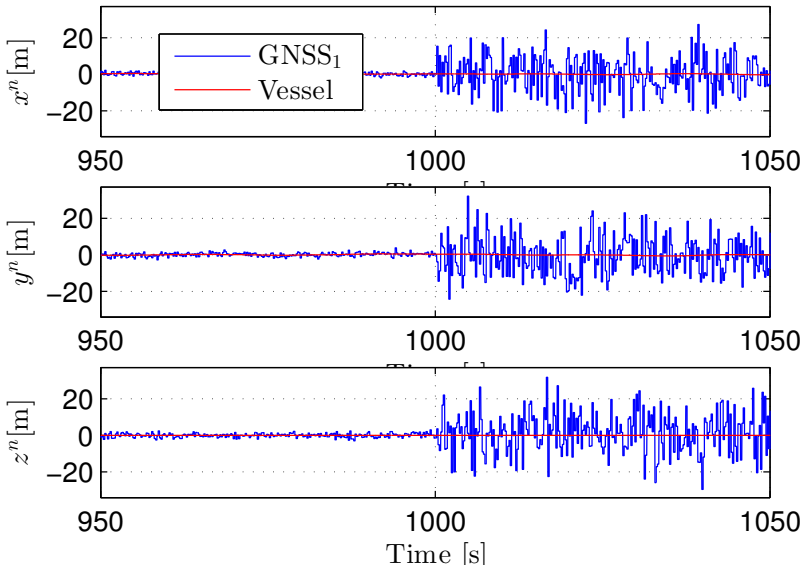

Figure 5.33: Case 4, Increased variance on GNSS 1. Zoom of measurement output around the event of increased variance.

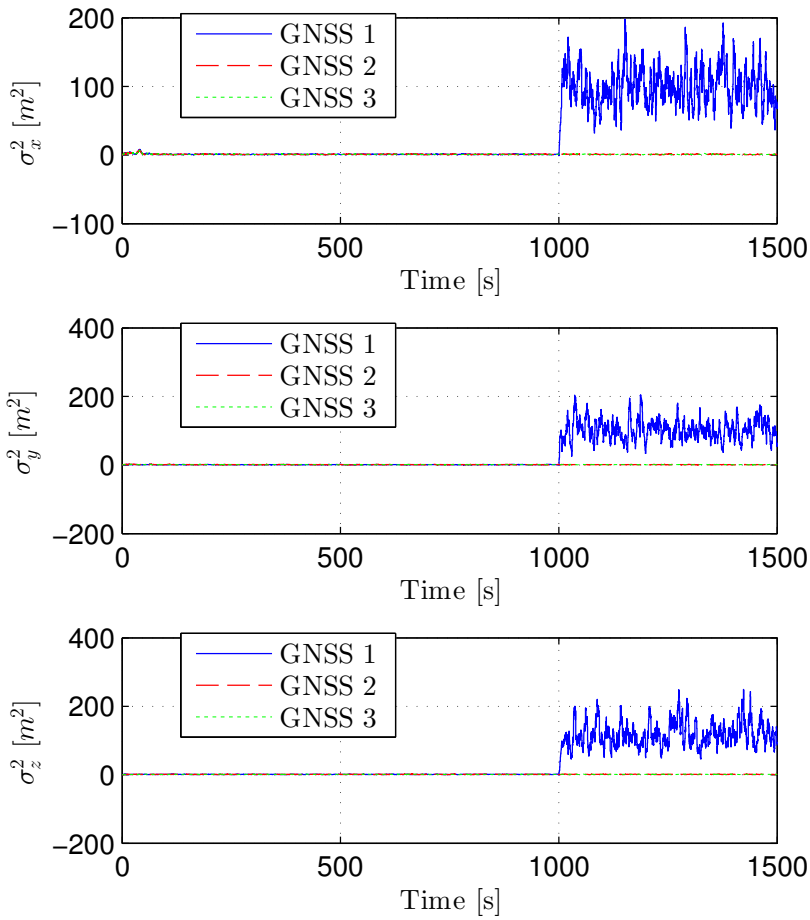

Figure 5.34: Case 4, Increased variance on GNSS 1. Reported variance of the three GNSS measurements.

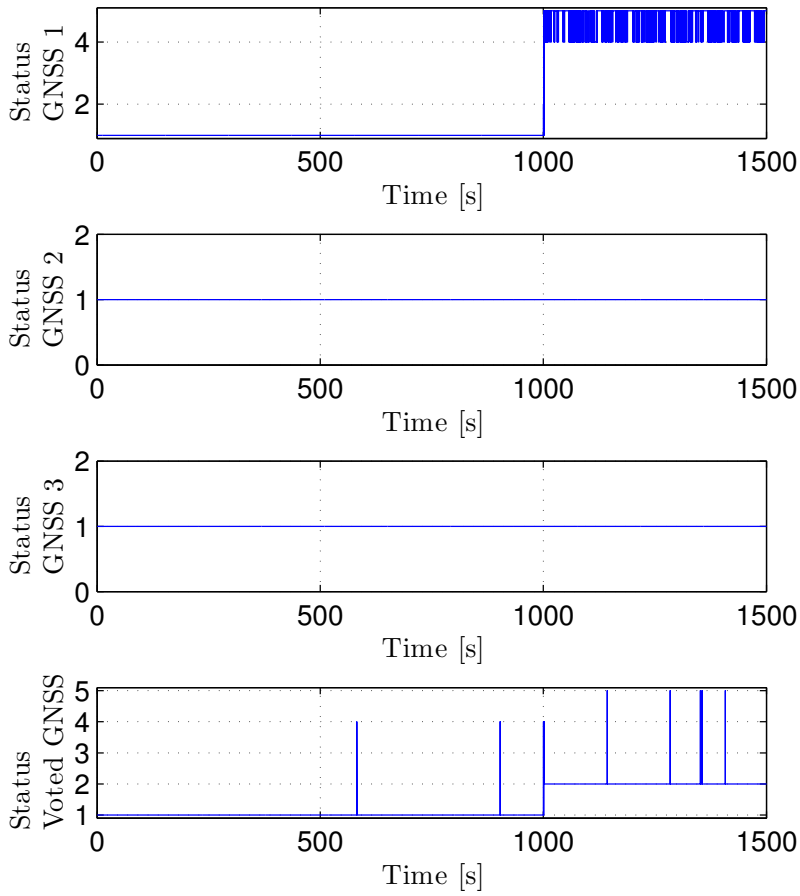

Figure 5.35: Case 4, Increased variance on GNSS 1

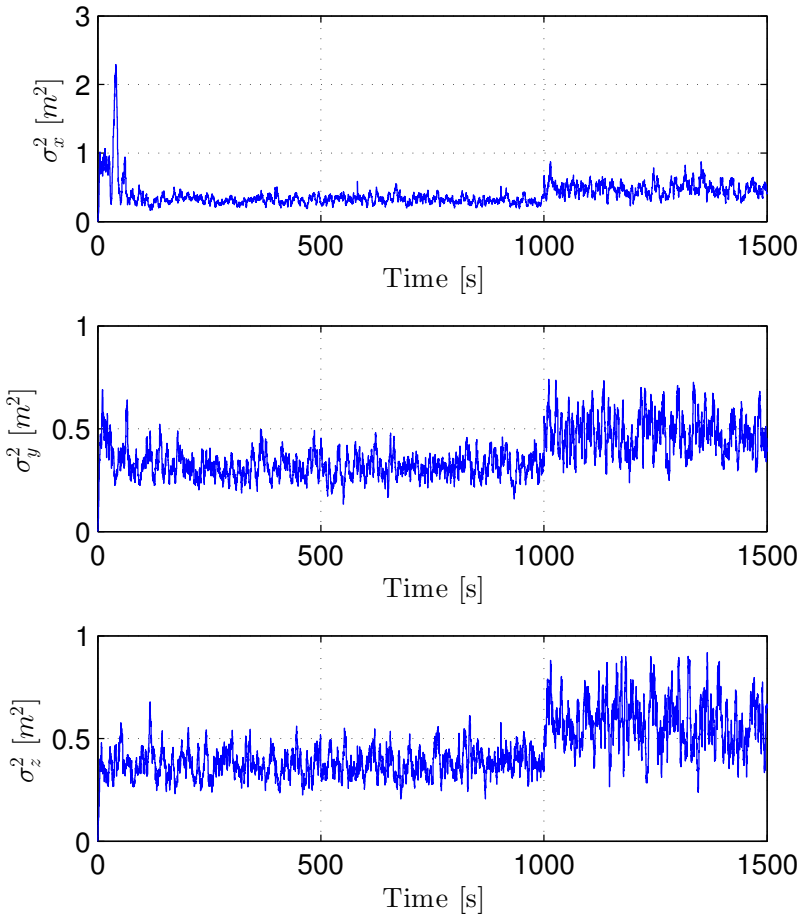

Figure 5.36: Case 4, Increased variance on GNSS 1. Weighted covariance of based on the three GNSS measurements.

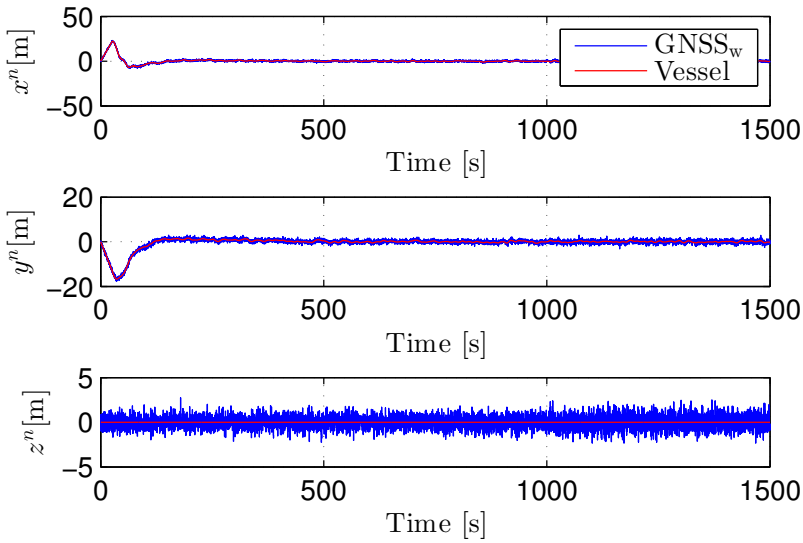

Figure 5.37: Case 4, Increased variance on GNSS 1. Weighted position measurements based on the three GNSS measurements.

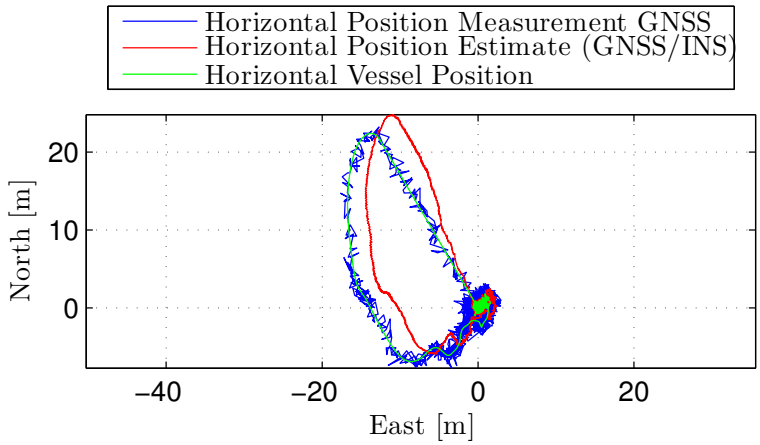

Figure 5.38: Case 4, Increased variance on GNSS 1. North-East position estimates with the corresponding weighted GNSS measurements and vessel position.

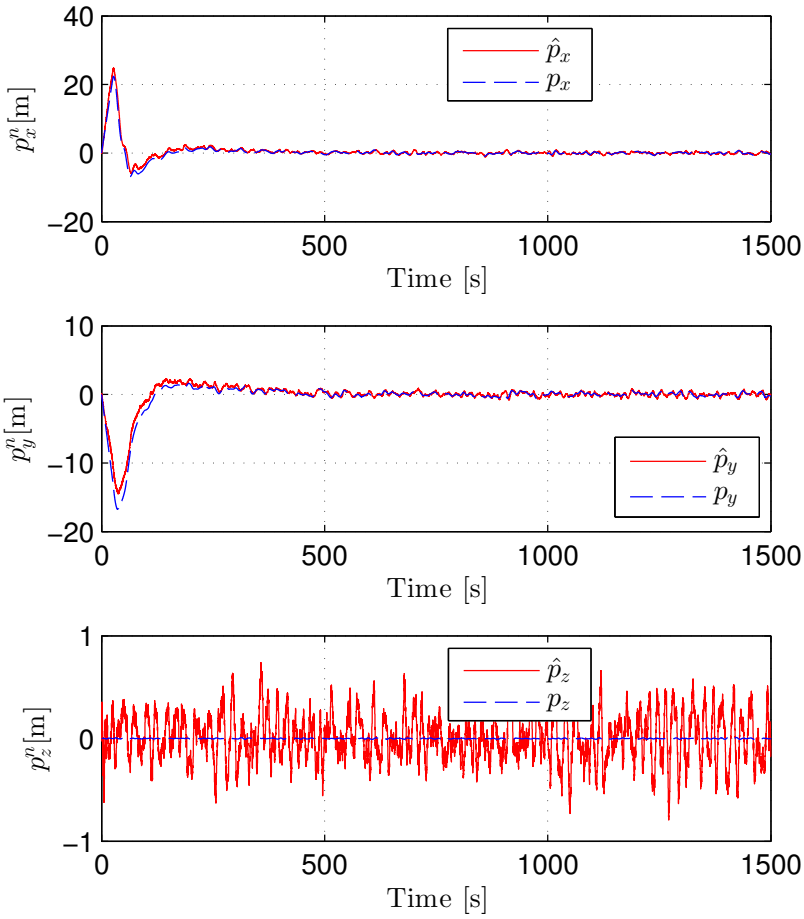

Figure 5.39: Case 4, Increased variance on GNSS 1. Position estimates together with the vessel position.

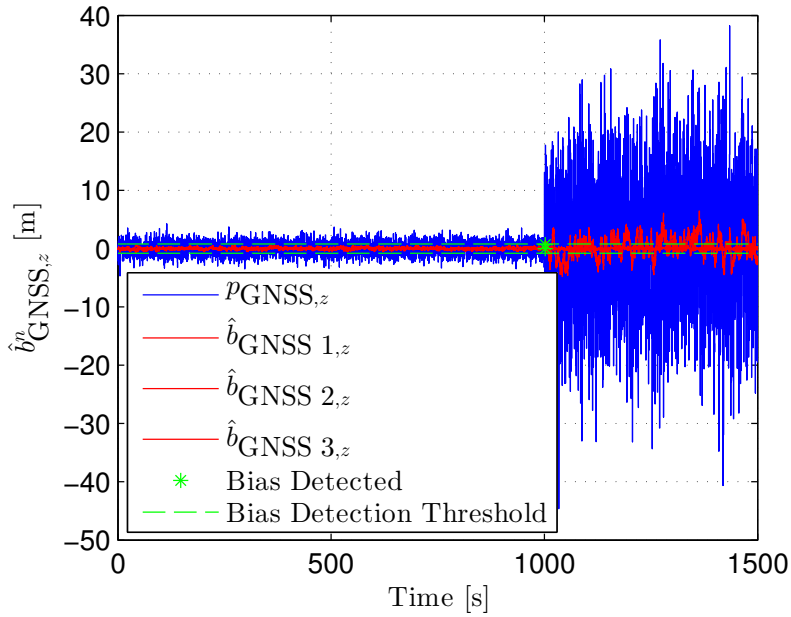

Figure 5.40: Case 4, Increased variance on GNSS 1. Vertical GNSS bias estimate.

Discussion

The reason for the increased weighted GNSS covariance, seen in Figure 5.36, is the result of GNSS 1 reported erroneous to the GNSS voting and weighting algorithm. This is reasonable since one less sensor is part of the co variance calculation. The reason for this can be found be studying the formula for covariance (2.52), stated in Section 2.6.

As seen in Figure 5.35 is status 4 provided by the voting algorithm three times before the signal check picks up the increased variance of GNSS 1. From Table 4.2 is this stated that status means that one of the sensors has been discarded by the voting algorithm. As in previous cases this is due to noise components are in the outer regions of the Gaussian distribution at this given time and therefore is not compliant with the two other measurements. After the increased variance of GNSS 1 has occurred reports the voting algorithm status 5 four time. From Table 4.2 is this status given as an indication that the two operational sensors are deviating at the given time. However, since no third measurement is deemed correct is it impossible to determine which one of the GNSS measurements is erroneous at the given times.

The reported status from GNSS 1 fluctuates between status 4 and 5. As stated above this means that both high variance and vertical GNSS bias is detected simultaneously. If the user is not familiar with the system might such fluctuating reported status be confusing. In a stressful situation should all data be provided to the operator in such a manner that the decision making process is simplified in largest possible extent. By having this in mind such fluctuating statuses should be picked up and handled by the signal processing system and presented to the operator in a more suitable manner.

The reason for the deviation of position estimate in northeastern direction seen in Figure 5.38 can be contributed too the fact the eastern position

estimates hadn't converge to the correct values even at time equals 100 seconds. In Figure 5.39 can it be seen that the position estimate in sway is a bit to the east of the actual vessel position at from the start of the simulation to around 100 seconds of simulation. Therefore is deviation of the estimates in the eastern direction probably not induced by the high variance of GNSS 1. This statement is further justified be Figure 5.41 where $\tilde{p}_y$, assassinated with the eastern direction, does not change significantly after the variance of GNSS 1 increase. One can seen the northern and vertical estimation error changes more than the eastern after time equals 1000 seconds.

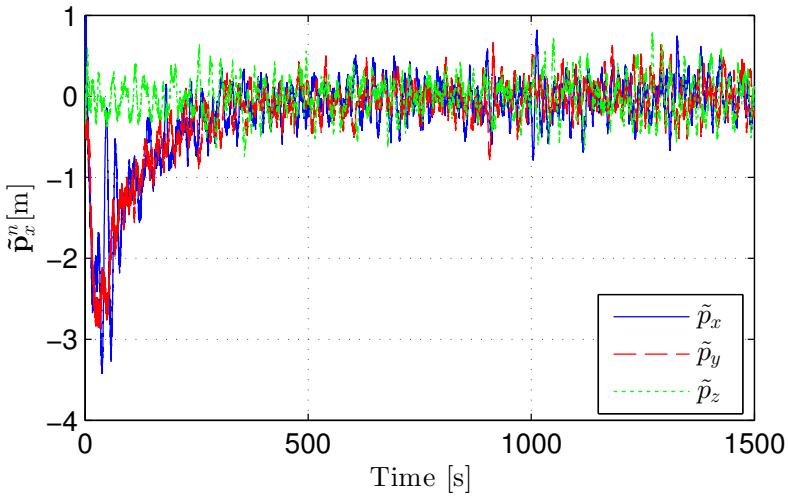

Figure 5.41: Case 4, Error of position estimate error $\tilde{\boldsymbol{p}} = \boldsymbol{p}_{\text{GNSS}} - \hat{\boldsymbol{p}}$.

5.5 Case 5: Horizontal Bias of One GNSS Sensor

The following results will show the voting algorithm's ability to detect long term errors of one position sensor. This is needed since the measurement weighing is based the assumption that the measurement only having zero

mean, Gassian error. See Section 4.5 for more. Thus, must the biased position measurements be excluded from sensor weighting to prevent any bias from propagating to the position estimates.

The bias was injected by the simulator at time equals 1000 seconds with a component of

$$\boldsymbol{b}^n_{\text{GNSS}} = \begin{bmatrix} 6.5 & -7 & 0 \end{bmatrix}^\intercal$$

as given in Table 3.4. The desired generalized position was set to a

$$\boldsymbol{\eta}_d = \begin{bmatrix} 0 & 0 & 0 \end{bmatrix}^\intercal. \tag{5.11}$$

The controller was enabled after 25 seconds.

The biased GNSS measurements are given 5.42. A close up of the measurements data around the event of bias at time equals 1000 seconds is found in Figure 5.43. The reported variance from the three GNSS sensors are given in Figure 5.44. Furthermore, Figure 5.45 show the respective GNSS status. Moreover, the weighted covariance is given in Figure 5.46, whereas the weighted GNSS measurements are given in Figure 5.47. Figure 5.48 shows the horizontal position estimates together with GNSS measurements and the vessel's position.

It can be seen form Figure 5.42 and Figure 5.43 that the horizontal measurements of GNSS 1 deviates from the vessels position at time equals 1000 to the end of the simulation. From Figure 5.44 can it be seen that the variance of GNSS 1 spikes at the time of event of the bias. When the bias is detected by the voting algorithm the variance is reduced stabilizes soon after. The GNSS status presented in Figure 5.45 shows that the voting algorithm discards GNSS 1 during the entire simulation after the bias is first picked up. At six times GNSS 1 is enabled before discarded again. Furthermore, bu studying the GNSS covariance is this not significantly affected by the spike of the variance of GNSS 1. The weighted GNSS measurements in Figure 5.47 can be seen to become more oscillatory occasionally after the bias was

injected into the measurements of GNSS 1 by the simulator. This also effects the position estimates seen in Figure 5.49.

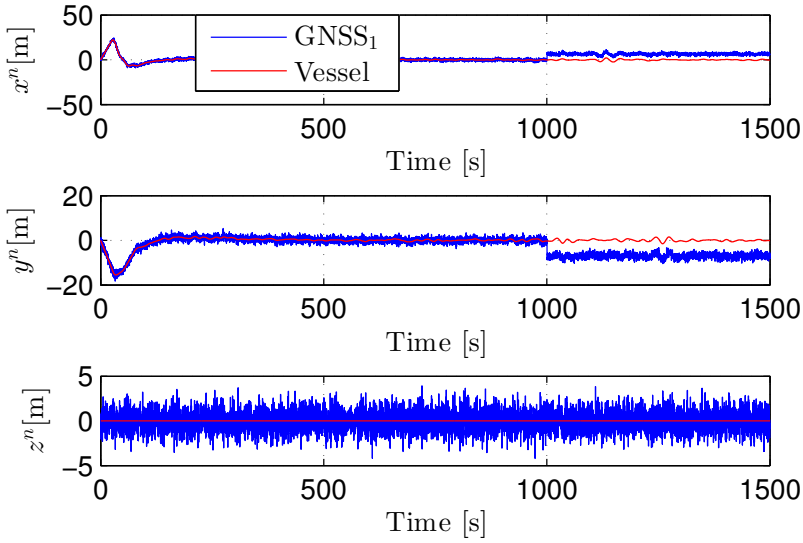

Figure 5.42: Case 5, Detection of horizontal GNSS bias. Measurements from GNSS 1

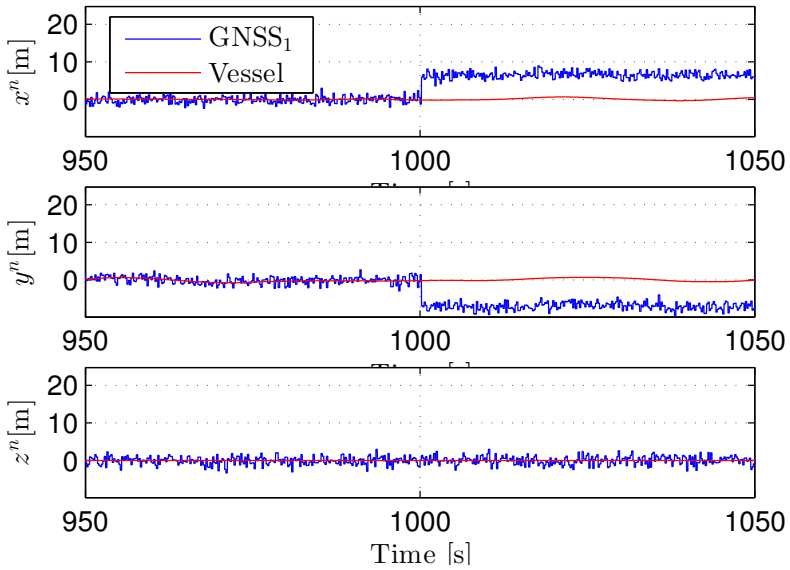

Figure 5.43: Case 5, Detection of horizontal GNSS bias. Zoomed measurements from GNSS 1

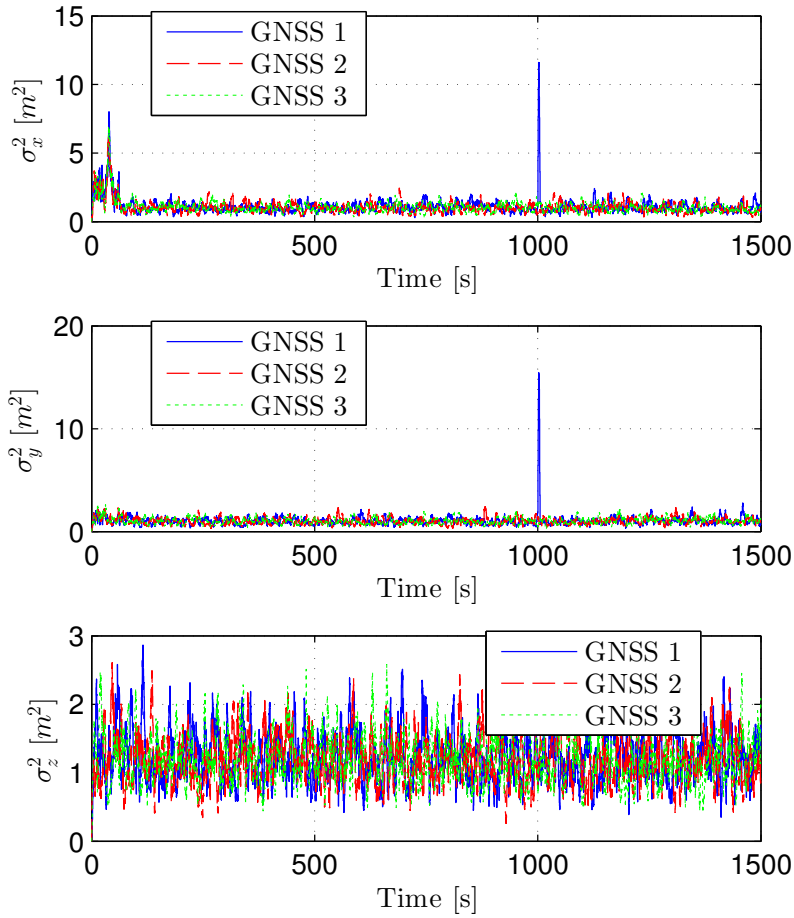

Figure 5.44: Case 5, Detection of horizontal GNSS bias. Reported variance from each GNSS

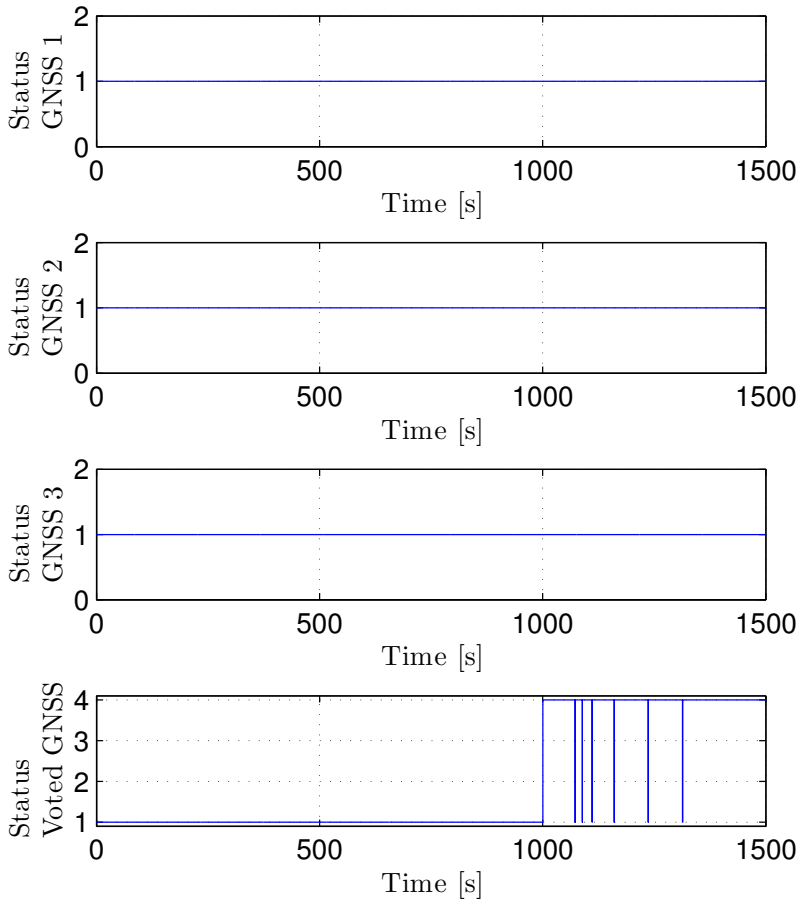

Figure 5.45: Case 5, Detection of horizontal GNSS bias. GNSS status

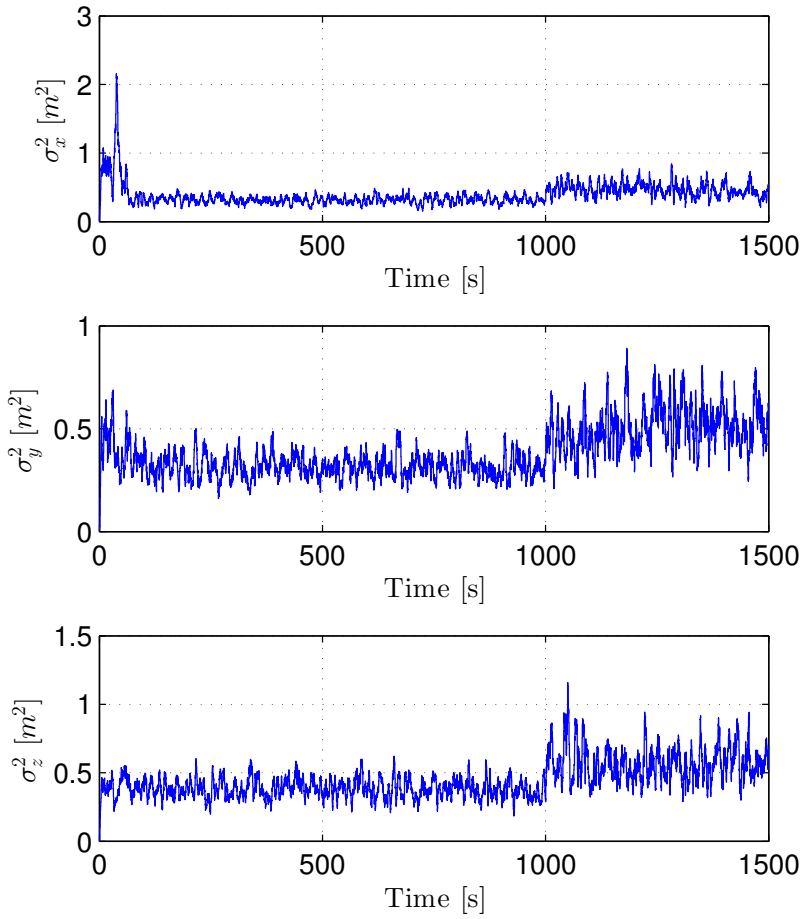

Figure 5.46: Case 5, Detection of horizontal GNSS bias. GNSS weighted covariance of the GNSS measurements.

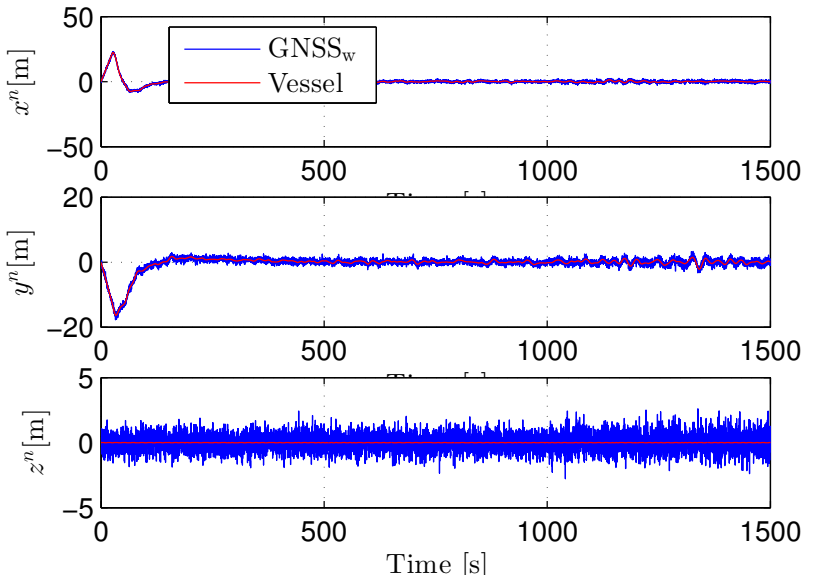

Figure 5.47: Case 5, Detection of horizontal GNSS bias. Weighted GNSS measurements

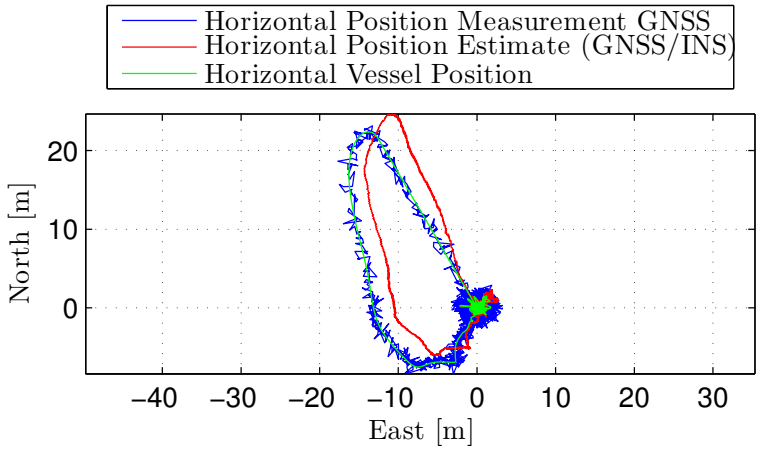

Figure 5.48: Case 5, Detection of horizontal GNSS bias. Horizontal position estimates with horizontal weighted GNSS measurements and the horizontal vessel position

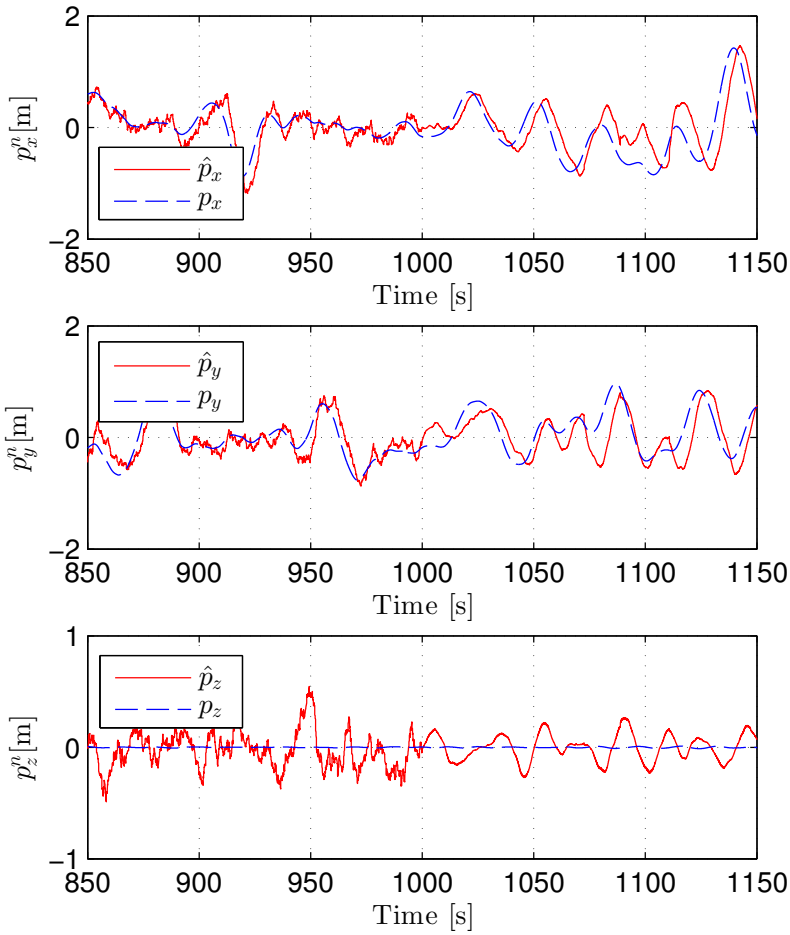

Figure 5.49: Case 5, Detection of horizontal GNSS bias. Zoomed position estimates together with the vessel position

Discussion

The position measurement weighing is based on the variance of the available GNSS sensors. A sensor with low variance will be given trusted where a noisy measurement will be given little credit. Therefor would the spike in the variance of GNSS 1 yield that GNSS 1 is not trusted in the weighing process if the voting algorithm do not detect the bias.

The reason for the increased oscillations seen in the weighted GNSS position, after the bias was introduced, can be explained by the voting algorithm discards and re-enables GNSS 1 multiple times. Since the GNSS is re-enabled and disabled six times is the weighted measurements inherently changed twelve times. Every time a GNSS sensor is disabled is the new weighted position measurement weighted by utilizing the exponential function to ensure smoothness of the calculated position reference. These twelve changes where a biased measurement is utilized six times is the probable the cause weighted GNSS measurements.

This varying weighted GNSS measurements has also other side effects. The increased oscillations in the position estimate, shown in Figure 5.49, is due to the increased oscillations of the weighted changes in the GNSS measurements. The additional phase lag and smoother estimates, on the other hand, is a result of the increased covarince shown in Figure 5.46. This again yield a more restraint correction by the injection term since the gain, $\boldsymbol{K}_{pp}$, is dependent on the reported covariance. The reduced amplitude of the vertical position estimate after GNSS 1 was discarded is due to the same cause. The more restraint correction yield that predicted vertical position estimate is given more credit compared to before the measurement bias was introduced.

If only the horizontal position estimates drift the voting the only possible for this thesis to detect this before the measurements enters the observer of Grip et al. (2013, Submitted). If the vertical measurement is biased would

also the vertical GNSS bias estimates pick up changes yield a discrepancy between the height of the vessel and the height measurements.

5.6 Case 6: Drift and Failure of All GNSS Sensors

This section will study slowly drifting GNSS measurements and the effects such errors entail on the position estimates and the actual vessel position. In order to prevent a drive-off during an DP operation must such sensor drift be detected and kept from propagating to position estimates.

Drifting of all GNSS sensors was enabled after 700 seconds of simulation. The enabled drift rate was set to

$$\boldsymbol{d} = \begin{bmatrix} d_x \\ d_y \\ d_z \end{bmatrix} = \begin{bmatrix} 0.1\,\mathrm{m/s} \\ 0.15\,\mathrm{m/s} \\ 0.25\,\mathrm{m/s} \end{bmatrix}. \tag{5.12}$$

The desired generalized 3 DOF position, as in the previous case studies, was set to

$$\boldsymbol{\eta}_d = \begin{bmatrix} 0 & 0 & 0 \end{bmatrix}^\intercal. \tag{5.13}$$

The controller was enabled after 25 seconds.

GNSS Drift Without Vertical GNSS Bias Estimation

From Figure 5.50 one can see that the horizontal position estimates follows the GNSS measurements after the initial phase of convergence. This is also indicated by the estimation error as seen in Figure 5.52. The estimation error can been seen to oscillate around zero after the position estimates have converged after approximately 300 seconds. Nevertheless, the estimates are faulty after 700 seconds of simulation. This can be seen in Figure 5.53 where

the GNSS measurement is beginning to deviate from the vessel's position. Figure 5.51 shows that the GNSS measurements, together with the position estimates, drifts. This drift is so slow that neither the velocity estimates nor the, observer integral effect, $\boldsymbol{\xi}$ show indication of spikes or other rapid changes seen in Figure 5.55.

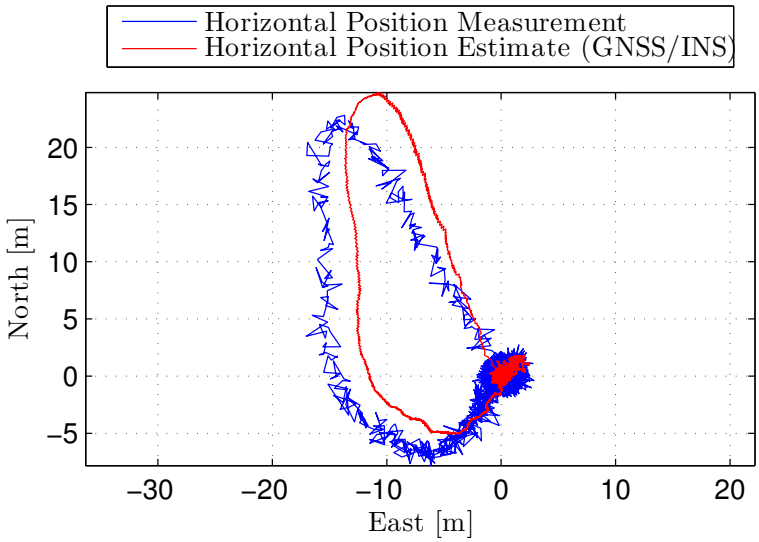

Figure 5.50: Case 6, Drift and Failure of All GNSS sensors. North-East: GNSS Position measurements and position estimates

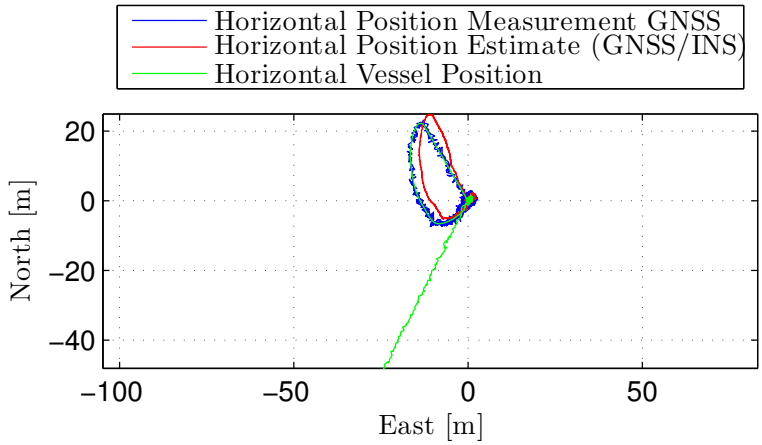

Figure 5.51: Case 6, Drift and Failure of All GNSS sensors. North-East: GNSS Position measurements and position estimates together with actual position of the vessel

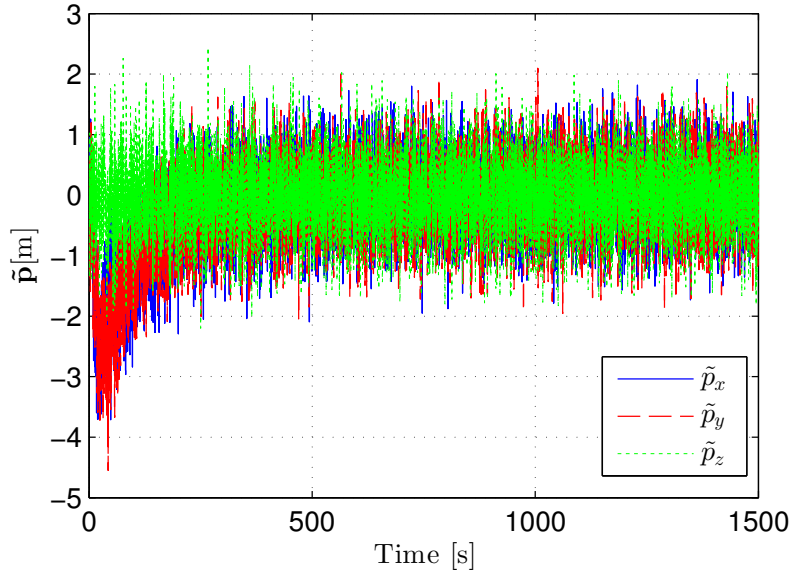

Figure 5.52: Case 6, Drift and Failure of All GNSS sensors. Estimation error, $\tilde{\boldsymbol{p}}$, when the weighted GNSS measurements drift

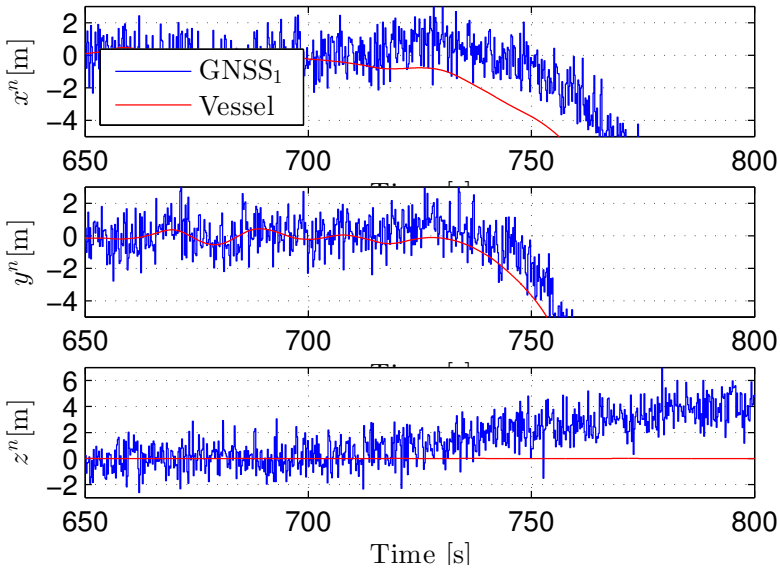

Figure 5.53: Case 6, Drift and Failure of All GNSS sensors. Zoomed Section of the Measurement from GNSS 1 together with vessel's position when the GNSS sensors start to drift.

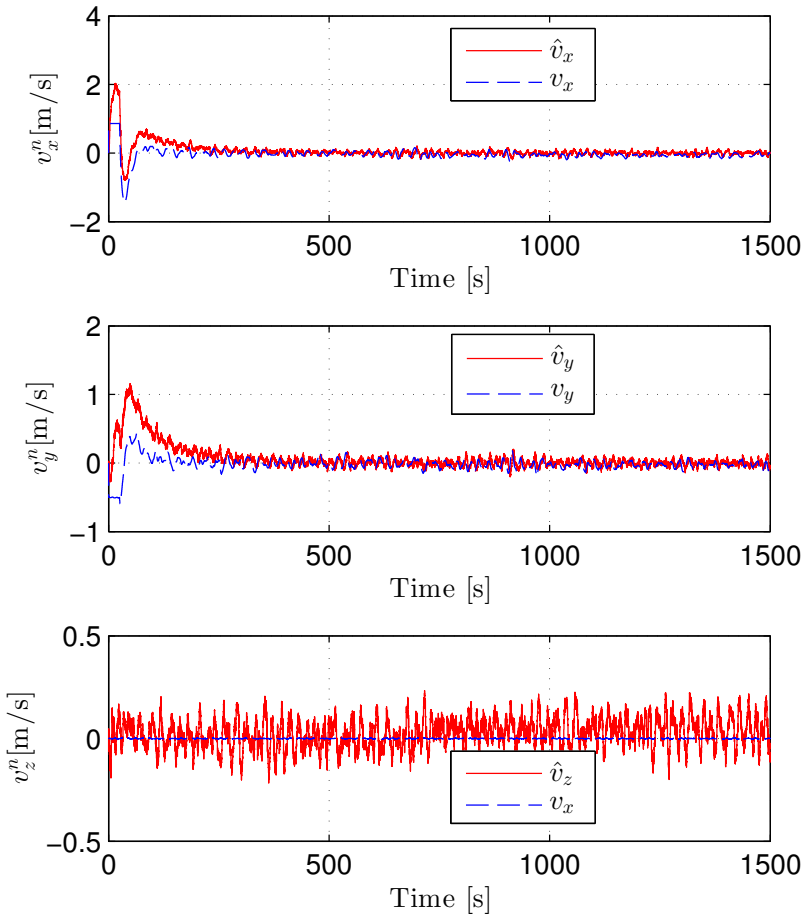

Figure 5.54: Case 6, Drift and Failure of All GNSS sensors. Velocity estimates when the weighted GNSS position measurements are drifting and the drift is not detected.

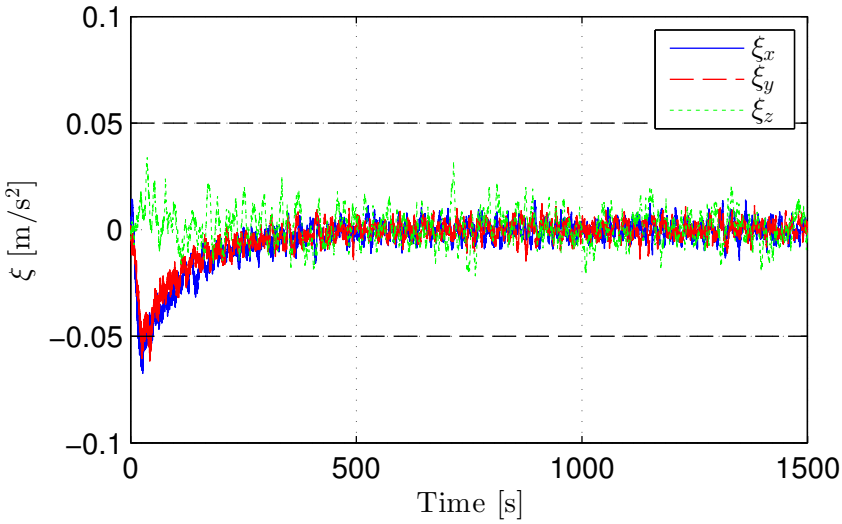

Figure 5.55: Case 6, Drift and Failure of All GNSS sensors. The threshold indicating errors was set to ±0.05.

Discussion

Frank (1990) stated that the estimation error, $\boldsymbol{e} = \boldsymbol{p}_{\text{GNSS}} - \hat{\boldsymbol{p}}$, could be used as residual. However, what can be seen from Figure 5.51 and 5.52 that certain sensor errors can be present without the estimation error or innovation sequence indicate this directly. Moreover, the GNSS drift is so slow that the velocity estimates in Figure 5.54 seems to be unaffected by these errors regard less of the injection term $\boldsymbol{K}_{vp}(\boldsymbol{p}_{\text{GNSS}} - \hat{\boldsymbol{p}})$. This can proably de explained by the fact that $\boldsymbol{K}_{vp} = 0.11\boldsymbol{I}_{3\times 3}$. Thus, is very small. When the drift slow too will no prominent effect of the injection term, $\boldsymbol{K}_{vp}(\boldsymbol{p}_{\text{GNSS}} - \hat{\boldsymbol{p}})$, present it selves in the velocity estimate. As explain above is $\boldsymbol{\xi}$ estimate seen in Figure 5.55 oscillating around zero as expected when the observer of Grip et al. (2013, Sumbitted) has converged. $\boldsymbol{\xi}$ is far from the threshold of ± 0.05, stated by Grip et al, after initial convergence. If the threshold is exceeded is this an indication of discrepancy between the attitude estimates and the position reference. From the fact that the drift was not detected is this indication that additional improvements have to be made to atone such slow sensor drift. In Section 4.5 a filtering of the vertical GNSS measurements was proposed, in the signal check procedure, to combat the problem of drifting GNSS measurements.

GNSS Drift With Vertical GNSS Bias Estimation

By applying the vertical GNSS bias detection algorithm from Section 4.5 the resulting the vertical GNSS bias estimates shown where obtained according to Figure 5.56.

Moreover, Figure 5.56 shows that the GNSS drift is detected for all sensors at simulation time 717.2 seconds. When the vertical GNSS drift was detected were all GNSS measurements where disabled since all sensor was deemed unreliable. The INS position and velocity observer requires aiding

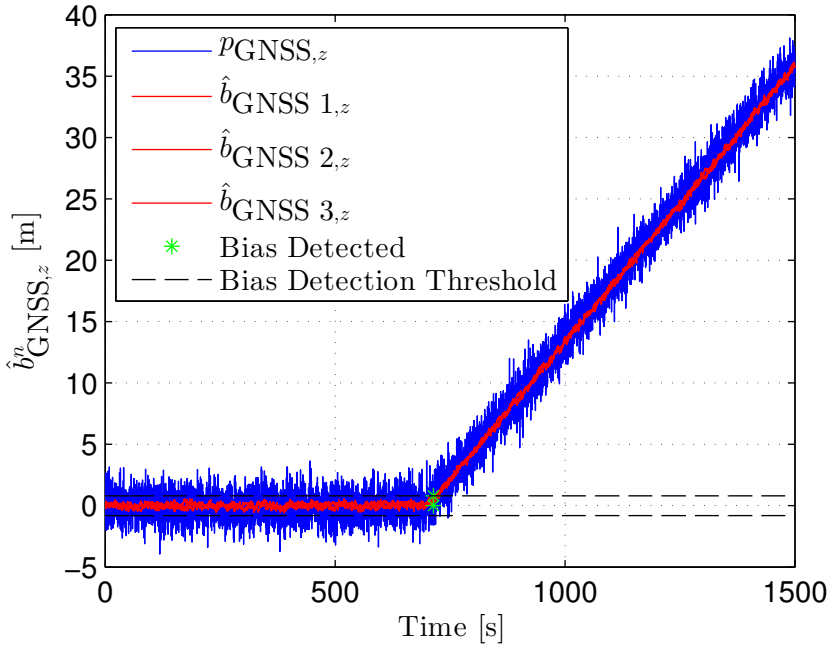

Figure 5.56: Case 6, Drift of all GNSS sensors. Vertical GNSS bias estimate. 21.7 seconds after the GNSS drift was introduced is the vertical drift detected.

measurements to prevent drifting estimates as stated in Section 2.2. Figure 5.57 shows this drift due to lack of correction measurements.

One can observer that the horizontal position estimates coincide with the desired reference position, while the actual vessel positions drifts.

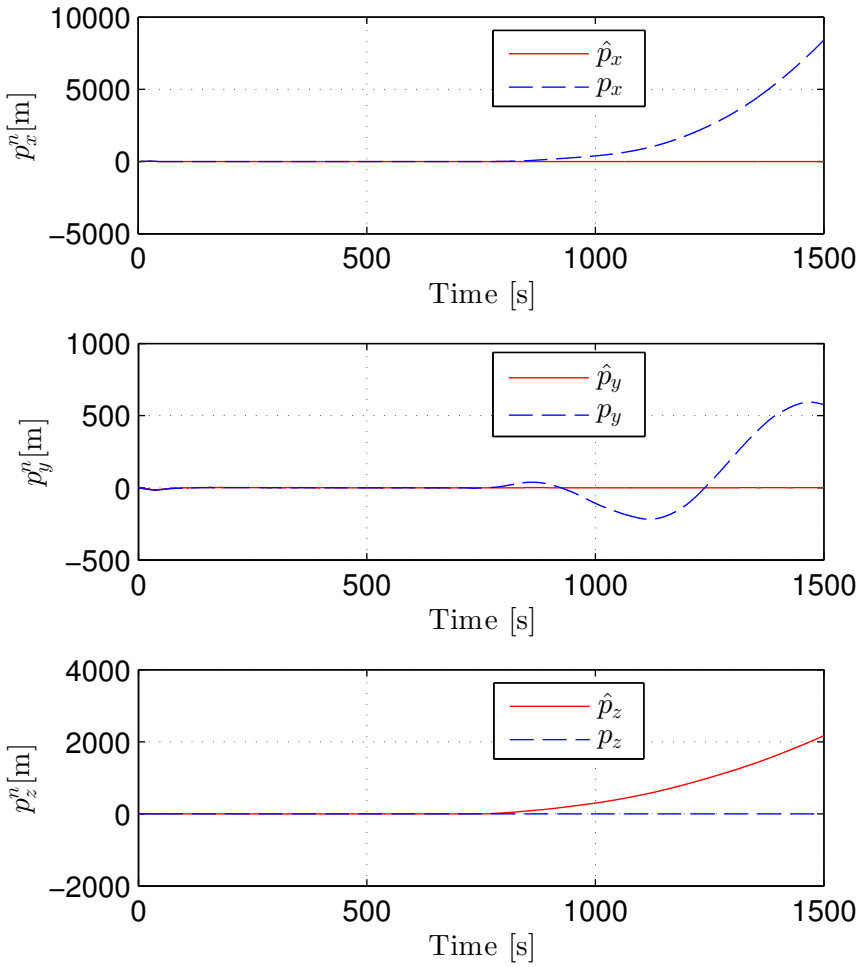

Figure 5.57: Case 6, Drift and Failure of All GNSS sensors. Position estimates when the GNSS measurements are disabled

Discussion

The reason for the drifting position estimates shown in Figure 5.57 is probably due to the inaccuracies in the system. One of these inaccuracies is the attitude estimates and especially the heading estimate. Even as the heading estimates are of a high qulaity as shown in Figure E.6 when no fault are present will even the smallest error propagate to position estimate trough two numerical interrogations at 100 Hz since

$$\ddot{\boldsymbol{p}}^n = \boldsymbol{R}_b^n(\hat{\boldsymbol{q}})(\boldsymbol{f}_{\text{IMU}}^b - \boldsymbol{b}_a^b) + \boldsymbol{g}^n \tag{5.14}$$

when no observer injection is utilized.

The probable reason for the total control system to maintain the position estimates at north-east position (0, 0) is due to the controller increases thrust quite drastically. This is supported by the thrust forces and moments shown in Figure 5.58. In fact, the thrust in surge is increased from approximately $\pm 2 \cdot 10$kN to the region of $\pm 1.6 \cdot 10^4$kN. This drastic increase in commanded thrust, seen in Figure 5.58 would probably not be possible to realize in a real-life position system due to physical constraints posed on the propulsion system. At least not is such short time frame. From this it might be of interest to monitor the propulsion and power managements system and utilized this in a fault-tolerant observer design to increase the robustness and the fault detection capability in event of a drifting position references.

These result also indicates that automatic control is not possible when all position references are lost. At least not for this 100 Hz INS based observer. Hence, manual control is the only option if all GNSS sensors seems to be drifting given that no other position reference is available such as HRP systems. In Det Norske Veritas (2011) is one the following requirements for DP control systems stated: *402: Manual thruster control mode shall be available at all times, also during all failure conditions in dynamic positioning or independent joystick control systems(...).* Thus, this recommendation would

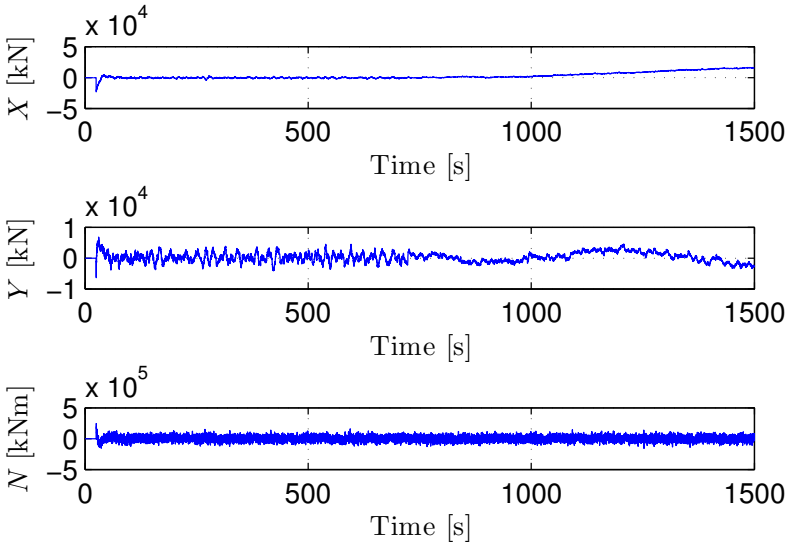

Figure 5.58: Case 6, Drift and Failure of All GNSS sensors. Thrust from the controller in surge, sway and yaw

comply with current rules and regulation related to DP operations.

Instead of only detecting the GNSS drift (fault detection) could one also hope to atone for error directly by estimating the drift in all three degrees of freedom. Since one cannot necessarily predict the horizontal drift when no other measurements are available one have to rely on the vertical drift estimates since this degree of freedom averages around zero for floating vessels. The vertical GNSS bias estimate could in theory be utilized to correct all DOFs if the vertical horizontal measurements drifted with the same amount. A.i the GNSS drift rate was the same same in all three degrees of freedom. This is not necessarily so. The coupling of between the vertical accuracy and the horizontal accuracy of GNSS can be obtained from the GDOP stated in Section 2.3. However, since the GDOP parameter is reported by the receiver can this also be faulty. Grip et al. (2013, Submitted) stated that the HDOP parameter is a lagging indicator of a potential GNSS problem.

Hence, was it deemed unsafe to assume that the GNSS drift had the same rate in all DOFs. Because of the sensor drift was simulated with different drift rate for each degree of freedom. Furthermore if such drift is caused by multipath, differential link errors or even satellite clock failure, as described in Section 2.3.2, can the drift be a unpredictable and hence difficult to monitor. According to Vik (2012) is the dominate error source for dGPS system multipath. All in all it would seem difficult to estimate the drift of horizontal GNSS measurements without any other independent source for position reference.

Even though the vertical GNSS bias estimates was not deemed sufficient to correct the drift of the horizontal measurements can on still see from Figure 5.56 that the vertical GNSS drift is estimated correctly with the purposed Butterworth filter. A possibility to increase downtime when the GNSS is deemed inaccurate could be reduced by feedback both the estimated drift and GNSS status calculated by the fault-tolerant observer the back to GNSS, as shown in Figure 5.59. Then appropriate fault-accommodation software could discard, for instance, differential corrections to check if these are the error sources. Starting to calculate a new position, based on other satellites in view, is also an other possibility when vertical GNSS bias is detected. The latter strategy might remove clock errors, or other error sources, provided by one specific satellite.

An other possibility is to monitor the GNSS measurments by applying fault detection methods directly to the Kalman fitler calculated GNSS solution. Such methods as Receiver Autonomous Integrity Monitoring (RAIM) can be utilized. The common denominator for RAIM-based methods consist of some kind of self-constancy check. For more on RAIM can Parkinson and Spilker (1996b) be advised.

The robustness of the bias estimate of the vertical component of the GNSS measurement is also dependent on the heave motion of the vessel. Thus, the threshold must by regarded as a tuning parameter. Utilizing the accelerom-

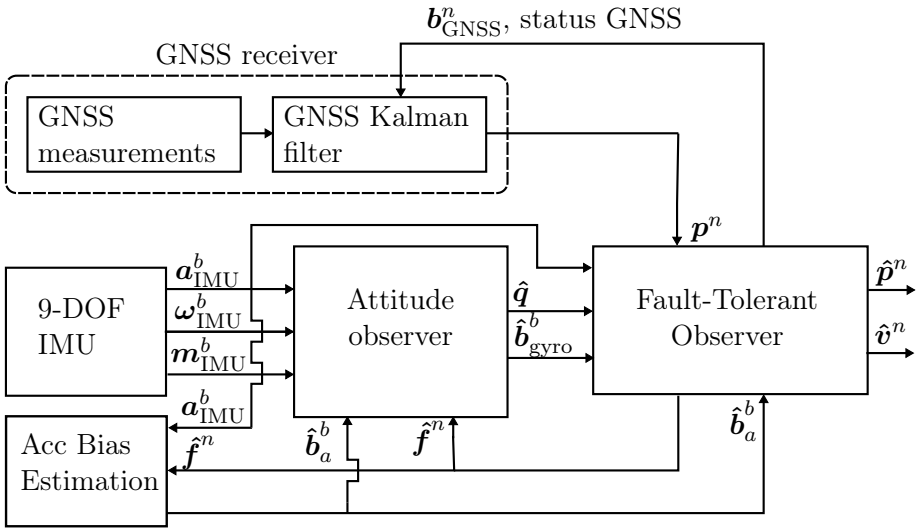

Figure 5.59: Overview on how the detected GNSS bias could be reported back to the receiver.

eter measurements for on-line tuning of this threshold might be a possible field of study to introduce a adaptive threshold to increased robustness and reliability while false alarms are avoided.

5.7 Case 7: Accelerometer Failure

This section will cover the event of the accelerometer failure. Such event requires another source of acceleration information when utilizing INS. This is due to the fact that these measurements are utilized in both the attitude and integration observer of Grip et al. (2013, Submitted) as reference vector and acceleration information respectively. As presented in Section 4.6 is the nonlinear passive observer of Fossen and Strand (1999) utilized as basis to obtain a estimates of the acceleration according to

$$\hat{\boldsymbol{f}}_{\text{model}} = \begin{bmatrix} \hat{\dot{\nu}}^b_x & \hat{\dot{\nu}}^b_y & -g \end{bmatrix}^\intercal$$

The acceleration estimate is a.i based upon the relative acceleration estimate, $\dot{\hat{\boldsymbol{\nu}}}_r^b$, and the acceleration component from the current estimate

$$\dot{\hat{\boldsymbol{\nu}}}_c^b = -\boldsymbol{S}(\omega_{b/n}^b)(\boldsymbol{R}_b^n(\hat{\psi}))^\intercal \hat{\boldsymbol{b}}^n. \tag{5.15}$$

Together, these two estimates yield the total acceleration estimate as stated in Section 4.6.

The case study involved first a change in position at 1500 seconds according to

$$\boldsymbol{\eta}_d = \begin{bmatrix} 0 \\ 0 \\ 0 \end{bmatrix} \overset{t=1500}{\rightarrow} \boldsymbol{\eta}_d = \begin{bmatrix} 100 \\ 100 \\ 0 \end{bmatrix}. \tag{5.16}$$

Then, at 2500 seconds, a change in heading was performed according to

$$\boldsymbol{\eta}_d = \begin{bmatrix} 100 \\ 100 \\ 0 \end{bmatrix} \overset{t=2500}{\rightarrow} \boldsymbol{\eta}_d = \begin{bmatrix} 100 \\ 100 \\ 40^\circ \end{bmatrix} \tag{5.17}$$

to see if such changes of position and heading would effect the current velocity estimate and hence change the acceleration provided by the nonlinear passive observer. The controller, as in the previous case studies, was enabled after 25 seconds.

Fault Free Accelerometer

First an fault free case will be shown for benchmarking purposes. The resulting horizontal position estimates were obtained and is shown shown in Figure 5.60 together with the GNSS measurements and the vessel's position.

Figure 5.61 shows the measured acceleration versus the estimates. One can observer that the acceleration estimates from the vessel model based observer

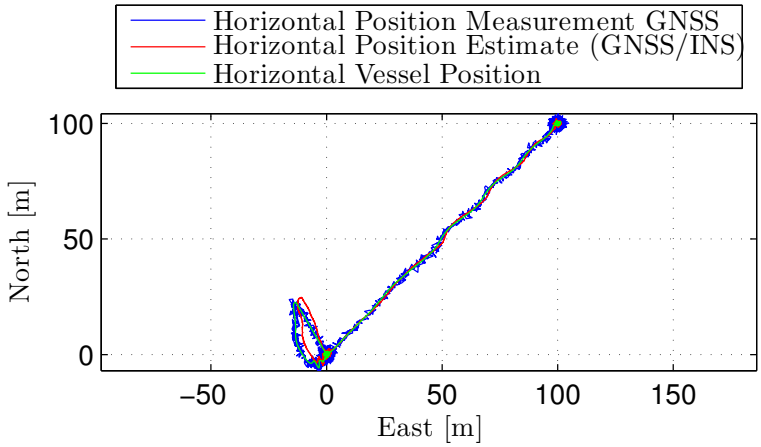

Figure 5.60: Case 7, North East position estimate of vessel with position measurements and actual vessel position

lies around the mean of the acceleration measurements provided by the IMU. However, the vessel model provides an acceleration with considerably lower amplitude. Figure 5.62 shows the estimates of the model uncertainty is present in the kinematics. One can see that estimates slowly converge to the actual current.

The relative velocity estimates are presented in Figure 5.63. One can see that the velocity in surge and sway is estimated to be non-zero, while the yaw rate estimate, $\hat{r}$ fluctuates around zero degrees per second when the vessel is not rotating. A change in the estimates are observed when the vessel changes horizontal position at time equals 1500 seconds. Moreover, the relative velocity estimates also changes at time equals 2500 seconds.

Also in this case the position and heading estimates from the observer based upon Grip et al. (2013, Submitted) are presented. The estimates can be found in in Figure 5.69 and Figure 5.70 respectively. These are of the same quality as in previous cases. One can observe from the position estimates that these follows the vessel's position well even in the event of change in

position. .

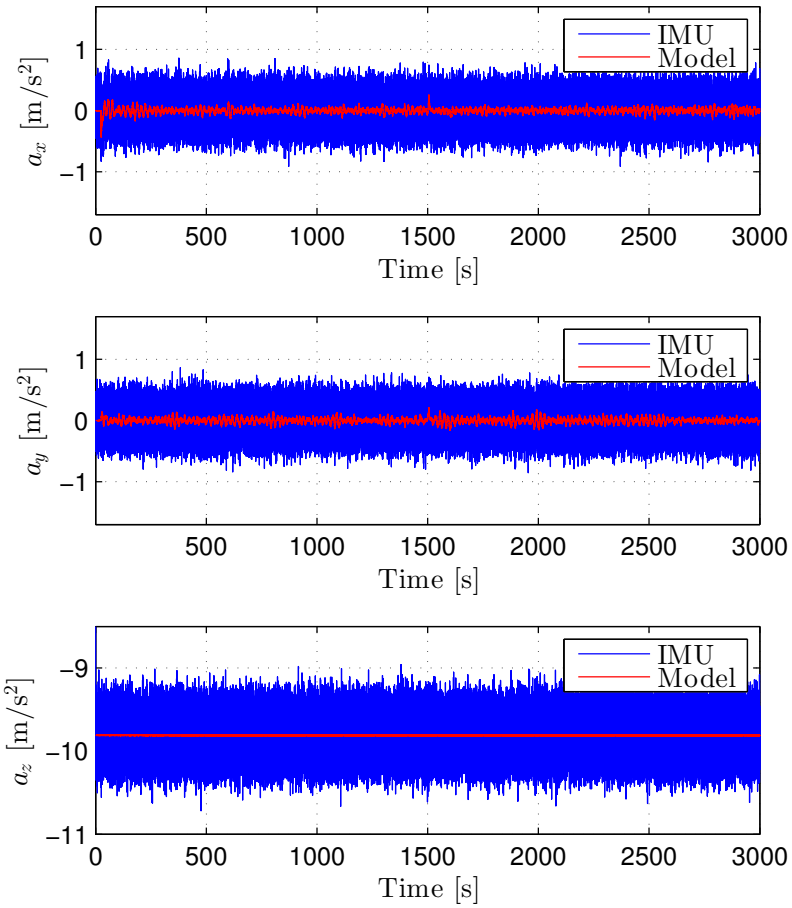

Figure 5.61: Case 7, Accelerometer vs. model acceleration when acceleromter fault has occurred.

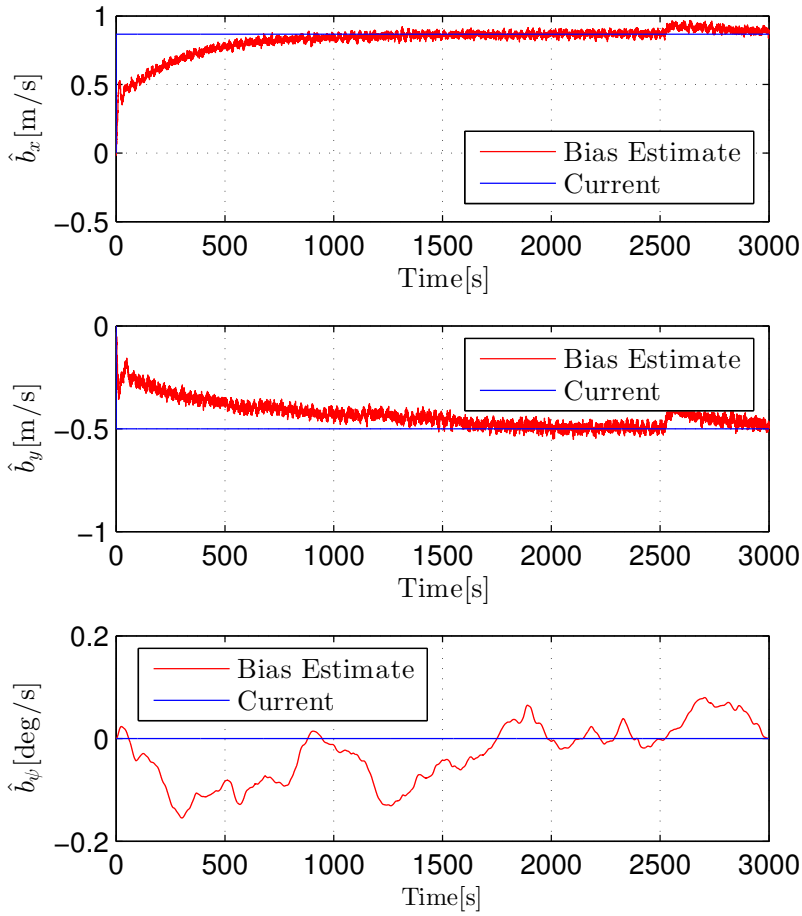

Figure 5.62: Case 7, Current velocity estimate when no acceleromter fault has occurred.

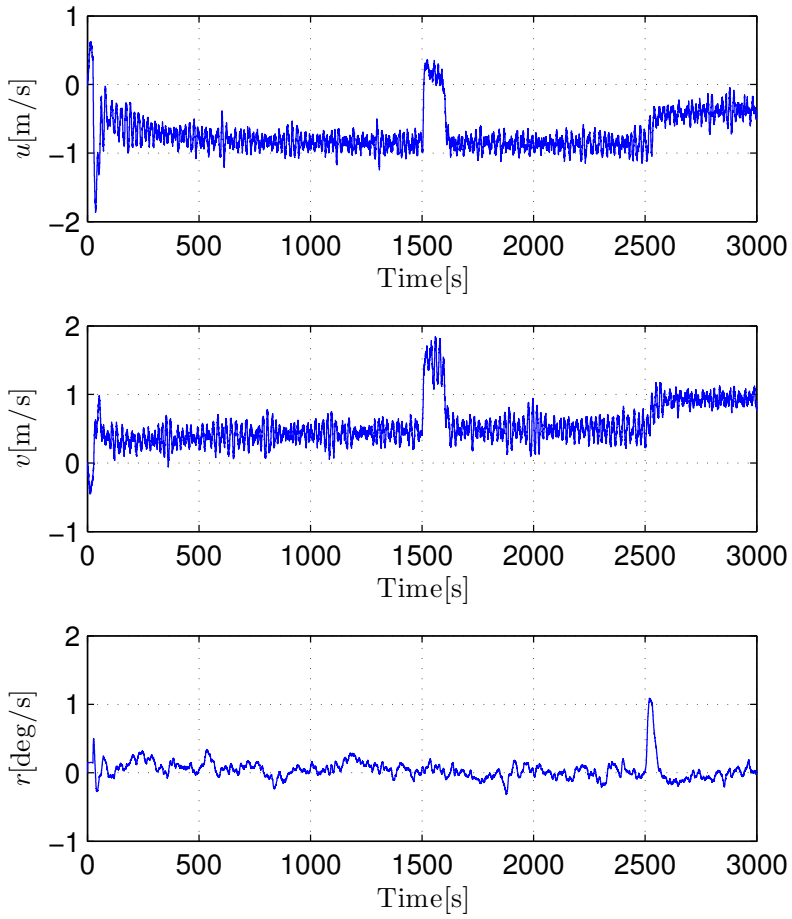

Figure 5.63: Case 7, Relative velocity estimate when no acceleromter fault has occurred.

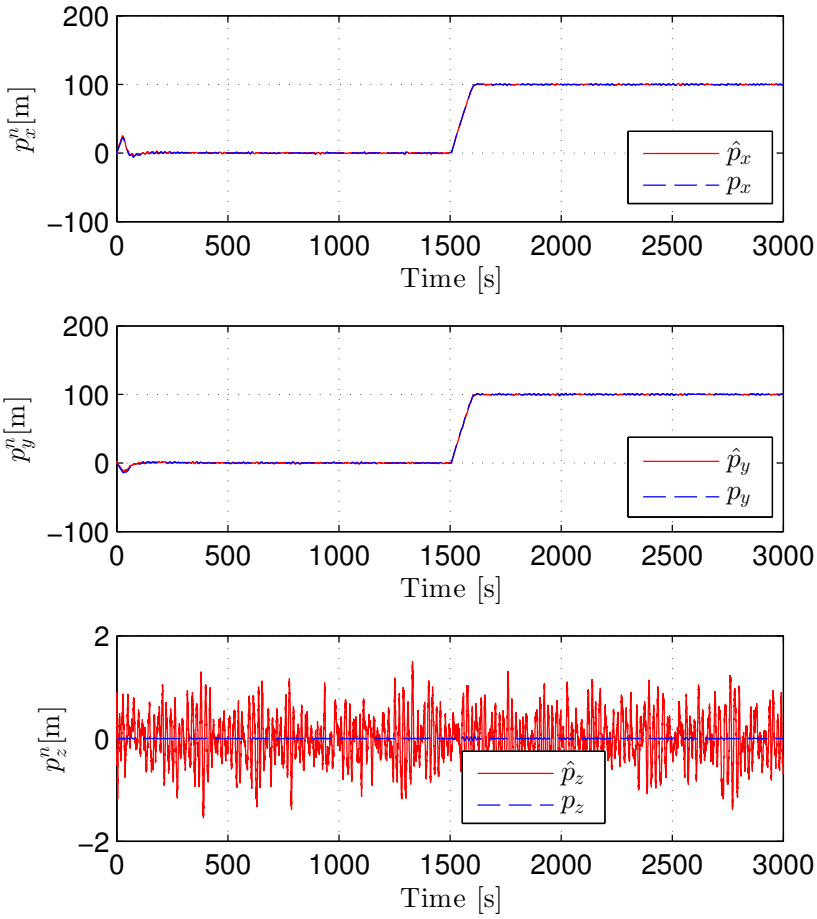

Figure 5.64: Case 7, Position estimates together with vessel's position with no accelerometer fault.

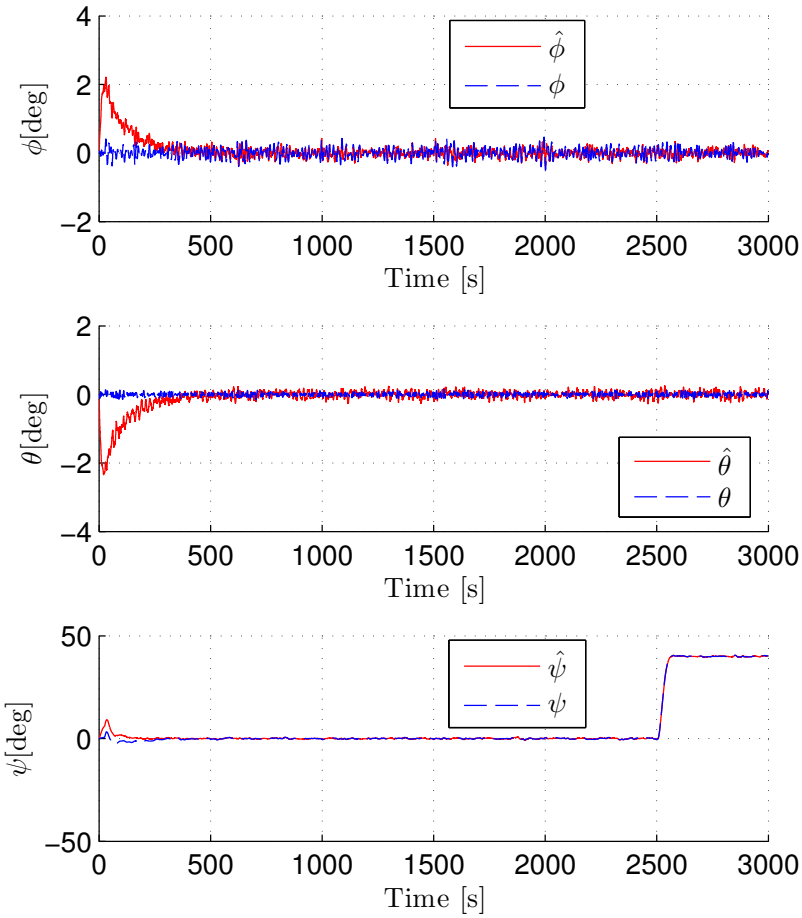

Figure 5.65: Case 7, Estimated and actual attitude of the vessel using Euler angles as representation when no accelerometer fault has occurred.

Discussion

A reason for the lower amplitude of model based acceleration might be that the measured control input was obtained without any measurement noise. The model based estimator of Fossen and Strand (1999) also employs wave filtering. Thus, much of the oscillatory motion is suppressed by the passive observer. In opposite will the accelerometer measurements has white noise components and picks up acceleration from wave-induced forces.

The slow dynamics of the estimates from the nonlinear passive observer is not unexpected because of the chosen bias model was model as

$$\dot{\boldsymbol{b}} = \mathbf{0} \tag{5.18}$$

equivalent to

$$\dot{\boldsymbol{v}}_c = \mathbf{0}. \tag{5.19}$$

Furthermore, this was how the current was model in the simulator. See, Chapter 3 for details. Moreover, one can observe that the current estimate is not significantly affected by the change of position. This is probably due to the position estimate of the nonlinear passive observer coincides with the GNSS measurements. However, the current estimates changes when the vessel rotates. This can possibly be explained by the change in estimated relative velocity at the given time, since both the relative velocity and current estimates are utilized in the update of the position estimate, of the nonlinear passive observer. When the relative velocity estimates in Figure 5.63 stabilizes, at time approximately equal to 2600 seconds, can it be seen from Figure 5.62 that the current estimates again begin to converge to the correct values. This however, happens slowly. A possible way to combat this problem is to increase the gain associated with the current/bias estimate.

Figure 5.63 shows that the relative velocity estimated non-zero velocities in

surge and sway even while the vessel was stationary. This is not unexpected. When the vessel is stationary the combined relative and current velocity should be equal to zero. On the other hand was the relative angular velocity estimate in yaw fluctuated around zero degrees per seconds. This is also not unexpected since the current applied by the simulator is irrationality. Thus, only affects the vessel in surge and sway. The change in the estimated relative velocity at time equals 1500 is due to the vessel changes horizontal position. The change in the relative velocity estimates at 2500 seconds is due to the rotation of the vessel. In surge and sway will this effect how the current yields velocity contribution in respective BODY frame axis. The estimated relative velocity is yaw, $\hat{r}_r$ peeks when the vessel rotates. This is as expected.

Fault in Accelerometer at Time Equals 2000 Seconds

The same observer was ran in parallel when an accelerometer failure occurred at time equals 2000 seconds. The results are shown in Figure 5.66 - Figure 5.68. From Figure 5.66 can one observe that at time 2000 seconds was the acceleration from model based estimator utilized as the acceleration measurement. The current estimate and relative velocity estimates are shown in Figure 5.67 and Figure 5.68 respectively. Comparing Figure 5.67 with 5.62 can one see the current / bias estimates are very similar both with and without accelerometer failure. Furthermore, by comparing Figure 5.68 and Figure 5.63 one can also observe a striking resemblance of the relative velocity estimates with or with fault accelerometer.

The position and heading estimates from the Grip et al. (2013, Submitted) are presented in Figure 5.64 and 5.65 respectively whereas the position estimate when the acceleration from the vessel model is utilized is shown in Figure 5.69. The estimated attitude, utilizing Euler angles as attitude representation, is shown in Figure 5.70. One can see that the position estimates

are unaffected by utilizing the estimated acceleration. This is also shown in Figure 5.71 where the position estimates coincides well with actual vessel position. However, the magnitude of angle roll angle, ψ, as increased both before and after the rotation compared with the fault free simulation above. Not only have the estimates changed, but also the actual roll of the vessel is fluctuating more in this simulation.

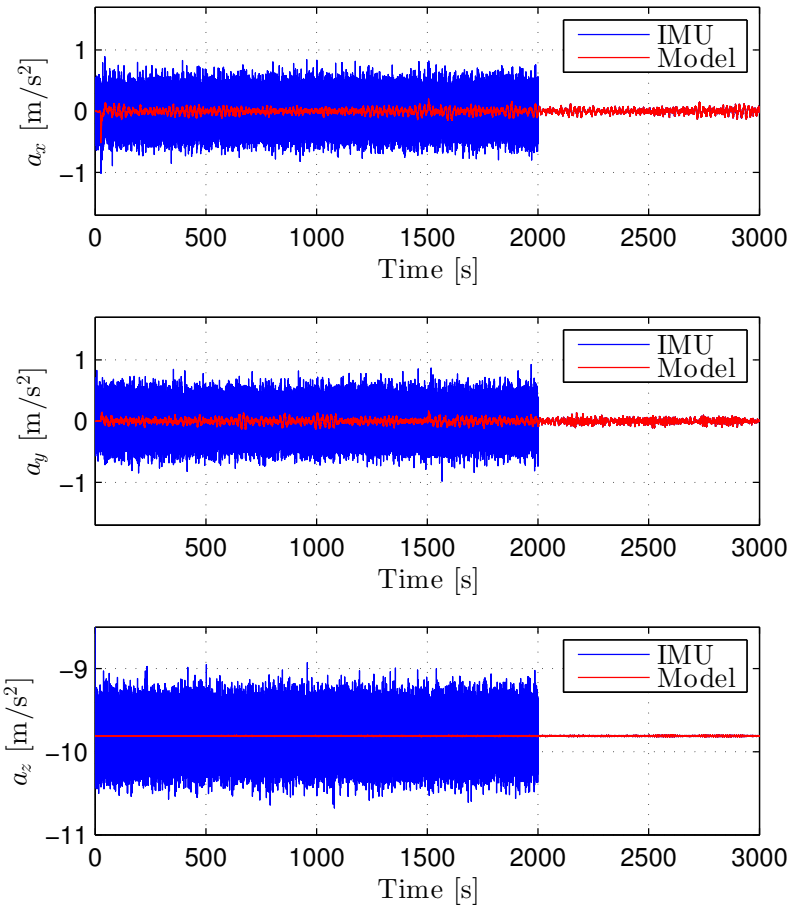

Figure 5.66: Case 7, Utilizing acceleration from vessel model. Accelerometer vs. model acceleration when acceleration from model is utilized after 200 seconds.

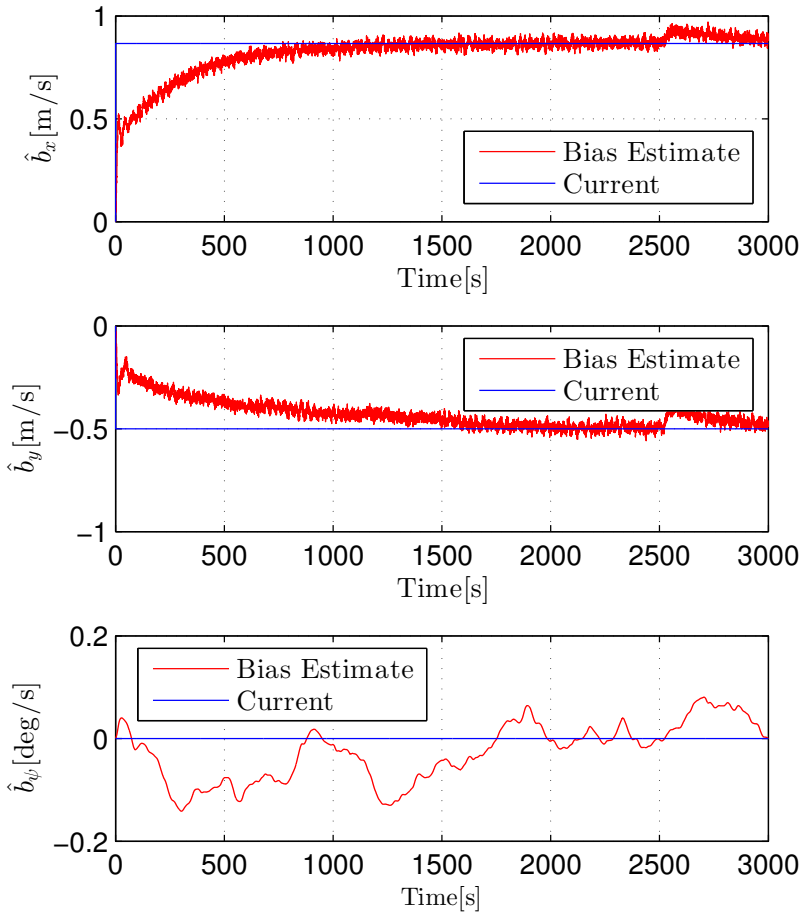

Figure 5.67: Case 7, Utilizing acceleration from vessel model. Current velocity estimate when when acceleration from model is utilized after 2000 seconds.

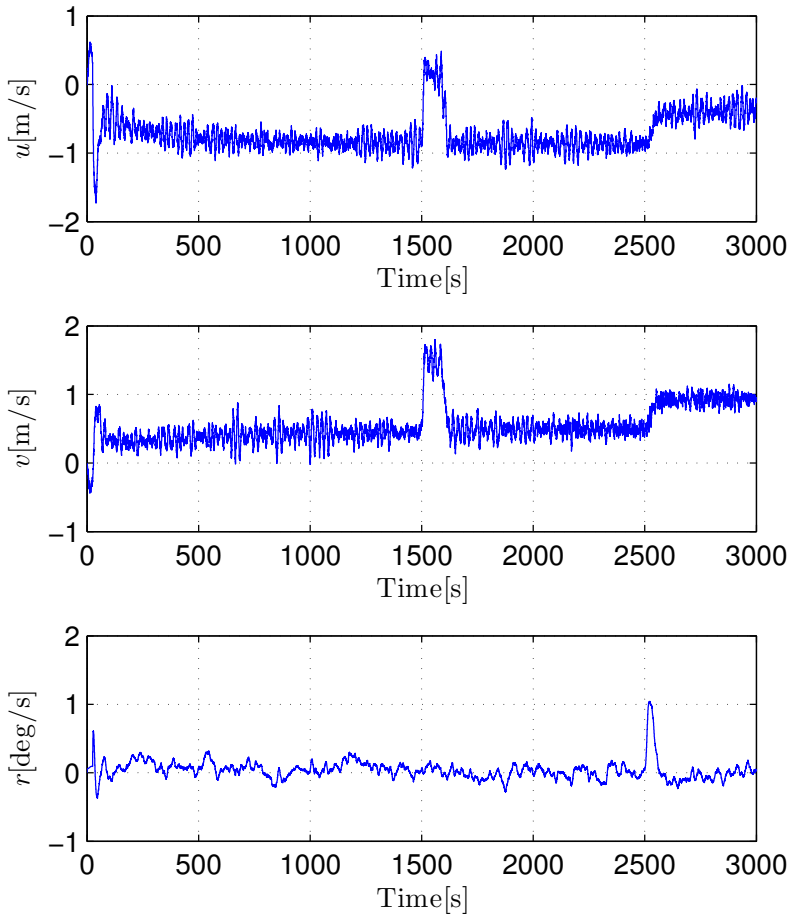

Figure 5.68: Case 7, Utilizing acceleration from vessel model. Relative velocity estimates from model based observer when acceleration from model is utilized after 2000 seconds.

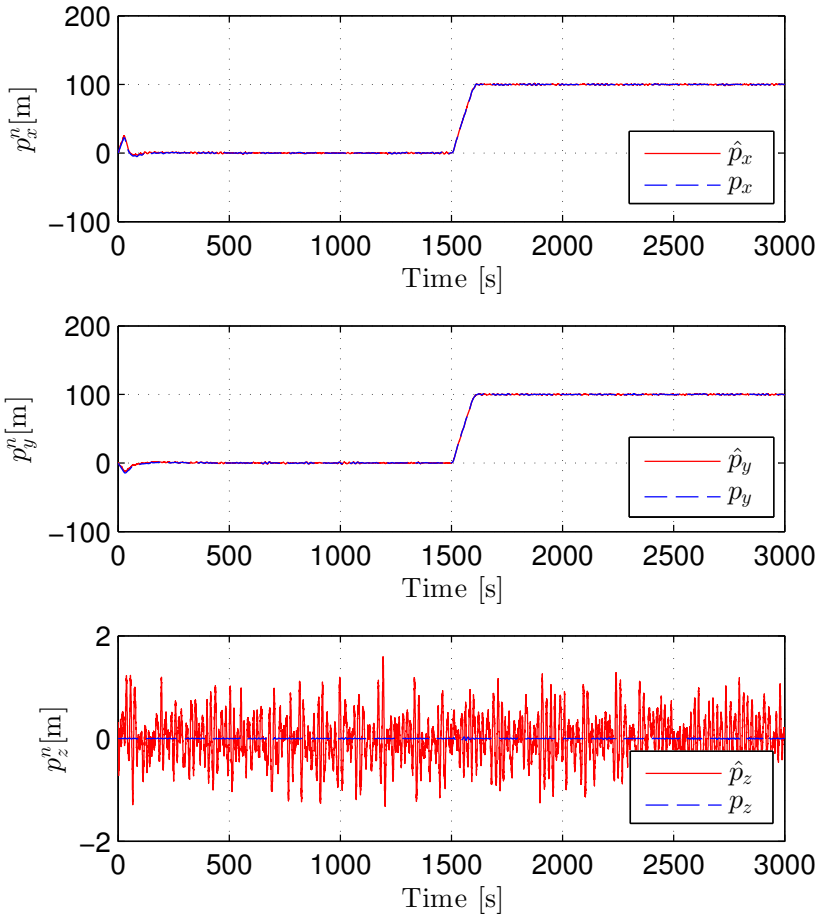

Figure 5.69: Case 7, Utilizing acceleration from vessel model. Position estimates together with vessel's position when acceleration from model is utilized after 2000 seconds.

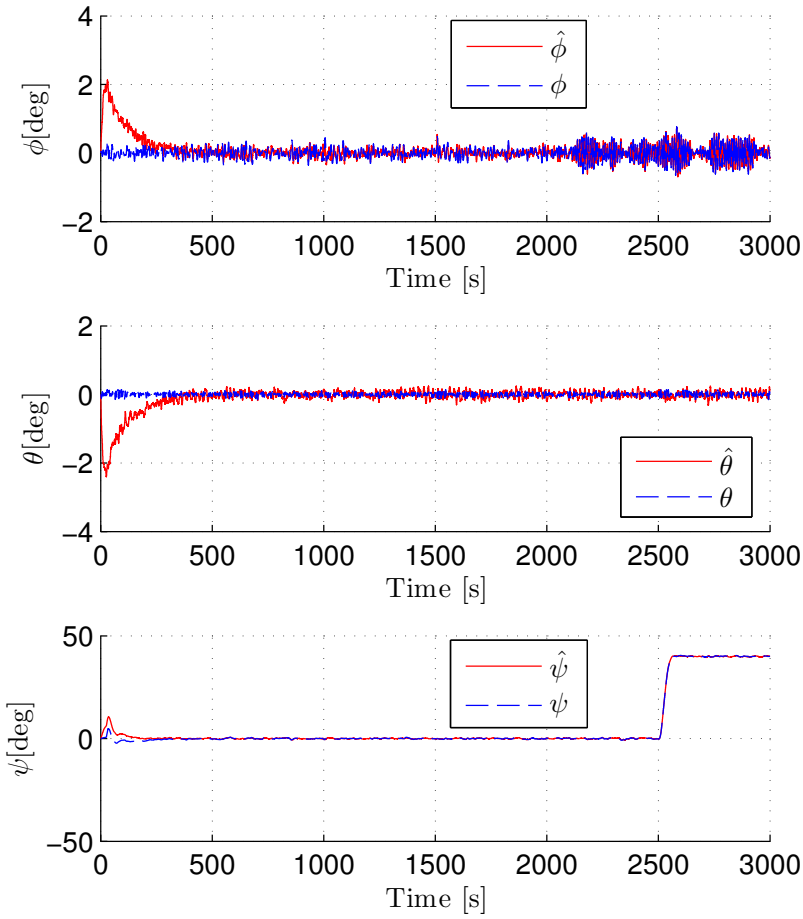

Figure 5.70: Case 7, Utilizing acceleration from vessel model. Estimated and actual attitude of the vessel using Euler angles as representation when acceleration from model is utilized after 200 seconds.

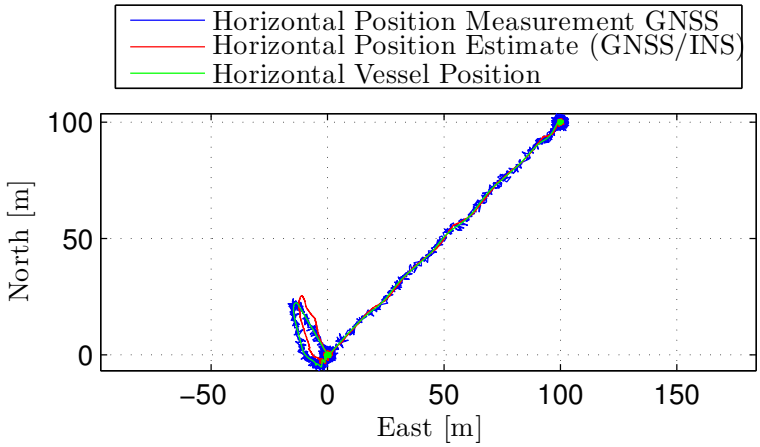

Figure 5.71: Case 7, Utilizing acceleration from vessel model. North-East position estimates together with the weighted GNSS measurements and the vessel's position when acceleration from model is utilized after 2000 seconds.

Discussion

The result from both simulations above show that the acceleration estimates from a vessel model based observer can be utilized as redundant acceleration information in an INS system for marine vessels. This substantiated by the fact that the estimates from the model based observer do not change even when the acceleration information, utilized by the INS/GNSS observer, changes. This is because the position estimates of the Grip et al. (2013) observer is little affected by those changes. The controller inputs are calculated base upon these position estimates in feedback. Since the position estimates are not effected by the change in the acceleration information, will no changes propagate to the vessel model based observer, where the control input is utilized.

Even though the position estimates are quite similar in both simulation is an increase in both actual and estimated pitch observed when the estimated acceleration is utilized. The changes in roll may be induced by the controller. There exist an sway-roll and yaw-roll coupling in the 6 DOF inertia matrix, seen in Appendix D, utilized in the vessel simulator. Sway and yaw are parts of the control objective. The change in the acceleration information could yield some changes in the velocity estimates. These again could affect the computed controller input since the estimated velocity also is utilized by the DP controller, posed in (2.46). It should be mentioned that the observed changes in roll are so small that these would probably not inflict any problems regarding operational use of the semi-submersible. This is backed up by the fact that the roll angle never exceeds ± 1 degree, as seen in Figure 5.70.

The estimated acceleration provided good quality estimates when the current was estimated in the NED frame. In real life this would not necessarily work so well. The result might be affected by wind forces and moments acting on the vessel. Because of this, it might be better to estimate the

current and wind forces in the kinetics as original proposed by Fossen and Strand (1999). Also possible uncertainties in the available 3 DOF inertia and damper matrices might affect the quality of the estimated acceleration. In this thesis was the 3 DOF matrices extracted directly from the 6 DOF matrices utilized in the vessel simulator.

Measurement of actual control inputs also difficult to obtain accurate. In this thesis was it assumed that the calculated thrust was measurable and provided as calculated by the controller. Since no thrust-losses are not taken in account, in this thesis, is it difficult to conclude on the robustness of the quality regarding the acceleration estimates. The model based acceleration should be tested in multiple weather conditions and other situations where thrust-losses might change, before such methodology is used as redundancy regarding the accelerometer in an INS context.

Because of all the uncertainties regarding the 3 DOF matrices and the control input, $\boldsymbol{\tau}$, might the change of acceleration information result in unwanted transient behavior, even though this was not observed during the simulations of this thesis. In a real-life operation should such changes be done with care. One possible strategy to pursue is bumpless transfer, such as Zaccarian and Teel (2002), from acceleration measurements to the estimated acceleration provided by the model based observer.

In this thesis is the change of acceleration source performed when the accelerometer reports a fault. In a real-life operation should this change also be done when a larger bias or sensor freeze is detected. Therefor could accelerometer bias estimation be utilized in a fault detection strategy. One should also work on freeze detection, as done in Section 4.5 where GNSS monitoring was carried out.

5.8 Overall Discussion

In real life none one the GNSS antennas would provide measurements in CG as model in the simulator in thesis. Hence, these measurements have to be transformed to a given CO, such as the CG and compensated for the roll and pitch motion. This can be done be utilizing theory from Fossen (2011, Ch. 3.2 and 7.5.4) and the attitude estimates from Mahony et al. (2008) or Grip et al. (2012a).

The assumption regarding pre-calibration of the accelerometer and magnetometer might not be valid over time. For instance might the magnetic field change due to induced magnetic field from electric components in the vicinity of the IMU. A semi-submersible rig is a large electric consumer, thus this is very likely to happen if not handled properly. Hence, it would be recommended to utilize a compass in conjunction with the heading estimate, from the Grip et al. (2012a) attitude observer, to obtain a heading estimate to be utilized for feedback purposes. This is also required, as seen in Appendix B.7 where at least two gyro compasses are required to fulfill the DP-class 3 requirements.

At start up of the attitude observer or after failure scenarios can for instance the QUEST algorithm be utilized to obtain initial values. By doing so, one may provide a warm start to the observer and hopefully will the correct attitude be determined faster since the initial attitude error is low.

Time-varying Observer Gain

The choice of exponential decaying gains during start up of observer would seems beneficial to speed up the convergence of the PVA estimates. In an event of sensor failure will such tuning results in lower converges time than without such functionality. This can for instance increase recovery time of the DP system if all GNSS sensors are lost e.g. in event of scintillations. A

general increase in the nominal gains could be feasible if wave filtering was added to the observer of Grip et al. (2013). This to prevent the wave-induced motion of the vessel to propagate to the position estimates. However, this would require addition research.

As discussed in previous section had the variance dependent gain, related to the position estimates, several advantages. However, more work should be put into such strategies in order improve the performance and fault-tolerance even more. Stability analysis of the Grip et al. (2013, Submitted) observer with time-varying gains should also be carried out.

Voting

The voting algorithm developed in this thesis could be extended to include the position estimate to validate this GNSS measurements. Utilizing statistical methods to determine the likeness of a correct or erogenous measurement may also be an possibility.

Low Pass Filtering of the Vertical GNSS Measurements

As seen in the Section 5.6 can low-pass filtered GNSS measurement provided extra capability in detecting drifting GNSS measurements. Even though only the vertical measurements drift's are detected, could such detection prevent an drive-off. However, the complexity of the fault-tolerant observer increases with such functionality. Differentiating between an sensor freeze must be done so the operator have the correct information available. The sea state also has to be taken in account when the drift detection threshold is set. Methods for changing this threshold online dependent on the heave motion should be investigated.

Utilization of the Vessel Model in a Fault-tolerant Design

The results related to the redundant acceleration provided by vessel model seen in Section 5.7 was good, but the robustness of the method is questionable. The model parameters might be erroneous. The same goes for the control input, $\boldsymbol{\tau}$, as explained in Section 5.7. Another possible weakness of the methods can be seen from Figure 4.5. The weakness comes from fact that the accelerometer affects the heading estimate thought the injection term, $\hat{\boldsymbol{\sigma}}$. This can be seen from the attitude estimate differential equation

$$\dot{\hat{\boldsymbol{q}}}_b^n = \boldsymbol{T}(\hat{\boldsymbol{q}}_{\boldsymbol{b}}^{\boldsymbol{n}})(\boldsymbol{\omega}_{b/n,\mathrm{IMU}}^b - \hat{\boldsymbol{b}}_g^b + \hat{\boldsymbol{\sigma}}) \tag{5.20}$$

as given by (4.33). Since $\hat{\boldsymbol{\sigma}}$ might be biased by an erroneous accelerometer. This may result in an erroneous attitude estimate. This attitude estimate is further utilized as heading reference in the model based observer. The end result of this can yield an erroneous acceleration in sway caused by sway-yaw coupling in the mass matrix, $\boldsymbol{M}$[1], as seen in Appendix A. Therefor should another source of heading information be utilized. An possible solution is shown in Figure 5.72 where a gyro compass is introduced. Since a compass is required by Det Norske Veritas (2011) will this not yield additional cost if the total system is supposed to be utilized in a DP operation.

Monitoring of the acceleration measurements should include bias estimation, freeze and wild-point detection. This might done by accelerometer bias estimation and monitoring the changes in $\boldsymbol{\xi}$, since the accelerometer measurements and bias estimates directly effects the change in $\boldsymbol{\xi}$, as can be

[1]Sway-yaw coupling often exist in the linear damper matrix, D, as seen in Fossen (2011). However, not her as shown in Appendix A where the damper matrix is a diagonal.

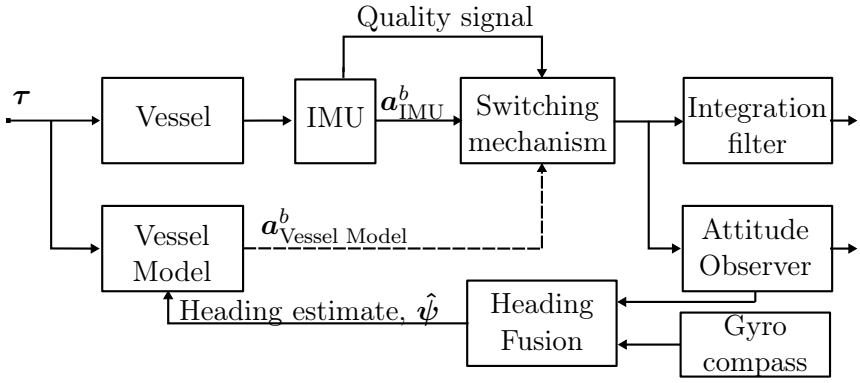

Figure 5.72: Overview of the suggested change in how the redundant acceleration estimate is obtained. Some heading fusion should be performed based upon the attitude estimate and some external sensor providing heading information. This sensor could be a gyro compass.

seen from (4.32) and

$$\begin{aligned}\dot{\hat{\boldsymbol{\xi}}} = &-\boldsymbol{R}(\hat{\boldsymbol{q}}_b^n)\boldsymbol{S}(\hat{\boldsymbol{\sigma}})(\boldsymbol{f}^b_{\text{IMU}} - \hat{\boldsymbol{b}}^b_a) \\ &+ \boldsymbol{R}(\hat{\boldsymbol{q}}_b^n)\begin{bmatrix}\boldsymbol{0}_{3\times 1} & \boldsymbol{I}_{3\times 3}\end{bmatrix}\text{Proj}(\hat{\boldsymbol{w}}, \boldsymbol{\Gamma}(\hat{\boldsymbol{y}} - \boldsymbol{\phi}^\intercal\hat{\boldsymbol{w}})) \\ &+ \theta^3\boldsymbol{K}_{\xi_p}(\boldsymbol{p}^n_{\text{GNSS}} - \hat{\boldsymbol{p}}^n) + \theta^2\boldsymbol{K}_{pv}(\boldsymbol{v}^n_{\text{GNSS}} - \boldsymbol{C}_{\boldsymbol{v}}\hat{\boldsymbol{v}}^n)\end{aligned} \quad . \tag{5.21}$$

However, this requires that the signal processing monitoring the GNSS to provides correct information at all times since the GNSS measurement also is included as a correction in (5.21). The magnetometer may also effect the change of $\boldsymbol{\xi}$ since

$$\hat{\boldsymbol{\sigma}} = k_1\underline{\boldsymbol{m}}^b \times \boldsymbol{R}(\boldsymbol{q}_b^n)^\intercal\underline{\boldsymbol{m}}^n + k_2\boldsymbol{f}^b \times \boldsymbol{R}(\boldsymbol{q}_b^n)^\intercal\underline{\hat{\boldsymbol{f}}}^n \tag{5.22}$$

where the reference vector $\underline{\boldsymbol{m}}$ is the normalized magnetometer measurements and $\hat{\boldsymbol{\sigma}}$ is a component in $\boldsymbol{\xi}$'s differential equation.

Other Possibilities to Increase Robustness and Reliable

Regarding extended robustness can hybrid theory be utilized in together with the INS. The navigation observer of Grip et al. (2013, Submitted) might been synchronized with a parallel observer based the vessel model. Information on obsever synchronization is found e.g. in Nijmeijer and Fossen (1999, Part IV)

This model could be change depending on the control objective. Tow different operating scenarios for a vessel could be transit and stationkeeping. A supply ship may navigate with, for instance, a Nomoto model

$$\dot{\psi} = \frac{K}{1+Ts}\delta \tag{5.23}$$

where δ is the rudder angle to the operational site. At site, or in the vicinity on the site, is a model change performed and the 3 DOF DP model is utilized. Also her should bumpless transfer, such as in Zaccarian and Teel (2002), be performed when the parallel observer is substituted.

Chapter 6
Conclusion and Further Work

6.1 Conclusion

This master thesis has considered a fault-tolerant observer by exploiting INS and GNSS. Methods for signal quality checks where chosen. Multiple GNSS single-point failure scenarios were simulated by constructing a vessel simulator in MATLAB®. These where outlier detection, GNSS sensor freeze, high sensor variance, constant bias and GNSS drift. Also one scenario related to accelerometer failure where an estimated acceleration, based on the vessel model, was carried out. Errors, faults and failures were detected and handle appropriately by by through fault isolation. This thesis did not focus of magnetometer and gyroscope failure.

This thesis concludes with

- The chosen signal quality methods for fault-tolerance worked well in detecting and handling GNSS sensor errors and faults. Outliers, freeze, high variance and bias was detected and handle accordingly. Such errors were prevented from propagating to the observer and the corresponding estimates.
- The developed voting algorithm was able to detect discrepancies among the individual sensor measurement, also when no faults were injected into the system.
- The developed GNSS drift detection algorithm was no only able to detect the drift, but also the magnitude of the fault at a given time. A possible drive-off was prevented.

- Sensor weighting yield good results. The same goes for the time-varying tuning of the gain associated with the position estimates. Even when the fault-tolerant methods was not applied was outliers attenuated since the calculated variance increased, thus decreasing the gain because of the variance dependent tuning. Time varying gains should also be utilized for the remaining gains in the observer.

- If drift of all position reference sensors are detected to be erroneous should automatic control be switch off. Manual control should be carried out until the sensor fault is accommodated.

- Utilizing an estimated acceleration, from a model-based approach, as redundant acceleration information was successful. The results yielded no noticeable changes in the position estimates. Increased roll motion was however observed.

Regarding the overall performance of the system does this thesis conclude with

- The observer of Grip et al. (2013, Sumibtted) is a good basis for developing a fault-tolerant observer by exploiting INS and position reference sensors, however many respects still remains to be resolved in order to make the observer applicable for dynamic positioning.

- Performance of the overall system is improved with the fault-tolerance additions compared to the original observer of Grip et al. (2013, Submitted) when system is exposed to error, fault and failure situations regarding the position sensors. Especially so with respect to the detection of the drifting GNSS measurements.

- Time-varying gains seems promising. Performance of the position measurements are increased when the variance associated with the position measurements changes.

- Estimating vertical GNSS bias works well and estimates the drift cor-

rectly. However, the drift may not be the same for the horizontal measurements since the error source is not necessarily know. Hence, vertical bias estimation, as purposed in this thesis, can only be used as fault detection, not fault accommodation.

6.2 Further Work

Even though a fault-tolerance observer was successfully developed are there many remaining aspects to be studied. These are aspects are related to faulty inertial sensors, online observer tuning, adaptive gains and proving stability of the total observer. This thesis recommends that the work related to the following items should be performed or investigated.

- Use QUEST or similar methods for initializing the attitude observer, so the correct attitude estimates could be obtained faster.
- Studying possible failure scenarios regarding the inertial sensors. Preprocessing and voting should looked into. Signal quality checks regarding inertial measurements should be carried out. Fault-detection may be preformed according to e.g. Gustafsson (2007).
- An other heading reference, such as a gyro compass should be included. Fusion of the attitude estimates and the heading from the gyro compass should be performed.
- Further study related to the tuning of the signal processing associated with the measurements. Adaptive tuning for changing ambient conditions is worth looking into.
- Further study related to the position reference voting algorithm is needed. Use of the position estimate and statistical methods is worth considering. Inclusion of other sensors, such as HPR systems, should also be carried out.

- Realistic simulation of sensors including GNSS antenna location should be carried out, such that the roll and pitch movements will be embedded in the GNSS measurements. Associated effects should be compensated before utilized by the observer.
- Study how the control input affects the model-based acceleration estimation when the control input cannot be directly measured due to thrust losses. The same should be done regarding the model insecurities.
- Ensuring bumpless transfer when the acceleration measurements are switched out and replaced with the estimated acceleration.
- Adaptive gains of the observer, taking in account the measurement accuracy and the estimates for position, velocity and attitude, should be studied.
- Stability analysis of the total observer with switching and adaptive gains should be performed.
- Study how wave filtering can be incorporated into the observer of Grip et al. (2013, Submitted).

Bibliography

Batista, P., Silvestre, C., and Oliveira, P. (2012). A GES attitude observer with single vector observations. *Automatica*, 48(2):388 – 395.

Blanke, M. (2001). Enhanced maritime safety through diagnosis and fault tolerant control. In *Proc. IFAC conference CAMS*.

Britting, K. R. (2010). *Inertial Navigation Systems Analysis*. Artech House, 685 Canton Street, Norwood, MA 02062. First published by John Wiley & Sons, Inc. in 1971.

Brown, R. G. and Hwang, P. Y. (2011). *Intoduction to Random Signals and Applied Kalman Filtering*. John Wiley & Sons, Inc., 4th edition.

Bryson, M. and Sukkarieh, S. (2004). Vehicle model aided inertial navigation for a UAV using low-cost sensors. In *Proc. Australasian Conference Robotics and Automation*, Canberra, Australia.

Chen, H., Moan, T., and Verhoeven, H. (2008). Safety of dynamic positioning operations on mobile offshore drilling units. *Reliability Engineering & System Safety*, 93(7):1072 – 1090.

Chen, H., Moan, T., and Verhoeven, H. (2009). Effect of dgps failures on dynamic positioning of mobile drilling units in the north sea. *Accident Analysis & Prevention*, 41(6):1164 – 1171.

Chen, H. and Verhoeven, H. (2005). Safety of dp operations on mobile offshore drilling units on the norwegian continental shelf - barriers to prevent loss of position. In *Proc. Dynamic Positioning Conference*, Houston, Tx.

Crassidis, J. L., Landis Markley, F., and Cheng, Y. (2007). Survey of non-

linear attitude estimation methods. *Journal of Guidance, Control, and Dynamics*, 30(1):12 – 28.

Det Norske Veritas (2011). Rules for classification of ships newbuildings; special equipment and systems additional class. Technical report, Det Norske Veritas. Chapter 7 Dynamic Positioning Systems.

Egeland, O. and Gravdahl, J. (2002). *Modeling and simulation for control*. Marine Cybernetics, Trondheim.

Fossen, T. and Perez, T. (2009). Kalman filtering for positioning and heading control of ships and offshore rigs. *IEEE Control Systems Magazine*, 29(6):33 – 46.

Fossen, T. I. (2011). *Handbook of Marine Craft Hydrodynamocs and Motion Control*. John Wiley & Sons, Ltd., 1th edition.

Fossen, T. I. (2012a). How to incorporate wind, waves and ocean currents in the marine craft equations of motion. In *Proc. IFAC MCMC'12*, Arenzano, Italy.

Fossen, T. I. (2012b). Low-cost integrated navigation systems for autonomos underwater vehicles. In *Plenary paper presented at the XXXIII Jornadas de Automatica*, Vigo, Spain.

Fossen, T. I. and Strand, J. (1999). Passive nonlinear observer design for ships using lyapunov methods: full-scale experiments with a supply vessel. *Automatica*, 35(1):3 – 16.

Frank, P. (1990). Fault diagnosis in dynamic systems using analytical and knowledge-based redundancy - A survey and some new results. *Automatica*, 26(3):459 – 474.

Frank, P., Schrier, G., and García, E. (1999). Nonlinear observers for fault detection and isolation. In Nijmeijer, H. and Fossen, T., editors, *New Directions in nonlinear observer design*, volume 244 of *Lecture Notes in*

Control and Information Sciences, pages 399–422. Springer-Verlag London Limited.

Grip, H. F., Fossen, T. I., Johansen, T. A., and Saberi, A. (2012a). Attitude estimation using biased gyro and vector measurements with time-varying reference vectors. *IEEE Transactions on Automatic Control*, 57(5):1332 – 1338.

Grip, H. F., Fossen, T. I., Johansen, T. A., and Saberi, A. (2012b). A nonlinear observer for integration of GNSS and IMU measurements with gyro bias estimation. In *Proc. American Control Conference 2012*, Fairmont Queen Elizabeth, Montréal, Canada.

Grip, H. F., Fossen, T. I., Johansen, T. A., and Saberi, A. (2013). Nonlinear observer for aided inertial navigation: Theory and experiments. Submitted to Control Engineering Practice.

Grip, H. F., Saberi, A., and Johansen, T. A. (2012c). Observers for interconnected nonlinear and linear systems. *Automatica*, 48(7):1339 – 1346.

Gustafsson, F. (2007). Statistical signal processing approaches to fault detection. *Annual Reviews in Control*, 31(1):41–54.

Gustafsson, F. (2012). *Statistical Sensor Fusion*. Studentlitteratur, 2 edition.

Hamel, T. and Mahony, R. (2006). Attitude estimation on $SO(3)$ based on direct inertial measurements. In *Proc. IEEE International Conference on Robotics and Automation*, pages 2170 – 2175, Orlando, FL, United states.

Hassani, V., Sorensen, A., Pascoal, A., and Aguiar, A. (2012). Multiple model adaptive wave filtering for dynamic positioning of marine vessels. In *Proc. of American Control Conference*, pages 6222–6228.

Hegrenæs, Ø., Berglund, E., and Hallingstad, O. (2008). Model-aided inertial navigation for underwater vehicles. In *Proc. IEEE International*

Conference on Robotics and Automation, pages 1069 – 1076, Pasadena, CA, United states.

Hegrenæs, Ø. and Hallingstad, O. (2011). Model-aided ins with sea current estimation for robust underwater navigation. *IEEE Journal of Oceanic Engineering*, 36(2):316 – 337.

Hsu, D. (1996). Comparison of four gravity models. In *Proc. IEEE 1996 Position Location and Navigation Symposium (Cat. No.96CH35879)*, pages 631 – 5, New York, NY, USA.

Hua, M.-D. (2010). Attitude estimation for accelerated vehicles using gps/ins measurements. *Control Engineering Practice*, 18(7):723 – 732. Special Issue on Aerial Robotics.

Iozan, L., Kirkko-Jaakkola, M., Collin, J., Takala, J., and Rusu, C. (2012). Using a MEMS gyroscope to measure the earth's rotation for gyrocompassing applications. *Measurement Science and Technology*, 23(2):025005 (8 pp.) –.

Isermann, R. (2006). *Fault-Diagnosis Systems*. Springer- Verlag Berlin Heidelberg.

Kalman, R. E. (1960). A new approach to linear filtering and prediction problems. *ASME Transactions, Series D: Journal of Basic Engineering*, 82:35–45.

Kane, T. R., Likins, P. W., and Levinson, D. A. (1983). *Spacecraft Dynamics*. McGraw Hill, New York, NY.

Khalil, H. K. (2002). *Nonlinear Systems*. Prentice Hall, third edition.

Krstic, M., Kanellakopoulos, I., and Kokotovic, P. (1995). *Nonlinear and Adaptive Control Design*. John Wiley and Sons, Inc.

Leondes, C. T., editor (1963). *Guidance and Control of Aerospace Vehicle*. McGraw-Hill, first edition.

Mahony, R., Hamel, T., and Pflimlin, J. M. (2008). Nonlinear complementary filters on the special orthogonal group. *IEEE Transactions on Automatic Control*, 53(5):1203 – 2018.

Maritime Safety Commitee (MSC) Circular 645 (1994). International maritime organization, guidelines for vessels with dynamic positioning systems. Technical report, International Marine Contractors Association.

Maybeck, P. (1979). *Stochastic models, estimation and control*, volume 1. Academic Press, New York.

MSS. Marine Systems Simulator (2010). www.marinecontrol.org. Viewed 14.01.2013.

National Geophysical Data Center (2013). Magnetic field calculators. www.ngdc.noaa.gov/geomag-web/. Viewed 14.01.2013.

National Imagery and Mapping Agency (2000). World geodetic system 1984. Technical report, Department Of Defence.

Nijmeijer, H. and Fossen, T., editors (1999). *New Directions in Nonlinear Observer Design*, volume 244 of *Lecture Notes in Control and Information Sciences*. Springer-Verlag London Limited, London, UK.

Parkinson, B. W. and Spilker, J. J., editors (1996a). *Global Positioning System: Theory and Applications*, volume 1 of *Progress in Astronautics and Aeronautics*. American Institute of Aeronautics and Astronautics, Inc, 370 L'Enfant Promendae, SW, Washington, DC 20024-2518.

Parkinson, B. W. and Spilker, J. J., editors (1996b). *Global Positioning System: Theory and Applications*, volume 2 of *Progress in Astronautics and Aeronautics*. American Institute of Aeronautics and Astronautics, Inc, 370 L'Enfant Promendae, SW, Washington, DC 20024-2518.

Salcudean, S. (1991). A globally convergent angular velocity observer for

rigid body motion. *IEEE Transactions on Automatic Control*, 36(12):1493 – 1497.

Savage, P. G. (1981). *Stochastic models, estimation and control*. Strapdown Associates, 4727 South Lake Sarah Drive Maple Plain, Minnesota 55359.

Schmidt, S. F. (1966). Application of state-space methods to navigation problems. *Advances in Control Systems*, page 293–340.

Shuster, M. and Oh, S. (1981). Three-axis attitude determination from vector observations. *Journal of Guidance and Control*, 4(1):70 – 7.

Smith, G., Schmidt, S., and McGee, L. (1962). Application of statistical filter theory to optimal estimation of position and velocity on board circumlunar vehicle. Technical report, National Aeronautics and Space Administration.

Sælid, S., Jenssen, N. A., and Balchen, J. G. (1983). Design and analysis of a dynamic positioning system based on the kalman filtering and optimal control. *IEEE Transactions on Automatic Control*, AC-28(3):331 – 339.

Sørensen, A. J. (2012). *Lecture Notes - Marine Control System*. Department of Marine technology University of Science and Technology. Lecture Notes in TMR4240 Marine Control System.

Thienel, J. and Sanner, R. (2003). A coupled nonlinear spacecraft attitude controller and observer with an unknown constant gyro bias and gyro noise. *IEEE Transactions on Automatic Control*, 48(11):2011 – 2014.

Vik, B. (2012). *Integrated Satellite and Interal Navigation Systems*. Department of Engineering Cybernetics University of Science and Technology. Lecture Notes in TTK5 Kalman Filtering and Navigation.

Vik, B. and Fossen, T. (2001). A nonlinear observer for GPS and INS integration. In *Proceedings of the IEEE Conference on Decision and Control*, volume 3, pages 2956–2961, Orlando, FL. cited By (since 1996) 25; Conference of 40th IEEE Conference on Decision and Control (CDC); Confer-

ence Date: 4 December 2001 through 7 December 2001; Conference Code: 59019.

Vik, B., Shiriaev, A., and Fossen, T. (1999). Nonlinear observer design for integration of DGPS and INS. In Nijmeijer, H. and Fossen, T., editors, *New Directions in Nonlinear Observer Design*, volume 244 of *Lecture Notes in Control and Information Sciences*, chapter 8. Springer-Verlag London Limited, London, UK.

Wahba, G. (1966). A a least squares estimate of satellite attitude. *SIAM Review*, 8(3):384–386.

Walpole, R. E., Myers, R. H., Myers, S. L., and Ye, K. (2007). *Probability & Statistics for Engineers & Scientists*. Pearson Prentics Hall, Pearson Education, Inc. Upper Saddle River, NJ 07458, 8th edition.

Zaccarian, L. and Teel, A. (2002). A common framework for anti-windup, bumpless transfer and reliable designs. *Automatica*, 38(10):1735 – 44.

Appendix A

Vessel and Simulator Parameters

Semi-Submersible Kinetic Parameters

`rig.m` in the GNC Toolbox, see MSS. Marine Systems Simulator (2010), was utilized to provide the $\boldsymbol{M}_{RB}$, $\boldsymbol{M}$, $\boldsymbol{D}$ and $\boldsymbol{G}$ matrices. From these a 6 DOF rig model was made and used as the basis for the simulator. The matrices $\boldsymbol{M}_{RB}$, $\boldsymbol{M}$, $\boldsymbol{D}$ and $\boldsymbol{G}$ matrices are specified on the two following pages.

$$\boldsymbol{M}_{RB} = \begin{bmatrix} 27162500.0 & 0 & 0 & 0, -529668750.0 & 0 & \\ 0 & 27162500.0 & 0 & 529668750.0 & 0 & -13581250.0 \\ 0 & 0, 27162500.0 & 013581250.0 & 0 & & \\ 0 & 529668750.0 & 0 & 34774790622.0 & 0 & -264834375.0 \\ -529668750.0 & 0 & 13581250.0 & 0 & 38149731255.0 & 0 \\ 0 & -13581250.0 & 0 & -264834375.0 & 0 & 37192253122.0 \end{bmatrix} \tag{A.1}$$

$$\boldsymbol{M} = \begin{bmatrix} 43795874.59 & 0 & 0 & 0 & 68482414.41 & 0 \\ 0 & 69181096.68 & 0 & -453738749.96 & 0 & 21009298.34 \\ 0 & 0 & 48135348.33 & 0 & -10486424.17 & 0 \\ 0 & -453738749.96 & 0 & 39600592072.32 & 0 & -226869374.98 \\ 68482414.41 & 0 & -10486424.17 & 0 & 46462378018.08 & 0 \\ 0 & 21009298.34 & 0 & -226869374.98 & 0 & 69288968589.77 \end{bmatrix} \tag{A.2}$$

$$\boldsymbol{D} = \begin{bmatrix} 437958.75 & 0 & 0 & 0 & 0 & 0 \\ 0 & 345905.48 & 0 & 0 & 0 & 0 \\ 0 & 0 & 3446293.77 & 0 & 0 & 0 \\ 0 & 0 & 0 & 4752909689.27 & 0 & 0 \\ 0 & 0 & 0 & 0 & 6971279683.59 & 0 \\ 0 & 0 & 0 & 0 & 0 & 866112107.37 \end{bmatrix} \tag{A.3}$$

$$\boldsymbol{G} = \begin{bmatrix} 0 & 0 & 0 & 0 & 0 & 0 \\ 0 & 0 & 0 & 0 & 0 & 0 \\ 0 & 0 & 6183972.86 & 0 & -3091986.43 & 0 \\ 0 & 0 & 0 & 142969879903.35 & 0 & 0 \\ 0 & 0 & -3091986.43 & 0 & 26215049605.50 & 0 \\ 0 & 0 & 0 & 0 & 0 & 0 \end{bmatrix} \tag{A.4}$$

Wave Simulator

When the wave induced forces and moments are computed by utilizing the linear states-space model presented in Section B.3.1, the eigenvaules of the wave linear state space system is given as.

$$\text{eigenvaules} = \begin{bmatrix} -0.2245 \pm 0.4468i \\ -0.2245 \pm 0.4468i \\ -0.2245 \pm 0.4468i \\ -0.2245 \pm 0.4468i \\ -0.2245 \pm 0.4468i \\ -0.2245 \pm 0.4468i \end{bmatrix} \tag{A.5}$$

From (A.5) it can be seen that this model is quite oscillatory. Hence, a numerical solver need to be stable for critically stable systems. Therefore RK-4 was chosen to compute the wave induced forces and moments. RK-4 is stable of for system with considerably higher complex conjugated eigenvaules. For more on RK-4 please Appendix C or Egeland and Gravdahl (2002) can be advised.

Appendix B
Background Theory

B.1 Kinematics

Rotation Matrices and Transformation Between Reference Frames

A rotation matrix describes the rotation between two given reference frames {a} and {b}. According to Fossen (2011, Ch. 2.2), the rotation matrix $\boldsymbol{R}_b^a \in SO(3)$. The special orthogonal group, $SO(3)$, implies the following relations

$$\det \boldsymbol{R}_b^a = 1, \quad (\boldsymbol{R}_b^a)^T \boldsymbol{R}_b^a = \boldsymbol{I}, \quad (\boldsymbol{R}_b^a)^{-1} = (\boldsymbol{R}_b^a)^T \tag{B.1}$$

From Fossen (2011, Ch. 2.2), the skew symmetric matrix is given with the following identity

$$\boldsymbol{S}(\boldsymbol{a}) = -\boldsymbol{S}^\intercal(\boldsymbol{a}) \tag{B.2}$$

where $\boldsymbol{S} \in SS(n)$ and n is the order of the matrix. The 3×3 skew symmetric matrix is defined as

$$\boldsymbol{S}(\boldsymbol{a}) := \begin{bmatrix} 0 & -\boldsymbol{a}_3 & \boldsymbol{a}_2 \\ \boldsymbol{a}_3 & 0 & -\boldsymbol{a}_1 \\ -\boldsymbol{a}_2 & \boldsymbol{a}_1 & 0 \end{bmatrix} \tag{B.3}$$

and can be used to calculate cross products as shown in (B.4)

$$\boldsymbol{a} \times \boldsymbol{b} = \boldsymbol{S}(\boldsymbol{a})\boldsymbol{b}. \tag{B.4}$$

A vector $\vec{p}$ decomposed in the frame {b}. $\boldsymbol{p}^b$ can then be rotated to the

coordinate system, {a} by the rotation matrix, $\boldsymbol{R}_b^a$

$$\boldsymbol{p}^a = \boldsymbol{R}_a^b \boldsymbol{p}^b \tag{B.5}$$

The derivative of the rotation matrix can be stated

$$\dot{\boldsymbol{R}}_b^a = \boldsymbol{R}_b^a \boldsymbol{S}(\boldsymbol{\omega}_{ab}^b) \tag{B.6}$$

from Fossen (2011, Ch. 2.2.1).

The skew symmetric matrix can $\boldsymbol{S}(\boldsymbol{\omega}_{ab}^a)$ be transformed to the reference frame {b} by a similarity transform

$$\boldsymbol{S}(\boldsymbol{\omega}_{ab}^b) = \boldsymbol{R}_a^b \boldsymbol{S}(\boldsymbol{\omega}_{ab}^a) \boldsymbol{R}_b^a \tag{B.7}$$

which will be utilized in Section 2.2.2.

Reference Frames

The motion and position of a marine craft is described in 6 degrees of freedom (DOF). In navigation of a such a craft, reference frames can by applied. By doing it can often be convenient to define several reference frames. Relevant coordinate system for this thesis are summarized in Table B.1. For a more detained explanation of these reference frame can Fossen (2011) by advised.

Table B.1: Thesis Relevant Coordinate Systems

Name	Notation	Definition
Inertial	$\{i\}$	An internal coordinate system (non accelerated). Newton's law of motion apply in this frame. This frame is approximately space fixed.
Earth Centered Earth Fixed (ECEF)	$\{e\}$	Earth fix coordinate system. The origin is located at the center of the Earth. The x-axis points north, the y-axis points 90 degrees in longitudinal direction and the yz-plane constitute the equatorial plane. E.g, GNSS measurements are provided in the {e} frame, see Section 2.3.
North, East, Down (NED)	$\{n\}$	From Fossen (2011) is the origin, o_n, located on the Earth surface relative the Earth's reference ellipsoid. The x-axis point towards true North, y-axis to the East while the z-axis points down towards the center of the Earth. For Flat Earth navigation, the {n} is assumed to be an internal coordinate system.
Body	$\{b\}$	Hull or Body fixed coordinate system. Origin is located at the craft's Center of Gravity (CG). The environmental and actuator forces and moments will present them selves in the {b} frame. Accordingly it will be useful to state the measurements of the motion sensors in this frame. In this thesis, two global frames are defined in conjunction with three geographical frames.
Flow	$\{f\}$	Flow fixed coordinate system. The {f} frame is useful to model lift and drag forces. The transformation from FLOW axis to a given reference frame is done be to principal rotations according to Fossen (2011). $\boldsymbol{R} = \boldsymbol{R}^{\intercal}_{z,-\alpha}\boldsymbol{R}^{\intercal}_{y,\beta}$ where the α is the angle of attack and $-\beta$ is the negative sideslip angle.

Transformation from the {b} to {n} Frame

$\boldsymbol{\Theta}_{nb}$ from (2.3) is the generalized coordinates in Euler angles, describing the orientation of the {n} frame related to the {b} frame of the craft. Furthermore, (2.1) can be written as

$$\dot{\boldsymbol{\eta}} = \begin{bmatrix} \dot{\boldsymbol{p}}^n_{b/n} \\ \dot{\boldsymbol{\Theta}}_{nb} \end{bmatrix} = \begin{bmatrix} \boldsymbol{R}^n_b(\boldsymbol{\Theta}_{nb}) & \mathbf{0}_{3x3} \\ \mathbf{0}_{3x3} & \boldsymbol{T}_\Theta(\boldsymbol{\Theta}_{nb}) \end{bmatrix} \begin{bmatrix} \boldsymbol{v}^b_{b/n} \\ \boldsymbol{\omega}^b_{b/n} \end{bmatrix} \tag{B.8}$$

The upper differential equation of (B.8) describes the linear velocity of the craft. $\boldsymbol{v}^b_{b/n}$ and $\dot{\boldsymbol{p}}^n_{b/n}$ is the body fixed velocity and NED composed velocity vector respectively. Whereas $\boldsymbol{R}^n_b$ is the rotation matrix from {b} to {n}. For the angular velocity differential equation, $\boldsymbol{\omega}^b_{b/n}$ is the angular velocity of the {b} frame with respect the {n}. $\boldsymbol{T}_\Theta(\boldsymbol{\Theta}_{nb})$ is the angular velocity transformation matrix.

Attitude Representation: Euler Angles

From Fossen (2011, Eq. (2.18)) one can utilize Euler angles, $\boldsymbol{\Theta}_{nb}$ to represent attitude by a rotation matrix, $\boldsymbol{R}^n_b(\boldsymbol{\Theta}_{nb})$, presented previously. The rotation matrix is given as

$$\boldsymbol{R}^n_b(\boldsymbol{\Theta}_{nb}) = \begin{bmatrix} \mathrm{c}\psi\mathrm{c}\theta & -\mathrm{s}\psi\mathrm{c}\phi + \mathrm{c}\psi\mathrm{s}\theta\mathrm{s}\phi & \mathrm{s}\psi\mathrm{s}\phi + \mathrm{c}\psi\mathrm{c}\phi\mathrm{s}\theta \\ \mathrm{s}\psi\mathrm{c}\theta & \mathrm{c}\psi\mathrm{c}\phi + \mathrm{s}\phi\mathrm{s}\theta\mathrm{s}\psi & -\mathrm{c}\psi\mathrm{s}\phi + \mathrm{s}\theta\mathrm{s}\psi\mathrm{c}\phi \\ -\mathrm{s}\theta & \mathrm{c}\theta\mathrm{s}\phi & \mathrm{c}\theta\mathrm{c}\phi \end{bmatrix} \tag{B.9}$$

where the Euler angles are given as

$$\boldsymbol{\Theta}_{nb} = \begin{bmatrix} \phi & \theta & \psi \end{bmatrix}^\mathsf{T}. \tag{B.10}$$

The transformation matrix $\boldsymbol{T}_\Theta(\boldsymbol{\Theta}_{nb})$ from (B.8) is given as

$$\boldsymbol{T}_\Theta(\boldsymbol{\Theta}_{nb}) = \begin{bmatrix} 1 & \mathrm{s}\phi\mathrm{t}\theta & \mathrm{c}\phi\mathrm{t}\theta \\ 0 & \mathrm{c}\phi & -\mathrm{s}\phi \\ 0 & \mathrm{s}\phi/\mathrm{c}\theta & \mathrm{c}\phi/\mathrm{c}\theta \end{bmatrix}. \tag{B.11}$$

Hence, (B.11) and the lower part of (B.8) is singular at $\theta = \pm 90°$.

Attitude Representation: The Unit Quaternion

A singular free approach in describing the kinematics can be based on the unit quaternion.

According to Fossen (2011) the quaternion $\boldsymbol{q}$ is a complex number containing a four parameters. One real η, and three imaginary, $\boldsymbol{\epsilon}$. From Fossen (2011) the following set, Q, of the unit quaternion is defined as

$$Q := \{\boldsymbol{q} | \boldsymbol{q}^\mathsf{T}\boldsymbol{q} = 1, \boldsymbol{q} = [\eta, \boldsymbol{\epsilon}^\mathsf{T}]^\mathsf{T}, \quad \boldsymbol{\epsilon} \in \mathbb{R}^3 \text{ and } \eta \in \mathbb{R}\} \tag{B.12}$$

From Fossen (2011) and the references therein the real and imaganery part of the unit quaternions are defined according to

$$\eta := \cos\left(\frac{\beta}{2}\right) \tag{B.13}$$

$$\boldsymbol{\epsilon} = [\epsilon_1,\, \epsilon_2,\, \epsilon_3]^\mathsf{T} := \boldsymbol{\lambda} \sin\left(\frac{\beta}{2}\right) \tag{B.14}$$

where $\boldsymbol{\lambda} = [\lambda_1,\, \lambda_2\, \lambda_3]^\mathsf{T}$ is the vector which the rotation, β, is rotated about an object. $\boldsymbol{\lambda}$ is a unit vector satisfying

$$\boldsymbol{\lambda} = \pm \frac{\boldsymbol{\epsilon}}{\sqrt{\boldsymbol{\epsilon}^{\boldsymbol{T}}\boldsymbol{\epsilon}}} \quad \text{if} \quad \sqrt{\boldsymbol{\epsilon}^{\boldsymbol{T}}\boldsymbol{\epsilon}} \neq 0 \tag{B.15}$$

Hence, the unit quaternion can be expressed in the following manner

$$\boldsymbol{q} = \begin{bmatrix} \eta \\ \xi_1 \\ \xi_2 \\ \xi_3 \end{bmatrix} = \begin{bmatrix} \cos\left(\frac{\beta}{2}\right) \\ \boldsymbol{\lambda} \sin\left(\frac{\beta}{2}\right) \end{bmatrix} \in Q, \quad 0 \leq \beta \leq 2\pi \tag{B.16}$$

given by Fossen (2011), where β is the rotation angle. From the given parameterization, the unit quaternion satisfy the following constraint

$$\boldsymbol{q}^\intercal \boldsymbol{q} = 1 \tag{B.17}$$

or

$$\eta^2 + \epsilon_1^2 + \epsilon_2^2 + \epsilon_3^2 = 1 \tag{B.18}$$

From Egeland and Gravdahl (2002, Ch. 6.7) can the quaternion product between two quaternion vectors, $\boldsymbol{q}_1$ and $\boldsymbol{q}_2$, be defined as

$$\boldsymbol{q}_1 \otimes \boldsymbol{q}_2 := \begin{bmatrix} \eta_1\eta_2 - \boldsymbol{\epsilon}_1^\intercal \boldsymbol{\epsilon}_2 \\ \eta_1\boldsymbol{\epsilon}_2 + \eta_2\boldsymbol{\epsilon}_1 + \boldsymbol{\epsilon}_2 \times \boldsymbol{\epsilon}_2 \end{bmatrix} \tag{B.19}$$

where η_1 and η_2 is the two respective real parts as in (B.13) whereas the two imaginary vectors, $\boldsymbol{\epsilon}_1$ and $\boldsymbol{\epsilon}_2$, as in (B.14).

The coordinate transformation for the unit quaternion is defined as

$$\boldsymbol{R}_b^n(\boldsymbol{q}) := \boldsymbol{R}_{\eta,\epsilon} \tag{B.20}$$

where $\boldsymbol{R}_b^n(\boldsymbol{q})$ is obtained by inserting (B.13)-(B.14) into the rotation

$$\begin{aligned} \boldsymbol{R}_b^n &= \boldsymbol{R}_{\alpha,\beta} \\ &= \boldsymbol{I}_{3\times 3} + \sin(\beta)\boldsymbol{S}(\boldsymbol{\lambda}) + [1 - \cos(\beta)]\boldsymbol{S}^2(\boldsymbol{\lambda}) \end{aligned} \tag{B.21}$$

decried by among others Kane et al. (1983). This yields

$$\boldsymbol{R}_b^n(\boldsymbol{q}) = \boldsymbol{R}_{\eta,\epsilon} = \boldsymbol{I_{3x3}} + 2\eta\boldsymbol{S}(\boldsymbol{\epsilon}) + 2\boldsymbol{S}^2(\boldsymbol{\epsilon}) \tag{B.22}$$

where

$$\boldsymbol{R}_b^n(\boldsymbol{q}) = \begin{bmatrix} 1-2(\epsilon_2^2+\epsilon_3^2) & 2(\epsilon_1\epsilon_2-\epsilon_3\eta) & 2(\epsilon_1\epsilon_3+\epsilon_2)\eta \\ 2(\epsilon_1\epsilon_2+\epsilon_3\eta) & 1-2({\epsilon_1}^2+{\epsilon_3}^2) & 2(\epsilon_2\epsilon_3-\epsilon_1\eta) \\ 2(\epsilon_1\epsilon_3+\epsilon_2\eta) & 2(\epsilon_2\epsilon_3+\epsilon_1\eta & 1-2(\epsilon_1^2+\epsilon_2^2) \end{bmatrix}. \tag{B.23}$$

Now, the angular velocity transform in (B.8) can be described in quaternion form by substituting (B.23) into (B.6). After some calculation this yields

$$\dot{\boldsymbol{q}} = \boldsymbol{T}_q(\boldsymbol{q})\boldsymbol{\omega}_{b/n}^b \tag{B.24}$$

as given in Fossen (2011). Hence, the angular transformation matrix, $\boldsymbol{T}_q$ is given as

$$\boldsymbol{T}_q(\boldsymbol{q}) = \frac{1}{2}\begin{bmatrix} -\epsilon_1 & -\epsilon_2 & -\epsilon_3 \\ \eta & -\epsilon_3 & \epsilon_2 \\ \epsilon_3 & \eta & -\epsilon_1 \\ -\epsilon_2 & \epsilon_1 & \eta \end{bmatrix}. \tag{B.25}$$

According to Egeland and Gravdahl (2002) can (B.24) can be written with a quaternion product as

$$\dot{\boldsymbol{q}} = \frac{1}{2}\boldsymbol{q} \otimes \begin{bmatrix} 0 \\ \boldsymbol{\omega}_{b/n}^b \end{bmatrix}. \tag{B.26}$$

(B.19) and (B.26) are relevant for the relationship between the quaternion differentiation equation proposed in Grip et al. (2013, Submitted) and (B.24), which will be studied in Section 2.2.2.

Furthermore, Fossen (2011, Ch. 2.2.2) states that (B.24) can violate the unit the quaternion constraint, i.e. $\|\boldsymbol{q}\| = 1$, when (B.24) is integrated numerically. Hence, normalization is needed. Fossen (2011) present a normalization

strategy when (B.24) is implemented in discrete time. Then the normalization can be preformed directly for each step of the integration according to

$$\boldsymbol{q}^b_{b/n}(k+1) = \frac{\boldsymbol{q}^b_{b/n}(k+1)}{\sqrt{\left(\boldsymbol{q}^b_{b/n}(k+1)\right)^\mathsf{T}\boldsymbol{q}^b_{b/n}(k+1)}} \tag{B.27}$$

where $\boldsymbol{q}^b_{b/n}(k+1)$ can be obtained by e.g Euler integration. See Section 2.7 For more on other numerical integration techniques, see Appendix C.

The quaternion, $\boldsymbol{q}$, can be calculated from the Euler angles, $\boldsymbol{\Theta}_{nb}$, and visa versa. These algorithms can be found in Fossen (2011, Ch. 2.2.3) and Fossen (2011, Ch. 2.2.4) respectively.

B.2 Kinetics

The vessel simulator in Chapter 3 is based on the six Degree of Freedom DOF kinetic vessel model of (2.2) is given as

$$\boldsymbol{M}\dot{\boldsymbol{\nu}} + \boldsymbol{C}(\boldsymbol{\nu})\boldsymbol{\nu} + \boldsymbol{D}(\boldsymbol{\nu})\boldsymbol{\nu} + \boldsymbol{g}(\boldsymbol{\eta}) = \boldsymbol{\tau} + \boldsymbol{\tau}_{\text{wind}} + \boldsymbol{\tau}_{\text{wave}}. \tag{B.28}$$

From Fossen (2012a) can the kinetics of a marine craft be written as

$$\boldsymbol{M}_{RB}\dot{\boldsymbol{\nu}} + \boldsymbol{C}(\boldsymbol{\nu})_{RB}\boldsymbol{\nu} = \boldsymbol{\tau}_{\text{RB}} \tag{B.29}$$

where

$$\boldsymbol{\tau}_{\text{RB}} = \boldsymbol{\tau}_{\text{hydrodynamic}} + \boldsymbol{\tau}_{\text{hydrostatic}} + \boldsymbol{\tau}_{\text{wind}} + \boldsymbol{\tau}_{\text{wave}} + \boldsymbol{\tau}. \tag{B.30}$$

Hence, the kinetics consist of rigid-body, hydrodynamic and hydrostatic components. The hydrodynamics forces and moments can be written as

$$\boldsymbol{\tau}_{\text{hydrodynamic}} = -\boldsymbol{M}_A\dot{\boldsymbol{\nu}} - \boldsymbol{C}_A(\boldsymbol{\nu}_r)\boldsymbol{\nu}_r - \boldsymbol{D}(\boldsymbol{\nu}_r)\boldsymbol{\nu}_r \tag{B.31}$$

while the restoring forces comes from the hydrostatic forces and moments as

$$\boldsymbol{\tau}_{\text{hydrostatic}} = -\boldsymbol{g}(\boldsymbol{\eta}). \tag{B.32}$$

The total mass, Coriolis, damping and restoring matrices, utilized in (B.28), can be written as

$$\begin{aligned} \boldsymbol{M} &= \boldsymbol{M}_{RB} + \boldsymbol{M}_A \\ \boldsymbol{C} &= \boldsymbol{C}_{RB} + \boldsymbol{C}_A \\ \boldsymbol{D} &= \boldsymbol{D}(\boldsymbol{\nu}_r) \end{aligned} \tag{B.33}$$

where the added mass, added Coriolis and damping matrices have subscript A. comes from the hydro dynamical forces and moments. The rigid-body terms have subscript, RB. By substituting (B.30) into (B.29) and inserting for the hydrodynamic and hydrostatic forces and moments is

$$\begin{aligned} \boldsymbol{M}_{RB}\dot{\boldsymbol{\nu}} + \boldsymbol{C}(\boldsymbol{\nu})_{RB}\boldsymbol{\nu} = -\boldsymbol{M}_A\dot{\boldsymbol{\nu}} - \boldsymbol{C}_A(\boldsymbol{\nu}_r)\boldsymbol{\nu}_r - \boldsymbol{D}(\boldsymbol{\nu}_r)\boldsymbol{\nu}_r - \boldsymbol{g}(\boldsymbol{\eta}) \\ + \boldsymbol{\tau}_{\text{wind}} + \boldsymbol{\tau}_{\text{wave}} + \boldsymbol{\tau} \end{aligned} \tag{B.34}$$

obtained. By rearranging (B.34) results in the following kinetics

$$\boldsymbol{M}\dot{\boldsymbol{\nu}}_r + \boldsymbol{C}(\boldsymbol{\nu}_r)\boldsymbol{\nu}_r + \boldsymbol{D}(\boldsymbol{\nu}_r)\boldsymbol{\nu}_r + \boldsymbol{g}(\boldsymbol{\eta}) = \boldsymbol{\tau} + \boldsymbol{\tau}_{\text{wind}} + \boldsymbol{\tau}_{\text{wave}}. \tag{B.35}$$

stated with relative generalize velocity, $\boldsymbol{\nu}_r$. This is done by exploiting property 8.1 in Fossen (2011). From Fossen (2011) the relative velocity is defined as

$$\boldsymbol{\nu_r} := \boldsymbol{\nu} - \boldsymbol{\nu_c} \tag{B.36}$$

where $\boldsymbol{\nu}_c$ is the generalized current velocity. For more of kinetic modeling Fossen (2012a, Ch. 5, 6 and 7) can be advised.

$\boldsymbol{g}(\boldsymbol{\eta})$ in (B.34) can be approximated according to Fossen (2011) as

$$\boldsymbol{g}(\boldsymbol{\eta}) \approx \boldsymbol{P}(\psi)^{\intercal}\boldsymbol{G}\,\boldsymbol{\eta} \tag{B.37}$$

which is valid for small roll and pitch angles, ϕ and θ, respectively. $\boldsymbol{\eta}$ and $\boldsymbol{g}(\boldsymbol{\eta})$ are given in the NED and BODY frame respectively. $\boldsymbol{G}$ is the linearized restoring forces matrix. Furthermore, $\boldsymbol{P}(\psi)$ is given as

$$\boldsymbol{P}(\psi) = \begin{bmatrix} \boldsymbol{R}(\psi) & \boldsymbol{0}_{3\times 3} \\ \boldsymbol{0}_{3\times 3} & \boldsymbol{I}_{3\times 3} \end{bmatrix} \tag{B.38}$$

This result is

$$\boldsymbol{g}(\boldsymbol{\eta}) \approx \boldsymbol{P}(\psi)^{\intercal} \boldsymbol{G}\, \boldsymbol{\eta} = \boldsymbol{G}\, \boldsymbol{\eta} \tag{B.39}$$

because of the structure of $\boldsymbol{G}$, which can found in Appendix A.

B.3 Modeling of Environmental Forces and Moments

The thesis relevant environmental forces and moments not presented in the formed Section are wave forces and moments together with current. Hence, these will be presented in the following Section. Modeling of wind forces and moments will not be described in this thesis since the simulator constructed in Chapter 3 will not include wind. See Chapter 3 for details.

B.3.1 Modeling of Waves

The JONSWAP wave spectra is a result of a measurement program carried out in the North Sea in 1968 and 1969. The spectra describes, according to Fossen (2011), *nonfully develop sea.*

According to Fossen (2011), the spectral density function of JONSWAP is written as

$$S(\omega) = 155\,\frac{H_s^2}{T_1^4}\,\omega^{-5}\,\exp\left(\frac{-944}{T_1^4}\omega^{-4}\right)\gamma^Y \tag{B.40}$$

It is common to chose $\gamma = 3.3$ and

$$Y = \exp\left[-\left(\frac{0.191\,\omega\,T_1 - 1}{\sqrt{2}\,\sigma}\right)^2\right] \tag{B.41}$$

According to Sørensen (2012) the typical wave period for the North Sea is i range of 5 to 20 seconds yielding

$$\omega_i = \frac{2\,\pi}{T}, \quad \omega_i \in [0.3142,\, 1.2566].$$

An examples of the JONSWAP spectra can be observed in Figure 3.4 in Chapter 3.

Other wave spectra are Nuemann, Bretschneider, Pierson-Moskowitz and

Torsethaugen. For more on wave spectra, see Fossen (2011, Ch. 8.2) and references therein.

From Fossen (2011) can the first-order wave frequency induced forces and moments, $\boldsymbol{\tau}_{\text{wave 1st}}$, be approximated as second-order transfer function driven by a Gaussian, zero mean process. For each degree of freedom the following transfer function can model the wave frequency motion according to Fossen (2011, Ch. 8)

$$h(s)_{\text{wave},i}(s) = \frac{K_w^{\{i\}} s}{s^2 + 2\lambda^{\{i\}}\omega_0^{\{i\}}\sigma + \left(\omega_0^{\{i\}}\right)^2} \tag{B.42}$$

where

$$K_w^{\{i\}} = 2\lambda^{\{i\}}\omega_0^{\{i\}}\sigma^{\{i\}} \tag{B.43}$$

Furthermore, σ^i is given as

$$\left(\sigma^{\{i\}}\right)^2 = \max_{o<\omega<\infty} S(\omega). \tag{B.44}$$

Moreover, Sørensen (2012) writes each of the transfer functions, for each DOF, given in (B.42) on state space form as

$$\dot{\boldsymbol{\xi}}_w = \boldsymbol{A}_w\boldsymbol{\xi}_w + \boldsymbol{E}_w\boldsymbol{w} \tag{B.45}$$

$$\boldsymbol{y}_{\text{wave}} = \boldsymbol{C}_w\boldsymbol{\xi}_w. \tag{B.46}$$

where $\boldsymbol{w}$ is the Gaussian, zero mean process. For a 6 DOF system, $\boldsymbol{A}_w$, $\boldsymbol{E}_w$ and $\boldsymbol{C}_w$ are given as

$$\boldsymbol{A}_w = \begin{bmatrix} \boldsymbol{0}_{6\times6} & \boldsymbol{I}_{6\times6} \\ -\boldsymbol{\Omega}^2 & -2\boldsymbol{\Lambda}\boldsymbol{\Omega} \end{bmatrix}, \quad \boldsymbol{E}_w = \begin{bmatrix} \boldsymbol{0}_{6\times6} \\ \boldsymbol{K_w} \end{bmatrix}, \quad \boldsymbol{C}_w = \begin{bmatrix} \boldsymbol{0}_{6\times6} & \boldsymbol{I}_{6\times6} \end{bmatrix} \tag{B.47}$$

where

$$\begin{aligned}\boldsymbol{\Omega} &= \text{diag}\{\omega_0^{\{1\}}, \omega_0^{\{2\}}, \omega_0^{\{3\}}, \omega_0^{\{4\}}, \omega_0^{\{5\}}, \omega_0^{\{6\}}\} \\ \boldsymbol{\Lambda} &= \text{diag}\{\lambda^{\{1\}}, \lambda^{\{2\}}, \lambda^{\{3\}}, \lambda^{\{4\}}, \lambda^{\{5\}}, \lambda^{\{6\}}\} \\ \boldsymbol{K}_w &= \text{diag}\{K_w^{\{1\}}, K_w^{\{2\}}, K_w^{\{3\}}, K_w^{\{4\}}, K_w^{\{5\}}, K_w^{\{6\}}\}.\end{aligned} \tag{B.48}$$

Moreover, Fossen (2011) states that in order to obtain a realistic wave induced motion of the vessel, the first-order wave forces and moments are approximated as

$$\boldsymbol{\tau}_{\text{wave 1st}} \approx \boldsymbol{K}\boldsymbol{H}_s(s)\boldsymbol{w}(s) \tag{B.49}$$

where $\boldsymbol{K}$ is a constant tunable gain. $\boldsymbol{K}$ is chosen such that the amplitude of the wave induced generalized position, $\boldsymbol{\eta}^n_{\text{wave}}$, of the vessel will be realistic. $\boldsymbol{H}_s$ is the multivariable system of (B.45)-(B.46) presented in the frequency domain.

B.3.2 Modeling of Ocean Currents

From Fossen (2012a) can forces moments of ocean currents acting on a marine craft be incorporated in the vessel model of (2.1) and (2.2) by replacing the $\boldsymbol{\nu}$ with the relative velocity given from (B.36) as

$$\boldsymbol{\nu}_r = \boldsymbol{\nu} - \boldsymbol{\nu}_c. \tag{B.50}$$

As mentioned in Section B.2 is the generalized current velocity given as $\boldsymbol{\nu}_c \in \mathbb{R}^6$. Moreover, Fossen (2011) presents that irrational current, $\boldsymbol{\nu}_c$, can be expressed as

$$\boldsymbol{\nu}_c = \begin{bmatrix} u_c & v_c & w_c & 0 & 0 & 0 \end{bmatrix}^\intercal \tag{B.51}$$

where $\boldsymbol{\nu}_c$ is given in {b}. The linear current velocity from (B.51) is given as

$$\boldsymbol{v}_c^b = \begin{bmatrix} u_c & v_c & w_c \end{bmatrix}^\intercal. \tag{B.52}$$

Hence, the relative velocity, $\boldsymbol{\nu}_r$, is given as

$$\boldsymbol{\nu_r} = \begin{bmatrix} \boldsymbol{v}^b - \boldsymbol{v}_c^b \\ \boldsymbol{\omega}_{b/n}^b \end{bmatrix}. \tag{B.53}$$

The definition of constant irrational current can found in Definition B.1 below.

A parameterization of the rigid-body Coriolis matrix, $\boldsymbol{C}_{RB}$, presented by Fossen (2011) and reference therein, not including linear velocity can be applied to make the following identity

$$\boldsymbol{M}_{RB}\dot{\boldsymbol{\nu}} + \boldsymbol{C}_{RB}(\boldsymbol{\nu})\boldsymbol{\nu} = \boldsymbol{M}_{RB}\dot{\boldsymbol{\nu}}_r + \boldsymbol{C}_{RB}(\boldsymbol{\nu}_r)\boldsymbol{\nu}_r \tag{B.54}$$

valid. See, Property B.1, Fossen (2011) or Fossen (2012a) for details. Then, a vessel model including ocean current can be given by substituting the generalized rigid-body velocity in (B.8) and (B.28) with the generalized relative velocity, $\boldsymbol{\nu}_r$. Furthermore, from Fossen (2012a) is the current added to the kinematics of (B.8). Then, then total kinematic and kinetic model then takes the form of

$$\dot{\boldsymbol{\eta}} = \boldsymbol{J}_{\boldsymbol{\Theta}}(\boldsymbol{\eta})\boldsymbol{\nu}_r + \begin{bmatrix} \boldsymbol{v}_c^n \\ \boldsymbol{0} \end{bmatrix} \tag{B.55}$$

$$\boldsymbol{M}\dot{\boldsymbol{\nu}}_r + \boldsymbol{C}(\boldsymbol{\nu}_r)\boldsymbol{\nu}_r + \boldsymbol{D}(\boldsymbol{\nu}_r)\boldsymbol{\nu}_r + \boldsymbol{g}(\boldsymbol{\eta}) = \boldsymbol{\tau} + \boldsymbol{\tau}_{\text{wind}} + \boldsymbol{\tau}_{\text{wave}}. \tag{B.56}$$

The current velocity in the {n} and {b} frames is given by the following relationship

$$\boldsymbol{v}_c^n = \boldsymbol{R}_b^n \boldsymbol{v}_c^b. \tag{B.57}$$

Moreover, from Fossen (2011) can a 3-D Irriational current can be obtained by transforming the current speed, V_c, from the FLOW axis, {f}, see Section

B.1, to {n} according to

$$\boldsymbol{v}_c^n = \boldsymbol{R}_{y,\alpha_c}^{\intercal} \boldsymbol{R}_{z,-\beta_c}^{\intercal} \begin{bmatrix} V_c \\ 0 \\ 0 \end{bmatrix}. \tag{B.58}$$

Furthermore, (B.58) can be expanded to

$$\boldsymbol{v}_c^n = \begin{bmatrix} V_c \cos(\alpha_c) \cos(\beta_c) \\ V_c \sin(\beta_c) \\ V_c \sin(\alpha_c) \cos(\beta_c) \end{bmatrix}. \tag{B.59}$$

where α_c and β_c are the angle of attack and the negative sideslip of the current respectively. The magnitude of the current velocity, V_c can according to Fossen (2011) be has high as $2 - 3$ m/s in fjords caused by tidal components.

Irrational Constant Ocean Currents

Fossen (2011) present the definition of a constant irrational constant ocean current as

Definition B.1. ***Irrational Constant Ocean Current***
An constant irrational ocean current in {n} is defined by

$$\dot{\boldsymbol{v}}_c^n = \dot{\boldsymbol{R}}_b^n(\boldsymbol{\Theta}_{nb}) \boldsymbol{v}_c^b + \boldsymbol{R}_b^n(\boldsymbol{\Theta}_{nb}) \dot{\boldsymbol{v}}_c^b := \boldsymbol{0} \tag{B.60}$$

where

$$\dot{\boldsymbol{R}}_b^n(\boldsymbol{\Theta}_{nb}) = \boldsymbol{R}_b^n(\boldsymbol{\Theta}_{nb}) \boldsymbol{S}(\boldsymbol{\omega}_{b/n}^b). \tag{B.61}$$

Consequently,

$$\dot{\boldsymbol{v}}_c^b = -\boldsymbol{S}(\boldsymbol{\omega}_{b/n}^b) \boldsymbol{v}_c^b. \tag{B.62}$$

From Fossen (2011) is Property 8.1 in given as:

Property B.1. ***Irrational Constant Ocean Current***
If the Coriolis and centripetal matrix $\boldsymbol{C}_{RB}(\boldsymbol{\nu}_r)$ *is parameterized independent of linear velocity* $\boldsymbol{\nu}_1 = [u,\, v,\, w]^\intercal$*, for instance by using* (B.65)*, and the ocean current is irrational and constant, Definition B.1, the rigid-body kinetics satisfy*

$$\boldsymbol{M}_{RB}\dot{\boldsymbol{\nu}} + \boldsymbol{C}_{RB}(\boldsymbol{\nu})\boldsymbol{\nu} = \boldsymbol{M}_{RB}\dot{\boldsymbol{\nu}}_r + \boldsymbol{C}_{RB}(\boldsymbol{\nu}_r)\boldsymbol{\nu}_r \tag{B.63}$$

with

$$\boldsymbol{\nu_r} = \begin{bmatrix} \boldsymbol{v}^b - \boldsymbol{v}_c^b \\ \boldsymbol{\omega}_{b/n}^b \end{bmatrix}. \tag{B.64}$$

Furthermore, the linear velocity independent rigid-body Coriolis parameterization mention in Property B.1 is given as

$$\boldsymbol{C}_{\mathrm{RB}}(\boldsymbol{\nu}_r) = \begin{bmatrix} m\boldsymbol{S}(\boldsymbol{\omega}_{b/n}^b) & -m\boldsymbol{S}(\boldsymbol{\omega}_{b/n}^b)\boldsymbol{S}(\boldsymbol{r}_g^b) \\ m\boldsymbol{S}(\boldsymbol{r}_g^b)\boldsymbol{S}(\boldsymbol{\omega}_{b/n}^b) & -\boldsymbol{S}(\boldsymbol{I}_b\boldsymbol{\omega}_{b/n}^b) \end{bmatrix}. \tag{B.65}$$

For more details, see Fossen (2011).

B.4 Assumptions Regarding the Observer of Grip et al. (2013, Submitted)

The assumptions listed below are stated based upon the special condition of the observer by Grip et al. (2013, Sumbitted) presented in Section4.1.

Grip et al. (2013, Sumbitted) makes the following assumption to ensure uniformly observability

Assumption B.1. *There exist a constant* $c_{\mathrm{obs}} > 0$ *such that, for all* $t \geq 0, \|\underline{\boldsymbol{f}^b} \times \underline{\boldsymbol{m}^b}\| \geq c_{\mathrm{obs}}$

where $\underline{\boldsymbol{f}^b} = \boldsymbol{f}^b / \|\boldsymbol{f}^b\|$ and $\underline{\boldsymbol{m}^b} = \boldsymbol{m}^b / \|\boldsymbol{m}^b\|$.

Assumption B.2. *Knowledge of the constant $M_{\boldsymbol{f}} > 0$ and $m_{\boldsymbol{f}} > 0$ such that $m_{\boldsymbol{f}} \leq \|\boldsymbol{f}^b\| \leq M_{\boldsymbol{f}}$ and a bound on $M_{\boldsymbol{b}_g} > 0$ such that $\|\boldsymbol{b}_g^b\| \leq M_{\boldsymbol{b}_g}$.*

Assumption B.3. *$\dot{\boldsymbol{f}}^{\boldsymbol{b}}$ and $\boldsymbol{\omega}_{\boldsymbol{b/n}}^{\boldsymbol{b}}$ are uniformly bounded.*

Assumption B.4. *The gravity, $\boldsymbol{g}(\boldsymbol{p}^n)$, is given as by a Lipchitz continuous function of the position $\boldsymbol{p}^n$.*

According to Grip et al. (2013, Sumbitted) can the PE assumption be written as

Assumption B.5. *There exist a constant $\epsilon > 0$ and $T > 0$ such that, for all $t \geq 0$, $\int_t^T \boldsymbol{\phi}(\tau)\boldsymbol{\phi}^\intercal(\tau)\mathrm{d}\tau \geq \epsilon \boldsymbol{I}$.*

B.5 Terminology

From Fossen (2011) is the following definition of Flat Earth Navigation is stated.

Definition B.2. ***Flat Earth Navigation:*** *For marine craft operating in a local area, approximately constant longitude and latiude, an Earth-fixed tangent plane on the surface is used for navigation. This is usually referred to as flat Earth navigation and will be denoted {n} for simplicity. For flat Earth navigation one can assume that {n} is inertial such that Newton's laws still apply.*

B.6 Causes of dGNSS Errors or Failures

Chen et al. (2009) writes that possible external error and failure sourcescan be:

- Low number of available satellites
- Poor satellite constellation
- Failure of GPS satellites
- Failure at reference or uplink stations
- Failure of differential link communication satellites
- Failure of IALA radio station

According to Chen et al. (2009), possible causes could be:

- Mechanical failures
- Short circuit
- Computer failures
- Antenna masking
- Cable interference
- Erroneous software configuration

Hence, there are many sources for fault dGNSS measurements.

B.7 DNV DP Class Summary

On the following page is page 19 of Det Norske Veritas (2011) included. Page 19 includes Table C.1 of Det Norske Veritas (2011) which consist of DNV's minimal retirements for different DP class notations.

Table C1 System arrangement

Subsystem or component			*Minimum requirements for class notations*			
			DYNPOS-AUTS	**DYNPOS-AUT**	**DYNPOS-AUTR**	**DYNPOS-AUTRO**
			DPS 0	**DPS 1**	**DPS 2**	**DPS 3**
Electrical power system	Electrical system		No-redundancy 3)	No-redundancy 3)	Redundancy in technical design	Redundancy in technical design and physical separation (separate compartments)
	Main switchboard		1 3)	1 3)	1	2 in separate compartments
	Bus-tie breaker		0 3)	0 3)	1	2, 1 breaker in each MSB
	Distribution system		Non-redundant 3)	Non-redundant 3)	Redundant	Redundant, through separate compartments
	Power management		No	No	**AUTR**: Yes **DPS 2**: No	**AUTRO**: Yes **DPS 3**: No
Thrusters	Arrangement of thrusters		No-redundancy	No-redundancy	Redundancy in technical design 4)	Redundancy in technical design and physical separation (separate compartments)
	Single levers for each thruster at main DP-control centre		Yes	Yes	Yes	Yes
Positioning control system	Automatic control; number of computer systems		1	1	2	2 + 1 in alternate control centre
	Manual control; independent joystick system with automatic heading control 2)		No	Yes	Yes	Yes
Sensors	Position reference systems		1	2	3	3 whereof 1 in alternate control centre
	External sensors	Wind	1	1	2	2 whereof 1 in alternate control centre
		Gyro compass	1	1	3 1)	3 1) whereof 1 in alternate control centre
		Vertical reference sensor (VRS)	1	1	**AUTR**: 3 **DPS 2**: 2 5)	3 whereof 1 in emergency control centre
UPS			0	1	2	2 + 1 in separate compartment
Printer			Yes	Yes	Yes	Yes
Alternate control centre for dynamic positioning control back-up unit			No	No	No	Yes

1) One of the three required gyros may be replaced by a heading device based upon another principle, as long as this heading device is type approved as a TDH (Transmitting Heading Device) as specified in IMO Res. MSC.116 (73). For notation **DYNPOS-AUTRO** and **DPS 3** this is not to be the gyro placed in the alternate control centre.

2) The heading input may be taken from any of the required gyro compasses.

3) When this is part of the ship normal electrical power system (i.e. used for normal ship systems, not only the DP system), then Pt.4 Ch.8 applies.

4) For **DPS 2** see also B202.

5) Where necessary for the correct functioning of position reference systems, at least three vertical reference sensors are to be provided for notation **DPS 2**. If the DP-control system can position the ship within the operating limits without VRS corrections, only 2 VRSs are required.

102 In general additional requirements to achieve higher availability and robustness will apply to the **DYNPOS-** series as compared to the **DPS**-series of notations. An overview of the main differences between the two series are summarised in Table C2 for quick reference. Specific requirements for each subsystem are presented under the respective section headings.

B.8 Gaussian Zero Mean Noise

All measurement noise in this thesis is Gaussian, zero mean, white noise. This noise have to following distribution function, according to Walpole et al. (2007)

$$p(x) = \frac{1}{\sqrt{2\pi}\sigma} \int_{x_1}^{x_2} e^{-\frac{1}{2\sigma^2}(x-\mu)^2} \mathrm{d}x \tag{B.66}$$

where μ is the mean and σ is the standard deviation. By calculating zero mean noise with standard deviation, $\sigma = 1$ yield the distribution shown in Figure B.1.

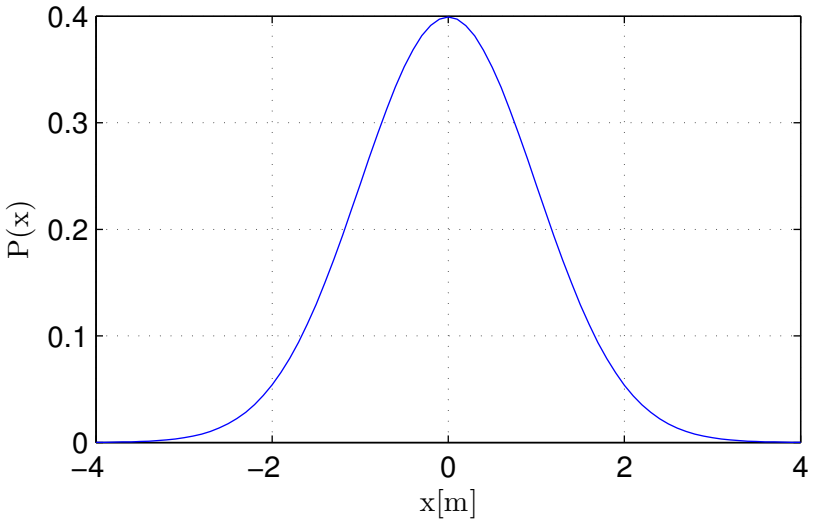

Figure B.1: Distribution of the Gaussian, zero mean, GNSS measurement noise components

Appendix C

Discrete Implementation of Continuous Systems

A computer implementation of a system on the form of

$$\dot{\boldsymbol{x}} = \boldsymbol{f}(\boldsymbol{x}, \boldsymbol{u}, t) \tag{C.1}$$

requires numerical methods. The control input, $\boldsymbol{u}$ is assumed constant over the sampling interval, h, as stated in Fossen (2011, App. B.2).

A simple method for numerical integration is forward Euler and is given as

$$\boldsymbol{x}(k+1) = \boldsymbol{x}(k) + h\boldsymbol{f}(\boldsymbol{x}, \boldsymbol{u}, t_k) \tag{C.2}$$

However forward Euler is not stable for undamped section-order systems. A stable numerical integration methods for such systems are combined forward and backwards Euler and can be described as following for simulating a mass-damper-spring-system, $\boldsymbol{x} = [x_1,\, x_2]^\intercal$

$$x_2(k+1) = x_2(k) + h\,\dot{x}_2(k) \tag{C.3}$$

$$x_1(k+1) = x_1(k) + h\,x_2(k+1) \tag{C.4}$$

where

$$\dot{x}_1 = x_2, \quad \dot{x}_2 = m^{-1}(-dx_2 - kx_1 + \tau) \tag{C.5}$$

A more complex numerical integration method is the Explicit Runge-Kutta

method of order 4 (RK4). From Fossen (2011) is the method given as

$$\begin{aligned}
\boldsymbol{k}_1 &= h\boldsymbol{f}(\boldsymbol{x}(k), \boldsymbol{u}(k), t_k) \\
\boldsymbol{k}_2 &= h\boldsymbol{f}(\boldsymbol{x}(k) + \boldsymbol{k}_1/2, \boldsymbol{u}(k), t_k + h/2) \\
\boldsymbol{k}_3 &= h\boldsymbol{f}(\boldsymbol{x}(k) + \boldsymbol{k}_2/2, \boldsymbol{u}(k), t_k + h/2) \\
\boldsymbol{k}_4 &= h\boldsymbol{f}(\boldsymbol{x}(k) + \boldsymbol{k}_3/2, \boldsymbol{u}(k), t_k + h)
\end{aligned} \tag{C.6}$$

$$\boldsymbol{x}(k+1) = \boldsymbol{x}(k) + \frac{1}{6}(\boldsymbol{k}_1 + 2\boldsymbol{k}_2 + 2\boldsymbol{k}_3 + \boldsymbol{k}_4).$$

For more on numerical integration methods can Egeland and Gravdahl (2002) be advised.

Appendix D
Vessel and Sensor Simulations

D.1 Vessel Simulation

Figure D.1 - D.4 show how the vessel response of the control based on the PVA estimates from the observer. The generalized position is shown in Figure D.1, the generalized velocity is shown in Figure D.2. The control input is shown in Figure D.3, whereas the first-order wave forces and moments acting on the vessel are shown in Figure D.4.

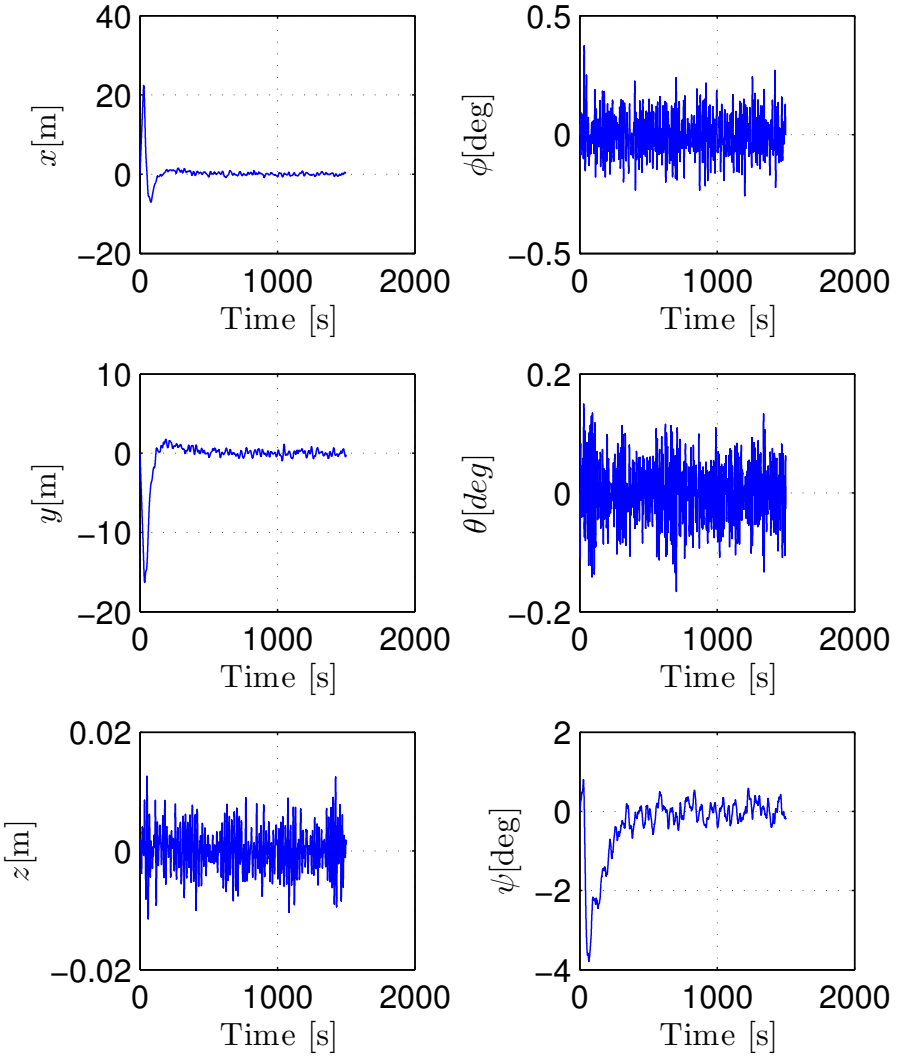

Figure D.1: Generalized Position in the {n} frame

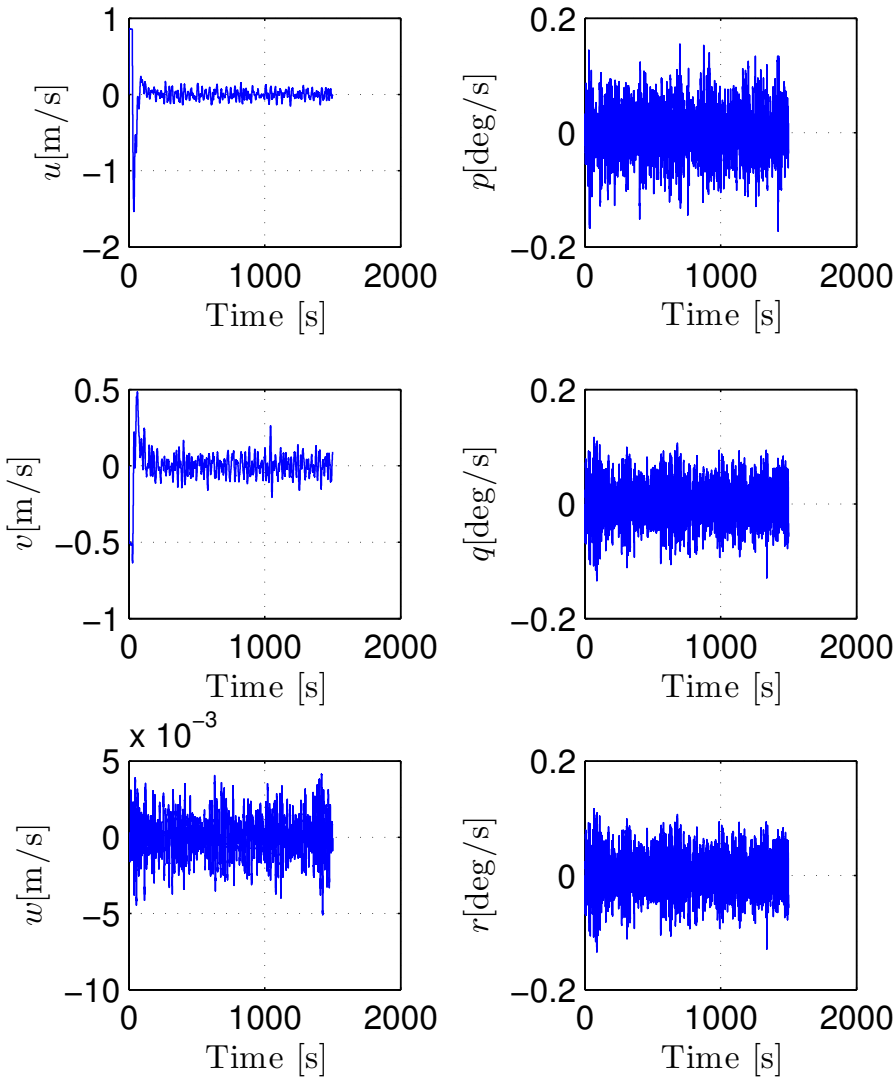

Figure D.2: Generalized Velocity in the {b} frame

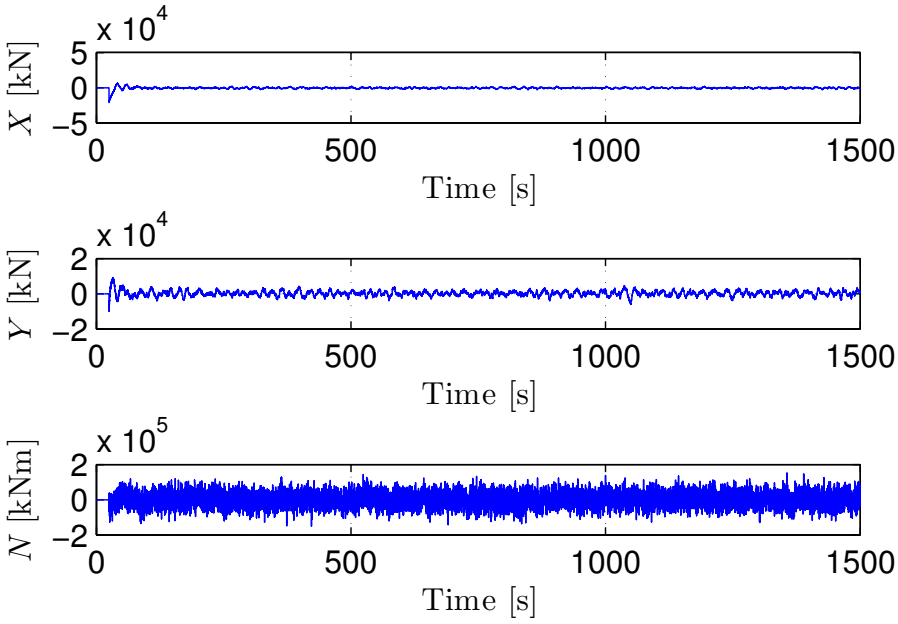

Figure D.3: Generalized Control Forces in the {b} frame

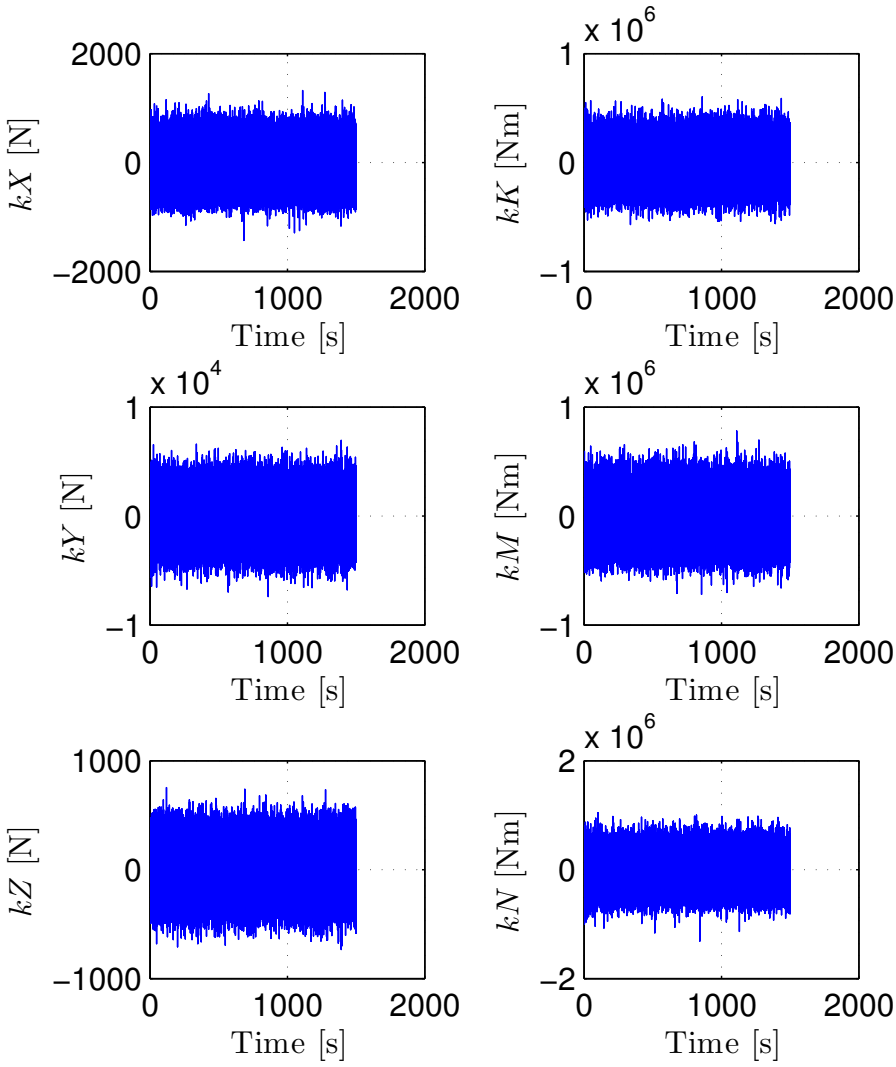

Figure D.4: Generalized Wave Forces in the {b} frame

D.2 Sensor Simulation

During one simulation the sensors readout is shown in Figure D.5-D.8. The accelerometer readout is given in D.5 whereas the gyroscope readout is given in D.6. Regarding the simualted GNSS measurements are these shown in FigureD.8 - Figure D.9.

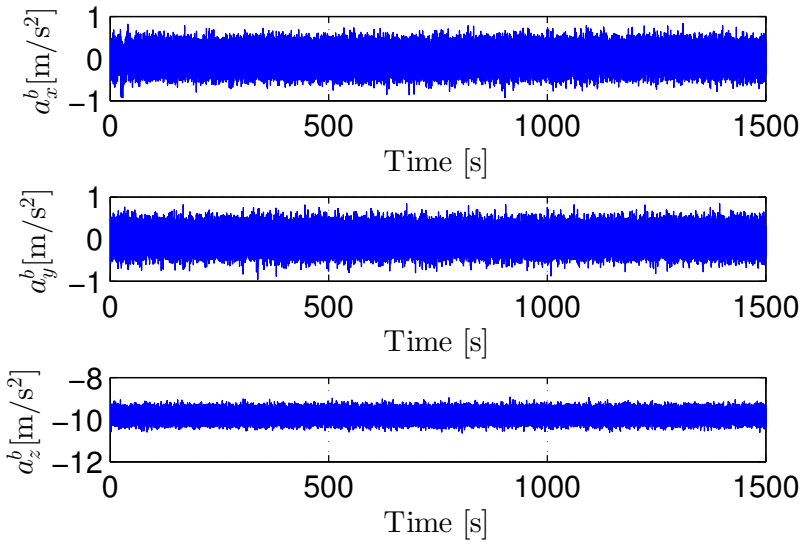

Figure D.5: Simulator. Sensor simulation of accelerometer.

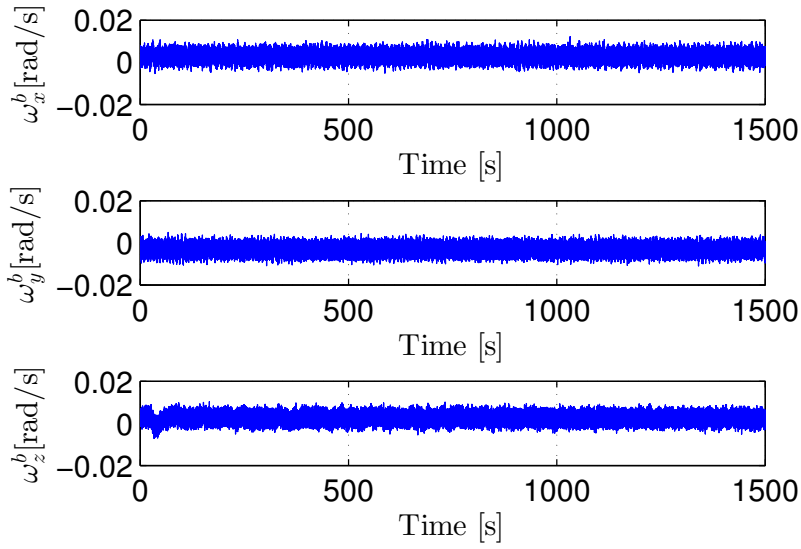

Figure D.6: Simulator. Sensor simulation of gyroscope.

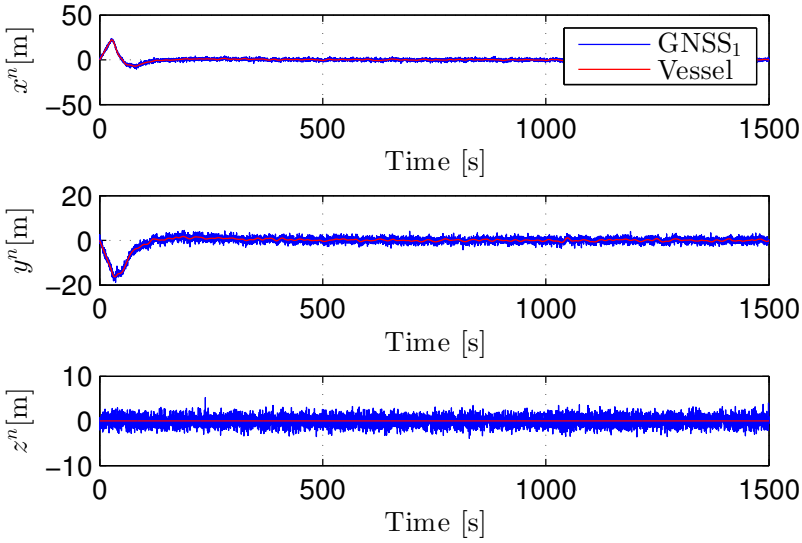

Figure D.7: Simulator. Sensor simulation of GNSS 1 together with the vessel's position.

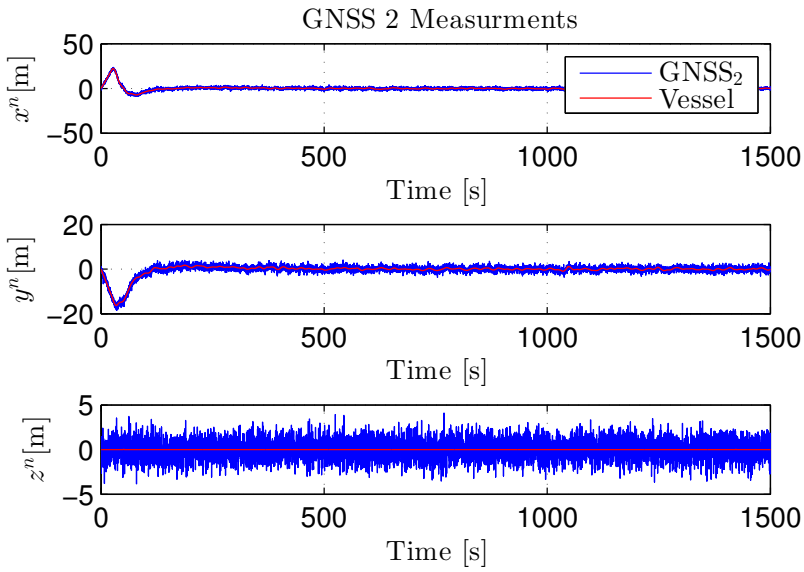

Figure D.8: Simulator. Sensor simulation of GNSS 2 together with the vessel's position.

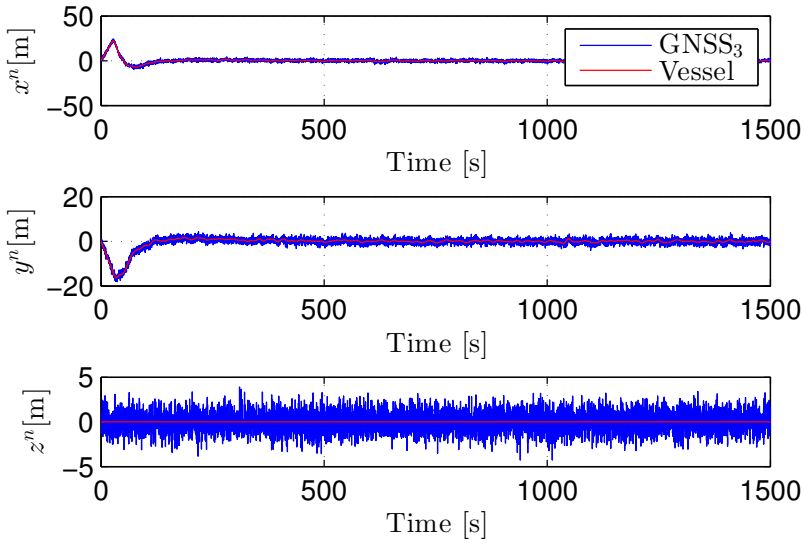

Figure D.9: Simulator. Sensor simulation of GNSS 3 together with the vessel's position.

Appendix E
Additional Results

E.1 Case: Fault Free System With One GNSS Measurement

This case will present the nominal estimate quality with one GNSS system sensor faults have occurred.

Figure shows that the signal check associated with E.1 reports no error or fault during the entire simulation since the reported status is 1.

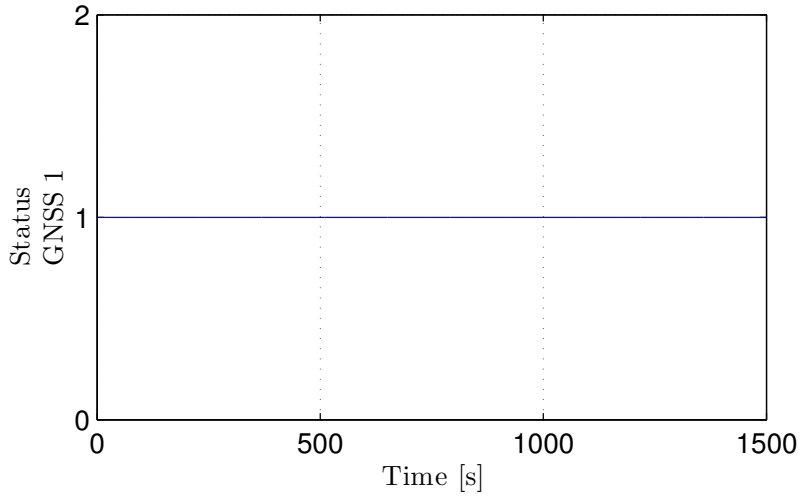

Figure E.1: Case 2. Status of GNSS 1. No fault are present

The vessel position is shown in Figure E.2 with the corresponding position measurements and estimates. One can observe the filtering properties of

the observer since the position estimates clearly lies within the GNSS raw measurements after the observer has converged.

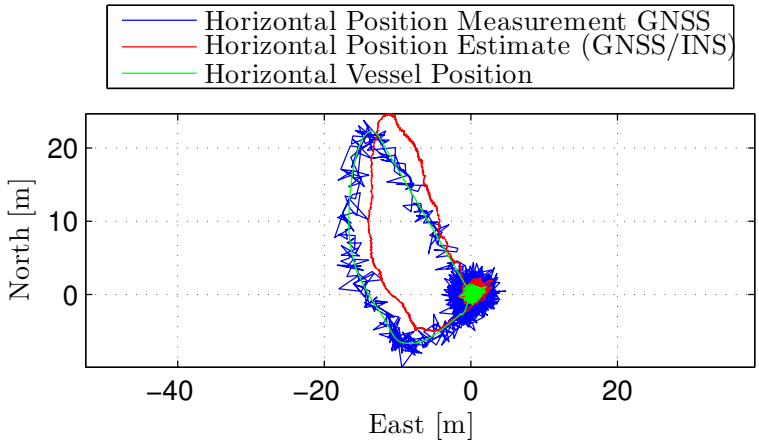

Figure E.2: North-East position of vessel together with potions measurements and position estimates when no faults are present.

The attitude estimates, using quaterions as representation, are given in Figure E.5, whereas the Euler representation of the estimates are shown in Figure E.6. After the initial time where the observers need to converge to the actual attitude of the vessel. The gyro biases estimates are shown in Figure E.7. Furthermore, the nonlinear injection term $\hat{\boldsymbol{\sigma}}$ is shown in Figure E.7. Moreover, Figure E.9 shows the time evolution of the $\boldsymbol{\xi}$. The attitude estimates shown with Euler angles representation in Figure

By studying Figure E.3 and Figure E.4 can one observe that the respective position and velocity estimates are fluctuating periodically with the respective vessel position and velocity. Zoomed versions E.3 and E.4 are given shown in Figure E.10 and Figure E.11. From Figure E.10 one can observer quite clearly that the horizontal position estimate follow the vessel position quite well with some larger amplitude. The same can be seen reading the velocity estimates E.10 where the estimates also have larger amplitudes than

the actual vessel velocity. This is probably caused by the measurement noise of the GNSS which is utilized in the observer correction as given in (4.30) and (4.31). The injection terms $\boldsymbol{K}_{pp}(\boldsymbol{p}^n_{\text{GNSS}} - \hat{\boldsymbol{p}}^{\boldsymbol{n}})$ and $\boldsymbol{K}_{vp}(\boldsymbol{p}^n_{\text{GNSS}} - \hat{\boldsymbol{p}}^{\boldsymbol{n}})$ are fluctuating around the vessel's respective position and velocity from the fluctuation position error $\tilde{\boldsymbol{p}}$ seen in Figure E.12. These fluctuations in $\tilde{\boldsymbol{p}}$ is caused by the Gaussian, zero mean noise component in the position measurements.

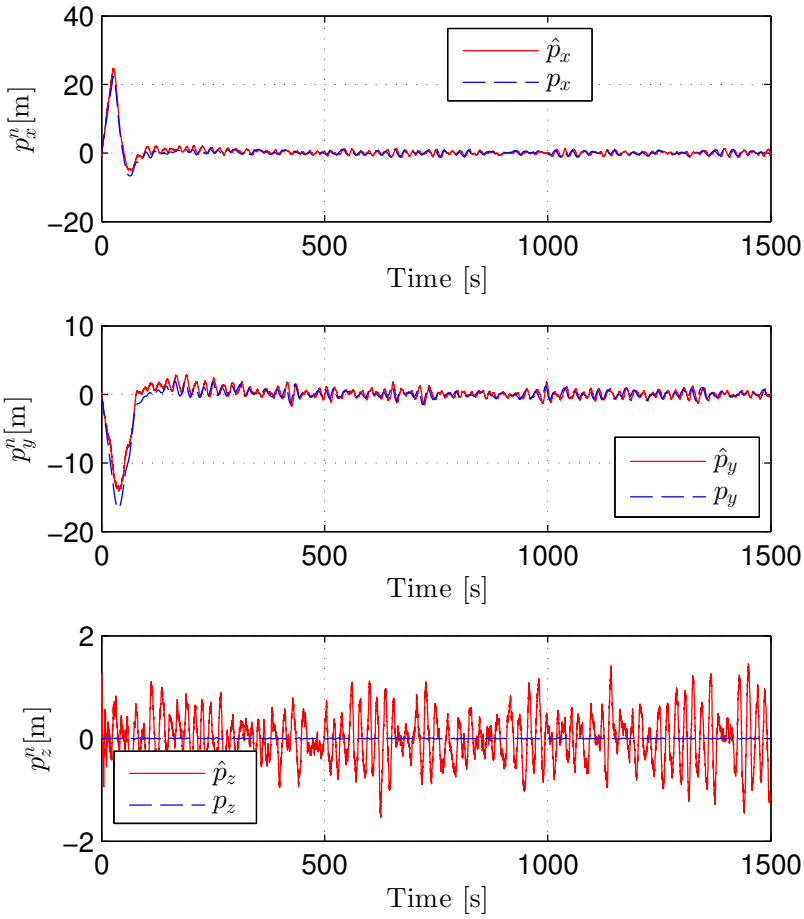

Figure E.3: Position estimates together with actual vessel position when no faults are present

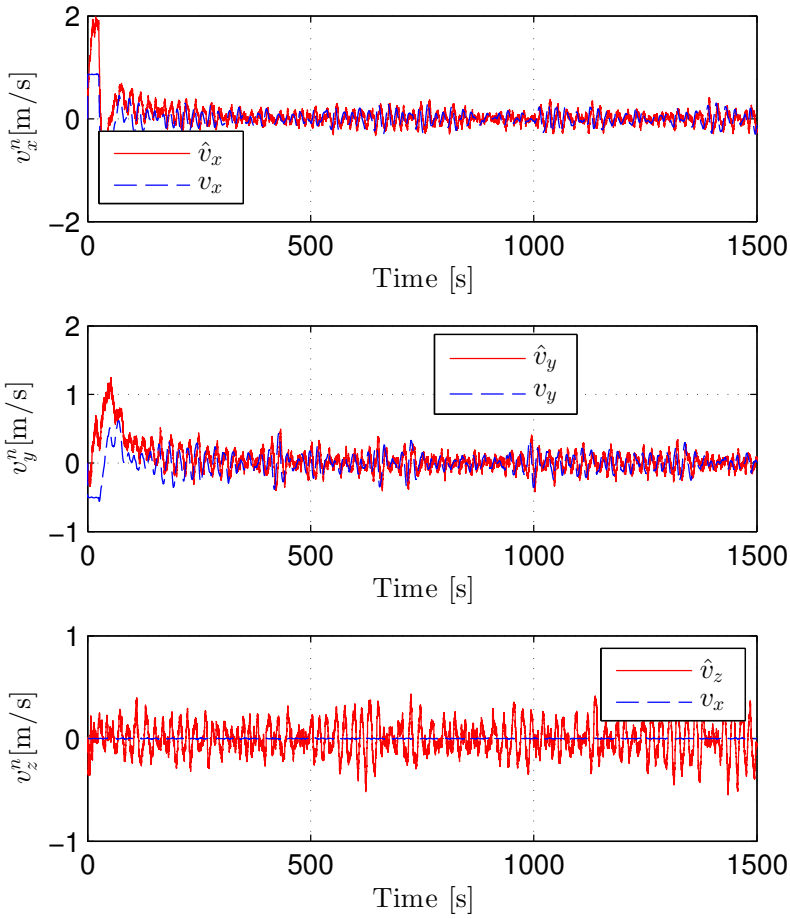

Figure E.4: Velocity estimates together with actual vessel velocity when no faults are present

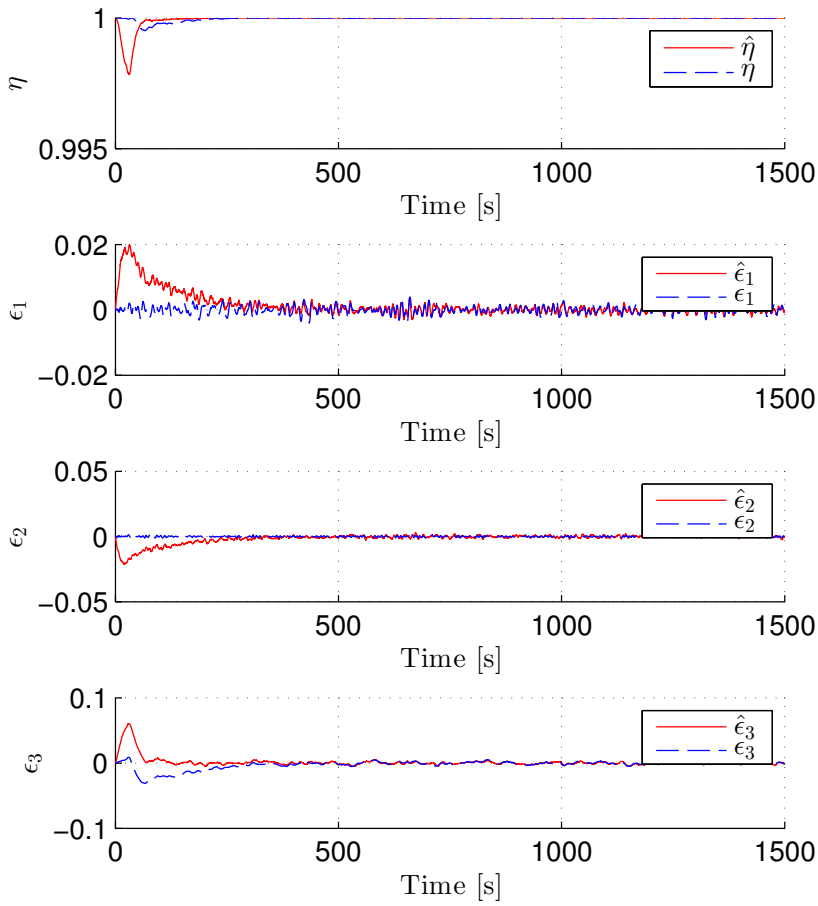

Figure E.5: Attitude estimates, using quaterions as representation when no faults are present

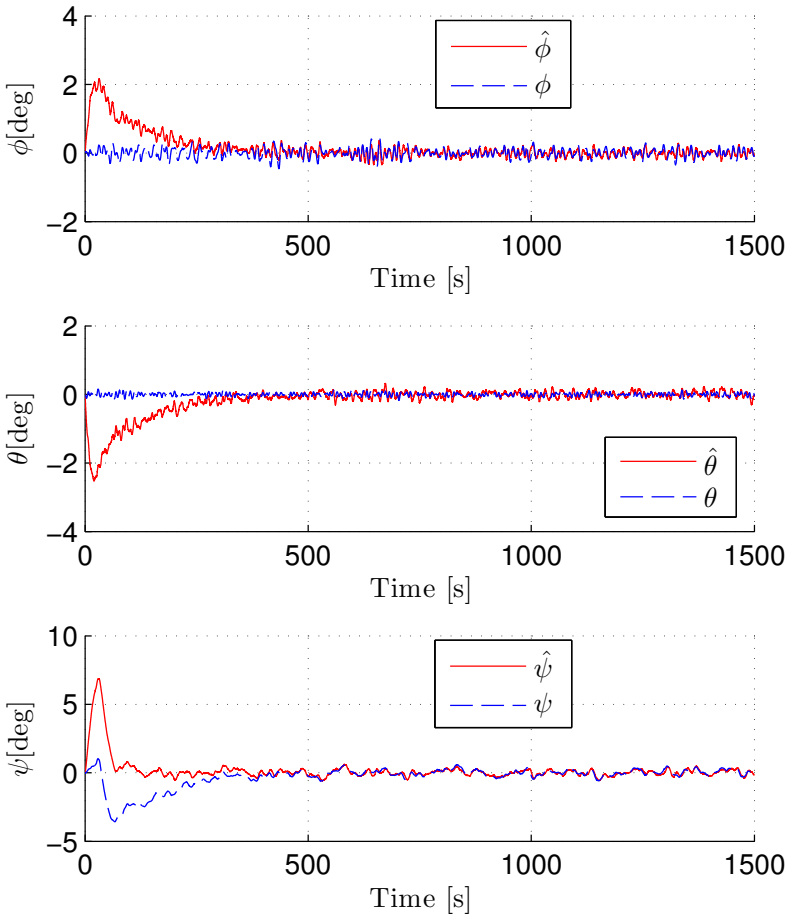

Figure E.6: Attitude estimates, using Euler angles as representation when no faults are present

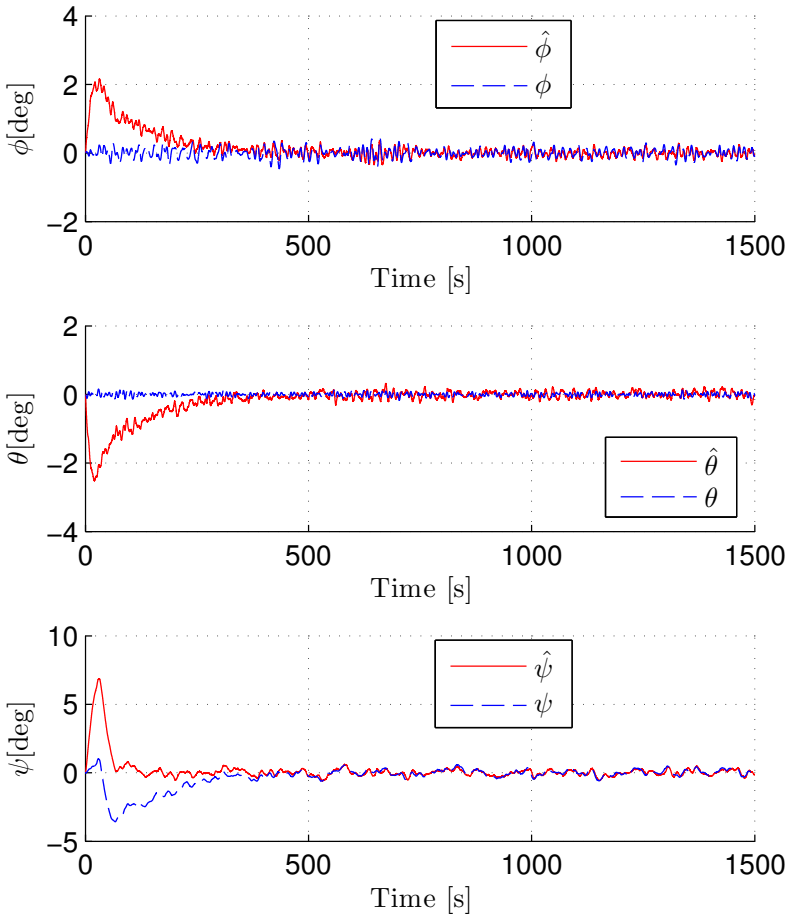

Figure E.7: Gyroscope Bias Estimates

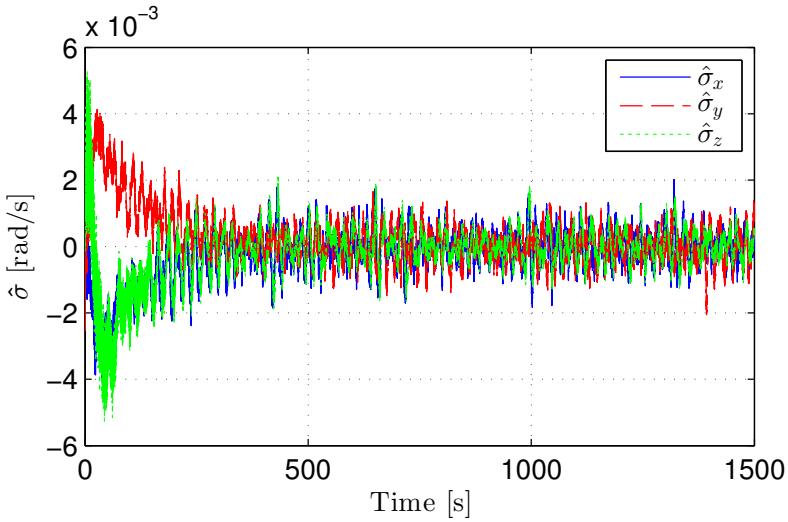

Figure E.8: The nonlinear injection term $\hat{\boldsymbol{\sigma}}$ when no faults are present

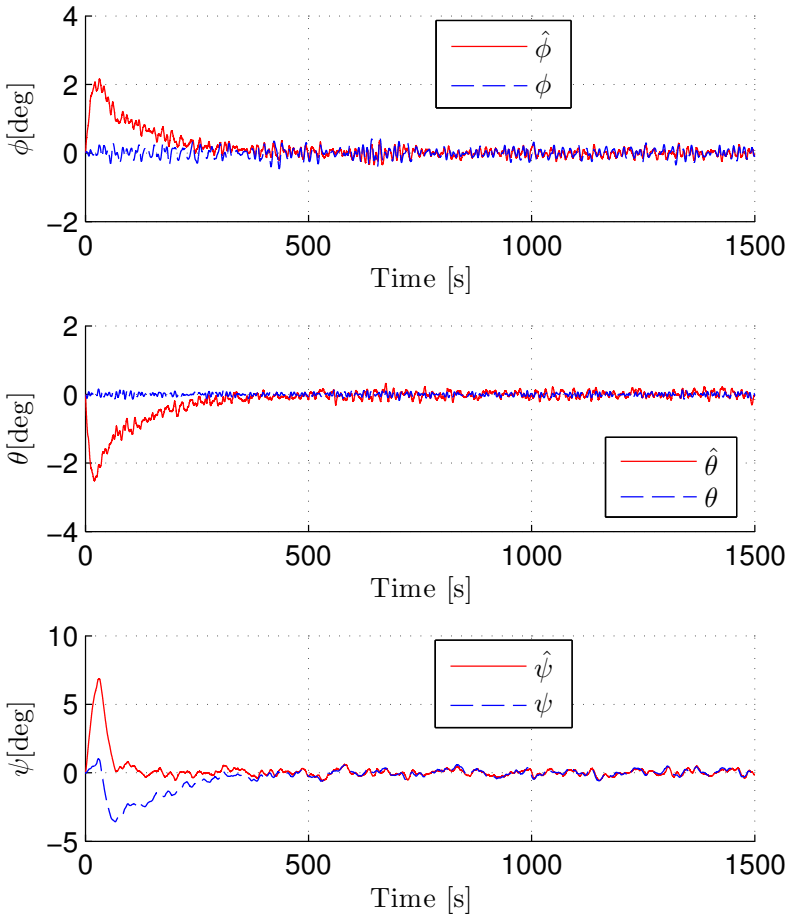

Figure E.9: $\boldsymbol{\xi}$ when no faults are present

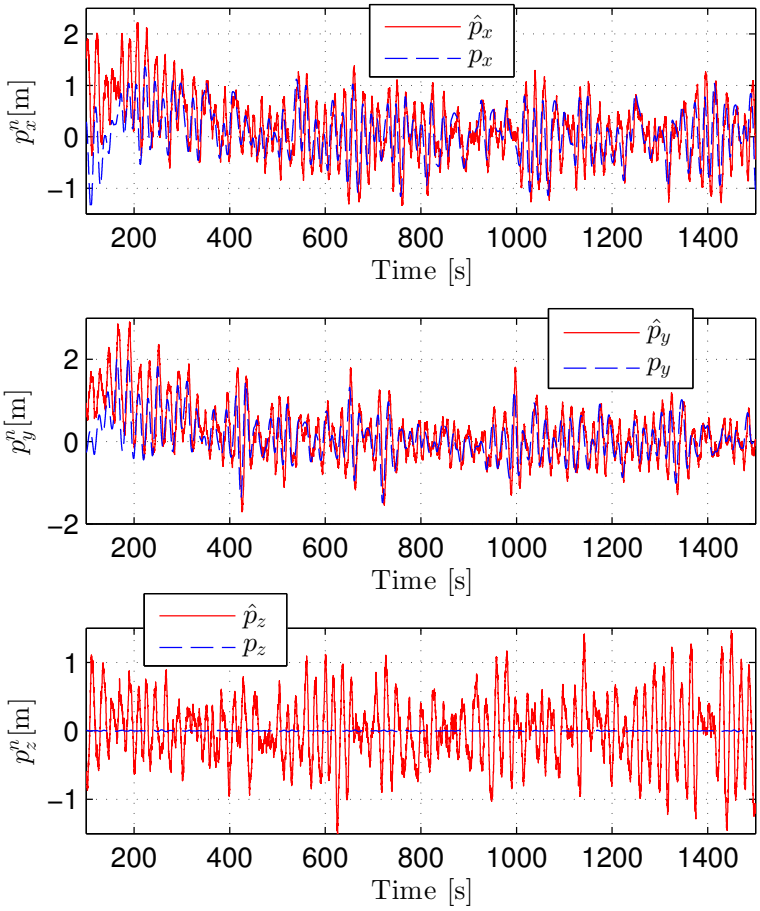

Figure E.10: Converged position estimates when no faults are present

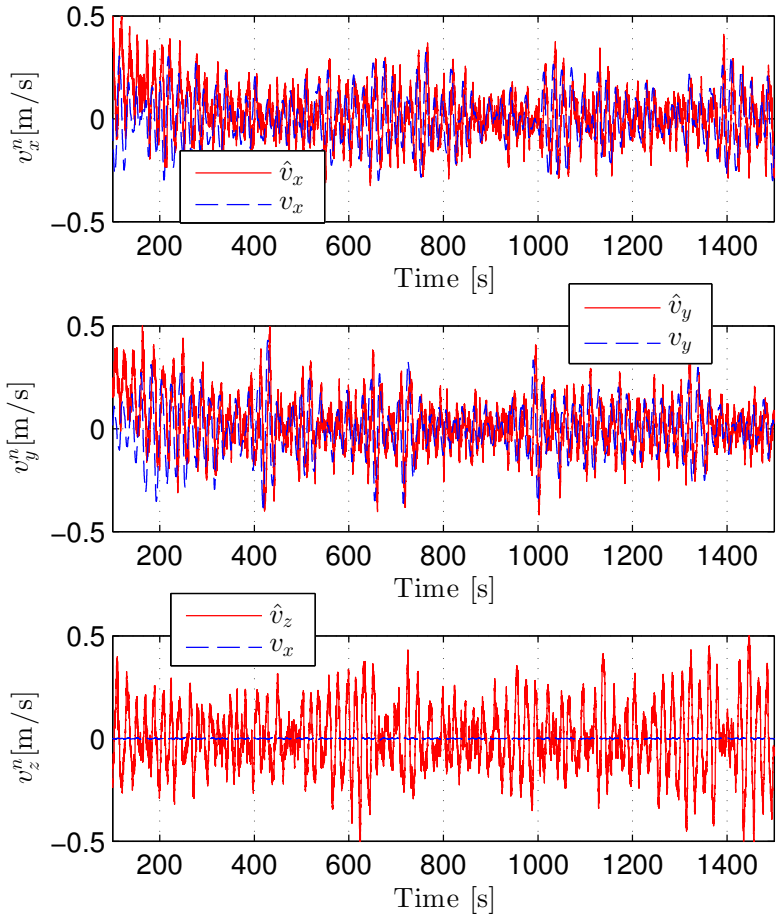

Figure E.11: Converged velocity estimates when no faults are present.

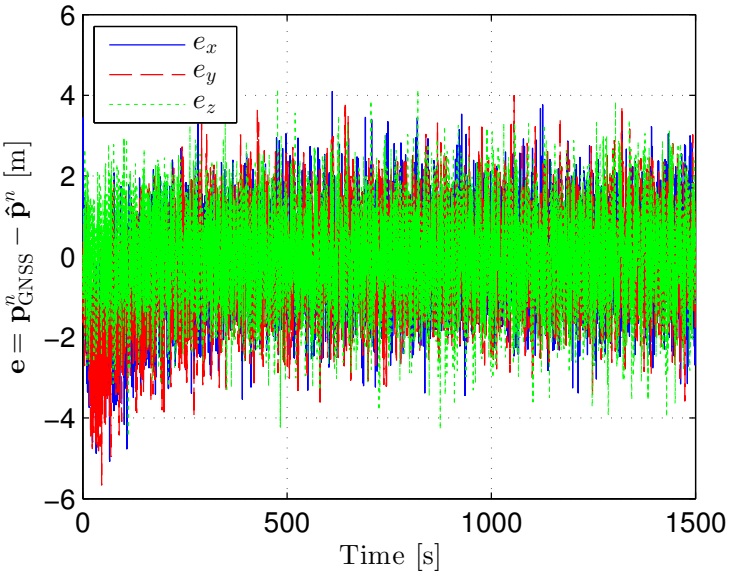

Figure E.12: Case 2, Fault free simulation. Estimation error, $\boldsymbol{e} = \boldsymbol{p}^n_{\text{GNSS}} - \hat{\boldsymbol{p}}^{\boldsymbol{n}}$.

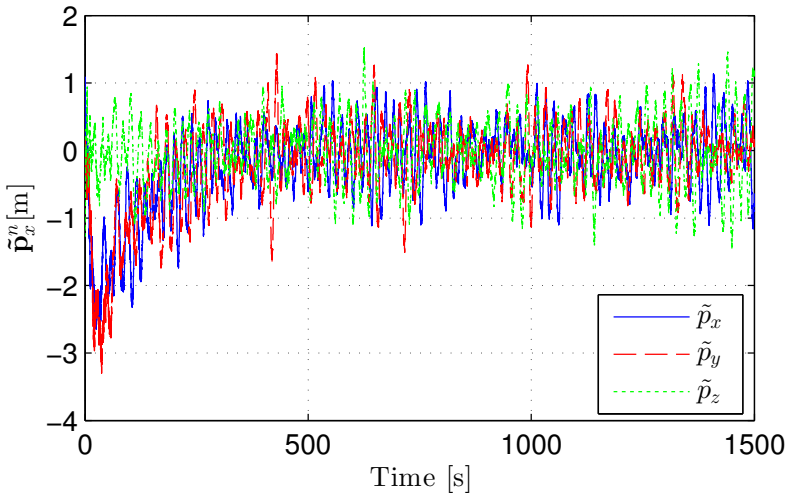

Figure E.13: Estimation error. Estimates , $\tilde{\boldsymbol{p}} = \boldsymbol{p} - \hat{\boldsymbol{p}}$[m] when no faults are present.

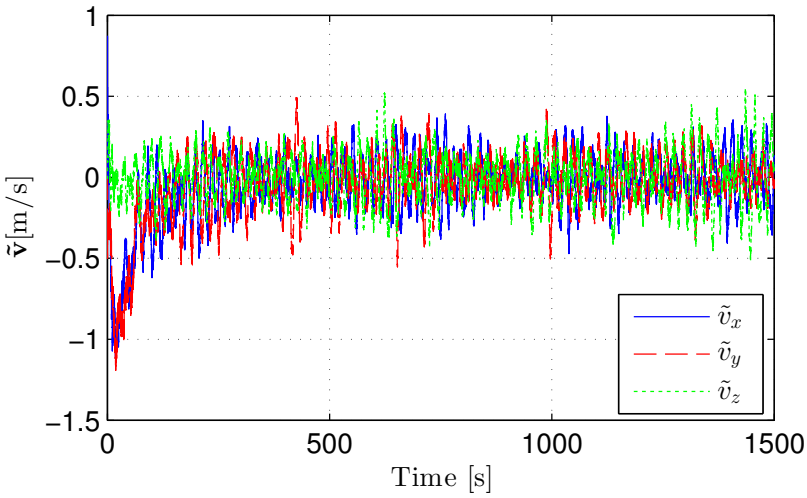

Figure E.14: Estimation error, $\tilde{\boldsymbol{v}} = \boldsymbol{v} - \hat{\boldsymbol{v}}$[m/s] when no faults are present.

E.2 Case: Increased Variance of One GNSS

The measurements from the two GNSS sensors which stay healthy are shown in Figure E.15 and E.16

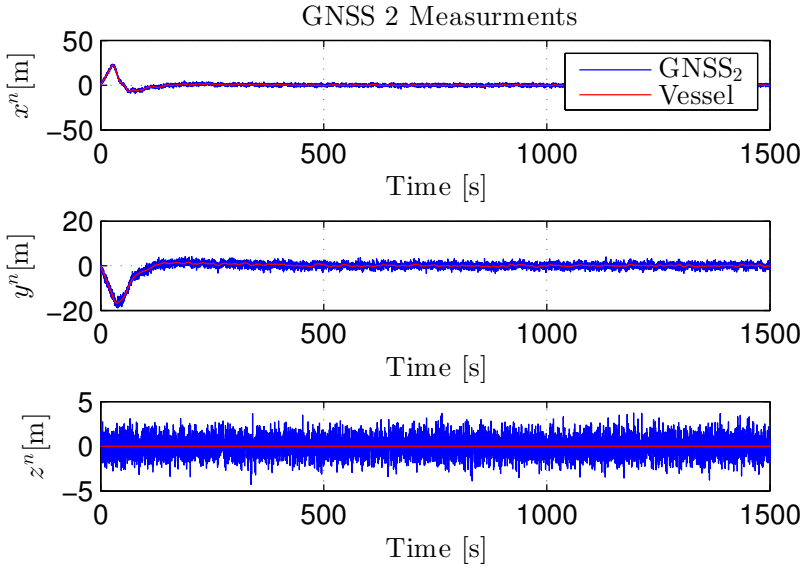

Figure E.15: Additional result regarding case 4. Measurements from GNSS 2

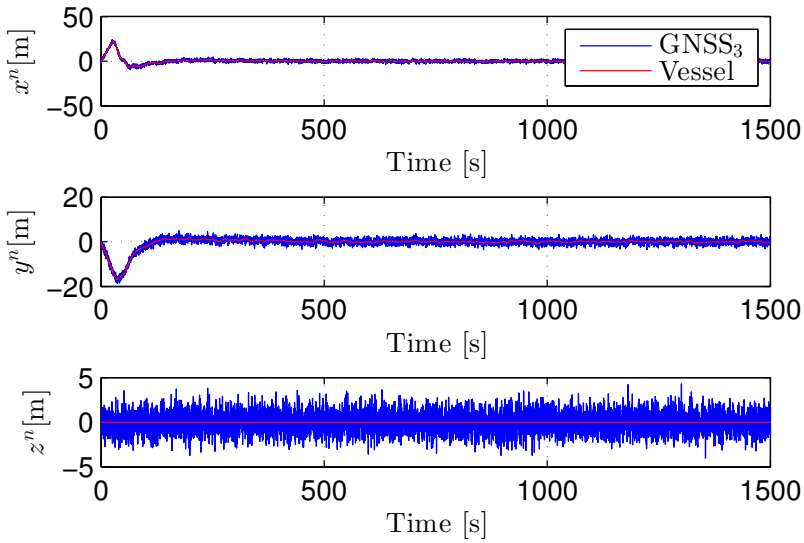

Figure E.16: Additional result regarding case 4. Measurements from GNSS 3

Appendix F

Digital Appendix

The digital appendix consist of a zip file with the MATLAB®scripts functions made during the work with this thesis.

A simulation is stated by running the `main.m` script file in MATLAB®. Simulation length, sensor and observer sampling time can be adjusted in the rig_simuation.txt configuration file. Sensor parameters are adjusted in the GNSS_config.txt and the IMU_config.txt file configuration files respectively.

The zip file also contains the following configurations files:

- rig_simuation.txt
- GNSS_config.txt
- IMU_config.txt

Change of injected sensor fault is done be opening the `fault_generator.m` function and enabled and disabled faults there, by setting the horizon of a given fault.

Some functions from the MSS. Marine Systems Simulator (2010) toolbox were utilized. The MSS toolbox must be located in the MATLAB®path in order to run any simulations. This toolbox may be downloaded, free of charge, at http://www.marinecontrol.org/.